UNIVERSITY OF ST ANDREWS

Monte Carlo Radiation Transfer Studies

of

Protoplanetary Environments

Christina Helen Walker M.Sci.(Hons) M.Sc.

A thesis submitted for the degree of Doctor of Philosophy

September, 2006

DECLARATION

I, Christina Helen Walker, hereby certify that this thesis, which is approximately 46000 words in length, has been written by me, that it is the record of work carried out by me and that it has not been submitted in any previous application for a higher degree.

Date: Signature of candidate:

I was admitted as a research student in October, 2002 and as a candidate for the degree of PhD in October 2003; the higher study for which this is a record was carried out in the University of St Andrews between [2002] and [2006].

Date: Signature of candidate:

I hereby certify that the candidate has fulfilled the conditions of the Resolution and Regulations appropriate for the degree of PhD in the University of St Andrews and that the candidate is qualified to submit this thesis in application for that degree.

Date: Signature of supervisor:

In submitting this thesis to the University of St Andrews I understand that I am giving permission for it to be made available for use in accordance with the regulations of the University Library for the time being in force, subject to any copyright vested in the work not being affected thereby. I also understand that the title and abstract will be published, and that a copy of the work may be made and supplied to any bona fide library or research worker, that my thesis will be electronically accessible for personal or research use, and that the library has the right to migrate my thesis into new electronic forms as required to ensure continued access to the thesis. I have obtained any third-party copyright permissions that may be required in order to allow such access and migration.

Date: Signature of candidate:

ABSTRACT

Monte Carlo radiation transfer provides an efficient modelling tool for probing the dusty local environment of young stars. Within this thesis, such theoretical models are used to study the disk structure of objects across the mass spectrum - young low mass Brown Dwarfs, solar mass T-Tauri stars, intermediate mass Herbig Ae stars, and candidate B-stars with massive disks. A Monte Carlo radiation transfer code is used to model images and photometric data in the UV - mm wavelength range. These models demonstrate how modelling techniques have been updated in an attempt to reduce the number of unknown parameters and extend the diversity of objects that can be studied.

ACKNOWLEDGEMENTS

"Just because you can't see something doesn't mean it's not there."

Small Soldiers 1998

CONTENTS

EXTENDED OUTLINE OF THESIS

The aim of this thesis is to study the structured dusty environments that are observed in the locality of young pre-main sequence objects. This is an environment that is beyond our immediate reach, but is one that we can model in an attempt to reflect reality. Chapter 1 begins by describing how the Interstellar Medium gives birth to stars and how, in the current paradigm for low mass star formation, the presence of an envelope and then a disk is natural at the protostellar phase. This chapter presents the indirect and direct evidence that has built up, primarily since the 1960s, in support of envelopes and disks and describes how modelling of these systems has become more advanced leading to greater understanding of the structure of the early circumstellar environment and the evolution of this structure. In this thesis, Monte Carlo scattered light and radiative equilibrium radiation transfer codes are used to model the circumstellar environment and make predictions of observational signatures. Chapter 2 introduces the theory behind these codes and presents benchmark tests as evidence of the reliability of the code. As Dawkin's points out in "The Ancestors Tale" models are only guides and cannot be expected to reproduce systems in a 100% accurate manner, however an obvious aim is to reduce and constrain parameters by utilizing as much information as possible. The vast majority of information we have about objects outwith our own solar system comes from observations of the electromagnetic radiation they emit. Our understanding of these objects is therefore restricted by the sensitivity of astronomical telescopes and detection technology. At ground level the atmosphere blocks or distorts much of the incoming electromagnetic radiation through scattering and absorption. The launch of instruments in space has removed many of the restrictions placed on ground-based instruments and have extended the range of pre-main sequence objects observed and the quality of the data received. Significant improvements have also been made at ground level through the use of adaptive optics. Increasing observations of disks in pre-main sequence stars have led to the belief they are common place and coupled with the suggestion that grain growth in disks may produce planets has led to a greater urge to understand the prevalence of disk systems and how they evolve with age. Chapters 3 to 6 show how improvements to the Monte Carlo radiation transfer techniques outlined in Chapter 2 have been applied to a wide range of pre-main sequence circumstellar environments. Chapter 3 investigates the possible structure of Brown Dwarf circumstellar disks. Chapter 4 presents models of the large scale structure of T-Tauri stars AA Tau and ASR 41, and the small scale structure of T-Tauri stars SU Aur, DR Tau and RY Tau. Chapter 5 presents models of Brown Dwarf, T-Tauri and intermediate mass Herbig Ae circumstellar disks that investigate grain growth and dust settling. Chapter 6 presents *Spitzer* observations of two objects that models suggest may be very large and massive disks illuminated by a B-star. Possible areas for future work are discussed in Chapter 7.

CHAPTER 1

DUSTY DISKS AROUND PRE-STELLAR OBJECTS

This chapter presents an overview of the main observational evidence for dusty disks in star systems and then describes how disks fit in with the current low mass star formation paradigm.

1.1   Introduction

The idea of a disk of dusty material surrounding a stellar object dates back to the 18th century when it was proposed that our own solar system was the remnant of such a disk, the so-called Kant-Laplace theory. This idea was supported by the observation that all of the eight major planets rotate in roughly the same plane, all revolve around Sun in the same sense (counterclockwise as viewed from above Earth's north pole) and most (but not all) rotate in the same counterclockwise sense. Venus and Uranus are the exceptions, however violent collisions may explain their retrograde orbits. Further evidence is provided by the fact there are planetesimals in orbit, the asteroids, and a thin debris dust disk remains - the zodiacal dust.

Debris disks are thought to be the remnant of earlier circumstellar disks, post planet formation, and may be composed of the left-overs from planet formation. Images of debris disks in AU Microscopii (Krist et al. 2005) and HD107146 (Ardila et al. 2004), which show inner gaps in the disk where planets may have swept up dust and cleared a path, along with infrared (IR) images taken by *Spitzer* of six further systems (Bryden et al. 2004) all of which have well confirmed planetary systems support this direct link between planet formation and disks. Most of the material in a planetary system will be trapped in the planets as opposed to the disk. Over time most debris will disappear, however our own solar system, thought to be ~ 5 billion years old, has a small amount remaining as mentioned above. This system is now thought to be in a quiet, stable phase lasting

10^{10} years. This quiet phase has allowed life to develop on Earth. If debris disks are indeed the remnants of circumstellar disks, and there is a link between disks and planet formation then an important reason for studying circumstellar disks is to try and gain a better understanding of how they evolve and possibly form planets.

It is now firmly established that dusty disks can be found in many of the younger sun-like systems, the T-Tauri stars. There is a multitude of both direct and indirect evidence for this. Over the past decade there has also been accumulating evidence for disks in lower and higher mass pre-main sequence objects. Whilst the conditions for planet formation in a disk are not fully understood, the discovery of disks around a variety of stellar masses at the very least opens up the tantalising possibility that a wide variety of planetary systems may be found in very different environments to our own. Evidence for disks around young Brown Dwarfs has also been a particularly exciting discovery as it suggests a star-like formation mechanism as opposed to a planet-like one, since disks are thought to be the natural consequence of star formation. As there is speculation that these disks may be the progenitors of debris disks harbouring planetary systems these disks will from this point onward be referred to as protoplanetary disks.

1.2 Observational Evidence for Protoplanetary Disks

1.2.1 Indirect Evidence

The first protoplanetary disks were discovered around Classical T-Tauri stars (CTTs) and they remain the most studied. This class of stars was identified by Joy (1945) and is characterized the presence of Balmer lines, Ca H and K lines in emission, a photospheric absorption spectra suggestive of late F type or later main sequence stars, but with the presence of lithium, and by photometric variability. The variability associated with CTTs is thought to arise in many cases from hot and cool spots on the surface, a feature now linked to accretion from disks (e.g. Lynden-Bell & Pringle 1974; Bouvier et al. 1993a). This is discussed more in Chapter 4. Many T-Tauri spectra show IR excess above the stellar spectrum and forbidden emission lines. Herbig (1961) suggested that the observed forbidden lines could arise in some form of circumstellar envelope and Low and Smith (1966) and Mendoza & Eugenio (1966) suggested (initially) that the observed IR excesses could arise from a spherical distribution of circumstellar dust.

The presence of an IR excess has now become synonymous with the presence of dusty circumstellar material. The IR excess results from the dust within the disk being heated through reprocessing of stellar radiation and viscous processes within the disk. The

dust emits at a wavelength dependent on its temperature and the further from the star the dust is located the cooler it will be so that the longer wavelengths sample further out in the disk. This point is illustrated in Fig. 1.1.
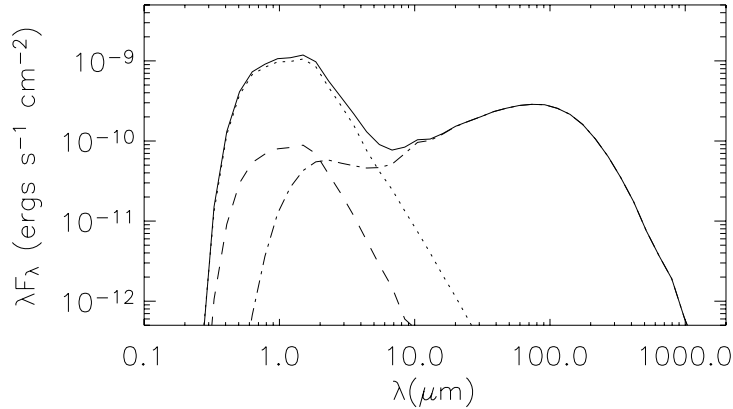
Figure 1.1: Example spectral energy distribution (SED) for a face-on star+disk system simulated using the Monte Carlo codes described in Chapter 2. The figure shows the various contributions from the star and disk that produce the resultant SED (solid line). The contributions are the input stellar spectrum (dotted line), the scattered light (dashed line) and the thermal emission from the disk material re-emitting at wavelengths determined by the local temperature (dot dash line).

Whilst a spherical distribution of dust would produce an IR excess it cannot explain some further observations. It was two years after their initial observation of an IR excess that Mendoza & Eugenio revised their theory on the required dust geometry. They were among the first to propose a flattened dust distribution (Mendoza & Eugenio 1968). Spherical distributions continued to be favoured for a time, models perhaps somewhat biased due to the ease of modelling this geometry, however within a few years further support for disks emerged: High optical polarization (Elsasser & Staude 1978) was interpreted as scattering within an elongated or flattened dust geometry, UV excesses were observed leading to accretion disk theory along with a plausible explanation for the variability associated with T-Tauri star, and millimetre continuum observations of several objects suggested masses of dust and gas that would preclude a spherical distribution of circumstellar material (Rydgren et al. 1982) as this would lead to higher optical extinctions than actually observed (e.g. Lada & Adams 1992). In addition, the presence of predominantly blue-shifted forbidden emission lines and a lack of red-shifted emission lines (Edwards et al. 1987; Hartigan et al. 1995) is hard to explain in the presence of an optically thick envelope, rather it is indicative of low density gas envelopes and/or stellar winds/jets/outflows which have their red-shifted component occluded by an optically thick

disk close to the star (Appenzeller et al. 1984; Edwards et al. 1987).

1.2.2 Imaging of Disks

For many years the evidence for circumstellar disks was all indirect. Their presence simply provided a means to account for the observations of IR excesses, high polarization, asymmetry in stellar winds, UV veiling and the observation of collimated jets. Whilst a disk like structure could tie these observations together, direct imaging was desirable to confirm what remained a hypothesis.

The first disks to be imaged were in fact debris disks and not protoplanetary disks. β Pic was the first, imaged optically by Smith & Terrile (1984). This was only one year after the presence of the disk was initially inferred from Infrared Astronomical Satellite (IRAS) measurements of an IR excess (Aumann 1984). In comparison, the first images of protoplanetary disks appeared in the mid-1990s despite the first evidence for T-Tauri disks appearing decades earlier. Imaging of disks in the optical and near-IR has been hampered by the large dynamic range. As discovered by Whitney & Hartmann (1992), who generated scattered light images of model disks, for many observational situations the star will be much more luminous than the disk and the wings of the point spread function (PSF) will veil any disk emission. β Pic was imaged with ground based coronography and this was only possible because of its youth, i.e. it still contains a significant amount of dust, and because it is close-by (19 parsecs (pc)). Most protostellar disks are located in star formation regions, which are at substantially greater distances presenting a major problem to observers. For example, a typical T-Tauri disk of 100 AU (Astronomical Unit) within Taurus or Rho Ophiucus ($\sim$140 pc), two of the closest star formation regions, would only extend a diameter of 1.4 arcsec. At the distance of the Orion molecular clouds, the nearest site of known high and low mass star formation ($\sim$ 500 pc away) the disk would only be 0.5 arcsec in diameter.

Sometimes nature provides a solution and disks are oriented close to edge-on obscuring the central star (e.g. Burrows et al. 1996; Padgett et al. 1999, see Fig. 1.2). A similar effect can be created by using coronographic techniques to block out the central star (e.g. Mayama et al. 2006; Grady 2004; Trilling et al. 2001). Disks can also sometimes be imaged silhouetted against background nebulosity (e.g. O'Dell & Wong 1996; McCaughrean & O'Dell 1996, see Fig. 1.3). These images were all taken with the Hubble Space Telescope (HST). Most imaging is of scattered starlight in the optical and near-IR. Scattered light from a few disks have also been imaged in the mid-IR (MacCabe et al. 2003; Duchêne et al. 2004).
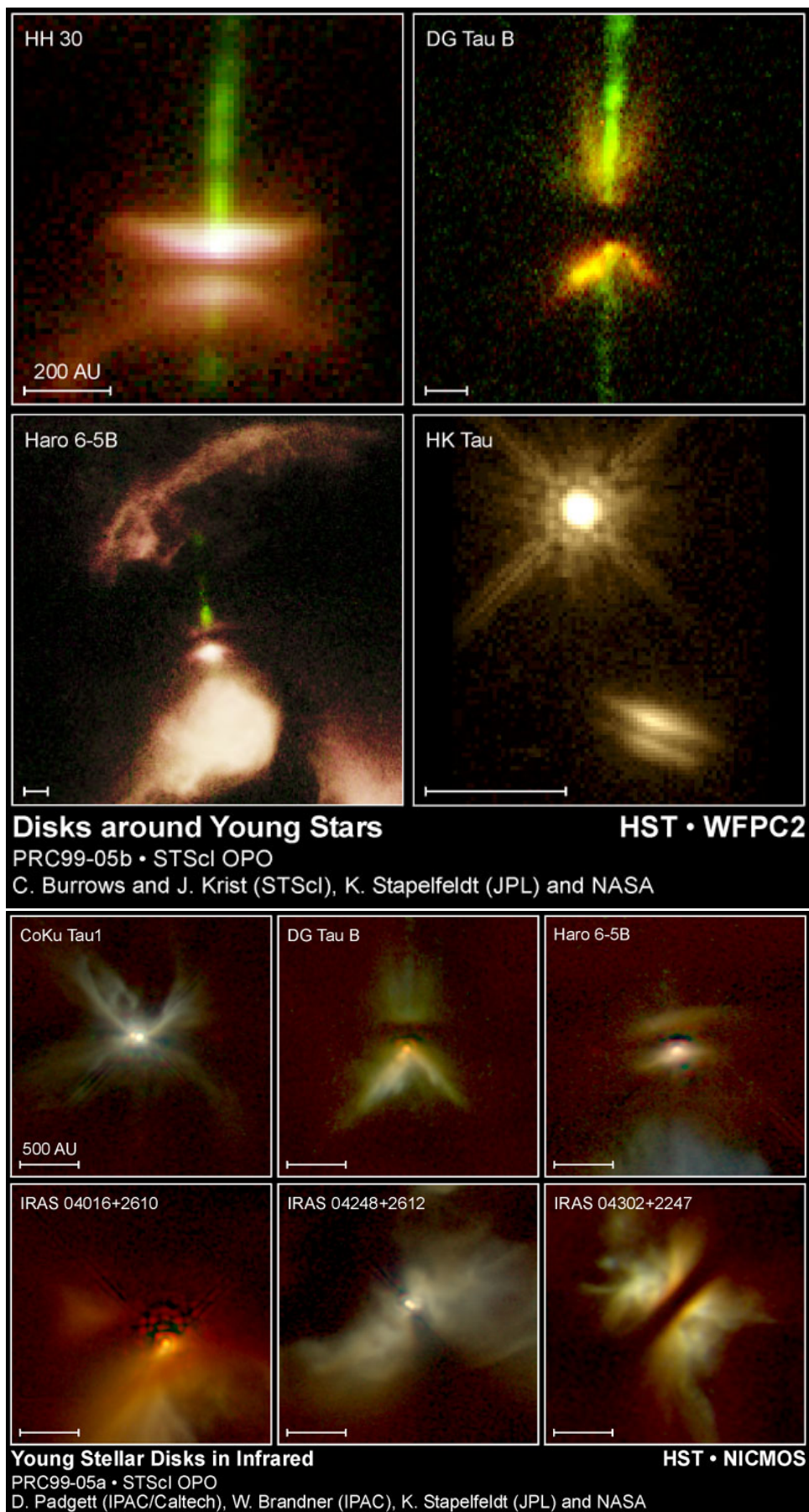
Figure 1.2: HST IR scattered light images of inclined disks around young newly forming stars. The source of the images is indicated.

**Protoplanetary Disks
Orion Nebula**

HST · WFPC2

PRC95-45b · ST Scl OPO · November 20, 1995
M. J. McCaughrean (MPIA), C. R. O'Dell (Rice University), NASA
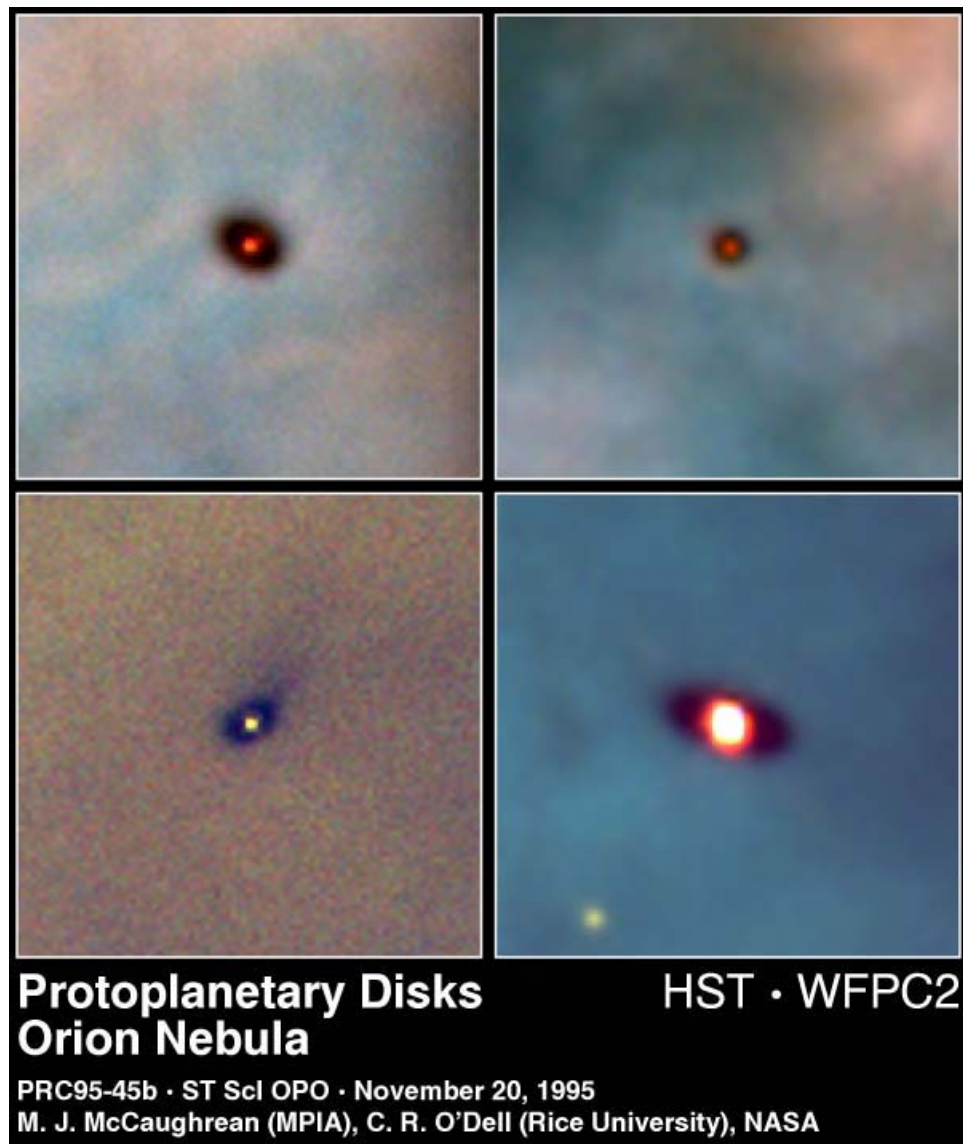
Figure 1.3: HST images of disks around young stars silhouetted against the bright background of the hot gas of the Orion Nebula. The red glow in the centre of each disk is a young newly forming star. The source of the images is indicated.

Thermal imaging is possible in the mid-IR, sub-millimetre and millimetre although it is usually of too low resolution to study the structure of the dust disk. However, it can be of use when studying the gas disk (e.g. Mundy et al. 1996). Other techniques include speckle interferometry, adaptive optics, and PSF subtraction and deconvolution by comparison with a similar diskless star (see Koerner 2001 for comprehensive review). Together these techniques help to reinforce theories and build up a more comprehensive picture of SOME circumstellar disks. However, indirect evidence still provides the vast majority of data and for many objects e.g the low luminosity, low mass Brown Dwarfs, the only data.

1.3 Disks and Star Formation

1.3.1 The Birth of a Star

In order to understand how disks are thought to form it is useful to review the star formation process. It is thought that star formation occurs as a result of the gravitational contraction within molecular clouds. This theory is supported by IRAS observations of protostars deeply embedded in the cores of giant molecular clouds (Beichman et al. 1986; Myers et al. 1987). A number of events are thought to be possible triggers for gravitational contraction including collisions and shocks. Whatever the cause, clouds become differentiated into regions of high and low density and it is widely accepted that the gravitational contraction of the densest regions (cores[1]) could result in the eventual formation of a star. These dense cores from which stars are thought to form are typically a few tenths of a parsec across and have densities of $n = 10^{5-6}$ cm^{-3}. This compares with number densities of $n = 10^3$ cm^{-3} within the bulk molecular cloud and with typical number densities of $n = 1$ cm^{-3} within the diffuse interstellar medium (ISM). A simple description of how a star forms follows:

If it is assumed that thermal motions of the molecular gas are all that oppose gravity, then the minimum mass that will start run-away self-contraction is given by the Jeans Mass (Jeans 1902),

$$M_J = \left(\frac{5k_b T}{G\mu m_h} \right)^{3/2} \left(\frac{3}{4\pi\rho_0} \right)^{1/2} \tag{1.1}$$

where k_b is the Boltzmann constant, T is the local temperature of the cloud, G is Newtons

---

[1]In some texts a core is said to fragment further into a clump out of which a star forms whilst in others a clump is said to fragment into cores. This is highly confusing. To clarify, in this thesis the term 'core' is used to describe the high density region out of which a single star forms.

constant, μ is the molecular weight, m_h is the mass of a hydrogen atom and ρ_0 is the density of the core.

If only gravitational forces are considered, collapse is expected to continue indefinitely unless a sufficient opposing force is presented. As collapse progresses the cloud fragments and small parts of the cloud contract on their own. Initially collapse is isothermal and as collapse progresses, the density will become increasingly higher and this implies increasingly lower M_J values. This will continue until the opacity of the cloud rises such that collapse becomes adiabatic and gravitational energy released from infall can heat the cloud such that T^3 increases at a faster rate than the base density. At this point free-fall time $t_{ff} > t_{sound} (=$ Radius/Local Sound Speed) and pressure forces win. The time for this free-fall or dynamical collapse phase can be estimated from (Spitzer 1978),

$$t_{ff} = \left(\frac{3\pi}{32G\rho} \right)^{1/2} \qquad (1.2)$$

Assuming a typical molecular cloud number density of $n = 10^5$ cm^{-3} and assuming a pure hydrogen (H_2) cloud this gives $t_{ff} \sim 10^5$ years, a relatively short time in comparison to the other stages of star formation. In reality, observations suggest many clouds of mass greater than M_J do not collapse. Indeed, if all clouds of mass greater than M_J were to collapse on a free-fall timescale the rate of star formation within the Galaxy would be far too high compared to observational estimates (Zuckerman & Palmer 1974). It has been clear for decades that additional forces must support these clouds against gravity. Various mechanisms of support have been proposed and whilst they vary in detail the majority involve the presence of magnetic fields (e.g. Chandrasekhar & Fermi 1953; Mestel 1965; Spitzer 1968; Mouschovias 1976; Norman & Silk 1980; Larson 1981).

The length of the protostellar phase is controlled by the build up of thermal pressure support. When the core is massive enough, and therefore hot enough, to trigger nuclear fusion of deuterium (~ 0.013 $M_\odot$), the outward pressure of radiation slows, but does not completely stop collapse. Material continues to accrete onto the central protostar and if the mass exceeds ~ 0.08 $M_\odot$ hydrogen burning begins and a star is formed. The final stellar radius will be many orders of magnitude smaller than its pre-collapse parent core radius.

1.3.2 The Formation of a Disk

During the initial collapse phase the protostar is heavily embedded within an accreting envelope. Assuming the parent core has non-zero angular momentum then material at large radii and close to the rotation plane will be unable to flow directly onto the star and

instead will fall onto the mid-plane forming a disk from which material then accretes onto the star.

Angular momentum L for a cloud of molecules (or any system of particles) is

$$L = \sum_n (r_n \times m_n v_n) \tag{1.3}$$

where r_n is the position vector of the particle relative to core centre, v_n is the velocity of the particle and m_n is the particle mass. In order to conserve angular momentum, which is a fundamental principle, then from Eqn.1.3 it can be seen that if the particle's position r_n decreases dramatically as it would during collapse onto the central protostar then v_n must increase proportionally in the direction perpendicular to L and r_n i.e. the angular velocity of the protostar would increase and even a very small initial rotation would result in a stellar velocity exceeding break-up. This problem is partially alleviated, however, because material falling in perpendicular to L must convert some of its infall velocity to rotational motion which slows infall in this direction such that a disk of material forms around the central point. Material will still accrete from the disk however it will do so at a reduced rate and there are a number of further mechanisms associated with the disk that are believed to redistribute angular momentum such that most of the mass can move inward and accrete without transferring too much angular momentum to the forming star. Further discussion on angular momentum transport follows below and in Chapter 2.

Over time the surrounding infalling envelope will diffuse and only a gradually shrinking accretion disk will remain. In some systems strong winds are observed radiating from the poles (e.g. HH 30; see Fig. 1.2). These outflows are often seen when they shock the surrounding medium giving rise to strong line emission. These shocked objects are called Herbig-Haro (HH) objects. The outflows may also be observed in radio line emission that escapes extinction. Outflows are thought to be powered by the interaction of a magnetic field with a rotating accretion disk (see Königl & Ruden 1993; Bachiller 1996). It is suggested that these outflows could help to remove angular momentum from the system (e.g. Ray & Bacciotti 2003) as although the angle between outflow and L is small, the outflow has a high velocity. It is also thought that by sweeping up envelope material, these outflows may be involved in reversing infall and clearing the envelope to expose the central star (Raga & Cabrit 1993; Li & Shu 1996; Padman et al. 1997).

The vast majority of mass accumulation by the central protostar is thought to take place during these early stages of evolution. This theory is supported by the apparent trend that accretion rate decreases with time (e.g. Hartmann et al. 1998). On average, accretion rate appears to decrease steadily with time, however in the very early stages of evolution young stars are thought to go through transient phases of high accretion possibly triggered by thermal instabilities in the inner disk (Lin et al. 1985; Clarke et al. 1990; Kawazoe

& Minesshige 1993; Bell & Lin 1994; Bell et al. 1995). This is a common explanation for the young low mass FU Ori objects. FU Ori objects are characterized by a sharp increase in brightness by several orders of magnitude over timescales of months to years (Herbig 1977). Luminosity increases from typical values for CTTs to a few hundred $L_{\odot}$. During FU Orionis outbursts emission is dominated by accretion rather than irradiation. Accretion rates have been estimated to be $\sim 10^{-4}$ to $10^{-6} M_{\odot} \mathrm{yr}^{-1}$ (see review by Calvet et al. 2000, and references therein). For T-Tauri stars typical accretion rates of 10^{-6} to $10^{-9} M_{\odot} \mathrm{yr}^{-1}$ have been derived through a variety of methods (e.g. Basri & Bertout 1989; Hatigan et al. 1995; Gullbring et al. 1998; Meyer et al. 1997).

When the protostar becomes optically visible it is often said that it is entering the T-Tauri phase as this is the name given to precursors to solar type stars and the star formation paradigm was originally designed to describe the evolution of a solar type star. As evidence in this thesis supports a similar phase for a wider range of objects, this will be referred to as the pre-stellar phase. At this stage little is likely to remain of the infalling envelope. Most parent material will now have accreted onto the star or be in the process of accreting from a disk.

During the pre-stellar phase it is speculated that dust particles in the disk grow larger and larger and stick to one another through collisions eventually forming planetesimals, the building blocks of planets (e.g. Beckwith et al. 2000). Sufficiently large bodies in a disk should be able to accrete gas providing the groundwork for atmospheres in smaller rocky planets and possibly generating gas giants in larger bodies (Pollack et al. 1996; Bodenheimer et al. 2000). The process of planet formation is still, however, not well understood. By the end of the pre-stellar phase the new-born star will be visible, little accretion will be taking place and the star may have companion(s) of stellar or planetary nature.

1.3.3 A Classification System for Pre-stellar Objects

It is clear the local environment of a protostellar object changes dramatically on the road to stardom. This change is nicely illustrated and simplified by the classification system of Adams et al. (1987), Myers et al. (1987) and later updated by André et al. (1993). This system describes a pre-main sequence star as class 0, I, II, or III depending on the shape of the SED. The changing shape of the SED indicates different dust distributions and therefore could represent different evolutionary stages. At Class 0 the forming protostar is deeply embedded in its parent molecular cloud. Class I describes the stage where the protostar still has an envelope of material accreting onto it, but this envelope is gradually

being cleared away due to winds and jets. By class II most parent material will have accreted onto the star or be in the process of accreting from a shrinking disk. For solar type stars observations suggest disks are at this stage typically a few 100 AU in radius (e.g Burrows et al. 1996; Lucas & Roche 1998; Stapelfeldt et al. 1998b; Padgett et al. 1999; Monin & Bouvier 2000; Brandner et al. 2000; Grosso et al. 2003; Jayawardhana et al. 2002). At the end of this phase the new-born class III star will be highly visible in the optical. This point is sometimes referred to as the birth of the protostar and the onset of the pre-main sequence phase (Stahler 1983). These stages are well summarized by Fig. 1.4.
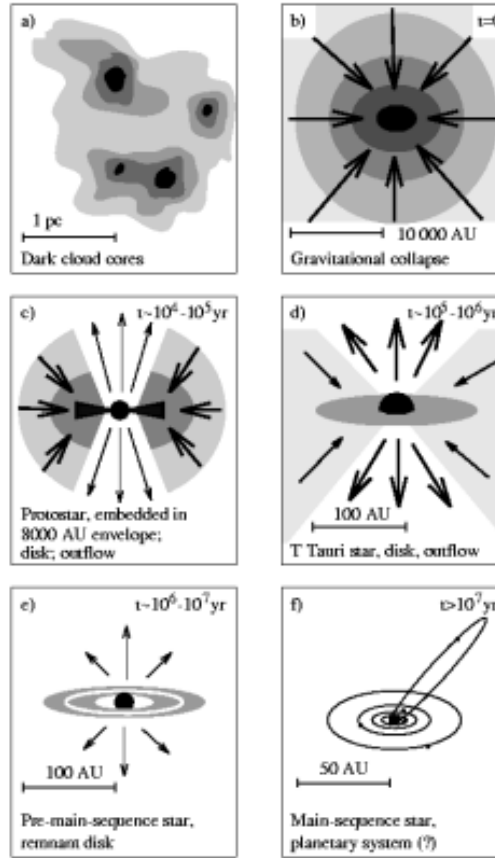
Figure 1.4: Illustration of star+disk formation and evolution based on Shu et al. (1987) and taken from Hogerheijde (1998).

1.4   Summary

In summary there is an abundance of indirect and direct observations that suggest the presence of dusty disks in pre-stellar objects. Disks are thought to be natural consequence of low mass star formation although there is increasing evidence for their presence in higher mass systems. It is therefore important to understand how these disks evolve in order to gain a greater understanding of the star formation and planet formation process. This thesis concentrates primarily on the pre-stellar environment at the Class I and II stages of star formation, with particular emphasis placed on pre-main sequence disks.

CHAPTER 2

DISK PHYSICS AND MODELLING

This chapter begins by introducing the Monte Carlo radiation transfer codes used for modelling in chapters 3 to 6. This code and its past developments are described in several papers (Code & Whitney 1995; Whitney & Hartmann 1992, 1993; Wood et al. 1996a; Bjorkman & Wood 2001) and therefore only an overview of how the code operates is presented here. This includes a review of important physics required for the realistic modelling of disks, namely the concept of passive and active disks, the temperature and density structure of disks, and the scattering and absorption properties of the opacity sources (dust). A number of new code developments have taken place and the physics behind these and their implementation are described in more detail. The final section of this chapter makes comparisons with other similar codes. Note, chapters 3 to 6 also contain a summary of the code development relevant to the work within the individual chapters.

2.1 Monte Carlo Radiation Transfer

Monte Carlo refers to a simulation that utilizes sequences of random numbers. The term is thought to have been first used in print by Metropolis & Ulam (1949) following the Manhattan Project of World War II. The capital of Monaco, Monte Carlo, was a centre for gambling and so it seems likely the expression arose due to the similarity of statistical simulation to games of chance. Monte Carlo methods can be used to describe the evolution of any physical or mathematical system that can be described by probability distribution functions (PDFs). A PDF describes the likelihood a parameter will have a certain value. A Monte Carlo simulation proceeds by sampling from these PDFs. Sampling requires a source of random numbers on the unit interval; here, RAN2 from Numerical Recipes in FORTRAN (Press et al. 1992) has been used. The aim is to sample parameters so that

their PDF is reproduced. This can be achieved using the cumulative distribution function (CDF), which is the area under the PDF. The probability that a particular value X will occur can be equated to a random number like so:

$$\xi = \frac{\int\limits_{xmin}^{X} P(x)dx}{\int\limits_{xmin}^{xmax} P(x)dx} \qquad (2.1)$$

Normalization occurs over the defined interval in which x exists. It follows that the parameter X is a function of ξ, which can be solved for.

In some cases, where it is hard to solve for X or there is no closed analytic expression for X, a rejection method is applied. This method requires that the peak value, P_{max}, of the PDF is known on the interval x[a,b]. This method works by sampling from a uniform distribution for X between a to b and either accepting or rejecting this value based on a sample from a uniform distribution in y between 0 and P_{max}. If $P > P(X)$ then X is rejected.

The work in this thesis is focused on the propagation of electromagnetic radiation and its interaction with any medium it encounters. These processes are simulated by sampling randomly from the various PDFs that determine the interaction lengths, scattering angles and absorption rates of photons. A total luminosity is allocated to a system, L, which is then split equally among a specified number, N_γ, of photon packets with energy, $E_\gamma = \frac{L\Delta t}{N_\gamma}$. Each photon packet has the same energy, but not necessarily the same number of photons as this depends on the frequency. These photon packets are individually released in a particular direction of travel, then travel some randomly sampled optical depth before undergoing a probabilistic interaction whose nature is determined by the scattering and absorption cross-sections of the particles in the medium.

Two Monte Carlo radiation transfer codes have been used in this thesis - a scattered light code that is used for generating optical and near-IR scattered light images and a Monte Carlo radiative equilibrium code used for producing model spectral energy distributions (SEDs) and multi-wavelength images. The radiative equilibrium code runs as follows:

Photons are released from the surface of a uniformly bright source in an outward direction into a hemisphere which prevents the photon packet from entering the star. The physical distance L travelled by a photon packet before it interacts (scatters or absorbs) can be indirectly determined using the definition for optical depth,

$$\tau = \int\limits_{0}^{L} n\sigma dl. \qquad (2.2)$$

$n\sigma$ is the fraction of photon scatters (or absorptions) per unit length, $\frac{1}{n\sigma}$ is the average distance travelled before an interaction occurs or the mean free path and therefore the optical depth over distance L is essentially the number of photon mean free paths over that distance. The probability of travelling a distance dl without interaction is 1-$n\sigma dl$. If a length L is made up of $N \times dl$ then the probability of travelling a distance L without an interaction is simply a multiple of the probability of travelling dl without an interaction,

$$P(L) = (1 - n\sigma L/N)^N \qquad (2.3)$$

$$\lim_{N\to\infty} P(L) = e^{-n\sigma L} = e^{-\tau} \qquad (2.4)$$

It is easy to sample from this PDF, using Eqn. 2.1, to obtain the relation,

$$\tau = -\log(1 - \xi) \qquad (2.5)$$

Once a photon packet has travelled L the interaction, whether the photon is absorbed or scattered, is determined by the albedo of the dust grains at that location. The albedo, the probability that a photon is scattered, is defined as

$$a = \frac{n_s\sigma_s}{n_s\sigma_s + n_a\sigma_a} \qquad (2.6)$$

The interaction is determined by sampling a uniform distribution between 0 and 1 and comparing it to the albedo. If $\xi < a$ the photon is scattered and its new direction of travel is determined by the angular phase function of the scattering medium. For dust scattering the code uses a single peaked Henyey-Greenstein phase function (e.g. White 1979),

$$HG(\theta) = \frac{1}{4\pi} \frac{1 - g^2}{(1 + g^2 - 2g\cos\theta)^{3/2}} \qquad (2.7)$$

where θ is the scattering angle and g is the scattering asymmetry parameter which describes how forward throwing the phase function is ($g = 1$: all radiation thrown forward, $g = 0$: scattering is isotropic). Equation 2.7 is normalised over 4π steradians. Cos θ is therefore sampled from $2\pi HG(\theta)$ as follows,

$$\cos\theta = \frac{1 + g^2 - [(1 - g^2)/1 - g + 2g\xi]^2}{2g} \qquad (2.8)$$

If a photon packet is absorbed then its energy will be transfered to the absorbing medium and to conserve radiative equilibrium the packet will then be re-released from the interaction location with a new frequency and in a new direction of travel. Thermally re-emitted photon packets are released isotropically.

The heating of the absorbing medium is discussed in Sect. 2.1.5 and Sect. 2.1.6. Following interaction the thermally re-emitted or scattered photon packet continues on to a new interaction location and this continues until the photon packet escapes the boundary

of the system. This method conserves energy because all photons escape. Once a photon packet escapes the system it is placed in a bin according to its frequency and direction of travel. This information allows SEDs to be generated for the different viewing angles since flux is proportional to the number of photon packets within a bin.

The code can also produce multi-wavelength images generated by mapping the position of exit of each photon onto a plane. For optical and near-IR simulations scattered starlight can normally be assumed to dominate images with little contribution from dust reprocessing, therefore it is often sufficient to use the scattered light code to generate images at short wavelengths. This code assumes all absorbed photons are reprocessed to long wavelengths beyond what is of interest. The code terminates each photon after a number of scattering events greatly reducing the computer processing time needed in comparison to the radiative equilibrium code.

Both the radiative equilibrium and scattered light codes make use of a peeling-off technique (Yusef-Zadeh et al. 1984) to improve signal to noise. In the case of the radiative equilibrium code this technique also produces a high resolution SED for the given viewing angle. Briefly, at each emission location a fraction of the photon's energy is 'peeled-off' and directed toward the observer. The total intensity is the sum of the weighted direct, scattered, and thermal photons. The weight of direct photons emitted from the stellar surface is,

$$W_{direct} = \frac{e^{-\tau}}{\pi d^2} \qquad (2.9)$$

where τ and d are the optical depth and physical distance from the point of emission to the observer. The factor $e^{-\tau}$ compensates for extinction along the line of sight. In the scattered light code all photons are forced to scatter once, at an optical depth sampled from,

$$\tau = -log[1 - \xi(1 - e^{-\tau_1})] \qquad (2.10)$$

(Witt 1977) where τ_1 is the optical depth from the point of emission of the edge of the grid. This reproduces the PDF for optical depths. Following this forced first scattering photons are scattered into directions randomly sampled from the scattering phase function (Eqn. 2.7) and will travel a random optical depth (Eqn. 2.5) before undergoing another interaction or being terminated if taken outside the grid. After N scatterings the weight of each peeled-off photon is,

$$W_{scatt} = a^N (1 - e^{-\tau_1}) e^{-\tau_2} HG(\theta)/d^2 \qquad (2.11)$$

where a is the albedo of the scattering particles in the medium and τ_1 is the first optical depth, τ_2 is the optical depth from the photons current position to the observer ($e^{-\tau_2}$ is the probability of escape toward the observer) and the function HG(θ) weights the photon

by the scattering phase function where θ is the angle through which the photon is being forced to scatter toward the observer. The factor $(1-e^{-\tau_1})$ compensates for the forced first scattering. In the radiative equilibrium code there is no forced first scattering reducing the weight of the photons that do scatter to,

$$W_{scatt} = e^{-\tau_2} HG(\theta)/d^2 \tag{2.12}$$

In the radiative equilibrium code, when a new photon packet is emitted following an absorption event, or when an accretion photon packet is generated and released within the disk, a fraction of the photon's energy is peeled-off and directed toward the observer. These photon packets are effectively released isotropically into 4π steradians from a point source which gives the weight of each peeled-off photon as,

$$W_{thermal(and\ accretion)} = \frac{e^{-\tau}}{4\pi d^2} \tag{2.13}$$

The peeling-off technique naturally increases computer processing time, but gives high signal-to-noise SEDs and images for a specified viewing angle.

2.1.1   The Model Grid

The program discretizes the density structure using a 3-D spherical polar grid (Whitney & Wolf 2002) so that each grid cell has its faces defined by radial (r), latitudinal (θ) and longitudinal co-ordinates (ϕ). When the systems being modelled are considered to be symmetric it is only necessary to consider r and θ. In radius the grid stretches from an inner radius R_{min} to outer radius R_{max}. The outer radius is always specified, whereas the inner radius can be specified or calculated as described in Sect. 2.1.3. Beyond the inner disk edge grid spacing in r is given by,

$$r(i) = R_{min} + (R_{max} - R_{min}) * [(i-2)/(nrg-1)]^3 \tag{2.14}$$

where i is the number of radial faces starting from $i = 2$. The first radial face ($i = 1$) is set to be the surface of the star. nrg is the number of cells in the radial direction. Using this griding, cells close in the centre are smaller than those further out which allows the density and temperature structure of the inner edge of the disk to be more highly resolved. Within the grid, spacing in θ and ϕ is even. However, when a photon packet exits the system it is binned in cosine of the inclination which ensures bins of equal solid angle.

2.1.2   Opacity and Dust Properties

The way in which a photon packet interacts with the medium into which it is released depends on the properties of the particles in that medium, in this case the dust and gas

18

of the circumstellar environment. Perhaps not surprisingly the solid particles within disks (and envelopes) are found to consist largely of silicate and carbon, the bulk materials of the ISM, and frozen ices, collectively referred to as dust grains. Dust only makes up $\sim 1\%$ of the ISM by mass however it is assumed that it is the dominant opacity source. In many cases disks have been modelled using an ISM grain distribution such as that of Kim et al. (1994, hereafter KMH). Collisions within the disk may however result in larger grains forming (e.g. Wetherhill 1980; Weidenschilling 1980) and indeed in many cases small grains do not appear to match observations.

Evidence for larger grains comes from millimetre observations (Beckwith et al. 1990; Beckwith & Sargent 1991; D'Alessio et al. 2001; Wood et al. 2002a), and optical and IR (OIR) scattering (D'Alessio et al. 2001; Cotera et al. 2001). Larger grains have higher millimetre opacity and are therefore better scatterers and absorbers producing shallower slopes of the long wavelength SEDs and larger millimetre fluxes compared with those expected for ISM dust parameters. Conversely, the opacity in the OIR is expected to fall as grains grow resulting in a flatter OIR spectrum. Larger grains therefore reduce or remove the silicate emission feature at $\sim 10~\mu$m. The presence or lack of a silicate feature is therefore often considered to be an important indicator of grain growth. The effect of increasing dust grain size on the SED is shown in Fig. 2.1. A lower opacity in the OIR will also affect the width of dust lanes visible in scattered light images of edge-on disks. The thickness of the dust lane depends on opacity (κ_ν) $\times$ disk mass and therefore without absolute measurement of disk mass it is not possible to constrain κ_ν. However, the relative dust lane width at different wavelengths will also vary depending on the grain size. For example, Cotera et al. (2001) found when fitting images of HH 30 that $\frac{\kappa_J}{\kappa_K} = 1.37$ which compares to 1.86 for the ISM. Similarly Watson & Stapelfeldt (2004) also model HH 30 however in this case over a wider wavelength range and find $1.0 \leq \frac{\kappa_B}{\kappa_K} \leq 3.0$ which compares to an expected value for ISM grains of $\frac{\kappa_B}{\kappa_K} > 8$.

For many of the models in this thesis the dust distribution used by Wood et al. (2002a) to model HH 30 IRS will be used. This distribution extends the grain size of the KMH ISM distribution up to 1 millimetre and also has an exponential cut-off added to the power law distribution of the KMH distribution. The functional form of this grain size distribution is,

$$n(a)~da = C_i~a^{-p}~\exp\left(-[a/a_c]^q\right)~da~. \tag{2.15}$$

The parameters p, a_c and q control the distribution shape. C_i is set by requiring the grains to completely deplete a solar abundance of carbon and silicone (see Wood et al. 2002a for details). When fitting HH 30, Wood et al. (2002a) found that a distribution with $p = 3$, $q = 0.6$ with grain size in the range 0.005 μm - 1 millimetre with the division of grain size power law and exponential distributions at $a_c = 50~\mu$m provided a fit to millimetre

observations. This dust distribution will be referred to as HH30 from this point onward. A comparison of parameters associated with the two dust distributions is presented below.
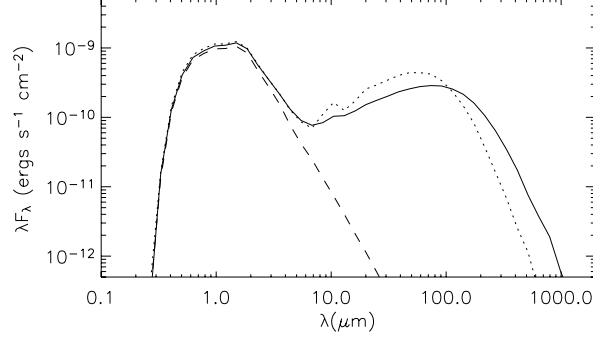
Figure 2.1: Model SEDs generated using the larger grained dust distribution of (Wood et al. 2002a)(solid line) and ISM dust (dotted line). The larger grains produce larger mm fluxes and a flatter OIR spectrum compared with the ISM model. All other input parameters are identical - $R_\star = 2\ R_\odot$, $T_\star = 4000\ K$, $M_\star = 0.5\ M_\odot$, $M_{disk} = 0.01\ M_\odot$, $R_{max} = 200\ AU$, $\beta = 1.275$, $\alpha = 2.275$ (see Eqn. 2.18)
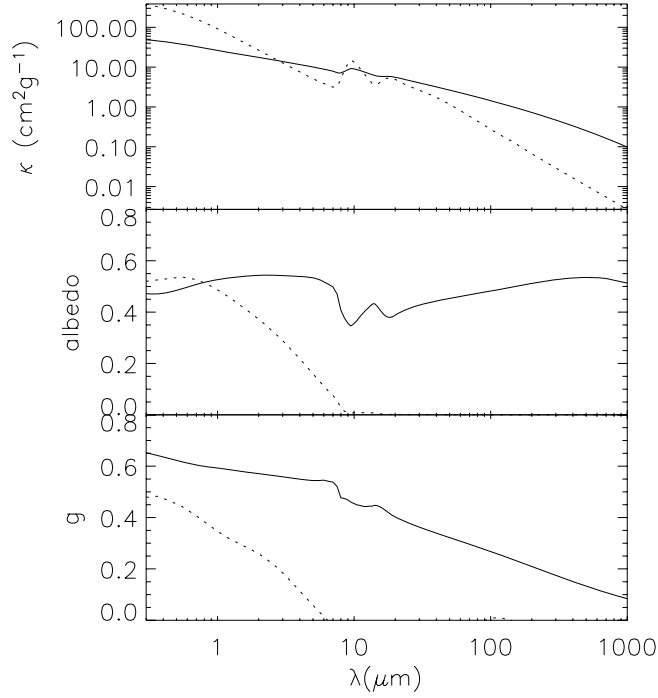
Figure 2.2: Dust opacity, albedo and scattering asymmetry parameters for ISM grains (dotted lines) and the HH30 size distribution (solid lines) use for fitting the HH 30 SED (Wood et al. 2002a).

2.1.3 Disk Geometry

Model dust disks extend from a sharply cut-off inner radius out to a specified distance. The minimum inner radius is normally defined by the dust destruction temperature which is taken to be 1600 K, the sublimation temperature for silicates (Duschl et al. 1996). The dust destruction radius, R_{dust}, will be different for grains of differing size and composition (Isella & Natta 2005), but to simplify matters a single temperature is assumed for all dust grains. This differs from other investigations in which different types of grains can have different temperatures at the same spatial location (e.g. the spherically symmetric radiation transfer code developed by Wolfire & Cassinelli 1986) A further simplifying assumption is made that the dust destruction radius is independent of latitude in the disk. The determination of the dust destruction radius is carried out after the temperature structure is obtained and involves a nested loop that counts how many grid cells at each radius have temperatures below 1600 K. The inner radius is shifted either toward or away from the irradiating source until the disk temperature falls below 1600 K. The disk density is then re-gridded and the temperature calculation/dust destruction radius determination repeated. This continues until a stable radius is established. Once the inner radius is fixed the program proceeds. At this point it is possible to solve for density structure assuming vertical hydrostatic equilibrium described below. Assuming the input density structure is not too far removed from the final density structure there is no need to repeat the dust destruction calculation on each iteration.

2.1.4 Density Structure

The program always adopts a flared disk structure where disk scaleheight increases with distance from the star. Flared disks naturally result if a disk is in vertical hydrostatic equilibrium. Observational support of this can be found in the images of HH 30 (see Fig. 1.2), which appear to show a flared disk structure (Burrows et al. 1996). Kenyon & Hartmann (1987) were the first to address this issue and subsequent SED and scattered light modelling of CTTs suggest this is typical (e.g. D'Alessio et al. 1999a; Whitney & Hartmann 1992; Burrows et al. 1996). The Kenyon & Hartmann (1987) argument is outlined below.

In passive disks where all heating is due to the central star the radial temperature obeys a power law, $T_d(\varpi) \propto \varpi^{-q}$, where ϖ is the radial coordinate in the disk mid-plane. For an optically thick flat disk surface temperature distribution $q = 3/4$ at large ϖ (Adams & Shu 1986; Adams et al. 1987). Self-consistent models of an isothermal flared disk by Kenyon & Hartmann (1987) suggest q ranges from a value of 3/4 within the centrifugal

radius (i.e. the radius at which the centrifugal barrier occurs; see e.g. Terebey et al. 1984) to 1/2 for $\varpi/R_\star \geq 1000$. In a system where the star contains essentially all of the mass the gravitational potential energy in the vertical direction is given by,

$$E_z \sim \frac{GM_\star}{\varpi} \times \frac{-z}{\varpi} \sim kT_d(\varpi) \qquad (2.16)$$

therefore,

$$z \sim -\frac{k\varpi^2 T_d(\varpi)}{GM_\star} \qquad (2.17)$$

If $T_d(\varpi)$ falls off more slowly than ϖ^{-1} it naturally follows that the ratio of thermal to gravitational energy will increase with disk radius and this will result in flaring. Gravity is too weak to confine material to a thin plane. Flaring exposes a greater area of the disk to direct radiation from the central star leading to greater IR emission compared to flat disks (Adams et al. 1987) and hence a flatter SED.

For the purpose of work within this thesis, the disk density can be fixed or iteratively solved for. If a fixed disk density is imposed then it is taken to be that of Shakura & Sunyeav (1973),

$$\rho = \rho_0 \left(\frac{R_\star}{\varpi}\right)^\alpha \exp{-1/2[z/h(\varpi)]^2} \ , \qquad (2.18)$$

where the scaleheight increases with radius, $h = h_0 \left(\varpi/R_\star\right)^\beta$. Fiducial models typically use $\alpha = 2.25$ and $\beta = 1.25$, which are the average parameters derived for CTTs disks from self-consistent models of irradiated disks (D'Alessio et al. 2001). The surface density profile is then $\Sigma \propto \varpi^{-p}$, where $p = \alpha - \beta$. These values will always be stated. In this parameterized configuration the code only runs once, a fixed density structure is assumed and from this a temperature structure is derived using the method outlined in Sect. 2.1.5. For some purposes this may be sufficient. However, a problem with this is that density and temperature are intricately related by hydrostatic equilibrium if dust and gas are coupled. It therefore seems natural to iterate until the two converge.

It is possible to obtain the density structure by solving the hydrostatic equation,

$$\frac{dP}{dz} = -\rho g_z \ . \qquad (2.19)$$

Here, $P = \rho c_s^2$ is the gas pressure, c_s is the isothermal sound speed, and $g_z = \frac{GM_\star z}{\varpi^3}$ is the vertical component of gravity in the disk. Radiation pressure is neglected as disks are assumed to be thin and non self-gravitating (Pringle 1981). Imposing a constant surface density profile as a boundary condition enforces conservation of mass. The hydrostatic equation can be solved numerically by approximating the integral of Eqn. 2.19 to a sum of finite contributions. Using the equation of state, the gas pressure $P = \rho c_s^2$, where $c_s^2 = kT/\mu m_H$ is the local sound speed squared, this leads to,

$$\ln\left(\frac{\rho}{\rho_0}\right) = -\sum \frac{1}{T}\left(\frac{dT}{dz} + \frac{g_z \mu \, m_H}{k}\right)\Delta z \qquad (2.20)$$

22

which can be solved using,

$$\frac{dT}{dz} = \cos\theta \frac{dT}{dr} - \frac{\sin\theta}{r}\frac{dT}{d\theta} \tag{2.21}$$

Throughout the spherical polar grid, the vertical component of gravity in the disk, g_z, is calculated at the mid-point of each cell. The cell temperature is assumed to be uniform within each cell and Δz is the incremental distance through each cell which lies directly below grid centre (r, θ, ϕ). It is therefore possible to obtain values of ρ/ρ_0 for each grid cell. The disk surface density is assumed to have the form, $\Sigma(\varpi) = \Sigma_0 (\varpi/R_\star)^{-p}$. Since the total mass is given by,

$$M_{disk} = \int_{R_{min}}^{R_{max}} \Sigma(\varpi) 2\pi\,\varpi\,\mathrm{d}\varpi\;, \tag{2.22}$$

it is possible to solve for Σ_0,

$$\Sigma_0 = \frac{M_{disk}}{2\pi R_\star^2 (\log R_{max} - \log R_{min})} \quad \text{(for p = 2)} \tag{2.23}$$

$$\Sigma_0 = \frac{M_{disk}(2-p)}{2\pi R_\star^p (R_{max}^{2-p} - R_{min}^{2-p})} \quad \text{(for p $\neq$ 2)} \tag{2.24}$$

For each cell ρ/ρ_0 is known and the cylindrical radius, ϖ, can be calculated from geometry, so it is possible to determine the density ρ in each cell,

$$\rho_0(\varpi) = \frac{\Sigma_0\,(R_\star/\varpi)^p}{\sum \frac{\rho}{\rho_0}\Delta z} \tag{2.25}$$

This method contains a number of implicit assumptions. All disks must be thin and non self-gravitating, with the system mass dominated by the central star (Pringle 1981). Disks must be in vertical hydrostatic equilibrium with dust and gas in the disk well mixed over a few scaleheights with negligible settling to the mid-plane such that $T_{gas} = T_{dust}$. Although calculations suggest grain coagulation and settling may occur on timescales as short as a few thousand years (e.g. Wetherhill 1980; Weidenschilling 1980) erosion and fragmentation processes are assumed to be sufficient to maintain a population of well mixed small particles (Weidenschilling 1984, Dullemond & Dominik 2005). This is the assumption for all models in chapter 3, 4, and 6. Chapter 5 explores the possibility of grain growth and dust settling in Brown Dwarf, T-Tauri and Herbig disks. There is mounting evidence of larger grains yet there is the question of their survival. Dominik & Dullemond (2005) do not completely discount the presence of large grains rather they suggest their presence may not be an evolutionary effect rather typical grain sizes found in disks reflect the state of the disk in some more complicated way, e.g. the strength of the turbulence, the amount of dust mass transformed into planetesimals, the amount of gas lost via evaporation etc.

2.1.5 Temperature Structure

A smooth temperature structure is required to accurately determine the hydrostatic equilibrium density. The calculation of temperature by the method outlined in Bjorkman & Wood (2001) has too low signal-to-noise for this purpose. This method makes use of the Monte Carlo simulations ability to track individual photon packets. The luminosity of the radiation source is divided into equal-energy, monochromatic photon packets that are emitted stochastically by the source. These photon packets are followed as they undergo interactions until the point at which they are absorbed or escape. If absorbed, the packet energy is added to the envelope, raising the local temperature. A problem with this method is it is not smooth i.e. a cell is only heated when a photon packet is absorbed within it and it is conceivable that no absorption may take place within certain cells. An indeterminate temperature leads to sharp discontinuities that result in anomalously large temperature gradients, which in turn results in sharp density spikes.

A method has been developed to smooth the temperature. This method is based on an observation by Lucy (1999) that a photon packet will contribute energy to every cell it transits not just the cell in which it is absorbed i.e. instead of sampling photon absorption, this method samples the photon density (equivalent to the mean intensity). More photon packets pass through an individual cell than are absorbed in that cell, so this method potentially produces a more accurate measurement of the temperature for any given total number of photon packets, especially in optically thin regions where few absorptions are likely to take place. What follows is an outline of the procedure used. A detailed treatment of the problem can be found in Lucy (1999).

Provided a system is in radiative equilibrium the rate at which it absorbs energy from the radiation field is balanced by the rate at which matter emits energy, $\dot{A} = \dot{E}$ or,

$$4\pi \int_0^\infty \rho(1 - a_\nu)\kappa_\nu J_\nu \, \mathrm{d}\nu = 4\pi \int_0^\infty \rho(1 - a_\nu)\kappa_\nu B_\nu \, \mathrm{d}\nu \qquad (2.26)$$

The aim is to express the rate of absorption as a discrete sum. As discussed by Lucy (1999) when a photon packet travels path-length l it contributes $E_\gamma \frac{\delta t}{\Delta t}$ to the time averaged content of the volume element that it is passing through where $\delta t = l/c$ and Δt is the simulation time. It follows that the volume elements energy density can be estimated by,

$$\frac{4\pi}{c} J_\nu d\nu = \frac{E_\gamma}{c\Delta t\Delta V} \sum_{d\nu} l \qquad (2.27)$$

The mean intensity, J_ν, and therefore heating is proportional to the path length, l, through the cells. Substituting Eqn. 2.27 into Eqn. 2.26 and integrating over all frequencies yeilds,

$$\dot{A} = \frac{E_\gamma}{\Delta t\Delta V} \sum l\rho(1 - a_\nu)\kappa_\nu \,, \qquad (2.28)$$

where ΔV is the cell volume, a_ν is the scattering albedo, and κ_ν is the total opacity in cm^2/g. The energy of each photon packet is $E_\gamma = L_\star \Delta t/N_\gamma$, where $L_\star$ is the stellar source luminosity and N_γ is the number of Monte Carlo stellar photon packets used in the simulation. The expression for the rate at which matter emits energy can also be simplified to

$$\dot{E} = 4\pi\rho\kappa_P B(T) \qquad (2.29)$$

where κ_P is the Planck mean opacity and $B(T) = \sigma T^4/\pi$ is the integrated Planck function. Since $B = \sigma T^4/\pi$ equating Eqn. 2.28 and Eqn. 2.29 leads to the following expression for temperature:

$$T^4 = \left(\frac{\dot{A}}{4\rho\kappa_p(T)\sigma}\right) . \qquad (2.30)$$

Replacing $\dot{A}$ in Eqn. 2.30 with the expression given in Eqn. 2.28 and substituting $L_\star = N_\gamma E_\gamma/\Delta t$ where $L_\star = 4\pi R_\star^2 \sigma T^4$ gives,

$$T_{cell} = T_\star \left(\frac{\pi l(1-a_\nu)\kappa_\nu R_\star^2}{N_\gamma \Delta V \kappa_p(T_{cell})}\right)^{0.25} \qquad (2.31)$$

As each packet transits the grid cells, the program uses the path-length in each cell through which it passes to cumulatively calculate $l(1 - a_\nu)\kappa_\nu$ for each cell. The first iteration is complete when the input number of photon packets have escaped from the system as defined by a spherical shell whose outer radius is specified. At this point the new temperature structure can be calculated using Eqn. 2.31. Since κ_p is a function of temperature this equation is solved iteratively using pre-tabulated values of $\kappa_p(T)$.

As noted by Bjorkman & Wood (2001) a problem faced by Lucy's method is the incorrect frequency distribution of the re-emitted photons. The Bjorkman & Wood (2001) technique, summarized below, enforces radiative equilibrium by ensuring an absorbed photon packet is immediately re-emitted at the appropriate frequency so that it corrects the temperature of the spectrum previously emitted by the cell. The emergent SED naturally relaxes to its equilibrium value without iteration. The code therefore uses the Bjorkman & Wood (2001) technique for reprocessing photon packets and the modified Lucy (1999) path-length technique to determine the cell temperature. It is not necessary to iterate for temperature in either case as it is assumed opacity is a weak function of temperature, the case for astrophysical dust (Isella & Natta 2005).

Temperature Correction Procedure

Whenever a photon packet is absorbed, its energy which is simply the total luminosity divided by the number of packets , $L_\star \Delta t/N_\gamma$, is added to the absorbing medium, raising

the local temperature. To conserve energy and enforce radiative equilibrium, the packet is re-emitted immediately at a new frequency determined by the local temperature. These re-emitted photons comprise the diffuse radiation field. The temperature of a cell will naturally change each time a packet is absorbed. The temperature of the cell can be determined by equating the absorbed energy within a cell to the emitted energy which is determined by the emissivity, $j_\nu = \kappa_\nu \rho B_\nu(T)$, where κ_ν is the opacity and $B_\nu(T)$ is the Planck function.

$$N_{cell} \times E_\gamma = 4\pi\Delta t \int\int (1 - a_\nu)\kappa_\nu \rho B_\nu(T)d\nu\,dV = 4\pi\Delta t \int \kappa_p(T)\rho B(T)dV \qquad (2.32)$$

N_{cell} is the number of photon packets absorbed in a cell. κ_p is the Planck mean absorptive opacity and $B(T)$ is the frequency integrated Planck function. Since $B(T) = \sigma T_{cell}^4/\pi$ and it is assumed the temperature is uniform within a cell then Eqn. 2.32 can be rearranged for T_{cell},

$$T_{cell}^4 = \frac{N_{cell}L_\star}{4N_\gamma \kappa_p(T_{cell}) \int \rho dV} = \frac{N_{cell}L_\star}{4N_\gamma \kappa_p(T_{cell})m_{cell}} \qquad (2.33)$$

As κ_p is a weak function of temperature, T_{cell} is calculated by iteration. The energy carried away from a cell following an absorption event is determined by the cells emissivity, $j_\nu' = \kappa_\nu B_\nu(T_{cell})$. The emissivity changes after each absorption as T_{cell} increases by ΔT, i.e.,

$$\Delta j_\nu' = \kappa_\nu(B_\nu(T_{cell}) - B_\nu(T_{cell} - \Delta T)). \qquad (2.34)$$

Which can be approximated by

$$\Delta j_\nu' \sim \kappa_\nu \Delta T \frac{dB_\nu}{dT} \qquad (2.35)$$

provided a large number of photon packets are used and therefore each packet's energy is small. To update the previously emitted spectrum for the new T_{cell} when a photon packet is emitted following an absorption event its frequency is chosen from the normalized probability distribution,

$$\frac{dP_{cell}}{d\nu} = \frac{\kappa_\nu}{K}\left(\frac{dB_\nu}{dT}\right)_{T=T_{cell}} \qquad (2.36)$$

where $K = \int\limits_0^\infty \kappa_\nu\left(\frac{dB_\nu}{dT}\right)d\nu$. This process is repeated until all the photon packets escape the dusty environment, whereupon they are placed into frequency and direction-of-observation bins that provide the emergent SED. Since all the injected photon packets eventually escape (either by scattering or absorption followed by re-emission), this method implicitly conserves the total energy. Furthermore, it automatically includes the diffuse radiation field when calculating both the temperature structure and the emergent SED. The robustness of the temperature correction procedure at determining the frequency distribution of the re-emitted photons has been confirmed by Baes et al. (2005).

26

2.1.6 Diffusion Approximation

A limitation of the Monte Carlo method is that it is not well suited to regions of very high optical depth such as the interior of some disks. One method to deal with this is to kill a photon packet that undergoes a high number of interactions due to being trapped for an extended period in optically thick regions and re-emit a new source photon packet. Increasing the number of allowed interactions before a photon packet is killed helps get over high optical depth problems as does running increased number of photon packets, however both methods increase CPU time which is not desirable. An alternative solution, used here, is to couple the Monte Carlo simulation in the optically thin regions with the diffusion approximation of Bjorkman, Whitney, & Wood (2002) in optically thick regions. The diffusion approximation essentially determines whether each cell is above a certain optical depth in r and θ i.e. there is no easy escape route for the photon energy packet, and defines a diffusion zone of such cells. Whenever a photon packet enters or is released from a diffusion cell it is diffused out of the diffusion region. The photon packet moves in a direction determined by the path of least resistance i.e. the lowest optical depth. Once the diffusion surface is found this gives a new release position. The temperature of the photon packet and therefore its frequency are determined as follows: In the diffusion limit the specific intensity of the radiation field is given by,

$$I_\nu = J_\nu + 3H_\nu\mu \tag{2.37}$$

where J_ν is the mean intensity, H_ν is the flux, and μ is the angular projection $cos(\theta)$, where θ is the direction along which the equation of radiative transfer is being solved. Radiative equilibrium gives $B_\nu = J_\nu$, which after integrating over frequency gives $J = B$, where B is the frequency integrated Planck function. Therefore,

$$J = B = \frac{\sigma T^4}{\pi}. \tag{2.38}$$

The surface temperature of the disk is found by considering the flux that crosses the surface. External photons cross the surface in the downward directions, so sampling them gives H^-. They are then re-emitted upward from the surface, so they do not contribute to the total flux H. Internally generated photons do not enter the disk from outside and therefore do not contribute to H^-, but they do contribute to the total H. Therefore,

$$H^- = (\frac{1}{4\pi})n_{ext}\frac{E_\gamma}{dA} \tag{2.39}$$

$$H = (\frac{1}{4\pi})n_{int}\frac{E_\gamma}{dA} \tag{2.40}$$

where n_{ext} is the number of external photons that cross the disk surface (going downward), n_{int} is the number of photons created below the surface and moving out from the diffusion

27

region, and dA is the surface area of the disk cell. E_γ is the energy of each photon. To find the cell temperature requires the mean intensity, J, in terms of flux, H^- and $H(= H^+ - H^-$, where H^- and H^+ are both defined as positive terms). Integrating I_ν gives,

$$H^- = \int_0^\infty d\nu \int_0^{-1} 0.5\mu I_\nu d\mu = J/4 - H/2 \tag{2.41}$$

$$H^+ = \int_0^\infty d\nu \int_0^1 0.5\mu I_\nu d\mu = J/4 + H/2 \tag{2.42}$$

Solving for J therefore gives,

$$J = 4H^- + 2H \tag{2.43}$$

which from Eqns. 2.38, 2.39 and 2.40 yields the disk surface temperature,

$$T_d^4 = \frac{\pi}{\sigma}[4H^- + 2H] = [n_{ext} + \frac{n_{int}}{2}]\frac{E_\gamma}{\sigma dA} \tag{2.44}$$

The change in disk surface temperature due to one photon packet is therefore,

$$\Delta T_d^4 = \frac{E_\gamma}{\sigma dA} \quad \text{(for external photons)} \tag{2.45}$$

$$\Delta T_d^4 = \frac{E_\gamma}{2\sigma dA} \quad \text{(for internal photons)} \tag{2.46}$$

The photon packet energy E_γ is the total luminosity of the system split equally among the photon packets which, since all the photon packets have equal energy, is also equal to the luminosity of the star split among the number of photon packets, $n_\star$, released from the star.

$$E_\gamma = \frac{L_\star}{n_\star} = \frac{4\pi R^2 \sigma T_\star^4}{n_\star} \tag{2.47}$$

From Eqns. 2.45 and 2.46 this gives,

$$\Delta T_d^4 = \frac{4\pi}{n_\star(dA/R^2)}T_\star^4 \quad \text{(for external photons)} \tag{2.48}$$

$$\Delta T_d^4 = \frac{2\pi}{n_\star(dA/R^2)}T_\star^4 \quad \text{(for internal photons)} \tag{2.49}$$

The surface temperature of the disk is therefore given by,

$$T^4 = T_{cell}^4 + \frac{2\pi T_\star^4}{n_\star(dA/R^2)} \quad \text{(for external photons)} \tag{2.50}$$

$$T^4 = T_{cell}^4 + \frac{2\pi T_\star^4}{n_\star(dA/R^2)} \quad \text{(for internal photons)} \tag{2.51}$$

In the disk interior, the diffusion approximation gives a temperature gradient,

$$dB/dl = -3\rho\kappa_R H \tag{2.52}$$

where κ_R is the Rosseland mean opacity, ρ is the cell density and dl is the path-length. The temperature within the disk interior is therefore given by,

$$Td^4 = T^4 + \left(\frac{3\pi T_\star^4}{n_\star(dA/R^2)} n_{int} \rho \kappa_R \Delta l \right)$$
(2.53)

The photon packet temperature is obtained using the gray atmosphere approximation,

$$T = (T^4 + 0.75\mu T_{eff}^4)^{0.25}$$
(2.54)

where $T_{eff}^4 = \frac{4\pi T_\star^4 n_{int}}{(dA/R^2)n_\star}$ and $\mu = \hat{n}_\gamma \times \hat{n}_s$ where $\hat{n}_\gamma$ is the photon packet direction and $\hat{n}_s$ the surface normal to the diffusion region. The frequency of the emitting photon packet is then sampled from the appropriate Planck spectrum for the photon packet temperature.

2.2   Accretion Disk Modelling

As was discussed in Chapter 1, all young disks are accretion disks, however heating within the disk due to viscous accretion is not always considered in models. When heating and illumination due to accretion processes is included, a model is said to be active, whereas if they are ignored the model is said to be passive with the only source of irradiation being from the central 'star'. Passive disks are successful at modelling many disk systems (e.g. Chiang & Goldreich 1997). It is assumed that within these systems accretion luminosity is negligible in comparison to the irradiation from the central source. These models bypass the uncertainty of the accretion process, but in some cases are not sufficient.

While accretion luminosity will naturally contribute to the SED, its influence will depend on the mass accretion rate and the nature of the accretion. In certain cases, such as modelling objects during FU Orionis outbursts, emission is dominated by accretion rather than irradiation and would need to be included. In other lower accretion scenarios, the choice is rather more subjective and largely depends on the amount of relevant information available.

In chapter 4 there are 3 objects modelled with accretion luminosity included. This is possible because these objects have estimates for their magnetic field strength and desirable as the models are for the inner regions of the disk where most of the accretion luminosity is likely to be emitted. The range of accretion rates also makes it possible to illustrate how low accretion rates make very little impact on the SED, but can affect the interferometric visibility.

2.2.1 The Physics of Accretion in Disks

If there is a constant flow of material through a disk at rate $\dot{M}$ then the total accretion luminosity, which is essentially the energy reserve available within a disk, is given by the change in gravitational potential energy per unit mass multiplied by the rate of accretion. For unit mass this change in gravitational potential energy, $\delta\phi$, when moving between any two points ϖ_1 and ϖ_2 is given by,

$$\delta\phi = \frac{GM}{\varpi_2} - \frac{GM}{\varpi_1} \tag{2.55}$$

therefore the accretion luminosity is

$$L_{accn} = \dot{M} \times \delta\phi \tag{2.56}$$

or if $\varpi_2 \ll \varpi_1$

$$L_{accn} = \frac{GM\dot{M}}{\varpi_2} \tag{2.57}$$

If all this potential energy was converted to thermal heating within the disk then $L_{disk} = L_{accn}$. It seems likely, however, that some of this energy will contribute also to kinetic motions within the disk and of a circular orbit around the central source. The exact contribution is somewhat hard to access, however virial arguments proposed along with the boundary layer model of accretion (cf. Bertout 1989) would suggest that $L_{disk} = 1/2 \times L_{accn}$. The remaining accretion energy can be released if disk material falls onto the central star creating shocks at the stellar surface.

The boundary layer model refers to the original belief that CTTs disks extended all the way into the star and the disk material joined the star at a hot boundary layer, where half the accretion luminosity was dissipated, while the other half was emitted in the disk. It was later suggested, however, that depending on the stellar magnetic field strength it may be possible for the disk to be disrupted by the magnetic field (e.g. Camenzind 1990; Königl 1991) and for material to fall along the magnetic field lines onto the star where it will create shocks at the surface. These shocks will heat the surface creating hot spots. Continuum emission from this hot region provides one explanation for ultraviolet (UV) and optical excess fluxes (Calvet & Gullbring 1998). The magnetospheric accretion model is illustrated in Fig. 2.3.

From Ghosh & Lamb (1979) an estimate of the magnetic truncation radius, R_{trunc}, is given by

$$R_{trunc} = \alpha_t R_\star \left(\frac{B_\star^4 R_\star^5}{GM_\star \dot{M}^2} \right)^{\frac{1}{7}} \tag{2.58}$$

where $B_\star$ is the magnetic field strength on the stellar surface, $R_\star$ the stellar radius and $\dot{M}$ the mass accretion rate. α_t is a dimensionless parameter of value less than 1. The above
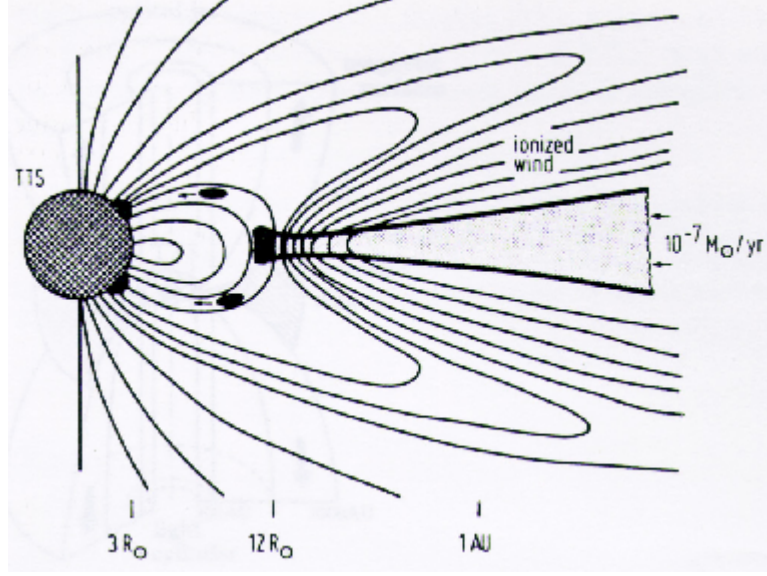
Figure 2.3: Illustration of magnetospheric accretion disk from Camenzind (1990).

expression for R_{trunc} is based on the idea that the ram pressure of the accreting material will at some point be offset by the magnetic pressure for a sufficiently strong field. Where the two pressures are equal, if the accreting material is sufficiently ionized, its motion will start to be controlled by the stellar field. Assuming spherical accretion and a dipolar field where $B(\varpi) = B_\star(R_\star/\varpi)^3$ and if the velocity of the material is set at the free-fall speed, the radius at which the magnetic field balances the ram pressure is given by Eqn. 2.58 with α_t=1. This gives an upper limit to R_{trunc} as low radial velocities in a disk result in higher densities than in the spherical free-fall case and therefore higher ram pressure and smaller R_{trunc}.

In this scenario the total accretion luminosity will be the sum of the luminosity radiated in the disk and the energy dissipated by the magnetic field lines. If the material starts at rest at R_{in} before falling in to the star along the magnetic field lines then the infalling material should dissipate its energy at the stellar surface at a rate of

$$L_{shk} \sim \frac{GM\dot{M}}{R_\star}\left(1 - \frac{R_\star}{R_{in}}\right) \tag{2.59}$$

Remember, previously it was said that roughly half L_{accn} was available for disk heating and the remaining half could be dissipated at the stellar surface if material found its way there. For the magnetospheric model however, most of the accretion energy is released at the stellar surface shocks, whose radiation is observed as the veiling continuum (Königl 1991; Calvet & Gullbring 1998).

Emission due to accretion and shock heating is incorporated into the radiative equilibrium code by inputing an accretion rate and from this calculating the fraction of addi-

31

tional luminosity that will arise. The accretion luminosity is calculated using Eqn. 2.57 with $\varpi_2 = R_{in}$ and shock luminosity using Eqn. 2.59. When each photon packet is released its properties are dependant on whether it is probable that it arises from the shock, disk or star.

Photon packets emerging from the 'shock' are assumed to have the spectrum of a 8000 K Planck function (Calvet & Gullbring 1998). They are emitted along with stellar photons as in Muzzerolle et al. (2003a) and not from hot spots which remains as future work. Accretion photons will be released from a random location within the central regions of the disk. If this location is out-with the diffusion region the photon is released in a random isotropic direction with a frequency determined by the dust temperature within the grid cell. If within the diffusion region the accretion photon must be relocated to out-with this region and its temperature determined from radiative equilibrium in the diffusion limit as described in Sect. 2.1.6. The frequency of the accretion photon is then sampled from the appropriate Planck spectrum. As in D'alessio et al. (1998) it is assumed there is a steady accretion rate through the disk.

The calculation of L_{shk} and L_{disk} requires a disk mass. Assuming the α prescription of Shakura & Sunyaev (1973) to describe the disk viscosity it is possible to obtain a first estimate for disk mass M_{disk} for a given mass accretion rate $\dot{M}$. The disk radial surface density in a steady α accretion disk is given by:

$$\Sigma_\infty = \frac{\dot{M}}{3\pi <\nu_t>}\left[1 - \left(\frac{R_\star}{\varpi}\right)^{1/2}\right] \quad (2.60)$$

where $<\nu_t> = \int_{-\infty}^{\infty} \nu_t(z,\varpi)\, \rho(z,\varpi)dz/\Sigma_\infty$ is a mean viscosity coefficient. Approximating $<\nu_t>$ by the viscosity coefficient evaluated at the disk mid-plane, $<\nu_t> = \alpha c_s H$ where $c_s^2 = kT_c/\mu m_H$ and $H = c_s\varpi/\Omega$ the surface density can be written as:

$$\Sigma(\varpi) = \frac{\dot{M}}{3\pi\alpha}\frac{\Omega}{kT_c}\mu m_H\left[1 - \left(\frac{R_\star}{\varpi}\right)^{1/2}\right] \quad (2.61)$$

where ϖ is cylindrical radius, $\Omega = \sqrt{GM/\varpi}$ is the Keplerian angular velocity, k is the Boltzmann constant, μ is the mean molecular weight (μ=2.3 for a hydrogen/helium mixture) and m_H is the mass of a hydrogen atom. The mid-plane temperature is T_c and in the iterative hydrostatic equilibrium procedure this is initially approximated using $T_c = T_0(\varpi/R_\star)^{-0.5}$ where,

$$T_0 = \frac{\mu m_H G M_\star}{k R_\star^3}h_0^2 \ . \quad (2.62)$$

G is Newton's constant and h_0 is an initial guess for the scaleheight at the stellar surface (typically use $h_0 = 0.01R_\star$). Given a surface density profile it is then possible to calculate the disk mass by summing up the contributions of mass at each radius from R_{in} to R_{max},

$$M_{disk} = 2\pi \int_{R_{in}}^{R_{max}} \Sigma(\varpi)\ \varpi\ d\varpi \quad (2.63)$$

2.2.2 Inner Gas Disk

In addition to accretion models where the void between the inner dust edge is empty, an inner gas disk can be included as a further possible contributer to the emission. This feature was added for the purpose of modelling T-Tauri sources where the dust destruction radius appears to be significantly larger than the magnetic truncation radius (see Chapter 4). The gas disk extends down to the magnetic truncation radius (R_{trunc}), calculated using Eqn. 2.58. The structure and temperature of the gas disk is not computed self-consistently, rather accretion luminosity is emitted following the temperature structure of an optically thick accretion disk (e.g. Lynden-Bell & Pringle 1974; Pringle 1981),

$$T_w^4 = \frac{3}{8\pi\sigma} \frac{GM_\star \dot{M}}{\varpi^3} (1 - \sqrt{Ro/w}) \qquad (2.64)$$

where σ is Stefan's constant and ϖ is the radial distance in the mid-plane. The gas disk is assumed to be infinitely thin, so after being emitted, the 'accretion photons' do not encounter any opacity in the gas, but may be scattered and absorbed and produce heating in the dust disk. Clearly, this is a simplification for the gas emission, but is sufficient for the models presented in Chapter 4. The assumed geometry of the gas disk is supported by recent modelling by Muzerolle et al. (2004) of Herbig Ae/Be sources in which the gas disk is geometrically thin, allowing direct radiation of the inner dust disk. Investigating the effects of possible shielding of the dust disk by a flared, and possibly optically thick, inner gas disk remains as future work.

2.3   Efficiency and Benchmark Tests

The advantage of Monte Carlo techniques is that they can easily follow the transfer of radiation through complex geometries which makes them a particularly attractive method for determining the temperature structure within non-spherical environments. A disadvantage is that the number of packets released determines the accuracy in the simulation of the physical system. An estimate of the error in total energy for each direction bin is given by $\sigma_E = E_i/\sqrt{N_i}$ where E_i is the energy and N_i the number of photons in the bin. The more photon packets the greater the accuracy, however the more packets the longer the simulation takes to run. A further complication is that the accuracy for a given number of photon packets varies with the system being studied. Methods employed to reduce running time and to measure efficiency were discussed in Sects. 2.1, 2.1.5, and 2.1.6.

There are several codes available to model disk structure and unfortunately all have their limitations. This does not necessarily mean they are wrong just that the assumptions

within them make it harder to be sure they are right. If codes produce the same results however at least meaningful comparisons can be made. For this reason a number of benchmark tests have been carried out between the radiative equilibrium and similar codes. The radiative equilibrium code using a fixed density structure within the disk has been tested against Tim Harries TORUS code. In this case good agreement was found as illustrated by the comparisons in Fig. 2.4.

The radiative equilibrium code that solves for disk density structure was tested against similar codes from Tim Harries, Sebastian Wolf and Kees Dullemond. Comparisons with Tim Harries TORUS code again showed good agreement as illustrated in Fig. 2.5.
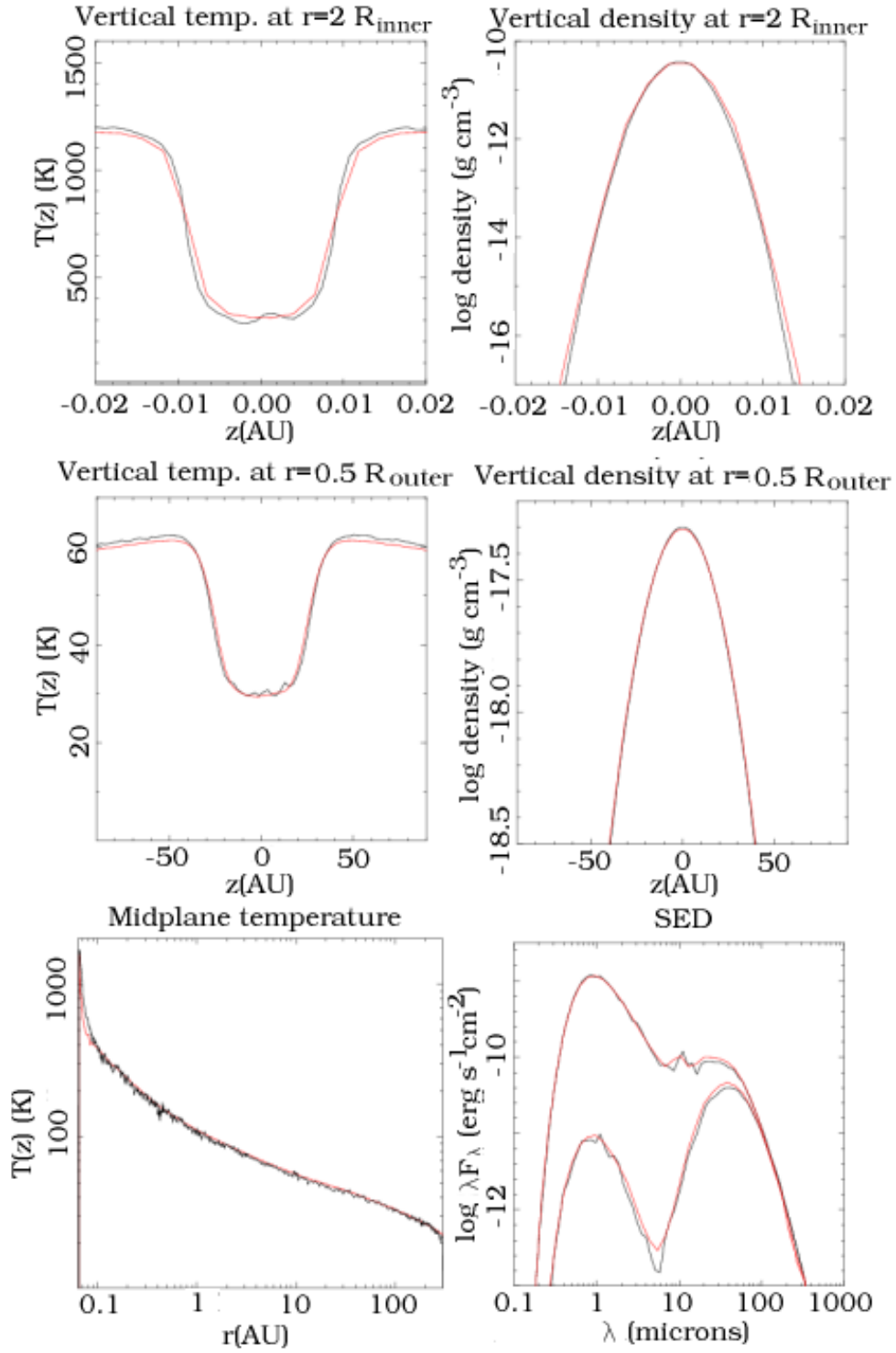
Figure 2.4: Plots comparing temperature and density structure, and the output SED generated using the parameterized density Monte Carlo radiative equilibrium code (red line) and model produced by Tim Harries TORUS code (black line). Model parameters are $M_\star = 0.5~M_\odot$, $R_\star = 2~R_\odot$, $T_\star = 4000$ K, $M_d = 10^{-4}~M_\odot$, $R_{min} = 7~R_\star$, $R_{max} = 300$ AU, $\beta = 1.25$, $\alpha = 2.25$, and KMH dust.
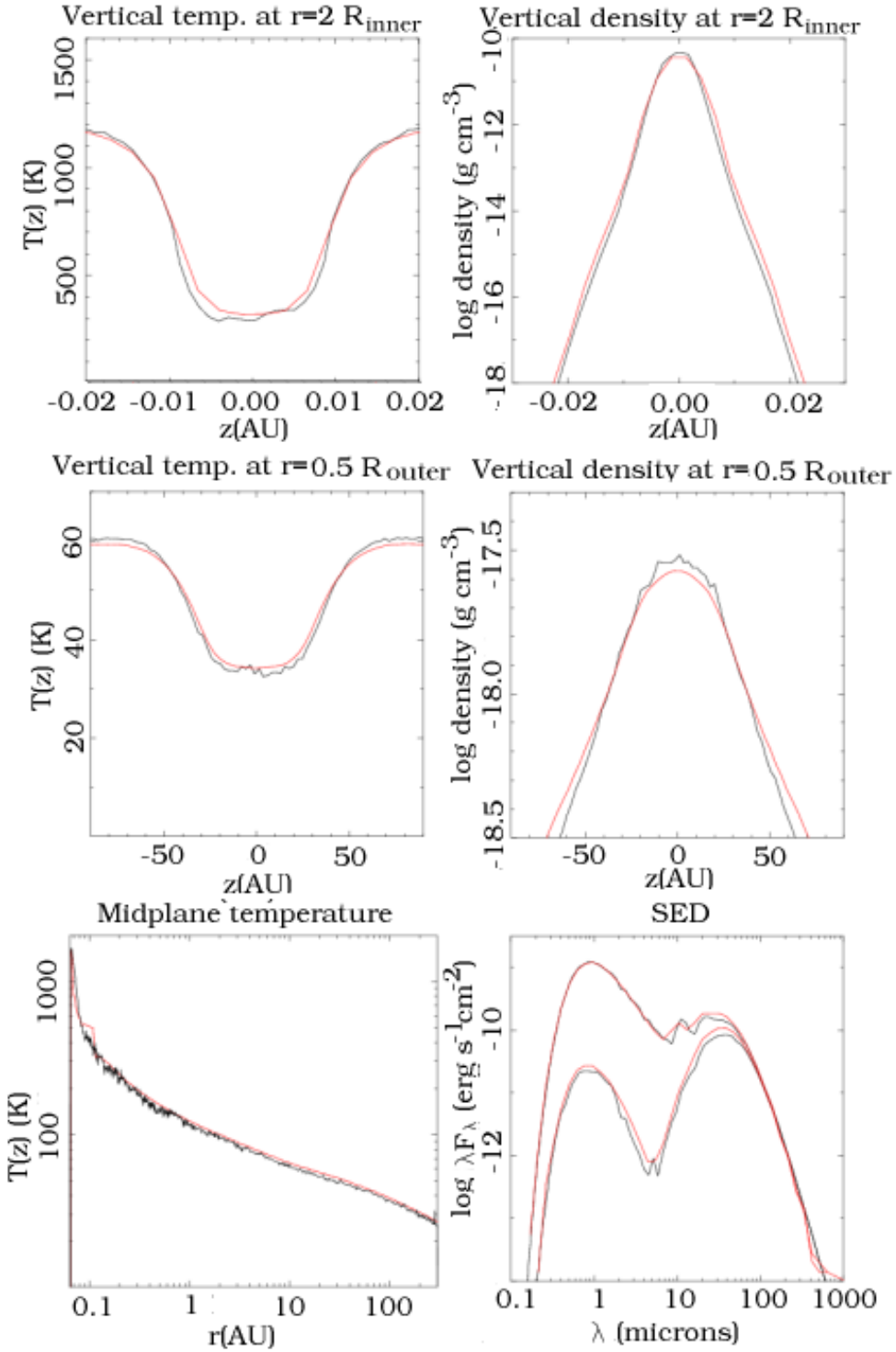
Figure 2.5: Plots comparing temperature and density structure, and the output SED generated using the hydrostatic equilibrium Monte Carlo radiative equilibrium code hat solves for density (red line) and model produced by Tim Harries TORUS code (black line). Model parameters are $M_\star = 0.5\ M_\odot$, $R_\star = 2\ R_\odot$, $T_\star = 4000$ K, $M_d = 10^{-4}\ M_\odot$, $R_{min} = 7\ R_\star$, $R_{max} = 300$ AU, $\beta = 1.25$, $\alpha = 2.25$, and KMH dust.

There are some small discrepancies in temperature and density (mainly at small radii near the mid-plane), however the comparison is difficult because this version of TORUS uses a Cartesian adaptive mesh refinement grid, not a spherical polar grid.

Comparisons with Alex Shegerer (using Sebastian Wolf's code) showed agreement to within a few percent in scaleheight. The most comprehensive comparison was made against Kees Dullemond's code. The temperature, density and SEDs of four models of varying input parameters were compared. Excellent agreement was found in most cases. The only slight discrepancy occurring in the innermost regions of the disk. This is a problem region due to high densities and optical depths and it is for this reason Dullemond has two codes for modelling. The Variable Eddington Tensor code (VET) and the Monte Carlo code (RADMC). The RADMC code is a Monte Code that is generally more accurate, but it is noisy at high optical depths. The VET code determines temperatures by way of the Variable Eddington Tensor algorithm (which is less noisy, but less accurate than RADMC). At radii $\geq 5\ AU$ the radiative equilibrium temperatures are in excellent agreement with those produced both by the RADMC and VET codes. At small radii our radiative equilibrium and the VET temperatures are generally the better match. Encouragingly, any small discrepancy makes virtually no difference to the SED which would be used in the modelling process. The model parameters were: $M_\star = 2.5\ M_\odot$, $R_\star = 2\ R_\odot$, $T_\star = 10000$ K, $M_d = 0.01, 0.0001\ M_\odot$ (dust and gas mass assuming 1:100 ratio), $R_{min} = 70\ R_\star$, $R_{max} = 200\ AU$, $p = -1, -4$ (surface density power). The results are compared in Figs. 2.6 to 2.8.
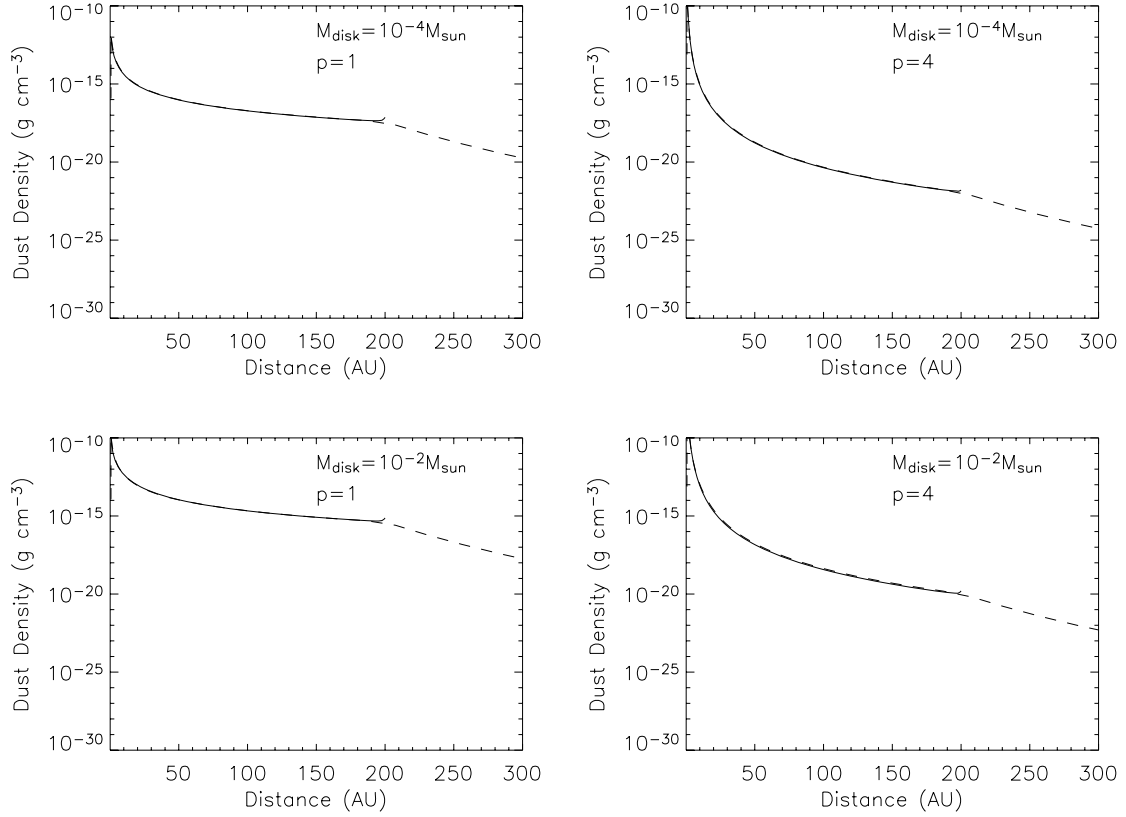
Figure 2.6: Comparison of mid-plane density generated with the radiative equilibrium code (solid line) and Dullemond's code (dashed line). There is good agreement between all models. Dullemond's models do not sharply cut off at the outer edge (200 AU) however the models are comparable as very little material lies beyond this.
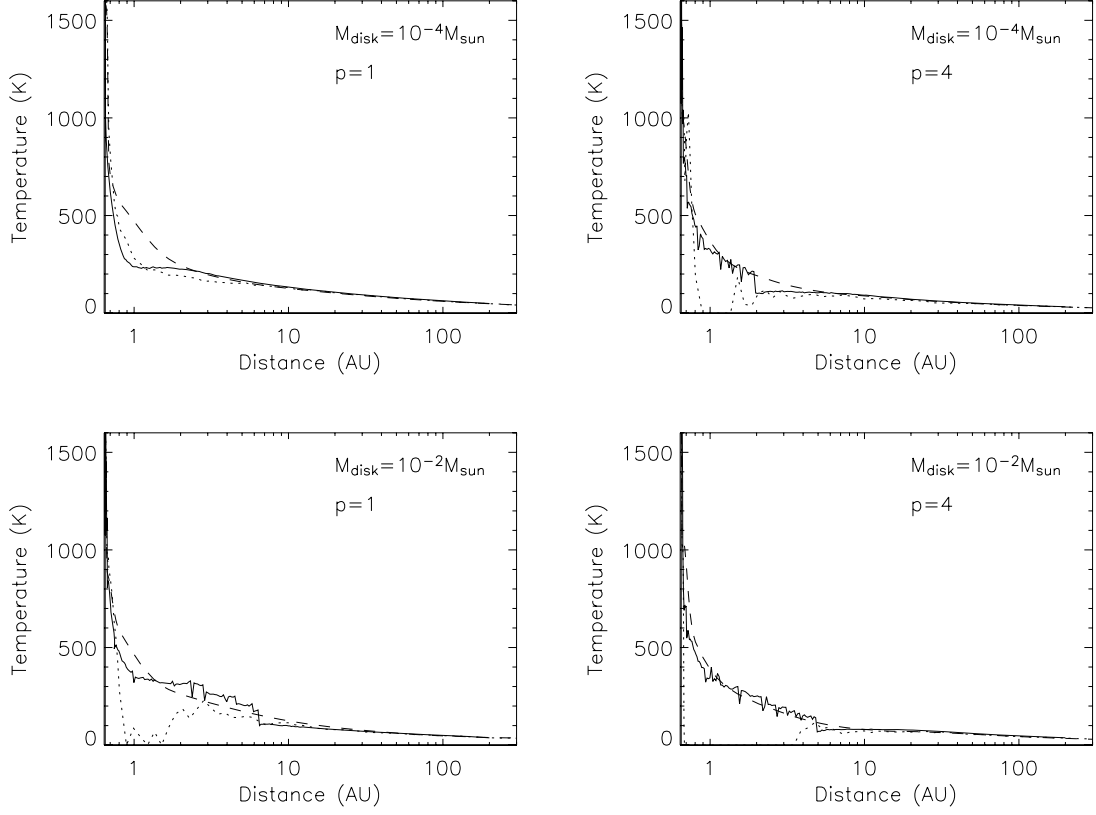
Figure 2.7: Comparison of mid-plane temperatures generated with the radiative equilibrium code (solid line) and Dullemond's VET(dashed line) and RADMC(dotted line) codes. There is good agreement in the low mass disk models throughout the disk and for the outer regions of the higher mass disks. There is a slight discrepancy in the inner regions of the high mass disk models with the VET model comparing best. This region is noted as 'difficult' and the discrepancy is likely due to the different approaches in the code for dealing with regions of high optical depth.
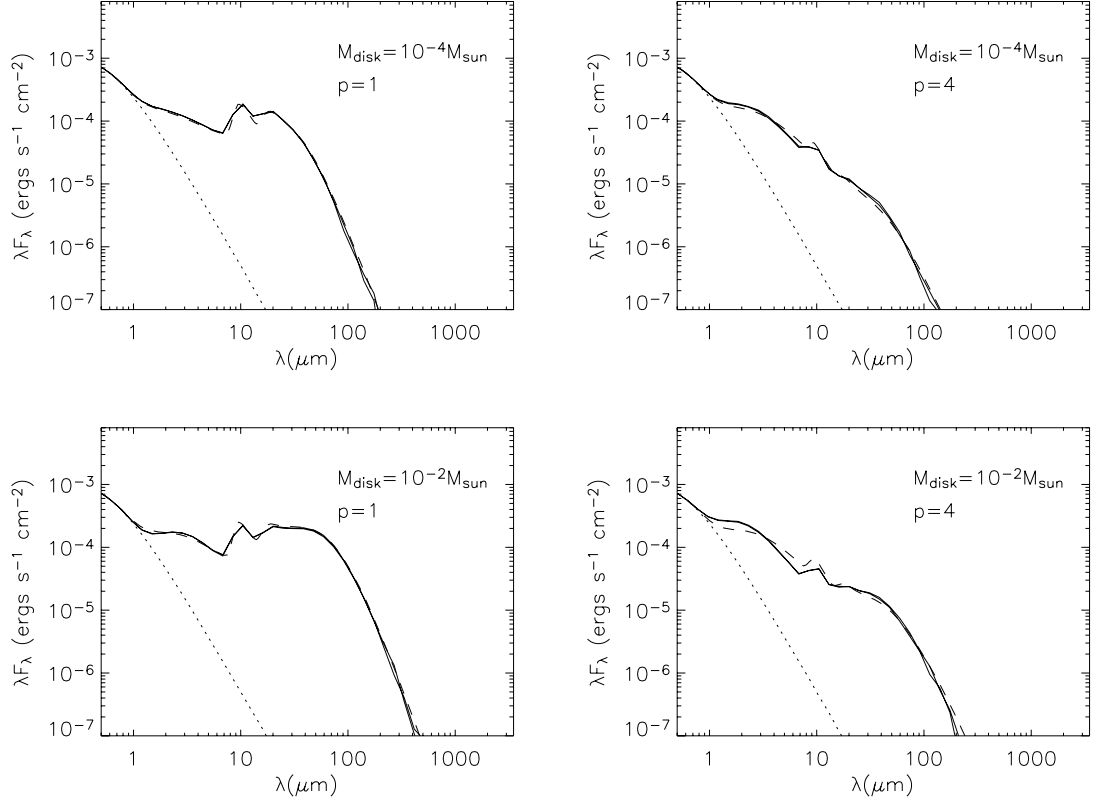
Figure 2.8: Example of the good fit between model SEDs generated with Dullemond's code (dashed line) and the radiative equilibrium code (solid line). These SEDs are for a viewing angle of 45 degrees.

A limitation of the tests with Kees Dullemond was that it was only possible to compare models with no scattering opacity. The other comparisons with Tim Harries and Sebastian Wolf's codes assumed isotropic scattering. The Dullemond models also treated the high optical depth regions differently.

This highlights a problem with comparing models - most codes have some differences. Comparisons can still be made it is just necessary to be aware of modelling restrictions and/or the effect these differences in technique will have on the result.

For example, the radiative equilibrium hydrostatic equilibrium code was also tested against Paola D'Alessio's code used for disk models in D'Alessio et al. (1998, 1999a, 2001). This comparison was a test to see how scattering and radial transport, accurately included in the radiative equilibrium code, could change the interpretation of the observed system from the SED.

The disk models of D'Alessio et al. (1998,1999a,2001) and the associated grid of models available via the WWW (D'Alessio 2005a) adopt a vertical-only approximation for radiation transfer within the disk. In their models the disk is heated by starlight and the dissipation of viscous accretion, the disk is divided into concentric plane-parallel annuli, and stellar radiation impinges the disk irradiation surface at an oblique angle. Figures 2.9 and 2.10 compare radiative equilibrium models with the fiducial disk model of D'Alessio et al. (1999a). This model has $R_\star = 2\ R_\odot$, $M_\star = 0.5\ M_\odot$, $T_\star = 4000$ K, $R_{min} = 3\ R_\star$, $R_{max} = 300$ AU, and a steady accretion rate of $\dot{M} = 10^{-8}\ M_\odot$ yr^{-1}. The dust opacity is that of ISM grains as in D'Alessio et al. (1999a) and for the purposes of comparison isotropic scattering is assumed in the radiative equilibrium code.

Figure 2.9 compares temperature and density structures. The temperature calculated with the radiative equilibrium code is generally higher by about 10% to 20%. The temperature differences do not lead to big differences in the computed density structures, since the disk scaleheight is proportional to $\sqrt{T}$. The comparison of the vertical density cuts at different radii shows that the disk structure calculations are in good agreement. The higher temperatures in the radiative equilibrium calculations do, however, lead to a difference in the flux levels at mid to far-IR wavelengths (20 μm $< \lambda <$ 300 μm) as can be seen in Fig. 2.10. The higher flux levels at mid to far-IR wavelengths were confirmed by Barbara Whitney's independently developed hydrostatic equilibrium code (personal communication). The higher temperatures are a two-dimensional radiation transfer effect that manifests itself most prominently in the long wavelength flux discrepancies. The temperature difference arises because photons reprocessed in the disk can heat other disk regions. Therefore radial transport, which is not accounted for in vertical-only models, is important for determining accurate temperatures in the disk and the correct flux in the

20 μm $\leq \lambda \leq$ 300 μm range. The SED in this wavelength regime is known to be very sensitive to disk flaring and dust settling.

It was confirmed that radial transport is the reason for the discrepancies between the two codes by modifying the radiative equilibrium code so photons reprocessed in the disk are re-emitted either straight up or straight down (with a 50% probability of up/down), thus simulating vertical-only radiation transport of the disk radiation field. Compared to the correct isotropic re-emission code, this vertical-only approximation results in lower temperatures and lower mid and far-IR fluxes at the same levels seen in Fig. 2.10.
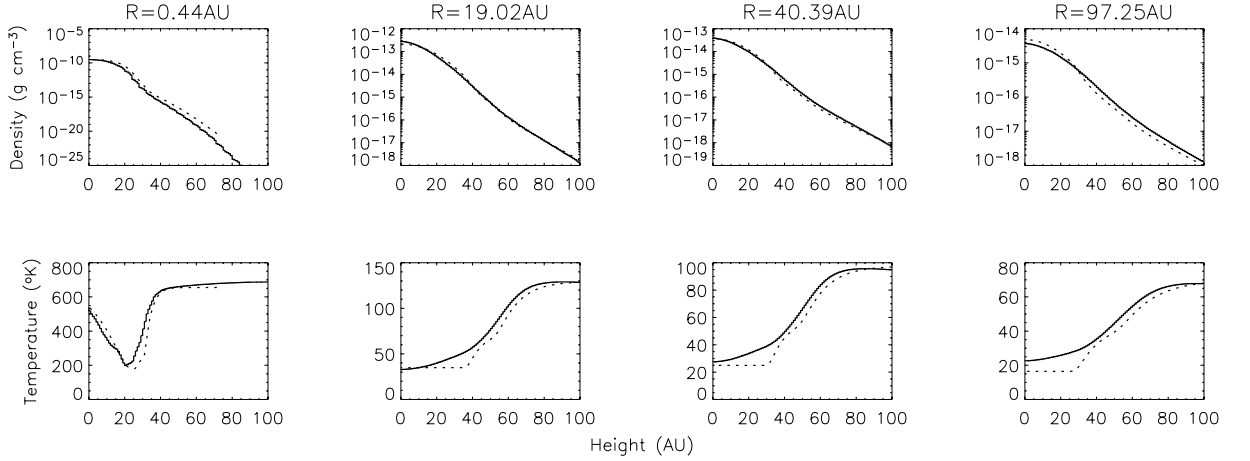
Figure 2.9: Vertical cuts showing the density and temperature at different radial distances for hydrostatic disk models. Solid lines show the results from the two dimensional (2-D) simulation and the dotted lines are for the vertical-only radiation transfer model of D'Alessio et al. (1998). The system parameters are $T_\star = 4000$ K, $R_\star = 2$ $R_\odot$, $M_\star = 0.5$ $M_\odot$, $\dot{M} = 10^{-8}$ $M_\odot$ yr^{-1}.
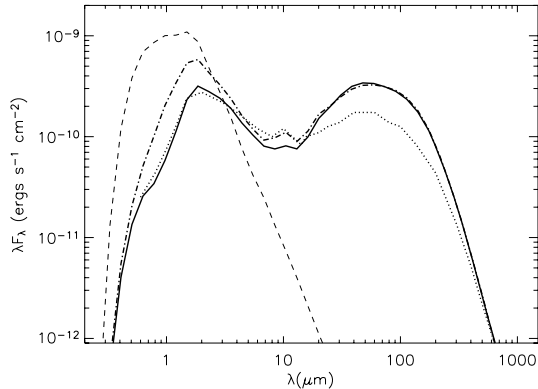
Figure 2.10: Comparison of SEDs resulting from the disk models shown in Fig. 2.9. The dotted line shows the SED computed using the D'Alessio et al. (1998) technique for $i = 60°$. The dash-dot line shows the 2-D model at $i = 60°$ and the solid line shows the model at $i = 63°$. The different flux values between the two techniques in the 20 μm to 300 μm range are due to the lower temperatures calculated in the vertical-only radiation transfer simulation. Although the higher temperature in the 2-D model leads to increased flaring and more sight-lines over which the central star is partially obscured, at $i = 60°$ there is a lower optical depth as disk material is distributed over a greater height. As a result, the short wavelength SED for vertical-only simulation at $i = 60°$ matches the 2-D $i = 63°$ model.

The above model comparison highlights the importance of 2-D radiation transfer. Another observation regarding this is that the disk models presented in this thesis do not show the level of small scale structure indicated by 1+1D radiation transfer (see Garaud et al. 2006). Using the D'Alessio comparison model as an illustration Figs. 2.11 and 2.12 show that the mid-plane temperature and density, and cross sections of disk surface brightness are smooth overall. There is a single noticeable drop in temperature as a consequence of the diffusion approximation region outer boundary, but other than that there are no significant rapid changes in slope. This contrasts with several rapid changes observed by Garaud et al. (2006, see Fig. 2.13). The models presented here and throughout this thesis are not a direct comparison to the models in Garaud et al. (2006) however they do cover a wide parameter range and therefore it is suggested that 2-D radiation transfer smooths out rapid changes in disk temperature and density structure.
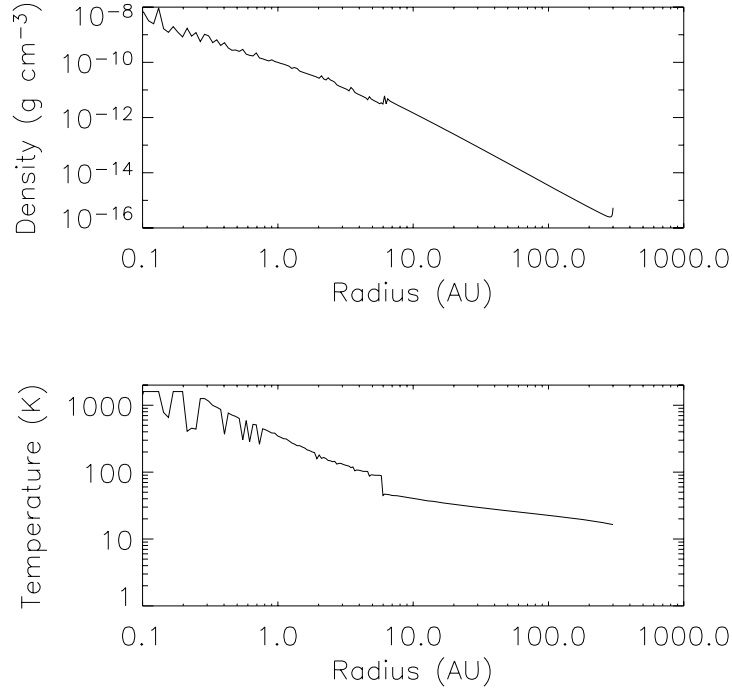
Figure 2.11: Model disk mid-plane density (left) and temperature (right) profiles. The model parameters are: $M_\star = 0.5\ M_\odot$, $R_\star = 2\ R_\odot$, $T_\star = 4000$ K, $R_{min} = 3\ R_\star$, $R_{max} = 300$ AU, $\dot{M} = 10^{-8}\ M_\odot\,\mathrm{yr}^{-1}$.
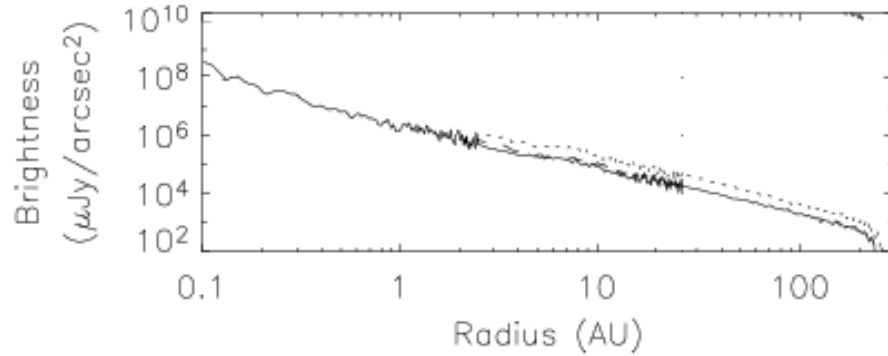
Figure 2.12: Surface brightness profiles of V(solid) J(dotted) K(dashed) scattered light from face-on model of Fig. 2.11 assuming KMH grains. The resolution of the profiles is 0.01 AU for the inner 1% of the disk radius, 0.1 AU for between 1% and 10% and 1 AU beyond 10%. Brightness levels assume source is at 350 pc.
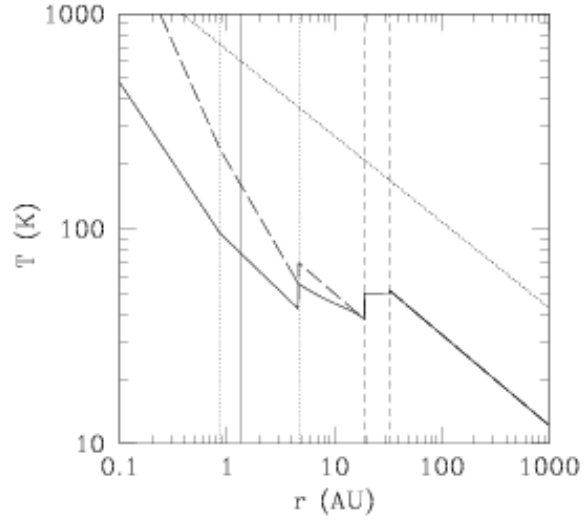
Figure 2.13: Mid-plane temperature profile (dashed line) for a T-Tauri disk with $\dot{M} = 10^{-8}$ $M_{\odot}$ yr^{-1} taken from Garaud & Lin (2006) from which further details can be obtained. A number of rapid changes are evident in this profile.

2.4   Summary

This chapter has introduced the Monte Carlo radiation transfer scattered light and radiative equilibrium code that is used in the following chapters to model the circumstellar environment of a variety of young stars. Considerable development of the radiative equilibrium code has taken place. The following list outlines the main features of the radiative equilibrium code, old and new, relevant to this thesis:

- correctly accounts for inclination effects

- can treat multiple anisotropic scattering

- disk density structure can be calculated assuming hydrostatic equilibrium

- temperature structure is calculated using a modified form of Lucy's (1999) pathlength technique which removes the problem of cells in optically thin regions with indeterminate temperature, higher signal-to-noise in temperature everywhere

- emission due to viscous heating (accretion) can be included

- emission due to shocks at the stellar surface can be included

- emission from an inner geometrically thin gas disk can be added within the dust destruction radius

- an estimate of dust destruction radius can be obtained

- a diffusion approximation has been included to help the code deal with optically thick regions

- includes a radiative equilibrium temperature correction procedure for re-emission of photons which yields simulated SEDs and multi-wavelength images

This code has been tested against a number of other similar, but independently developed codes, and in all cases shows good agreement.

CHAPTER 3

THE STRUCTURE OF BROWN DWARF DISKS

This chapter begins by introducing the low-mass Brown Dwarfs and the surprising discovery that these objects appear to have circumstellar disks. Radiative equilibrium models that assume vertical hydrostatic equilibrium are then presented that investigate the possible structure of Brown Dwarfs circumstellar disks. This work was published in Walker et al. (2004).

3.1   Introduction

Brown Dwarfs are sub-stellar objects that unlike main sequence stars do not fuse hydrogen into helium in their cores, but are fully convective with no significant chemical differentiation with depth. For some reason these objects do not accumulate enough mass to raise their core temperature and pressure to a point at which they can stably burn hydrogen. Their upper mass limit is roughly defined by the hydrogen burning limit ($\sim 0.07 - 0.09\ M_\odot$ depending on initial metallicity from $Z = Z_\odot$ to $Z = 0$, respectively (Chabrier & Baraffe 1997; Kumar 1963) whilst their lower mass limit is often quoted as being in the region of 13 Jupiter masses. If heavier than 13 Jupiter masses Brown Dwarfs will fuse deuterium and higher mass Brown Dwarfs may sporadically burn hydrogen, however they are unable to maintain this and will fade quickly once their deuterium supply is depleted.

In the past what are now called Brown Dwarfs were referred to as Black Dwarfs. The term 'Black Dwarfs' was seen as appropriate given their low luminosity makes them difficult to detect (e.g. Kumar 1963). The term 'Black Dwarfs' is however also given to the extremely old remains of a Sun-sized star which has evolved to a White Dwarf and subsequently cooled down such that it only emits black-body radiation. Perhaps because of this double meaning, when Jill Tarter coined the term Brown Dwarfs for use in her thesis (Tarter 1975) it was quickly adopted by astronomers. The term 'Brown Dwarf' was

chosen because the atmospheres dominated by molecules would be hard to understand. It was not chosen because of the colour of Brown Dwarfs which are in fact redder than any main sequence star due to their low temperature and possibly due to the presence of deuterated sodium (Na D) absorption lines which suppress green wavelengths.

Brown Dwarfs were first hypothesised by Kumar (1963) however their low luminosity meant that they remained elusive for many years with the first independent conclusive detections of Brown Dwarfs, Gleise 229B (Nakajima et al. 1995) and Teide 1 (Rebolo et al. 1995), eventually made almost simultaneously. Since these initial observations many more Brown Dwarfs have been identified as binary companions (e.g. Bouy et al. 2003), as isolated field objects (e.g. Kirkpatrick et al. 2000), as members of young stellar clusters (e.g. Bouvier et al. 1998), and associated with star-forming regions (e.g. Hillenbrand 1997).

A number of studies focusing on young stellar clusters, have uncovered evidence for the presence of dusty disks around many Brown Dwarfs. This evidence consists of near-IR (Oasa et al. 1999; Muench et al. 2001; Liu, Najita & Tokunaga 2003) and mid-IR excess emission (Comerón et al. 1998, 2000), Hα (Muzerolle et al. 2000, 2003a, 2005; White & Basri. 2003; Jayawardhana et al. 2003a) and optical continuum veiling (White & Basri 2003; Muzerolle et al. 2003a; Jayawardhana et al. 2003a), signatures of accretion and recently spectro-astrometric signatures of outflows (Whelan et al. 2005) all analogous to that seen in T-Tauri stars with circumstellar disks and envelopes. The suggestion that Brown Dwarfs may also have disks has profound implications for the debate on how these objects form and evolve.

As Brown Dwarfs effectively fill the gap between giant planets and low-mass stars it is perhaps not surprising that a number of star-like and planet-like formation mechanisms have been proposed to explain their presence. These include turbulent fragmentation of clouds (Klessen 2001; Padoan & Nordlund 2002), irradiation/photo-erosion of pre-stellar cores (Hester et al. 1996; Whitworth & Zinnecker 2004), ejection of embryos from stellar clusters (Reipurth & Clarke 2001; Bate et al. 2003; Kroupa & Bouvier 2003), planet-like formation through core accretion and gas accumulation due to gravitational instabilities of self-gravitating disks (see Whitworth & Goodwin 2005, and references therein). It is possible that more than one formation scenario may be responsible for their presence given the different environments in which Brown Dwarfs are found.

The increasing evidence for dusty disks around Brown Dwarfs is seen as a strong indicator that many Brown Dwarfs form in a similar manner to low mass stars. This interpretation follows directly from the current paradigm for star formation (Shu et al. 1987) which, as explained in Chapter 1, suggests that disks are a natural consequence of

angular momentum conservation during molecular cloud collapse. The presence of a disk also seems unlikely if a Brown Dwarf were to form as a planet through core accretion and gas accumulation presumably within a disk with subsequent dynamical ejection, or indeed if the Brown Dwarf were to be a pre-stellar core remnant stripped of its outer layers by ionizing radiation. It also seems unlikely that formation through fragmentation within massive disks would be consistent with the presence of substantial circumstellar dust. This interpretation does raise the question if Brown Dwarfs form as stars why do they not gain enough mass to stably burn hydrogen? One suggestion is that Brown Dwarfs form initially in dynamically unstable multiple star forming systems and are subsequently ejected (Reipurth & Clarke 2001; Bate et al. 2003; Kroupa & Bouvier 2003). This theory leads to loss of the proto-stellar envelope and truncation of any disk. Therefore, data indicating significant masses and extents of circumstellar material may cause problems for this formation scenario.

The percentage of the Brown Dwarf population with disks is now thought to be high, 40-80% within young stellar clusters (see Liu, Najita & Tokunaga 2003; Jayawardhana et al. 2003b; Luhman et al. 2005), and their presence is seen all the way down to 15 Jupiter masses (Luhman et al. 2005). In the older 3-8 Myr σ Orionis cluster a lower disk frequency was observed (Oliveira et al. 2002), however this does not necessarily cause any conflict with the proposed star-like formation scenario as it may simply suggest that Brown Dwarf disks have a short lifetime of a few million years. The evidence clearly suggests many Brown Dwarfs have, at some point, disks, however there is still much debate over their structure and as discussed this may have a significant impact on formation scenarios, the evolution of the disk and our ability to observe these faint objects.

The observed SEDs and IR excess emission of some Brown Dwarfs have been previously modelled using both flat and flared reprocessing disks (e.g. Natta & Testi 2001; Testi et al. 2002; Liu, Najita & Tokunaga 2003; Apai et al. 2002). The study presented in this chapter and published in Walker et al. (2004) proposes that Brown Dwarf disks can be modelled using a flared geometry analogous to that used to model the SEDs and scattered light images of many T-Tauri stars (e.g. Kenyon & Hartmann 1987; D'Alessio et al. 1999b; Whitney & Hartmann 1992; Burrows et al. 1996). This flared geometry naturally arises if you assume the disk is in vertical hydrostatic equilibrium (Kenyon & Hartmann 1987) and the degree of flaring depends on the disk temperature and stellar mass.

The hydrostatic models presented yield scaleheights for Brown Dwarf disks in excess of three times those derived for CTTs disks and the radiation transfer calculations show that such highly flared disks will result in a large fraction of obscured sources due to

extinction of direct starlight by the disk over a wide range of sight-lines. This implies that if the near-IR excess emission observed from Brown Dwarfs is indeed due to circumstellar disks and the models are indeed representative, then the large scaleheights found could have a significant impact on the optical and near-IR detectability of such systems depending on typical stellar and disk mass.

A comment is also made on possible confusion in identifying Brown Dwarfs via colour-magnitude diagrams: edge-on CTTs display similar colours and magnitudes as a face-on Brown Dwarf plus disk systems.

The model SEDs also indicate to what extent observations in various spectral regions can diagnose disk parameters. Deriving disk parameters for large numbers of sources may help to discriminate Brown Dwarf formation mechanisms and whether they are different for dense and sparse star forming regions.

3.2   Modelling

3.2.1   Code Development

This study adopted the same working hypothesis as Natta & Testi (2001) that Brown Dwarf disks are in vertical hydrostatic equilibrium, and therefore flared, with dust and gas well mixed throughout the disk.

Only passive disks are considered, since disk heating from viscous accretion is negligible compared to stellar heating in low accretion rate systems (Muzerolle et al. 2000; D'Alessio et al. 1999b). Accretion rates for Brown Dwarfs appear to be lower than in T-Tauri stars by at least one order of magnitude and range from 10^{-9} $M_\odot \mathrm{yr}^{-1}$ to 10^{-12} $M_\odot \mathrm{yr}^{-1}$ (Muzerolle et al. 2003a). The model disks extend from the dust destruction radius to an outer radius of 100 AU. The disks are truncated sharply at their inner edge and there is no material between the inner edge and the star, equivalent to assuming material in this region is optically thin.

The model disks are not vertically isothermal or two-layered (Natta & Testi, 2001) rather 2-D disk temperature structure is calculated in the Monte Carlo simulation based on the technique described by Lucy (1999) (see Chapter 2 Sect. 2.1.5). An iterative scheme was adopted to determine the disk density structure. This is summarized here and described in more detail in Chapter 2 Sect. 2.1.4. Having calculated the disk temperature structure, vertical hydrostatic equilibrium is imposed and the following equation is solved

to determine the disk density,

$$\frac{dP}{dz} = -\rho g_z \ . \tag{3.1}$$

where, $P = \rho c_s^2$ is the gas pressure, c_s is the isothermal sound speed, and $g_z = \frac{GM_\star z}{\varpi^3}$ is the vertical component of gravity in the disk. The usual thin disk assumptions are made and the disks are considered to be non self-gravitating (Pringle 1981). A boundary condition is imposed that the disk surface density $\Sigma \sim \varpi^{-1}$, in accordance with the detailed disk structure models of D'Alessio et al. (1999b). Simulations begin with the disk structure given by Eqn. 2.18 with $\alpha = 2.25$, $\beta = 1.25$, and then iterations are carried out to derive a self-consistent vertical density structure. The density converges within five iterations.

In hydrostatic disk models, the disk scaleheight scales with radius as $h/\varpi = c_s/v_c$, where $c_s^2 = kT/\mu m_H$ and $v_c^2 = GM_\star/\varpi$ are the isothermal sound speed and circular velocity at ϖ (e.g. Shakara & Sunyaev 1973; Lynden-Bell & Pringle 1974). For CTTs, $h(100AU)$ is in the range 7 AU to 20 AU as found from radiative and hydrostatic equilibrium models (D'Alessio et al. 1999b) and from fitting SEDs and scattered light images of disks using Eqn. 2.18 with h_0 as a free parameter (Burrows et al. 1996; Stapelfeldt et al. 1998a; Grosso et al. 2003; Schneider et al. 2003). However, for disks around Brown Dwarfs the scaleheights may be larger due to the smaller circular velocity of these low mass objects. If Brown Dwarf disks are indeed more vertically extended, then there may be a larger fraction of obscured Brown Dwarfs compared with CTTs. The Monte Carlo radiation transfer technique naturally includes scattered light and the inclination dependence of the SED. This allows the effects of highly flared disks and the relative importance of the scattered light contribution to the SEDs and colours to be investigated.

3.2.2 Input Parameters

The circumstellar dust opacity and scattering properties are taken to be those of the HH30 dust size distribution adopted for modelling the SEDs of HH 30 IRS and GM Aur (Wood et al. 2002a; Schneider et al. 2003; Rice et al. 2003). This dust model is described in Chapter 2 Sect. 2.1.2, but in summary has a larger average grain size and a shallower wavelength dependent opacity than ISM dust models (e.g. Mathis et al. 1977; Kim et al. 1994). An important point to note is that this larger grain dust model does not exhibit strong silicate features. The input stellar spectra for the Brown Dwarf models are the BD_Dusty model atmospheres presented by Allard et al. (2001), with $\log g = 3.5$ and effective temperatures of $T_\star = 2200$ K, 2600 K and 2800 K. For CTTs models a 4000 K Kurucz model atmosphere (Kurucz 1994) was used.

Radiative and hydrostatic equilibrium models were constructed for Brown Dwarf

systems with the range of stellar and circumstellar disk parameters given in Table 3.1. The corresponding stellar radii and temperatures yield models representative of 1 Myr old systems from the evolutionary tracks of Baraffe et al. (2002). For each set of stellar parameters, disk to star mass ratios of $\log(M_{disk}/M_\star)$ = -1, -2 and -3 were initially considered. (As usual, the disk mass M_{disk} refers to the total disk mass of dust and gas. and does not include very large particles such as rocks or planetessimals making it a lower limit.) The resulting Brown Dwarf disk structures are compared with those of disks around a typical CTTs with $M_\star = 0.5$ $M_\odot$, $R_\star = 2$ $R_\odot$, and $T_\star = 4000$ K (e.g. Kenyon & Hartmann 1995; D'Alessio et al. 1999b).

$M_\star$	$T_\star$	$R_\star$	$L_\star$
$(M_\odot)$	(K)	$(R_\odot)$	$(L_\odot)$
0.01	2200	0.25	0.0013
0.04	2600	0.50	0.0038
0.08	2800	0.90	0.044

Table 3.1: Model Parameters

3.3 Results

3.3.1 Disk Structure Models

This section presents the disk structure that results for the theoretical models of Table 3.1 under the assumption the disk is in vertical hydrostatic equilibrium. All Brown Dwarf models were checked to have Toomre parameter, Q, > 1, throughout their disks. The Toomre stability parameter Q_T is given by (Toomre 1964),

$$Q_T = \frac{c_s \Omega}{\pi G \Sigma} \tag{3.2}$$

where c_s is the local sound speed, Ω is the angular velocity, Σ the surface density and G the gravitational constant. The regions of the disk where $Q_T \geq 1$ are gravitationally stable against axisymmetric perturbations. As $Q_T \geq 1$ the thin disk assumption implicit in the models is still valid (e.g. D'Alessio et al. 1999b).

Fig. 3.1 shows scaleheights and mid-plane temperatures for the grid of models. Although the full disk structure is now calculated, the scaleheight is defined using the mid-plane temperature. For comparison, the scaleheight and mid-plane temperature for
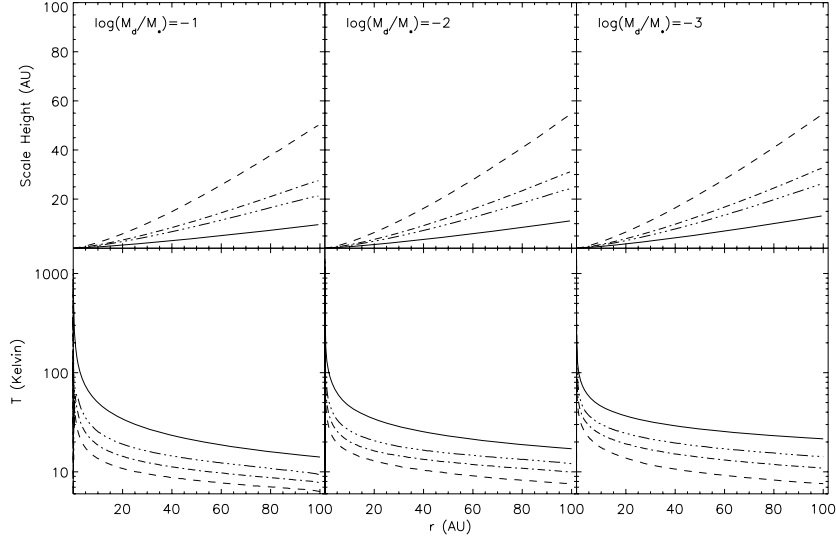
Figure 3.1: Upper: Scaleheights of Brown Dwarf models compared to CTTs models with matching disk mass. Lower: Mid-plane temperatures. In each plot the dashed, dot-dashed and triple dot dashed lines represent central stars of mass 0.01 $M_\odot$, 0.04 $M_\odot$ and 0.08 $M_\odot$ respectively and the solid line represents the CTTs model. The disk to stellar mass ratio is indicated in each panel.

a CTTs illuminating disks of the same mass ratio as in the Brown Dwarf models are also shown. The scaleheights of the CTTs disks are $h(100\,\mathrm{AU}) \sim 15$ AU, in agreement with the simulations of D'Alessio et al. (1999b). The Brown Dwarf disks have scaleheights significantly in excess of those obtained for CTTs, with $h(100\,\mathrm{AU})$ ranging from just over 20 AU for $M_\star = 0.08$ $M_\odot$ to almost 60 AU for $M_\star = 0.01$ $M_\odot$. The temperature calculations in Fig. 3.1 for Brown Dwarf disks show that $T(100\,\mathrm{AU}) \sim 10$ K with ~factor of 2 variation among the models. This small variation suggests that the stellar mass predominantly controls the disk scaleheights. The Brown Dwarf models show disk scaleheights up to three times larger than for comparative disks illuminated by a CTTs. Such large scaleheights will result in a large range of viewing angles for which direct starlight will be extincted by the disk. The effects of large scaleheights on the SED and colours are discussed in the following section.

The extended nature of the Brown Dwarf disks is also clear in Fig. 3.2 which shows K-band scattered light images of disks viewed at an inclination of 85° from face-on. As with CTTs models (Wood et al. 1998), the dust lane narrows with decreasing disk mass. Hence, it seems that the detection of low mass disks via scattered light may only be possible for edge-on systems or if coronographic techniques are used to block the starlight.
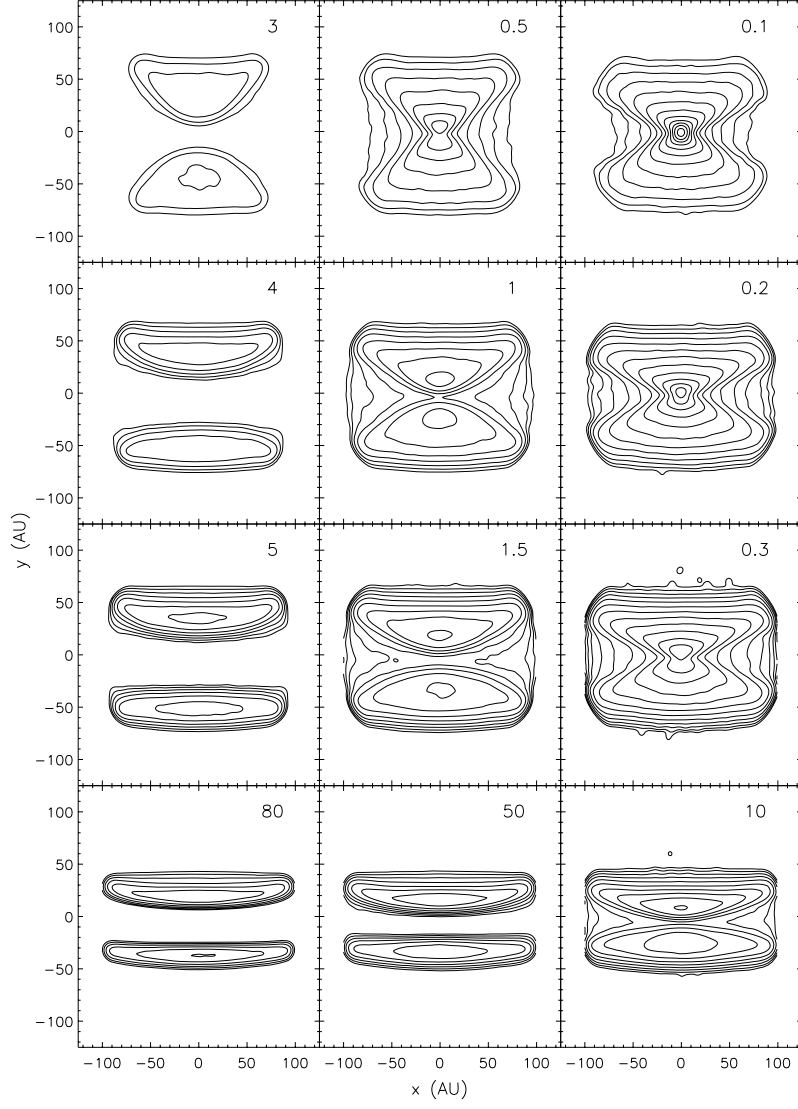
Figure 3.2: *K*-band contour plots of 9 Brown Dwarf models and 3 comparison CTTs models. In declining order each row represents models of stellar mass 0.01, 0.04, and 0.08 $M_\odot$ and the bottom row is the CTTs model. Moving from left to right each column represents models with $\log(M_{disk}/M_\star)$ = -1, -2, and -3. The inclination is 85°. The number in each panel is the lowest contour level in μJy/arcsec^2, assuming source is at 150 pc. Contours increase in 1 mag intervals.

3.3.2 SEDs of Face-On Disks

The Brown Dwarf model SEDs have similar spectral characteristics to those of CTTs disks (e.g. Wood et al. 2002b). Fig. 3.3 shows SEDs of face-on disks for the grid of models. Face-on covers $0 \rightarrow 18^o$ due to binning of the photons in the Monte Carlo code. The dependence of SED on disk mass is readily evident and, as with CTTs, observations at long wavelengths provide the best diagnostics of disk mass.

As commented by Natta & Testi (2001) it is difficult to produce significant near-IR excesses for Brown Dwarfs because the stellar spectrum peaks at longer wavelengths than CTTs and can therefore dominate the disk thermal emission. At longer wavelengths however Fig. 3.3 shows that the brown dwarf models are capable of producing varying degrees of IR excess emission. As stellar mass decreases, scaleheights increase allowing the disk to intercept, scatter, and thermally reprocess more stellar radiation, which in turn gives rise to increasingly large IR excesses.

Fig. 3.4 shows the relative contribution of stellar, scattered, and thermal disk radiation for the highly flared $M_\star = 0.01\ M_\odot$, $T_\star = 2200$ K Brown Dwarf disk system with $\log(M_{disk}/M_\star) = $ -1 and includes a CTTs model for comparison. Scattered light makes little contribution to face-on models, but it can account for up to 90% of K-band flux as disks become more inclined (see Wood et al. 2002b, Fig. 9). The importance of including scattered light will be highlighted when looking at the model colours.
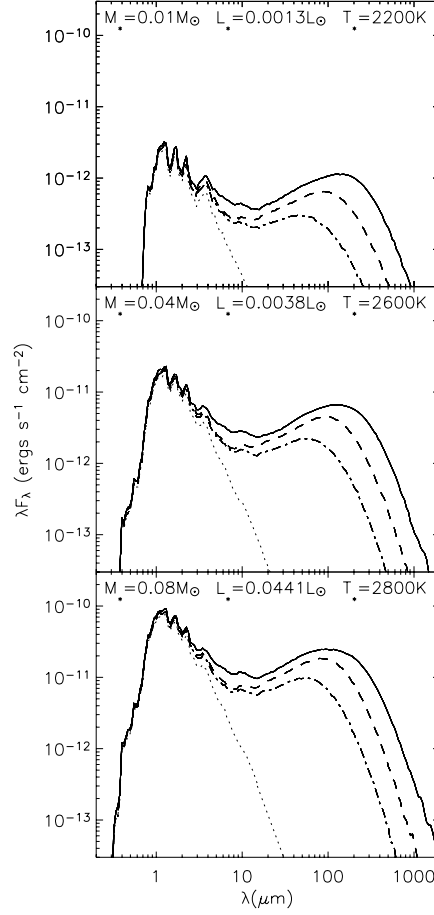
Figure 3.3: Face-on model SEDs showing the effects of varying stellar properties and disk mass. Each plot contains three separate SEDs for $\log(M_{disk}/M_\star)$ = -1 (solid line), -2 (dashed line) and -3 (dot-dash line). The dotted line represents the input stellar spectrum. Other parameters are as described in the text.
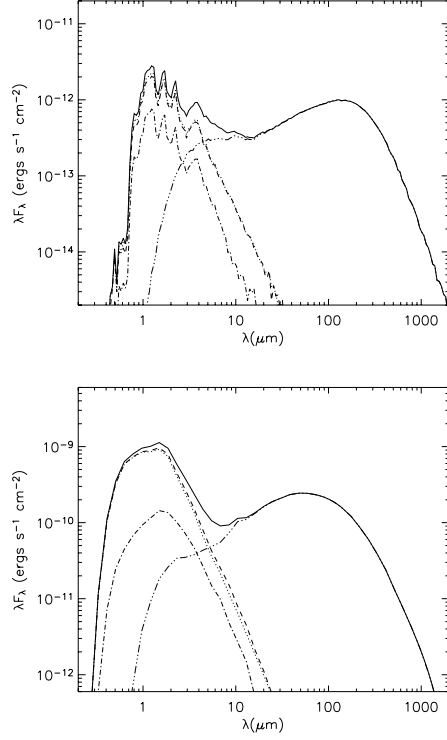
Figure 3.4: SEDs showing contributions from direct (dashed line), scattered (dot-dashed line) and disk reprocessed photons (triple dot-dash line) along with the input stellar spectrum (dotted line) and the total SED (solid line). Upper: Face-on Brown Dwarf model with $M_\star = 0.01\ M_\odot$, $\log(M_{disk}/M_\star) = $ -1 and $L_\star = 0.0013\ L_\odot$. Lower: Face-on CTTs model with $\log(M_{disk}/M_\star) = $ -1.

3.3.3   Near-IR Colour-Colour Diagrams

By far the most popular technique of identifying circumstellar disks is to identify sources with near-IR excess emission in colour-colour diagrams (e.g. Lada & Adams 1992; Rebull et al. 2002). It was through near-IR colour-magnitude and colour-colour diagrams that Meunch et al. (2001) and Liu, Najita & Tokunaga (2003) identified many candidate Brown Dwarfs that exhibit the tell-tale IR excess emission indicative of circumstellar disks.

All colours presented here are relative to Vega and are computed using the Two Micron All-Sky Survey (2MASS[1]) JHK and the United Kingdom Infrared Telescope (UKIRT) L filter transparency curves. The BD_Dusty model atmospheres that are used have near-IR colours that are bluer than observations of the corresponding spectral type (e.g. Bessell & Brett 1988; Kirkpatrick et al. 2000). However, what is important is the relative colour of the models (e.g. $[H - K] - [H - K]_\star$) and the underlying stellar spectrum does not affect this. As ultimately the models are compared with observations, a similar approach to Liu, Najita & Tokunaga (2003) has been adopted where a colour offset has been applied to the models so that the model stellar colours match observations. Adopted spectral types are M9.5, M8.5 and M6 for the 2200, 2400 and 2800 K models respectively. There is no well defined temperature scale for M dwarfs and so classifications were chosen on consideration of observations and discussion by Luhman (1999), Pavlenko et al. (2000) and Dahn et al. (2002). The stellar colours of the models are shifted to match the field M dwarf locus taken from Bessell & Brett (1988) and average colours from Kirkpatrick et al. (2000). This results in the following offsets for the M9.5, M8.5 and M6 fits: $\Delta(J - H) = 0.34, 0.23, 0.10$, $\Delta(H - K) = 0.12, 0.06, 0.00$. No shift in $K - L$ is applied.

Fig. 3.5 shows JHK and $JHKL$ colour-colour diagrams for the model disks viewed face-on, and following the afore mentioned adjustments. In general, excess emission is more readily detected at long wavelengths (e.g. Haisch et al. 2000; Natta & Testi 2001) and this is again seen here with models showing larger excesses at $K - L$ than at $J - H$ or $H - K$. The trend of the models is that the more massive and more flared disks exhibit the largest IR excesses. Inclination effects yield a spread in colour-colour diagrams and this is explored in the next section.

---

[1]The Two Micron All Sky Survey is a joint project of the University of Massachusetts and the Infrared Processing and Analysis Center/California Institute of Technology, funded by the National Aeronautics and Space Administration and the National Science Foundation.
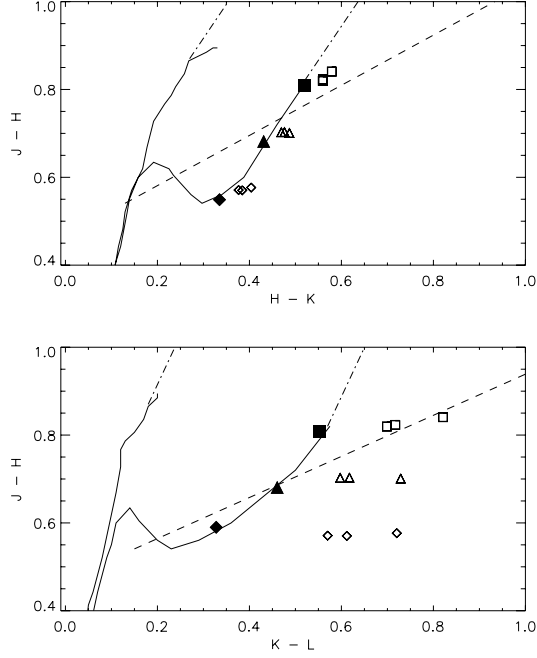
Figure 3.5: $JHKL$ colour-colour diagrams containing face-on colours for Brown Dwarf models with different $T_\star$, M_{disk} and $M_\star$. The reddest colours correspond to low stellar masses and therefore highly flared disks. The filled symbols of corresponding shape represent the average stellar colour of all models at fixed temperatures of 2200 K, 2600 K and 2800 K. The CTTs locus (dashed line) is taken from Meyer et al. (1997). The giant branch and M dwarf locus (solid lines) are taken from Bessell & Brett (1988) and Kirkpatrick et al. (2000). The dot-dash lines represent reddening vectors. Models have been shifted so that average stellar colours lie on the 'Brown Dwarf locus'.

3.3.4 Inclination, Scattered Light, and Obscured Fractions

For highly inclined CTTs, direct starlight is blocked by the optically thick disk and such systems will be very faint in the optical and near-IR (e.g. D'Alessio et al. 1999b; Wood et al. 2002a,b). Compared to CTTs, the larger disk scaleheights derived here for the Brown Dwarf models will result in a larger fraction of viewing angles over which the central starlight is blocked by the disk. Here an 'obscured source' is defined to be one where the near-IR flux is at least three magnitudes fainter than the corresponding face-on source. The obscured fraction therefore depends on the disk size, mass, and scaleheight. For CTTs, the obscured fraction is $\sim 20\%$ (D'Alessio et al. 1999b; Wood et al. 2002b) for disks of $M_{disk} \sim 10^{-3}\ M_\odot$.

Figure 3.6 shows the inclination effect on the SEDs for various Brown Dwarf disk models. The SEDs are shown for ten viewing angles evenly spaced in $\cos i$, so that each curve represents 10% of sources by number if sources are assumed to be randomly distributed in inclination angle. Obscured fractions from 20% to 60% are found with highly inclined sources only detected in the near-IR via scattered light and weak thermal emission. The largest obscured fraction occurs for the lowest stellar mass of $M_\star = 0.01\ M_\odot$ with $\log(M_{disk}/M_\star) =$ -1 and $T_\star = 2200$ K. The smallest obscured fraction occurs for the highest stellar mass of $M_\star = 0.08\ M_\odot$ with $\log(M_{disk}/M_\star) =$ -3 and $T_\star = 2800$ K.

Studies of the initial mass function (IMF) in Trapezium, ρ Ophiucus and IC348 show a relatively flat distribution over the range $0.08 \leq M_\star(M_\odot) \leq 0.04$ and then a sharp fall off below this (Luhman 2000; Muench et al. 2002). If the IMF is flat and the fall-off due to small number statistics then within a young cluster population up to 55% of Brown Dwarf candidates, as defined by the parameter range used here, may be obscured. This is an upper limit produced using maximum obscuration fractions for each stellar mass assuming a disk to stellar mass ratio of $\log(M_{disk}/M_\star) =$ -1. For a declining IMF, and a distribution of disk masses, the obscured fraction will be less. Within the parameter range of this study a minimum of 20% of sources are likely to be obscured regardless of stellar mass distribution and assuming disk to stellar mass ratios of $\log(M_{disk}/M_\star) =$ -3.

The relatively low luminosity of Brown Dwarfs and the increased obscuration due to highly flared disks may present detection problems. At a distance of 150 pc (as used in Fig. 3.6) it would be possible to detect some obscured sources in the K-band assuming a sensitivity limit of 16.5 mags. In the absence of high resolution imaging however these sources may be incorrectly identified as low luminosity highly inclined disk systems. A three fold increase in distance would be sufficient to make all obscured sources undetectable at this sensitivity limit. Naturally as instruments improve sensitivity generally increases making this less of a problem, however it may suggest problems with older surveys.
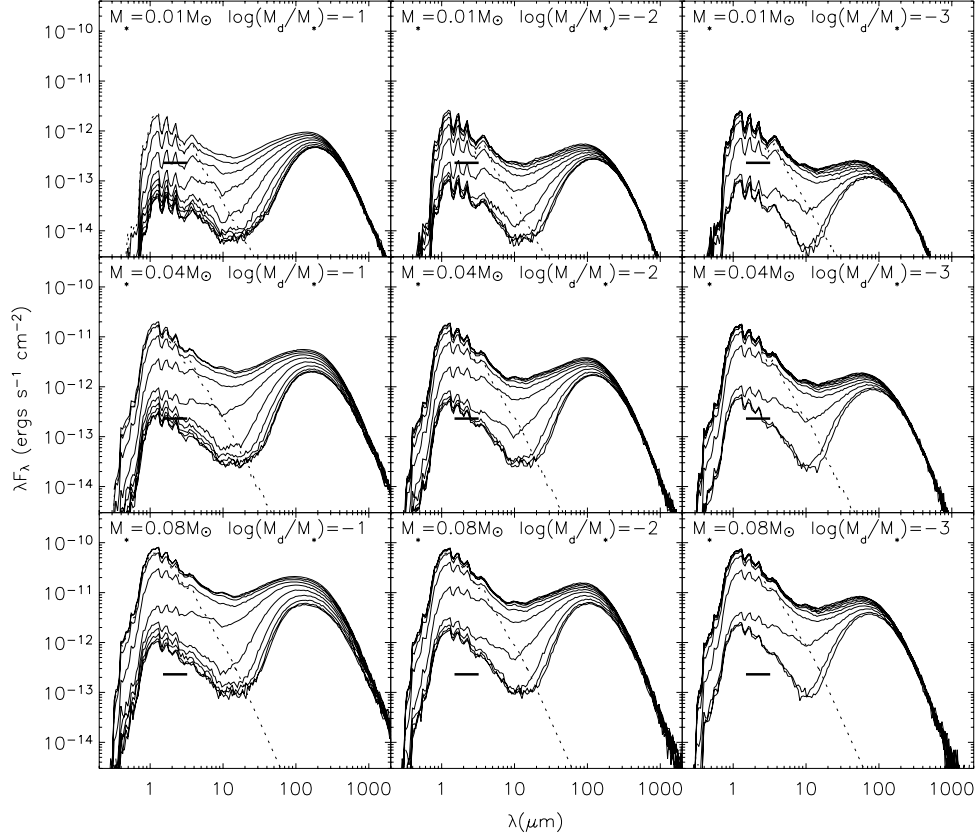
Figure 3.6: SEDs illustrating obscured fractions for our grid of Brown Dwarf models. Obscured fractions range from 20% up to 60% whereas comparable CTTs models show 20%. The greatest obscuration in a Brown Dwarf model occurs for the lowest stellar mass of $M_\star = 0.01$ $M_\odot$, with $\log(M_{disk}/M_\star) = $ -1 and $T_\star = 2200$ K$/L_\star = 0.0013$ $L_\odot$. Least obscuration occurs for the highest stellar mass of $M_\star = 0.08$ $M_\odot$, with $\log(M_{disk}/M_\star) = $ -3 and $T_\star = 2800$ K$/L_\star = 0.044$ $L_\odot$. The thick horizontal solid line represents a detection limit of 16.5 mags at K.

Figure 3.7 shows the inclination dependence in the Brown Dwarf $JHKL$ colour-colour diagrams. Relative colours are plotted for ten inclinations with the change in colour at each inclination indicated by an arrow. Similar to the behaviour observed by Kenyon et al. (1993) and Whitney et al. (1997) a loop in the colour-colour plane with inclination is seen. Starting from face-on, the sources generally get redder with increasing inclination and then loop around and end up with edge-on sources being slightly bluer than face-on, but still redder than the intrinsic stellar colours. Edge-on sources are seen almost entirely via scattered light. Note that these are slightly redder than the star because the scattered light, which is relatively blue, suffers extinction and becomes somewhat reddened. This trend is seen in all of the models.

Figure 3.8 contains data for the same model as in Fig. 3.7, but also shows the change in colour with inclination if scattered light is ignored. The removal of scattered light makes the colours much redder, with the effect being particularly significant at moderate to high inclinations. This emphasizes the importance of including scattering when creating and studying models of such systems.

3.3.5   CTTs/Brown Dwarf Confusion

When only unresolved photometry is available the models show that edge-on CTTs could be mistaken for Brown Dwarfs. CTTs have edge-on flux levels that are comparable to face-on Brown Dwarfs and similar colours. Muench et al. (2001) identified sources within the Trapezium cluster with $13.5 \leq H \leq 17.5$ as candidate Brown Dwarfs. They note that 21 of their 109 Brown Dwarf candidates are coincident with optically resolved proplyds (Bally et al. 2000; O'Dell & Wong 1996) and 21% of the candidates that exhibit IR excess, indicative of circumstellar disks, are represented by these proplyds. In the absence of high resolution imaging the task of identifying faint sources such as Brown Dwarfs may be problematic. If no central star is seen then these sources could be edge-on CTTs that happen to have the same magnitude and colours as a pole-on Brown Dwarf and disk. This confusion could lead to an overestimation of Brown Dwarf numbers.
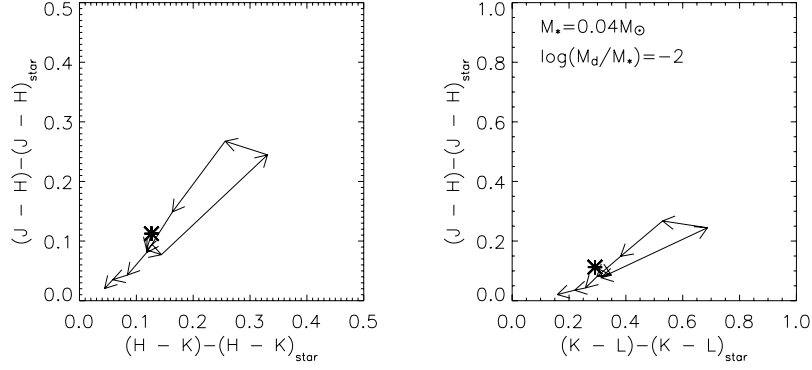
Figure 3.7: $JHKL$ plot for the $M_\star = 0.04$ $M_\odot$ and $\log(M_{disk}/M_\star) = $ -2 Brown Dwarf model. Arrows indicate the change in colours as inclination varies from nearly edge-on (indicated by bold asterisk) to face-on and colours are relative to central star's colours. This plot is indicative of the behaviour of all the Brown Dwarf models.
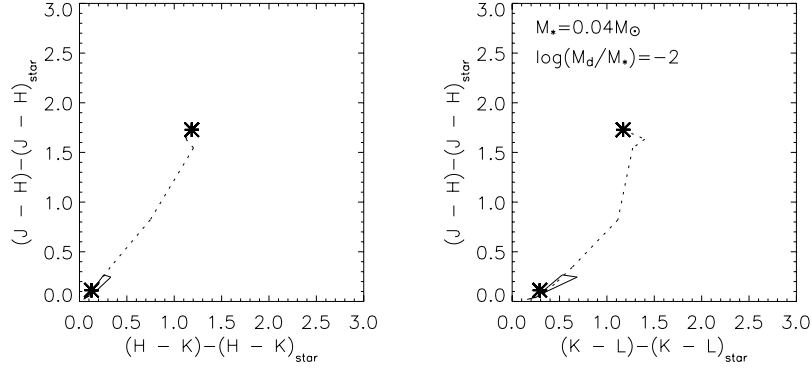
Figure 3.8: $JHKL$ plots as in Fig. 3.7, but also with dotted lines showing the change at each inclination that would result if scattering effects were removed.

3.4 Comparison to Observations

This section compares the synthetic models with published observations of suspected Brown Dwarf disks. For the Chameleon cluster the SED data is taken from Comerón et al. (2000) and Apai et al. (2002); ρ Ophiucus data comes from Barsony et al. (1997), Comerón et al. (1998), Bontemps et al. (2001) and Natta et al. (2002). $JHKL$ data is taken from the above papers along with Kirkpatrick et al. (2000) and Liu, Najita & Tokunaga (2003). All near-IR photometry has been converted to the 2MASS system (Carpenter 2001).

Figure 3.9 shows flared disk model fits to the SED data for candidate Brown Dwarfs in the ρ Ophiucus and Chameleon star clusters. Table 3.2. contains details of the model parameters used to produce the fits. As starting points for each of the models stellar parameters from Natta & Testi (2001) and Natta et al. (2002) were used.

Object	$T_\star$ (K)	$R_\star$ ($R_\odot$)	$M_\star$ ($M_\odot$)	M_{disk} ($M_\odot$)	A_v (mags)	Inclination (deg)
ISO#023	2600	0.95	0.04	10^{-5}	8	0
ISO#030	2600	1.2	0.08	10^{-5}	2	0
ISO#032	2600	1.2	0.08	10^{-5}	3	0
ISO#033	2200	0.63	0.01	10^{-3}	7	0
ISO#102	3000	1.17	0.08	10^{-7}	3.5	0
ISO#160	2600	0.95	0.08	10^{-7}	6	0
ISO#164	2600	1.36	0.08	10^{-3}	4	63
ISO#176	3000	1.17	0.08	10^{-7}	7	60
ISO#193	3000	1.5	0.08	10^{-5}	7	78
CHA Hα1	2600	0.5	0.01	10^{-5}	0.3	0
CHA Hα2	2600	1.05	0.04	10^{-5}	1.1	37
CHA Hα9	2600	0.95	0.08	10^{-5}	3.2	72

Table 3.2: Model Fit Parameters
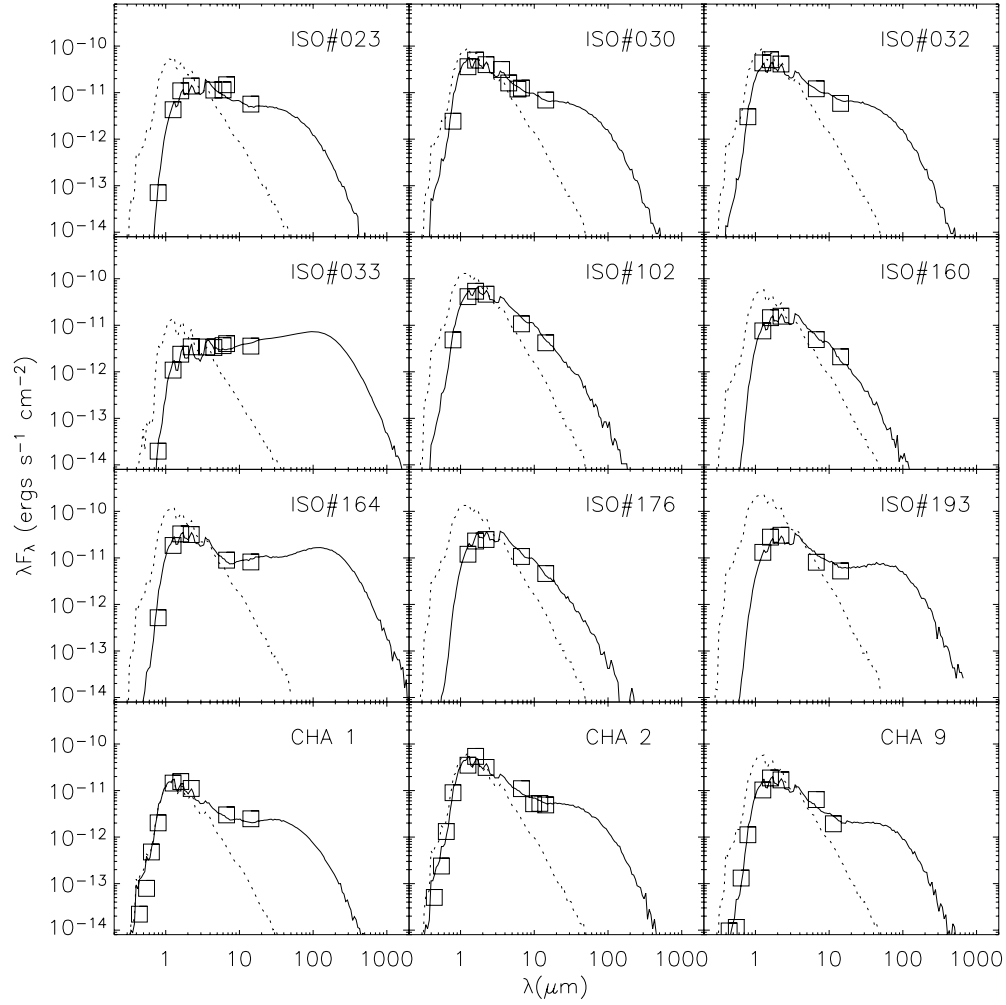
Figure 3.9: Models SED fits to observed data in ρ Ophiucus and Chameleon star clusters as indicated. All models are of a flared disk around a central star with an inner gap of radius 2 $R_\star$. A distance of 150 pc is assumed for both clusters. Further model parameters are given in Table. 3.2. The dotted line represents the input spectrum. In all cases a solid line indicates surface density $\Sigma \sim \varpi^{-1}$. The data is not corrected for the effects of reddening, instead the models are reddened according to Cardelli et al. (1989) with $R_v = 4$.

Natta & Testi (2001) modelled Cha Hα1, 2, & 9 using a flared disk model. Their models produced a successful fit in the mid-IR region of the spectrum and predicted a strong 10 μm silicate emission feature. Apai et al. (2002) later made observations of Cha Hα2 at 9.8 and 11.9 μm and did not detect the silicate feature. They presented an optically thick flat disk model which produced no silicate feature. The SEDs of ρ Oph sources have been modelled by Natta et al. (2002) and they found indications that as many as eight of these stars may have flat disks.

The models presented here open up the possibility that the absence of a silicate feature may be explained with larger circumstellar dust grains. In addition, low mass disks may fit SEDs previously modelled with flat disks. As Fig. 3.9 demonstrates, it is possible to fit the observed data for all sources with a flared disk geometry. The use of larger grains naturally suppresses the silicate feature which has been shown to be missing from the Chameleon data[2] and low mass disks of 10^{-5} $M_{\odot}$ and 10^{-7} $M_{\odot}$ allow a fit to the IR data of the candidates where flat disks were previously suspected. It should be noted that many of these fits have disk to stellar mass ratios outside the typical range of $-1 \leq \log(M_{disk}/M_{\star}) \leq -3$ (Natta et al. 2000; Klein et al. 2003) and flat disks (Natta et al. 2002) remain a possibility (see Chapter 5 Sect. 5.3).

Another alternative, testable with long wavelength observations, is that steeper surface density profiles can also be used to fit the data with higher mass disks. In Fig. 3.10, ISO#030 has been modelled using both surface density $\Sigma \sim \varpi^{-1}$ and $\Sigma \sim \varpi^{-2}$. Using $\Sigma \sim \varpi^{-2}$ allows us to fit the data with a disk eight times more massive than used in the $\Sigma \sim \varpi^{-1}$ case. Both models fit the data well in the near-IR/mid-IR, but are quite different in the far-IR. Long wavelength observations would help to discriminate between flat disk, low mass flared disks and steeper surface density disk models.

If lower mass flared disk models are representative of disks in Brown Dwarf populations, as opposed to higher mass disks, then problems with obscuration may not be as significant as suggested in Sect. 3.3.4. Equally flat disks do not result in severe obscuration of the central star unless at very high inclinations.

Figure 3.11 shows the derived scaleheights for the disks used to model the observed SEDs of Fig. 3.9 and Fig. 3.10. This illustrates the range of disk structures that can produce fits to the observed data. In each plot the scaleheight of a model CTTs of corresponding disk to stellar mass ratio is presented as a comparison. For these models scaleheights up to three times that of the corresponding CTTs are found.

---

[2]New observations of Cha Hα1 by Sterzik et al. (2004) suggest that small grains may also be required for this source.
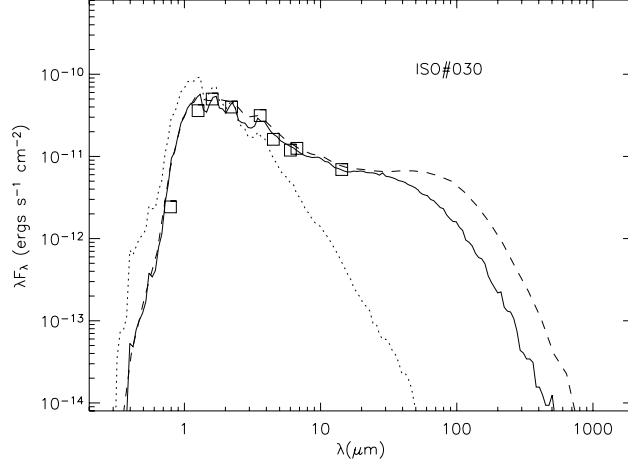
Figure 3.10: Models SED fits as in Fig. 3.9. Two models are presented for ISO#030. The solid line indicates surface density $\Sigma \sim \varpi^{-1}$. The dashed line indicates $\Sigma \sim \varpi^{-2}$. Model parameters for $\Sigma \sim \varpi^{-1}$ case are given in Table 3.2. The $\Sigma \sim \varpi^{-2}$ model has a disk eight time more massive.
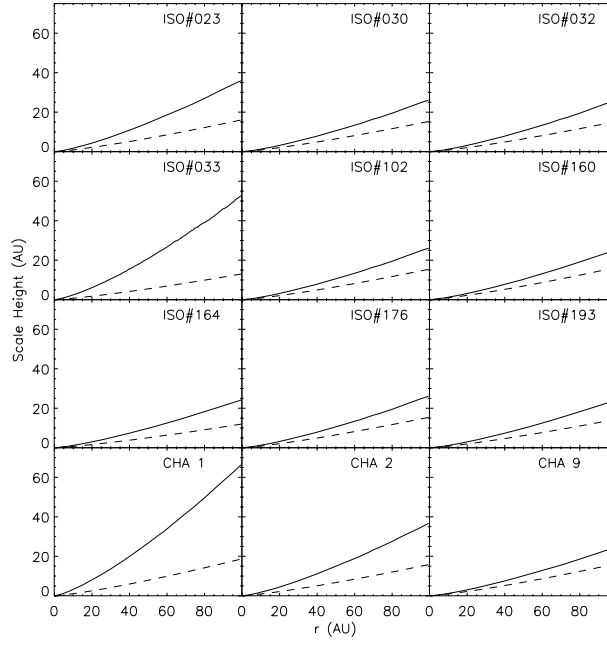
Figure 3.11: Scaleheights for our models (solid lines) presented in Fig. 3.9. The scaleheight for our 'typical CTTs' at matching disk to stellar mass ratio is given as a comparison (dashed line). For ISO#030 scaleheights are virtually coincident for the two models presented in Fig. 3.10 and therefore only the $\Sigma \sim \varpi^{-1}$ case is shown here.

Figure 3.12 shows $JHKL$ plots of the face-on models and published data. Following the adjustments discussed in Sect. 3.3.3, Fig. 3.12 shows that the models (if reddening were included) can reproduce the observed spread in colours of suspected Brown Dwarf disk systems. Including all inclinations (Fig. 3.13) allows for the redder colours of inclined disks and produces a spread in the $JHKL$ plots that is in very good agreement with the observed colours.

Figure 3.13 also shows the CTTs locus taken from Meyer et al. (1997). This again demonstrates that there is an overlap between CTTs and Brown Dwarf colours which may lead to incorrect identification of sources if only colour-magnitude data is available.

3.5   Discussion

Model SEDs and colour-colour diagrams have been presented for Brown Dwarf disks. The main assumptions in the models are that the disks are in vertical hydrostatic equilibrium with dust and gas well mixed throughout. This will be re-visited in Chapter 5 in light of new data. The models are self-consistent and employ an iterative procedure to determine the hydrostatic density structure for passively heated disks. Compared to CTTs, Brown Dwarf disks have larger scaleheights due to the lower mass of the central star. In some cases the scaleheights of Brown Dwarf disks are more than three times larger than for the same disk to stellar mass ratio for a CTTs. The larger scaleheights result in more inclinations over which the direct stellar radiation is blocked or obscured by the flared disk. The fraction of optically obscured systems depends on the stellar mass and disk optical depth and in the models presented here is in the range $20\% \leq f_{\mathrm{obs}} \leq 60\%$. For a typical CTTs about 20% of sources will be optically obscured.

If, as the models suggest, Brown Dwarf disks are highly flared, detection of Brown Dwarf disk systems will be biased toward face-on systems. It is also shown that without direct imaging or spectroscopic identification, it will be difficult to distinguish between edge-on CTTs and face-on Brown Dwarfs. Colour-colour diagrams show that edge-on sources, which are only detected in the optical/near-IR via scattered light, have similar colours to face-on sources. This may lead to incorrect identification of sources. In particular, it is found that an edge-on CTTs will have similar near-IR magnitudes and colours as face-on Brown Dwarf disk systems.
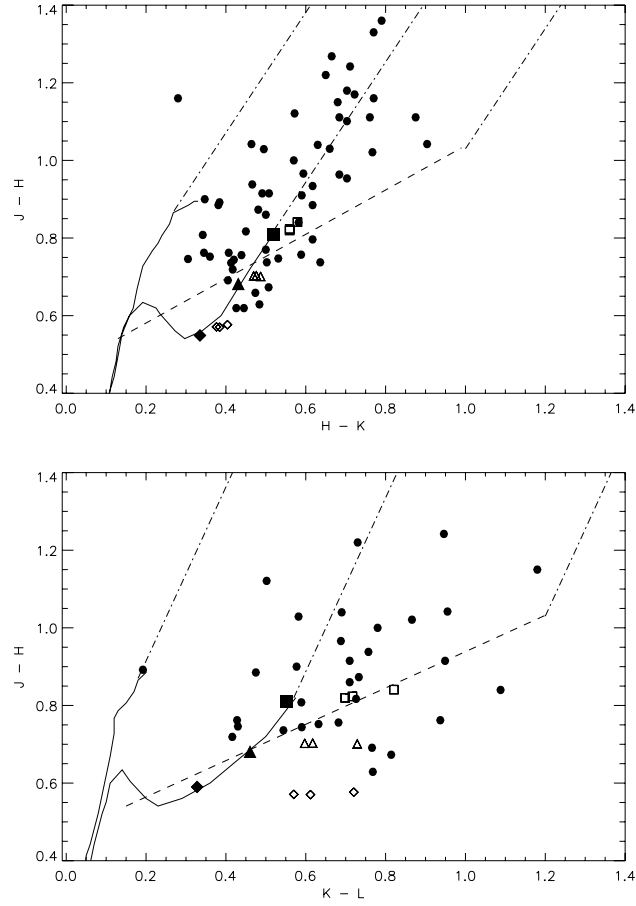
Figure 3.12: *JHKL* plots containing observed (•) and face-on model (square,triangle,diamond) colours. Where possible data was obtained directly from the 2MASS second incremental data release (Carpenter 2001). Remaining data was retrieved from the papers of Comerón et al. (1998/2000), Martín et al. (2000), Briceño et al. (1998), Luhman et al. (1998), Luhman (1999), Najita et al. (2000) and Liu, Najita & Tokunaga (2003). As previously the solid shapes represent the average stellar colour obtained for models of $T_\star =$ 2200, 2600 and 2800 K. The CTTs locus (dashed line) is taken from Meyer et al. (1997). The giant branch and M dwarf locus (solid lines) are taken from Bessell & Brett (1988) and Kirkpatrick et al. (2000). The dot-dash lines represent reddening vectors. Models have been shifted so that stellar colours lie on the 'Brown Dwarf locus'.
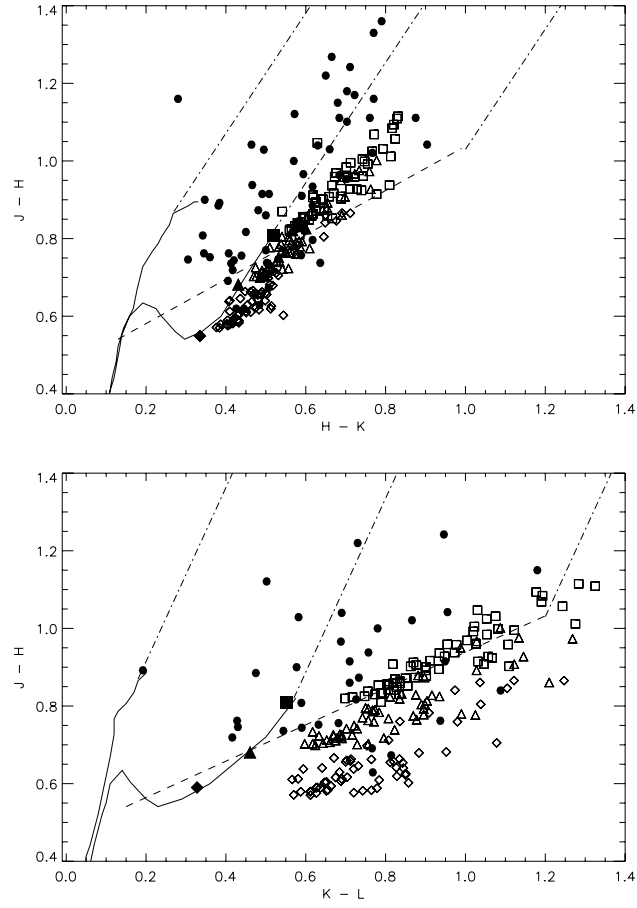
Figure 3.13: *JHKL* plots as in Fig. 3.12, but with model colours for all inclinations.

Comparing the synthetic models to SED and colour-colour observations of suspected Brown Dwarfs shows that flared disks of varying mass can account for the observed SEDs and colours. The adopted circumstellar dust model naturally suppresses the 10 μm silicate feature that is absent in the observations of Cha Hα2. Long wavelength observations are however required to discriminate between the flared disk models and alternative flat disk models that have been proposed for some sources.

Some millimetre observations of Brown Dwarfs have recently become available. Scholz et al. (2006a) carried out sensitive 1.3 millimetre observations of 20 young Brown Dwarfs in the Taurus-Auriga star-forming region. They find evidence for disks in 5 of these sources and derive disk masses ranging from less than ∼0.4 to several Jupiter masses. Their relative disk masses are comparable to those derived for the T-Tauri stars; most are approximately in the $< 1\% - 5\%$ range. They model the millimetre data along with mid-IR data from the *Spitzer* Space Telescope with the Monte Carlo radiative equilibrium code and a multiple dust species code (see Fig. 3.14). They find lower flux levels in the mid-IR than predicted by hydrostatic models, implying dust settling to the disk mid-plane. Models that study grain growth and dust settling in Brown Dwarf disks are discussed in Chapter 5.

Recent work on Brown Dwarf formation suggests that many Brown Dwarfs are ejected from multiple systems and that any circumstellar disks that survive the ejection will be very small (∼5%). In the numerical simulations of Bate et al. (2003), no disks survive around ejected Brown Dwarfs down to their simulation resolution of approximately 10 AU. Scholz et al. (2006a) report no evidence for disk truncation with at least 25% of their targets likely to have disks with radii > 10 AU based on models with smaller disks being unable to reproduce the millimetre fluxes. It is, however, very difficult to determine disk radii from SED data alone (see for example Chapter 5 Fig. 5.16) and more stringent tests of the small disks prediction of Bate et al. (2003) will require high resolution imaging to resolve the disks via their scattered light and thermal emission (see also Beckwith et al. 1990; Chiang et al. 2001).
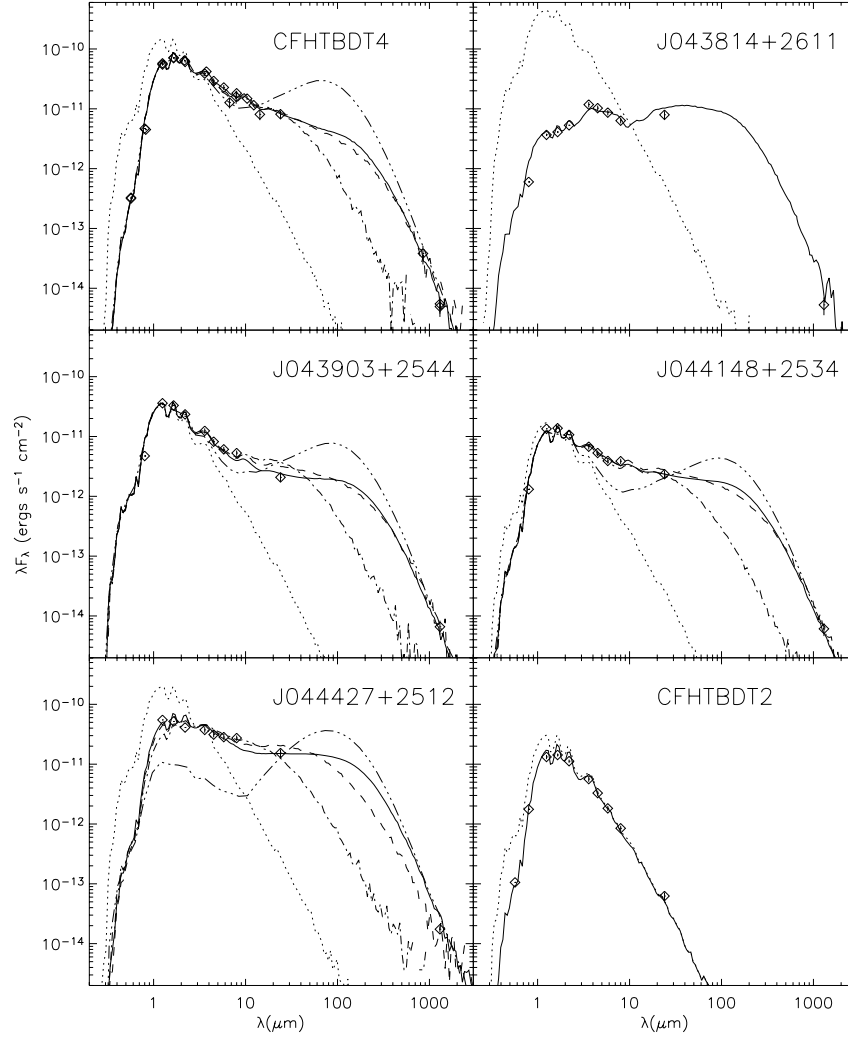
Figure 3.14: SED data and model fits for six sources from Scholz et al. 2006a. Most panels show five curves: input stellar spectrum (dots), best fitting disk model using two dust components (KMH and HH30) with $R_{max} = 100$ AU (solid), two-component disk model with $R_{max} = 10$ AU (dashed), two component disk model with $R_{max} = 1$ AU (dot-dash), and a hydrostatic model with the same total mass as the best fitting disk model and radius $R_{max} = 100$ AU (dash-triple dot). For the almost edge-on system J043814+2611, only the best fit two-component dust model with $R_{max} = 100$ AU is shown. For the moderately inclined system J044427+2512 the hydrostatic disk structure is more vertically extended than the two-component model and as such obscures the star at optical and near-IR wavelengths. For CFHTBDT2 the data are consistent with no disk and only the stellar atmosphere (dots) and reddened stellar atmosphere (solid) are shown. For further details of the models see Scholz et al. (2006a).

CHAPTER 4

MODELS OF T-TAURI ENVIRONMENTS

This chapter presents models of large and small-scale structure in the circumstellar environment of several T-Tauri stars.

4.1 Introduction

As described in Chapter 1, T-Tauri stars are pre-main sequence objects that have attracted immense interest over the past few decades due to the suggestion that our own Sun may have formed via a T-Tauri phase. Defining features of T-Tauri stars are the presence of Balmer lines, Ca H and K lines in emission, photospheric absorption spectra suggestive of late F type or later main sequence stars, and variability that occurs over a wide range of timescales from minutes to at least a century and can be quasi-periodic or highly irregular (Appenzeller & Mundt 1989, and references therein). Their youth is implied by the kinematic association of many T-Tauri stars with dark molecular clouds where stars are formed (Jones & Herbig 1979) and the presence of Lithium in absorption (Bertout 1989) which is rapidly destroyed once nuclear fusion begins. It is accepted that T-Tauri stars evolve to the zero age main sequence within a few $\times 10^7$ yrs.

T-Tauri stars are classified as either 'Weak Line T-Tauri stars' (WTTs) or 'Classical T-Tauri stars' (CTTs). CTTs are characterized by both UV and IR excesses relative to a main sequence star of the same effective temperature. This excess is usually attributed to the presence of a protoplanetary disk resulting from a combination of reprocessing photospheric radiation and from heating of gas and dust by dissipation of viscous accretion energy (Lynden-Bell & Pringle 1974; Kenyon & Hartmann 1987; Adams et al. 1987; Bertout et al. 1988; Bertout 1989). Winds and outflows are also a common phenomenon in CTTs and they seem to be ultimately powered by accretion onto the star (Cabrit et al. 1990). WTTs, in contrast, display no UV excess, little or no IR excess and they show very

weak, if any emission lines (Montmerle et al. 1993). It is thought the WTTs are more evolved than CTTs with little or no disk remaining, however they may not be any older than CTTs.

As discussed in Chapter 1, CTTs were the first pre-main sequence objects to reveal the presence of a protoplanetary disk and, partly as a result of this, there is more information available on CTTs disks than any other type. Models of other disk systems begin with the understanding that has been gained from studying CTTs disks, however it is clear that even within the CTTs there is great variety in the nature of the disks quite possibly relating to their exact evolutionary stage. In some cases, where enough information is available, it may be possible to model the fine details of the disk systems, however it is also important to know that more basic models can provide an estimate of the large scale-structure without the need for such detail.

The models in Section 4.1 illustrate the ability of the Monte Carlo radiation transfer codes to model a wide range of environments on a large scale. To contrast with this Section 4.2 then presents small-scale models for SU Aur, DR Tau and RY Tau. Accretion disk models are used in conjunction with interferometric observations to study the structure within the inner few AU of circumstellar disks. These models have been presented in O'Sullivan et al. (2005), Hodapp et al. (2004), and Akeson et al. (2005).

4.2   Models of Large Scale Structure

4.2.1   AA Tau

In O'Sullivan et al. (2005) the photometric variability of classical T-Tauri star AA Tau is modelled using a magnetospheric accretion model (Königl 1991). Photometric variability is a defining feature of T-Tauri stars (Joy 1945) and is thought to be a result of hot and cold spots on the stellar surface (e.g. Bouvier et al. 1993b; Herbst et al. 1994; Kenyon et al. 1994; Eaton, Herbst & Hillenbrand 1995; Choi & Herbst 1996). The magnetospheric accretion model predicts hot-spots where material from the circumstellar disk is being accreted onto the stellar surface along magnetic field lines (Ghosh & Lamb 1979; Camerzind 1990, Königl 1991; Shu et al. 1994). It has also been suggested in the case of HH 30 IRS (Stapelfeldt et al. 1999) and in earlier modelling of AA Tau (Bouvier et al. 1999, Bouvier et al. 2003) that an associated warp in the inner disk could provide the necessary occultation.

AA Tau exhibits a large IR excess in its spectral energy distribution indicative of a

class II object i.e. a star+disk. The SED was used here to study the large-scale structure of AA Tau's disk.

SED Models

SED modelling was carried out using the self-consistent radiative equilibrium code detailed in Chapter 2. In summary, the code assumes the disk is in vertical hydrostatic equilibrium and has been updated to include calculations for steady accretion. The models adopt Shakura & Sunyaev (1973) α-disk theory to describe CTTs accretion disks. The disk density is not parametrized by power laws as in previous SED models (e.g. Wood et al. 2002a, Rice et al. 2003) rather the density and temperature structure are solved for in an iterative loop. The inclusion of accretion in the modelling algorithm is described in Chapter 2, Sect. 2.2. The models adopt the large grain dust opacity model (HH30), that has been used to successfully model the SEDs of the HH 30 IRS and GM Aur disks (Wood et al. 2002a; Rice et al. 2003; Schneider et al. 2003). This dust model is described in Chapter 2 Sect. 2.1.2.

Results

The code produces emergent spectra at a range of viewing angles. It is found to be possible to fit the SED of AA Tau with a disk of 150 AU inclined at $\sim 70°$ with stellar parameters $T_{star} = 4000$ K and $R_{star} = 1.9 R_{\odot}$, and with an accretion rate of $\dot{M}$=7.5 $\times 10^{-9}$ $M_{\odot}\mathrm{yr}^{-1}$ which corresponds to a disk mass of 0.02 $M_{\odot}$. These parameters are all within the typical range for T-Tauri stars (Calvet et al. 2000; Natta et al. 2000, and references therein). The code calculates an inner radius for the disk of 7 $R_{\star}$, corresponding to a dust destruction temperature of 1600 K. Figure 4.1 shows observations of AA Tau and the SED model for the system described above, viewed at $i = 65°$, $68°$ and $71°$.

Note, since this study was completed and published *Spitzer* Infrared Spectrograph (IRS) data has become available. This is shown in Fig. 4.2 and is discussed in Chapter 5 Sect. 5.3. These new data does not significantly change the results presented here.

The purpose of the SED modelling here was simply to determine the large-scale structure of the AA Tau disk and use the derived disk mass and density structure in non-axisymetric scattered light models. Two SED models were used as part of this study. Both models have their large-scale structure calculated by enforcing vertical hydrostatic equilibrium in the disk as described earlier. The first model uses this structure fully throughout the disk and is used to derive a likely inclination for the disk system. The
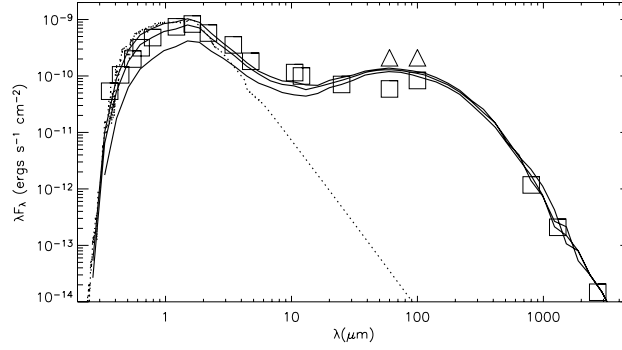
Figure 4.1: SED data and model for AA Tau. The dotted line is the adopted input stellar spectrum and the three solid lines are the model SEDs for inclinations of (from top to bottom) $65°$, $68°$ and $71°$. The different data points at 60 and 100 μm represent $IRAS$ (squares) and Infrared Space Observatory (ISO) (triangles) observations.

second model takes an analytic description for the warp in the inner disk, couples it at the appropriate point to the outer disk structure derived in model 1. The purpose of model 2 is to study the photopolarimetric variability.

Photopolarimetric Modelling

In O'Sullivan et al. (2005) the inner disk is studied using the Monte Carlo scattered light and radiative equilibrium code coupled with hydrodynamic simulations. Previous Monte Carlo photopolarimetry simulations of systems with hot-spots (Wood et al. 1996b; Wood & Whitney 1998; Stassun & Wood 1999) are extended to include the effects of disk warps. The Monte Carlo simulations were used to determine what dimension of warp is required to reproduce the observations and then the smooth particle hydrodynamic (SPH) code was used to explore the required magnetic field strength. The results from this modelling suggest a warp at approximately the co-rotation radius (where the Keplerian angular velocity equals the stellar angular velocity) can reproduce the observed variability if the system is at an inclination of $75 \pm 2°$. Other parameters can be found in O'Sullivan et al. (2005) along with details of the modelling.

Discussion

It is found to be possible to model the SED of AA Tau with a disk of 150 AU inclined at $\sim 70°$ with stellar parameters $T_\star = 4000\ K$ and $R_\star = 1.9\ R_\odot$, and with an accretion rate of $\dot{M} = 7.5 \times 10^{-9}\ M_\odot \mathrm{yr}^{-1}$ which corresponds to a disk mass of 0.02 $M_\odot$. As can be seen
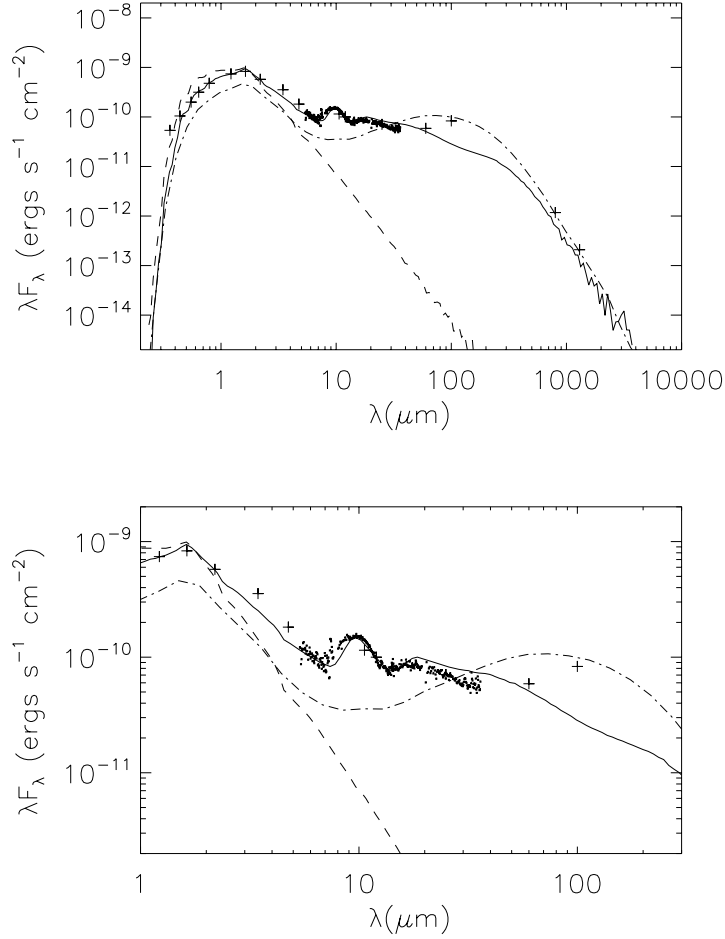
Figure 4.2: SED models for AA Tau. Broken line is hydrostatic equilibrium disk and the solid line is multiple dust species model (O'Sullivan et al. 2005). Both SEDs are for disks inclined at 71°. The small filled dots are the *Spitzer* IRS data and the crosses are the IRAS data from the Kenyon & Hartmann (1995) compilation.

in Fig. 4.1, for inclinations of greater than 70°, direct optical star-light becomes obscured by the flared disk. If the system inclination is in fact greater than 70° as suggested by the photopolarimetric modelling, this suggests shortcomings in the models. One possible explanation could be dust settling which would effectively reduce the disk scaleheight and therefore allow the star to be viewed at inclinations $i > 75°$ (Dullemond & Dominik 2004a). No great attempt was made to fit the optical flux, because that is observed to vary. The purpose of the SED model was simply to obtain estimates for the disk mass and density structure based on a physically plausible disk model.

4.2.2   HH 30

HH 30 IRS is a CTTs that has been observed to have a near-to edge on disk (Burrows et al.1996). Two groups have studied the multi-wavelength images (Burrows et al. 1996; Wood et al.1998; Cotera et al. 2001; Watson & Stapelfeldt 2004), variability (Wood et al. 1998; Stapelfeldt et al. 1999; Wood et al. 2000), and SED (Wood et al. 2002a) of this system using the parametrized fixed density models described in Chapter 2 Sect. 2.1.4. Broad agreement is found on the disk mass ($M_{disk} \sim 10^{-3}\ M_{\odot}$), size ($R_{max} \sim 200$ AU), and scaleheight ($h[100\ \text{AU}] \sim 15$ AU). Modelling of multi-wavelength images and the sub-millimetre SED indicates the circumstellar dust has a grayer opacity and hence a larger average grain size than interstellar grains.

The purpose here of modelling HH 30 IRS was to investigate whether a steady accretion disk in vertical hydrostatic equilibrium could reproduce SED and scattered light observations of this system. No attempt was made to model the variability. The variability has previously been studied by Wood et al. (2000) and Watson et al. (2000).

Modelling and Discussion

HH 30 IRS was modelled with the iterative code that solves for density and temperature structure adapted to include steady accretion (see Chapter 2). The adopted dust model was the large grain distribution HH30 and it properties are described in Chapter 2 Sect. 2.1.2.

A model fit is presented in Figs. 4.3 and 4.4, for a disk inclined at 81°. This model has $R_{\star} = 1.5\ R_{\odot}$, $M_{\star} = 0.64\ M_{\odot}$, $T_{\star} = 3500$ K, $R_{max} = 250$ AU, and a steady accretion rate of $\dot{M} = 2 \times 10^{-9}\ M_{\odot}\text{yr}^{-1}$, giving $M_{disk} = 3 \times 10^{-3}\ M_{\odot}$. These parameters are consistent with those previously derived.

Although not a definitive model due to the variability of this system and the non-uniqueness in the modelling, this fit does illustrate the ability of the code to fit the large-scale structure of HH 30 IRS as a disk in hydrostatic equilibrium with dust and gas well mixed. *Spitzer* data is required to critically test this model.
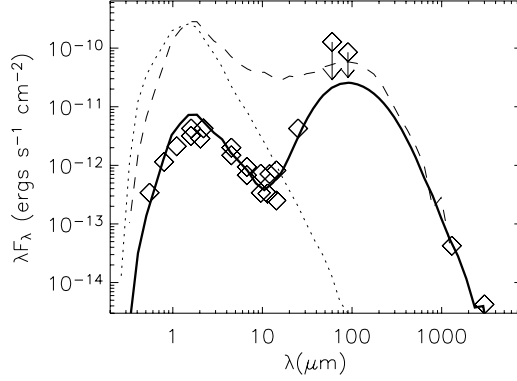
Figure 4.3: SED model fit to HH 30 data from Mundt & Fried (1983:V and I); Vrba et al. (1985: H,K, and an upper limit at L); Reipurth et al (1993: 1.3 mm) and Stapelfeldt & Moneti (1999: 4.5 - 90 μm). IRAS data at 60 and 100 μm are upper limits. Model fit (solid line) is for a 250 AU disk inclined at 81°. Model SED has been reddened by $A_v = 2$ and disk is assumed to be at 140 pc. Other parameters are: $\dot{M} = 2 \times 10^{-9}$ $M_\odot \mathrm{yr}^{-1}$, $M_{disk} = 3 \times 10^{-3}$ $M_\odot$, $T_\star = 3500$ K, $R_\star = 1.5$ $R_\odot$, $M_\star = 0.64$ $M_\odot$, $R_{in} = 5$ $R_\star$. The dashed line is the SED for a face-on disk given the same input parameters and the dotted line is the input stellar spectrum.
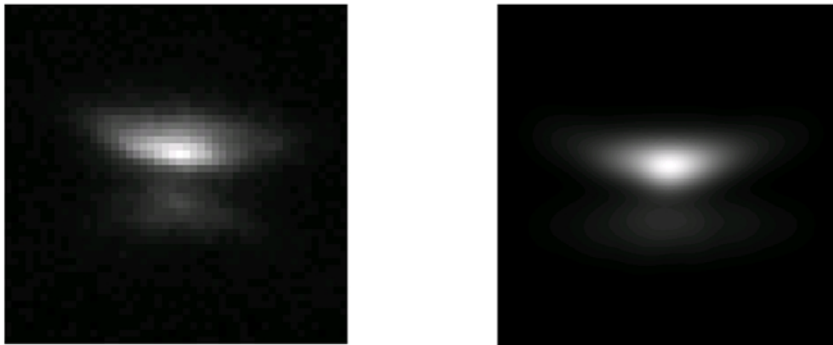
Figure 4.4: K-band HST near-IR camera and multi-object spectrometer (NICMOS) image (left) and model (right) for HH 30. Model parameters are as for Fig. 4.3. Images are 400 AU on a side, assuming HH 30 is at a distance of 140 pc.

4.2.3   ASR 41

ASR 41 is a young stellar object located in the NGC 1333 star formation region in the Per OB2 complex. During a near-IR study of NGC 1333, Hodapp et al. (2004) observed that ASR 41 (Aspin et al. 1994) exhibits the morphology of an edge-on disk object with two very large scattering lobes. The edge-on disk structure of ASR 41 was also discovered by Elston et al. (2003) as part of their survey of giant molecular clouds. The aim of this study, presented in Hodapp et al. (2004), was to model this object and demonstrate that its features can be well explained within the current paradigm of star-formation.

At near-IR wavelengths images clearly show the bifurcation of the extended emission by a dark band at an angle of $\sim 137^\circ$ (see Fig. 4.5). The reflection nebula extends out approx 10 arcsec from the centre point. Here NGC 1333 is assumed to be at the same distance of 316 pc that Herbig (1998) determined for the IC 348 cluster since they are both located in the same Per OB2 molecular cloud complex. 10 arcsec therefore equates to $\sim 3000\ AU$. Although scattering is seen beyond this, it is confused with artifacts from sky subtraction. Typical T-Tauri disks have radii up to a few 100 AU (e.g. Burrows et al. 1996; Lucas & Roche 1998; Stapelfeldt et al. 1998a; Padgett et al. 1999; Monin & Bouvier 2000; Grosso et al. 2003; Jayawardhana et al. 2002) and therefore this scattering region is many times larger than this. This leaves two obvious options to explore - (A) that ASR 41 has a huge extended disk or (B) that the observed dark lane is a shadow cast by a smaller disk projected onto the extensive surrounding dusty environment. Although there is now support for large disks around a few higher mass systems (Cesaroni et al. 1997; Zhang et al. 1998) the shallow wavelength dependence of the images suggest that scenario B is more likely in this case. A large disk would be expected to show a wider, more pronounced dust lane at shorter wavelengths. There is also a clearly defined central source located at $3^h\ 28^m\ 51^s.3\ +31^\circ\ 17'\ 40"$ (J2000) (with estimated errors of ≈ 0.25 arcsec) in all images from [SII] to the K band. and no evidence for a wavelength dependent position of the central brightness peak as is often observed in class 1 objects dominated by absorption from a large massive disk (Hodapp et al. 1988).

Aside from modelling the wavelength dependent morphology of ASR 41 it was observed that this is not a strong sub-mm source. An upper limit of 200 mJy at 850 μm was estimated placing constraints on the mass of the dusty material surrounding ASR 41.
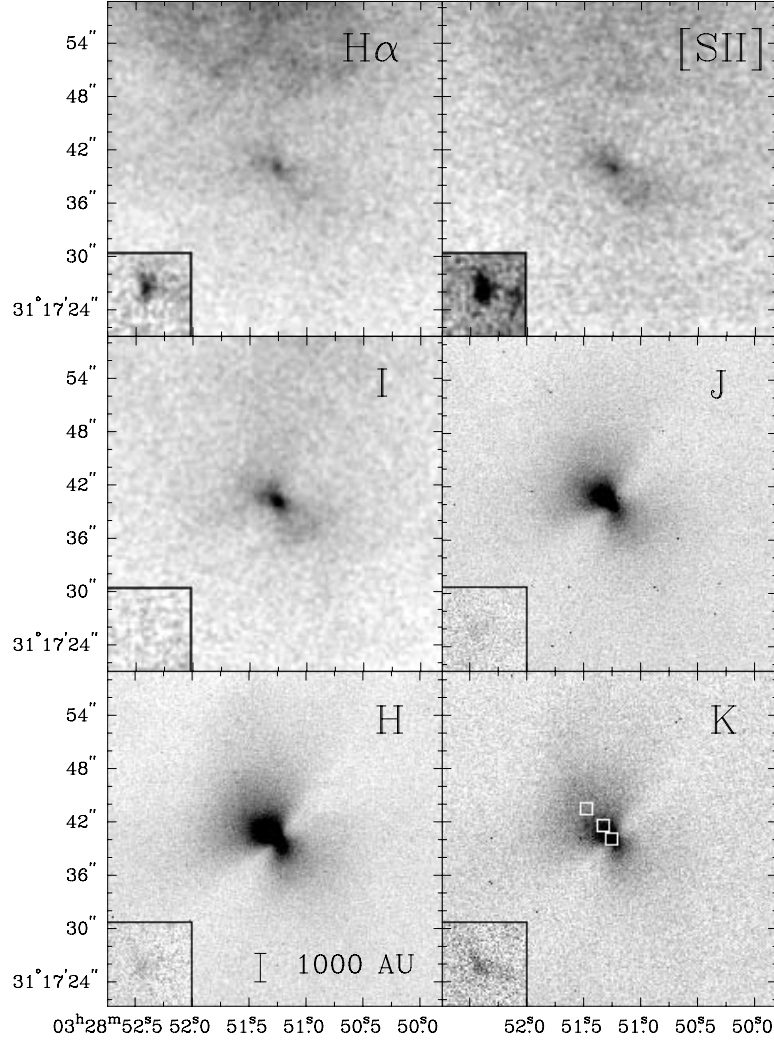
Figure 4.5: Hα, [SII], *I*, *J*, *H*, and *K*-band images of ASR 41. Inserted in each image is a smaller image of the HH-object 727, at the same spatial scale, but with the intensity scale stretched by a factor of two. The observed morphology of ASR 41 changes dramatically from Hα and [SII], where an extended nebula with a central, almost point-like source is visible, to the *I* band, where the bifurcating dark band becomes noticeable. The bipolar nature of the object and the full extent of the dark band are fully established in the *J* band, and the morphology then remains virtually identical in the *H* and *K* bands. The inserted image of the HH object 727 is strongest in Hα and [SII], and indicated in *K* (due to H_2 line emission), but is not detectable or very weak in the *I*, *J*, and *H* bands.

Modelling

Models were computed using the Monte Carlo scattered light code and the radiative equilibrium code of Chapter 2 with a parameterized disk density and envelope structure. The scattered light code outputs wavelength specific scattered light images and was used to model the morphology of ASR 41. This code is described in Whitney & Hartmann (1992), Whitney & Hartmann (1993) and updated in Whitney et al. (2003a). The radiative equilibrium code was used to produce SEDs to check the sub-millimetre flux level limit was not violated.

The aim was to explain the features of ASR 41 in-line with the current paradigm for star formation and therefore it is assumed that this is a class II T-Tauri star surrounded by a typical disk of a few 100 AU in radius. Two models are presented: (Model A) a disk plus constant density cloud (Model A) and (Model B) a disk plus infalling envelope with the density distribution of the free-fall models of Ulrich (1976) and Cassen & Moosman (1981).

Results

Both models are able to reproduce the dark band as the projected shadow of a smaller disk. Fig. 4.6 shows the K-band image of ASR 41 (top, rotated to have the polar axis vertical for comparison with the models), and the two model flux distributions. Some noise was added to the model images to make them more visually comparable to the real image.

A 'disk+envelope' model is the common geometry used to explain young extended bipolar nebulae. The rate of infall depends on the age of the system (Whitney & Hartmann 1993; Whitney et al. 2003a). For ASR 41 the upper limit to the sub-millimetre provides a constraint on the infall rate. The 'disk+envelope' model presented in Fig. 4.6 has an outer disk radius of 200 AU, a disk mass of 0.06 $M_{\odot}$, an outer envelope radius of 7000 AU, and an infall rate of 3.5 $\times 10^{-6}$ $M_{\odot}\mathrm{yr}^{-1}$. This infall rate is similar to the rate used in other models of young stellar objects (Whitney & Hartmann 1993). This successfully reproduces the basic features of the observations, but shows a steeper intensity gradient with distance from the illuminating object than was observed which results in the flux is falling off too rapidly. It predicts a 850 μm flux of 71 mJy, consistent with the sub-millimetre upper limit (see Fig. 4.7).
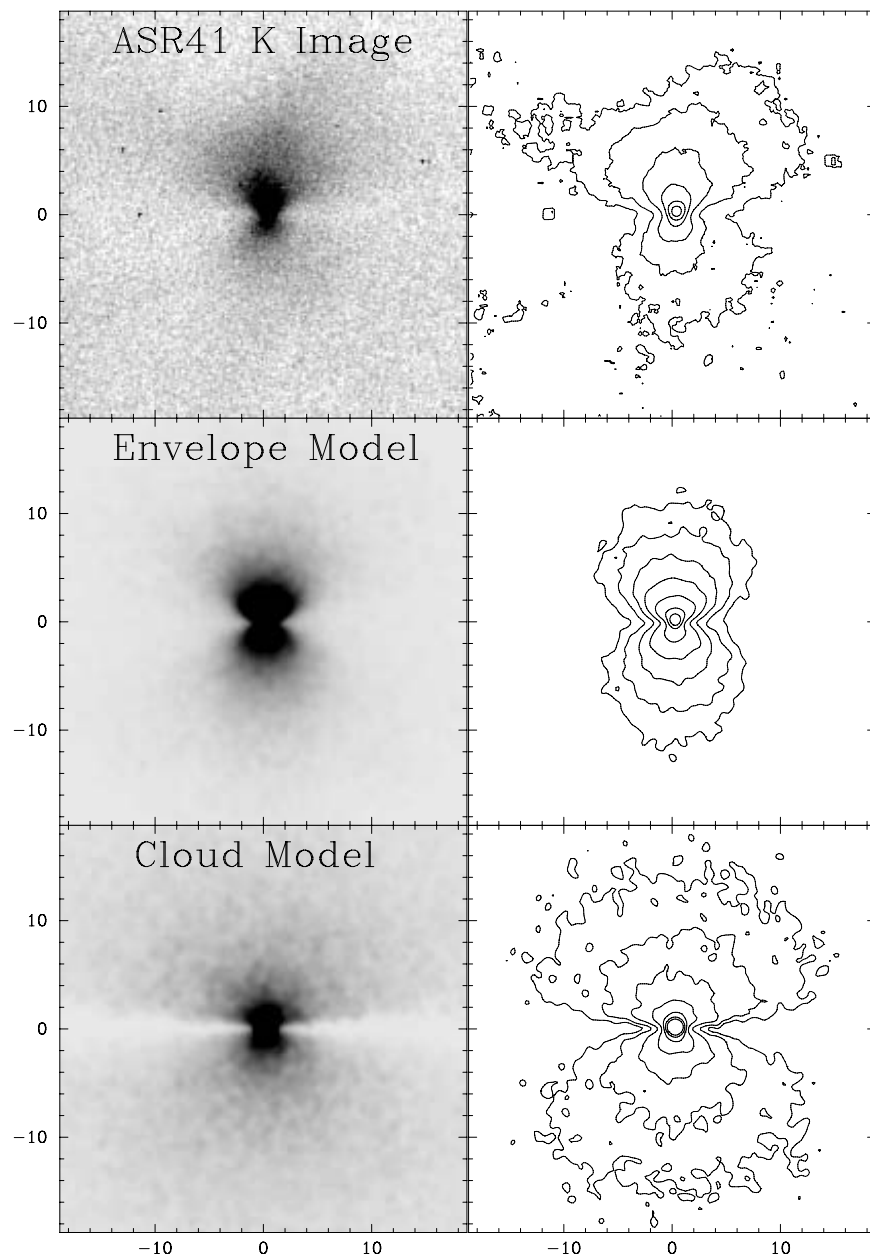
Figure 4.6: Comparison of the *K*-band image (rotated) of ASR 41 (top) with a 'disk+envelope model' (centre), and a 'disk+cloud' model (bottom).
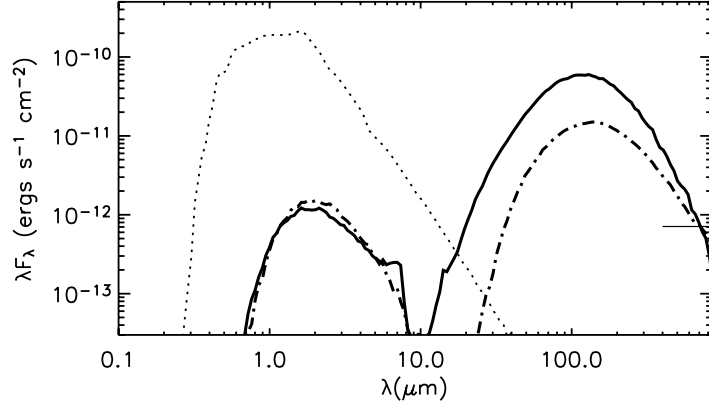
Figure 4.7: SEDs for the 'disk + envelope model' (dashed-dot), and the 'disk + cloud' model (solid). Stellar source is assumed to be at a distance of 316 pc. The thin horizontal line shows 200 mJy limit at 850μm.

.

The 'disk+cloud' model matches the near-IR morphology better, including the large extent of the reflection nebulosity. This model is a simplification of the infalling envelope model where the disk is now surrounded by a scattering cloud of uniform density. The disk in this model has an outer radius of 100 AU and mass of 0.005 $M_\odot$. The cloud has an outer radius of 10,000 AU and a constant density of 2×10^{-20} g cm^{-3}, which is in the range of typical densities in large molecular clouds. This model produces a 850 μm flux of 40 mJy, well below the sub-mm flux limit (see Fig. 4.7). Slightly better fits to the near-IR fluxes can be achieved by an order of magnitude increase in cloud density and disk mass, however this predicts a 850μm flux of 234 mJy, well above the flux limit.

Both model fits to the observed photometry indicate inclinations of $\sim 80°$, even though the match to the observed morphology, in particular the difference in flux from the two lobes, could probably be improved by assuming somewhat lower inclinations.

Discussion

Hodapp et al. (2004) present images of the young stellar object ASR 41 in NGC 1333 at wavelengths ranging from Hα to the K-band. In these images an associated bipolar nebula is seen to be much larger than typical edge-on disk systems, but can be understood as the shadow of a smaller disk being projected into the dusty material of the surrounding molecular cloud. Presented here are detailed model calculations of the scattering and radiative transfer in this object. These models show that the morphological features and

the near-IR fluxes can be modelled by a small, low-mass disk and surrounding scattering medium without violating the upper limit on the sub-mm flux. ASR 41 is, most likely, a Class II T-Tauri star with a disk of roughly the size of our solar system, and overall similar to other edge-on-disk objects. It is distinguished from those objects by the casting of a disk shadow in the surrounding dusty molecular material.

The models do not precisely match the near-IR photometry and morphology of the object which may be due to shortcomings in the dust model used here. At the time of modelling the code was limited to one dust model throughout, and given the extent of the object an interstellar grain model was chosen. This is a good approximation for the particles expected in a thin molecular cloud, but may not be a good model for the grains in a much denser, protoplanetary dust disk in the close vicinity of a young star where grain growth and dust settling may be taking place, (e.g. Beckwith et al. 1990; Wood et al. 2002a). Due to the simplifications in the models, they have not been used to derive the luminosity or any detailed information about the evolutionary state of the star at the centre of ASR 41. The models do demonstrate that it is possible to understand the morphology of ASR 41 in terms of the current star formation paradigm.

4.3   Models of Small Scale Structure

4.3.1   Modelling of the Inner Disk Region of T-Tauri Stars

Akeson et al. (2005) present IR interferometry observations of four T-Tauri stars - T Tau N, SU Aur, RY Tau and DR Tau - made using the Palomar Testbed interferometer (PTI) located on Palomar Mountain near San Diego, CA (Colavita et al. 1999). All four sources are located in the Taurus-Auriga molecular cloud at a distance of $\sim$ 140 parsecs and all have significant IR excess indicative of protoplanetary disks. The near-IR interferometry measurements sample the inner regions of the disk and the aim of this study was to model these new observations to constrain the properties of this little explored region of the protoplanetary disk.

Two types of models are presented. The first set are purely geometric models of the emission that are used to constrain the physical size of the emission region. The second set are Monte Carlo radiation transfer models of accretion disks, which model both the SED of these objects and the interferometric observations. Although observations are presented for all four objects only SU Aur, RY Tau and DR Tau are modelled. The new observations of T Tau N are consistent with the results of Akeson et al. (2002). No models have been calculated here for T Tau N due to the complicated nature of the source i.e. it is a binary

star, has a disk plus envelope with asymmetric outflow cavities; scattered light models of T Tau N that reproduce the observed asymmetry (Stapelfeldt et al. 1998b) are detailed in Wood et al. (2001).

Interferometry Measurements

IR interferometry data were taken at the PTI, which is described in detail by Colavita et al.(1999). PTI combines starlight from two 40-cm aperture telescopes using a Michelson beam combiner, and the resulting fringe visibilities provide a measure of the brightness distribution on the sky via the van Cittert-Zernike theorem, which states that the visibility distribution in u-v space and the brightness distribution in the sky are Fourier transform pairs (Born & Wolf 1999). Data was obtained in the K-band (2.2 μm) in all three PTI baselines: NS (110 meter), NW (85 meter) and SW (85 meters). SU Aur observations described in Akeson et al. (2002) and Akeson et al. (2000) are also considered in the analysis that follows. A summary of the new observations is given in Table 4.1.

Observations						
	NS		NW		SW	
	nights	ints	nights	ints	nights	ints
T Tau N					1	6
SU Aur					1	6
DR Tau	3	5	1	3	1	4
RY Tau	4	27	3	14	2	8
Calibrators						
Calibrator	size est.(mas)	Sources				
HD 28024	0.68	T Tau N, SU Aur, DR Tau, RY Tau				
HD 30111	0.60	T Tau N, SU Aur				
HD 30122	0.11	T Tau N, SU Aur				
HD 28677	0.34	DR Tau, RY Tau				
HD 26737	0.24	DR Tau, RY Tau				

Table 4.1: New observations of T-Tauri sources from PTI. Each integration represents 125 seconds of fringe data.

The data were calibrated using the usual PTI method (Boden et al. 1998). In brief, a synthetic wide-band channel is formed from five spectrometer channels ($\lambda = 2.0-2.4$). The system visibility, the response of the interferometer to an unresolved object, is measured

using calibrator stars. The calibrator star sizes were estimated using a blackbody fit to photometric data from the literature. Calibrators were chosen for their proximity to the source and for small angular size, minimizing systematic errors in deriving the system visibility. All calibrators used here have angular diameters < 0.7 milliarcseconds and were assigned uncertainties of 0.1 milliarcseconds (Table 4.1). The calibrated data are presented in normalized squared visibility ($V^2 = 1$ for an unresolved source, less for a resolved source), which is referred to as visibility here. The calibrated visibility uncertainties are a combination of the calibrator size uncertainty and the internal scatter in the data. DR Tau is near the tracking limit for PTI, therefore wide-band data are used rather than synthetic wide-band (spectral channel) data. The main difference between these two channels is that the spectral channels are spatially filtered and the wide-band channel is not. The accuracy of the wide-band data were confirmed by comparing the wide-band and synthetic wide-band data for other sources observed on the same night as DR Tau.

The calibrated data were edited to remove integrations with very high jitter (a measure of the phase noise) and integrations for which the estimates of the system visibility from separate calibrator observations disagreed by more than 3σ. No more than 10% of the data for any given source was removed, except for DR Tau on the NS baseline, and inclusion of these data points would not substantially change the results given below.

The calibrated and edited data are shown in Fig. 4.8 for each source as a function of projected baseline length and position angle. Three of the four sources, T Tau N, SU Aur and RY Tau are clearly resolved. The new observations of T Tau N are consistent with the results of Akeson et al. (2002).

4.3.2   IR photometry

A sample of young stellar objects, including DR Tau, SU Aur and RY Tau and a sequence of photometric standard stars taken from Landolt (1992) were observed over seven nights from December 2003 to March 2004 (December 16, January 10, 13, 15, 22, 23, and March 9) using the Pomona College 1-m telescope with the Claremont-Riverside-Infrared Camera (CLIRCAM) in the J and K bands. For each object, a series of at least five dithered exposures was used to create individual sky images for each field. The sky background and instrumental noise was subtracted from all the images, and repeat exposures were median combined after shifting to a common astrometric reference frame to remove a majority of the background noise. Instrumental magnitudes were converted to standard J and K magnitudes using a combination of the published magnitudes and the J and K magnitudes from bright 2MASS stars in the image frames. The magnitudes given in
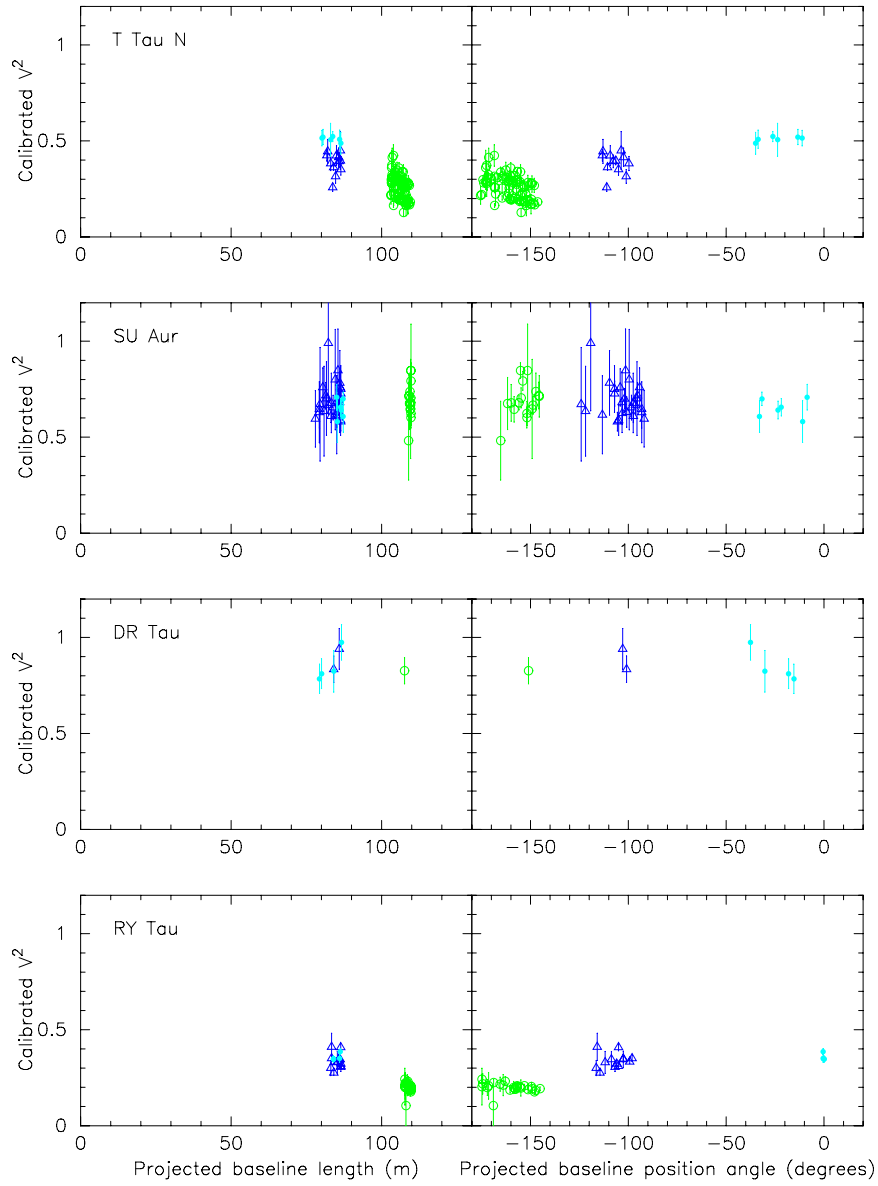
Figure 4.8: Calibrated PTI visibilities for each of the four sources by baseline: NS (open circles), NW (open triangles) and SW (closed circles). For T Tau N and SU Aur the data from Akeson et al. (2002) is also plotted.

Table 4.2 are the average magnitudes over all six nights using the average calibration zero points from the complete sample of photometric standards and 2MASS stars. The three sources observed showed no statistically significant variability over the nights observed, and were constant in magnitude within the photometric error of 0.15 magnitudes in J and 0.15 magnitudes in K. For comparison, the 2MASS J and K magnitude and observation date are also given. Together, the Pomona and 2MASS data bracket the PTI observations. At K band, only RY Tau shows a significant difference between the 2MASS measurement and these more recent observations; however, past observations of these sources have shown

IR variability (particularly DR Tau (Kenyon et al. 1994)). Additional information on the IR observations from Table 4.2 is presented in Scire et al. (2004).

Source	# nights	mag	rms	2MASS mag	2MASS rms	2MASS date
			J band			
SU Aur	6	7.24	0.143	7.20	0.020	1/30/98
DR Tau	6	8.75	0.195	8.84	0.024	10/10/97
RY Tau	5	7.52	0.226	7.15	0.019	10/29/97
			K band			
SU Aur	6	6.17	0.114	5.99	0.022	1/30/98
DR Tau	6	6.87	0.183	6.87	0.017	10/10/97
RY Tau	6	5.76	0.168	5.39	0.022	10/29/97

Table 4.2: Results of IR Photometry Observations

4.3.3 Geometric Models

This section describes simple geometric models of the emission which are used to characterize the source size and inclination. These models adopt a configuration of an unresolved point source (stars have diameters ≤ 0.1 milliarcseconds and therefore a $V^2 > 0.99$ at PTI) and a resolved component. The contribution of the stellar component is taken from measurements of the IR veiling, f_{excess}, from Muzerolle et al. (2003b) for SU Aur and DR Tau and from Folha & Emerson (1999) for RY Tau. In Akeson et al. (2005) two types of geometric fits were considered - a uniform disk and a ring model.

Here only the ring models are discussed as the uniform disk models measure outer diameters of the emission region, whereas ring models measure inner ring diameters, thus better providing a closer analogy to a model in which significant IR emission arises from the inner wall of the dust disk as is the case for the radiation transfer models that follow in the next section. For the ring model, visibilities were calculated for a range of inner diameters and compared to the observed visibilities. For each ring diameter considered, the width was determined by matching the excess flux, derived using the measured *K*-band veiling, with a blackbody emission source at a temperature of 1600 K, the assumed dust destruction temperature (Duschl et al. 1996). In these models, the dust destruction temperature controls the width of the ring, but affects the fit radius only through the shape of the model visibility curve. For example, changing the blackbody temperature of the

ring from 1200 to 2000 K would change the fit radius for RY Tau by 30%. For comparison with the radiation transfer models the results of the geometric models are presented in Table 4.3 and Fig. 4.9. A face-on model is presented along with a best fit inclined model. The uncertainties in the model fits due to the uncertainty in the stellar contribution are also given. The geometric models are described further in Akeson et al. (2005).

	SU Aur	DR Tau	RY Tau
f^a_{excess}	0.44 ± 0.09	0.8 ± 0.3	0.71 ± 0.11
K_m (2MASS)	5.99	6.87	5.40
Face-on ring models			
Inner radius (AU)	0.13 ± 0.021	0.057 ± 0.027	0.17 ± 0.01
Width (AU)	0.050	0.028	0.035
σ_v (AU)	0.036	0.010	0.059
χ^2/dof	2.5	0.85	4.6
Inclined ring models			
Inner radius (AU)	0.18 ± 0.025	0.070 ± 0.026	0.19 ± 0.01
Width (AU)	0.008	0.019	0.029
PA (degr)	114 ± 23	160 ± 55	110 ± 22
Incl (degr)	52 ± 10	40 ± 30	25 ± 3
χ^2/dof	0.9	0.78	3.0

Table 4.3: Results from geometric model fits. Inclination is defined such that a face-on disk has $\phi = 0$, and position angle, ψ, is measured east of north. The systematic error, σ_v is from the uncertainty in the stellar contribution. χ^2 values given have been normalized by the degrees of freedom. $^a f_{excess} = F_{excess}/F_{total}$, where $F_{total} = F_{star} + F_{excess}$

The ring model fits are graphically shown in Fig. 4.9. In this sky plane representation, the radial coordinate for each data point is the inner ring size corresponding to the measured visibility and accounting for the stellar component listed in Table 4.3. The error bars include the errors on the data points, but not the uncertainty in the stellar contribution. The polar coordinate is determined by the projected baseline position angle. In this way, the constraint provided by the data on both the size and the inclination are visible. The best fit face-on and inclined ring models are also plotted.

The geometric fit ring radii for SU Aur and RY Tau of 0.13 AU and 0.17 AU respectively correspond to 10 $R_\star$ and 11 $R_\star$, both of which are larger than the expected
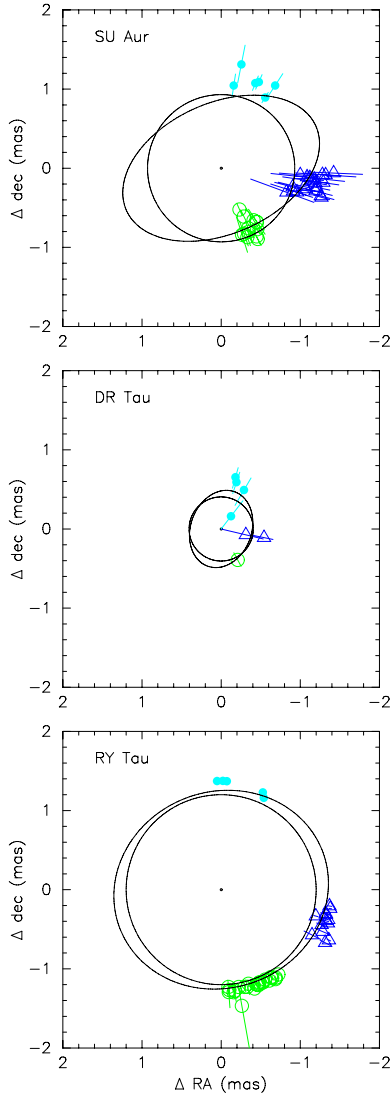
Figure 4.9: The data and uniform disk fits for the best fit face-on and inclined models. An unresolved stellar component is included as described in Akeson et al. (2005). Separate symbols are used for each baseline: NS (open circles), NW (open triangles) and SW (closed circles).

magnetic truncation radius, 3 - 5 $R_\star$ (Shu et al. 1994). In the next section it will be shown, using the radiation transfer models for accretion disks and adding a gas disk component, that emission from gas between the magnetic truncation radius and the dust destruction radius can reconcile accretion disk models with these interferometry observations.

The inclination is considered well constrained for SU Aur and RY Tau, but poorly so for DR Tau. For RY Tau the geometric models suggest an inclination of $19 - 25°$ in agreement with earlier millimetre studies (Koerner & Sargent 1995). The position angle is however poorly constrained and suggested values for this object vary from $27 \pm 7°$

(Kitamura et al. 2002) to $110 \pm 22°$ (Akeson et al. 2005). For SU Aur an inclination of $52 \pm 10°$ is in good agreement with the $60°$ estimate of Unruh et al. (2004). High inclinations of $86°$ for both SU Aur and RY Tau were suggested by Muzerolle et al. (2003b), but this conclusion is not supported by the PTI data. This is also inconsistent with the low visible extinctions ($A_v = 2.1$ and 0.9, respectively) as at such high viewing angles, the star would be heavily occulted by the flared circumstellar disk. Akeson et al. (2005) note that the geometric fits will underestimate the inclination angle if there is a large incoherent component for any of the sources. However, in the detailed radiation transfer models that follow for these three objects the extended light contribution is less than 10%, which is insufficient to change the measured RY Tau inclination by $60°$ as required to match the estimate of Muzerolle et al. (2003b). As will be seen in Sect. 4.3.4, the inclinations suggested by the geometric models are in broad agreement with the detailed radiation transfer models.

4.3.4   Radiation Transfer Models

A shortfall in the geometric models discussed above is that they do not include any extended emission. The radiation transfer models are therefore employed here to estimate the emission contribution made by the outer disk. In addition to earlier accretion models where the void between the inner dust edge is empty, here an inner gas disk is included as a further possible contributer to the emission. The goal is to reconcile the PTI data with the SED data.

The three targets are modelled using the self-consistent radiative equilibrium code described in Chapter 2 and adapted for the study of accretion disks according to Calvet & Gullbring (1998) as described in Chapter 2 Sect. 2.2. In summary the code iteratively solves for the disk density structure, assuming the dust and gas are well-mixed with a standard gas to dust ratio of 100:1 and the system is in vertical hydrostatic equilibrium. In addition to stellar irradiation, the code includes accretion and shock/boundary layer luminosity calculations according to Calvet & Gullbring (1998). Multiple scattering is treated alongside the heating and reprocessing of photons in the disk. Output data includes synthetic SEDs and multi-wavelength images for any viewing angle of the disk system.

The code computes the flared density structure of a steady accretion disk extending from the inner dust destruction radius to a specified outer radius (see Fig. 4.10). The Monte Carlo technique naturally accounts for radiation transfer effects and the heating and hydrostatic structure of the inner wall of the dust disk. The vertical height of the inner wall of dust is not pre-set, but rather calculated as part of the modelling process.

For these models the scale height of the density distribution is 0.3 to 0.7 $R_\star$ at the inner edge. The position of the inner dust disk edge, R_{dust}, is determined from the destruction temperature of silicates, taken to be 1600 K (Duschl et al. 1996). Within the disk the dust-size distribution HH30 (see Chapter 2 Sect. 2.1.2 for details), previously used for the modelling of HH 30 IRS and GM Aur (Wood et al 2002b; Schneider et al. 2003; Rice et al. 2003), is adopted. With a distribution of grain sizes or compositions, the dust destruction may take place over a range of radii (Isella & Natta 2005), but this is beyond the scope of this work. Monnier & Millan-Gabet (2002) discuss the constraints on the dust properties from IR interferometry observations.
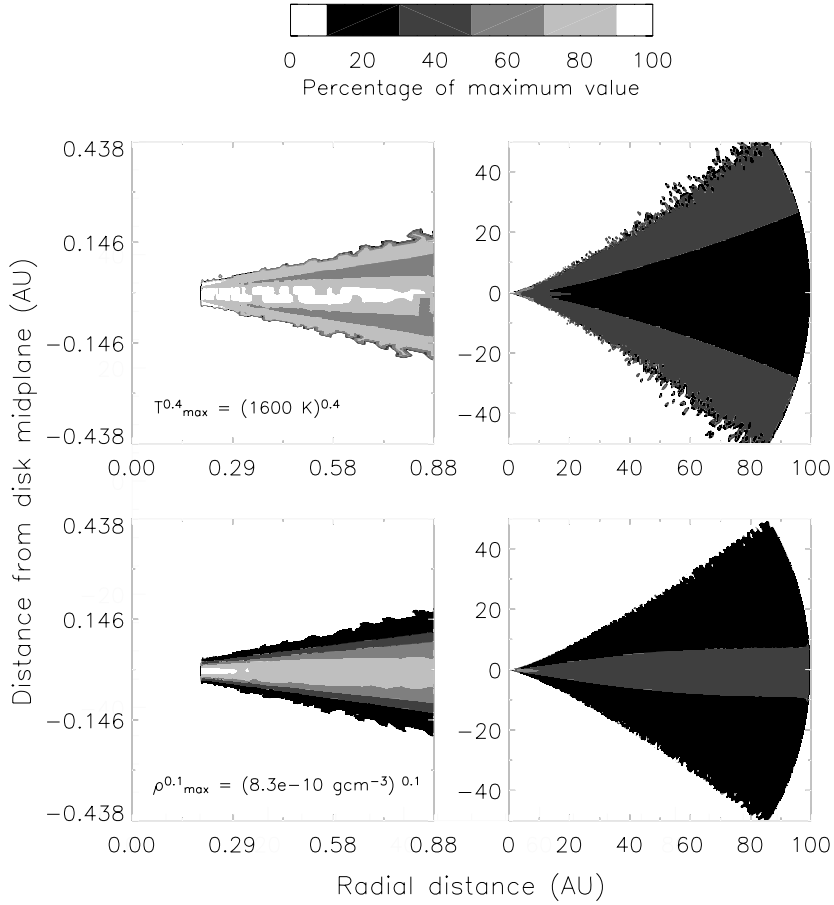
Figure 4.10: Temperature and density distributions for an example disk model. The upper images are temperature scaled to the 0.5 power and the lower are density to the 0.1 power. Note the geometrically thin gas is not shown.

For some sources R_{dust} is large enough ($> 0.2\ AU$) that continuum emission from gas within R_{dust} may make a significant contribution to the PTI observations and therefore a gas disk has been incorporated into the models. The structure and temperature of the gas disk is not computed self-consistently rather accretion luminosity is emitted following

the temperature structure of an optically thick accretion disk (e.g. Lynden-Bell & Pringle 1974; Pringle 1981),

$$T_{gas}(\varpi) = \left[\left(\frac{3GM_{\star}\dot{M}}{8\pi\sigma\varpi^3} \right) (1 - \sqrt{R_{\star}/\varpi}) \right]^{1/4} \tag{4.1}$$

where ϖ is the radial distance in the mid-plane. The gas disk is assumed to be infinitely thin, so after being emitted, the 'accretion photons' do not encounter any opacity in the gas but may be scattered and absorbed and produce heating in the dust disk. Clearly, this is a simplification for the gas emission, but is sufficient here. The assumed geometry of the gas disk is supported by recent modelling by Muzerolle et al. (2004) of Herbig Ae/Be sources in which the gas disk is geometrically thin, allowing direct radiation of the inner edge wall of the dust disk. Investigating the effects of possible shielding of the dust disk by a flared, and possibly optically thick, inner gas disk remains as future work.

The gas disk extends down to the magnetic truncation radius (R_{gas}), at which point material is thought to be channelled along magnetic field lines onto the star at a high-latitude shock zone (e.g. D'Alessio 2004; Kenyon et al. 1994, Mahdavi & Kenyon 1998). It is assumed that the gas disk is truncated at a magnetospheric radius dependent on the stellar radius, mass, accretion rate, and surface magnetic field (Ghosh & Lamb 1979),

$$R_{gas} = R_{trunc} = \alpha_t R_{\star} \left(\frac{B_{\star}^4 R_{\star}^5}{GM_{\star}\dot{M}^2} \right)^{\frac{1}{7}} \tag{4.2}$$

where α_t is a dimensionless parameter of value less than 1, $B_{\star}$ is the magnetic field strength on the stellar surface, $R_{\star}$ the stellar radius and $\dot{M}$ the mass accretion rate. Photons emitted from the shock/boundary layers have a spectrum of an 8000 K Planck function Calvet & Gullbring (1998) and are emitted along with stellar photons, as in Muzerolle et al. (2003b).

The two aims of the detailed radiation transfer modelling were to fit the SED and the PTI visibility measurements. For each target a set of models was calculated so as to explore parameter configurations. The code outputs model SEDs and images for any specified inclination. The optical and IR SED observation data is taken from the compilation of Kenyon & Hartmann (1995) and represents an average for each source. The millimetre data comes from Akeson et al. (2002) and Beckwith et al. (1990). To calculate model visibilities for comparison with the PTI data, simulated K-band images were generated for each model with 0.05 milliarcseconds pixels and a total width of 12.5 milliarcseconds. This outer size is large enough to contain any component likely to contribute substantially to the model visibility. The K-band emission in the models is dominated by structures a few milliarcsec in size or less (Fig. 4.11). To calculate the extended component in the models, larger images were also constructed with 2 milliarcsecond pixels and a 1 arcsecond field. The emission outside the central 12 milliarcseconds is calculated and included in

the visibility calculation as an incoherent contribution. For each PTI baseline, model visibilities are calculated using the Fourier transform of the image taking the average baseline length and position angle for the disk as given in Table 4.3. Further details of the visibility calculations can be found in Akeson et al. (2005).

For each model, the stellar luminosity has been fixed as detailed in Table 4.4 and for input stellar spectra the appropriate Kurucz (1994) model atmosphere is applied. Stellar masses of 2.25 $M_\odot$, 2 $M_\odot$, and 1 $M_\odot$ are used for SU Aur, RY Tau and DR Tau, respectively (Cohen & Kuhi 1979; Kenyon et al. 1994); note that the stellar mass is not a critical parameter in the near-IR. The disk properties such as mass, accretion rate and inclination were varied in order to produce a grid of synthetic SEDs. These models allowed likely parameter configurations to be explored.

Source	Sp Type	$L_\star$ ($L_\odot$)	$R_\star$ ($R_\odot$)	$T_\star$ (K)	Ref.
T Tau N	K0	7.3	2.8	5697	White & Ghez (2001)
SU Aur	G2	12.9	3.5	5875	Muzerolle et al. (2003b)
DR Tau	K7	0.87	1.9	4064	Muzerolle et al. (2003b)
RY Tau	K1	12.8	3.6	5782	Muzerolle et al. (2003b)

Table 4.4: Stellar parameters for the observed sources.

A selection of models for each object is given in Table 4.5. The range of inclination angle explored was restricted using the results from the geometric fits. The model with the total lowest χ^2 is shown for each object in Fig. 4.11 and the corresponding SED fit in Fig. 4.12. The models are discussed below.

SU Aur

Input stellar parameters for G2 type star SU Aur were $L_\star = 12.9$ $L_\odot$, $R_\star = 3.5$ $R_\odot$, $T_\star = 5875$ K and $M_\star = 2.25$ $M_\odot$. An inner radius, R_{gas}, of 2 $R_\star$ was used as SU Aur is thought to be weakly magnetic and has only inconclusive evidence for hot spots (Unruh et al. 2004).

Model SU-A provides a good fit to the SED data and the measured visibility. This model has an inclination of 60° as suggested by the geometric models and the inner dust radius is found to be 0.21 AU in reasonable agreement with the geometric ring model radius of 0.18 AU. R_{gas} is so close to the star in this model that whilst emission is visible, it is limited by a small surface area.

Model	$\dot{M}$	r_{in}	M_{disk}	incl.	$L_{disk+shk}$	χ^2_{PTI}	χ^2_{SED}	notes
	$M_\odot$/yr	AU	$M_\odot$	deg	$L_\odot$			
SU Aur								
SU-A	1×10^{-9}	0.21	0.001	60	0.02	7	118	
SU-B	1×10^{-9}	0.21	0.001	50	0.02	29	101	
SU-C	1×10^{-9}	0.22	0.001	50	0.02	60	198	
SU-D	2×10^{-9}	0.21	0.001	50	0.02	48	163	
SU-E	4×10^{-9}	0.24	0.005	50	0.02	99	893	
DR Tau								
DR-A	8×10^{-8}	0.09	0.16	30	1.3	12	24	$R_{gas} = 2R_\star$
DR-B	8×10^{-8}	0.09	0.16	30	1.3	30	19	
DR-C	8×10^{-8}	0.09	0.12	30	1.3	30	59	
DR-D	6×10^{-8}	0.09	0.15	60	0.97	9	55	
DR-E	0	0.08	0.08	60	0	3	82	no accretion
RY Tau								
RY-A	2.5×10^{-7}	0.27	0.015	25	4.28	8	37	
RY-B	3×10^{-7}	0.27	0.015	25	5.13	1	294	
RY-C	2×10^{-7}	0.27	0.012	25	3.42	135	31	
RY-D	2.5×10^{-7}	0.27	0.015	25	4.28	4	145	no gas
RY-E	2.5×10^{-7}	0.27	0.015	25	4.28	36	313	envelope

Table 4.5: Representative model parameters for each source. The best fit model is listed first. χ^2 values given have *not* been normalized by the degrees of freedom.
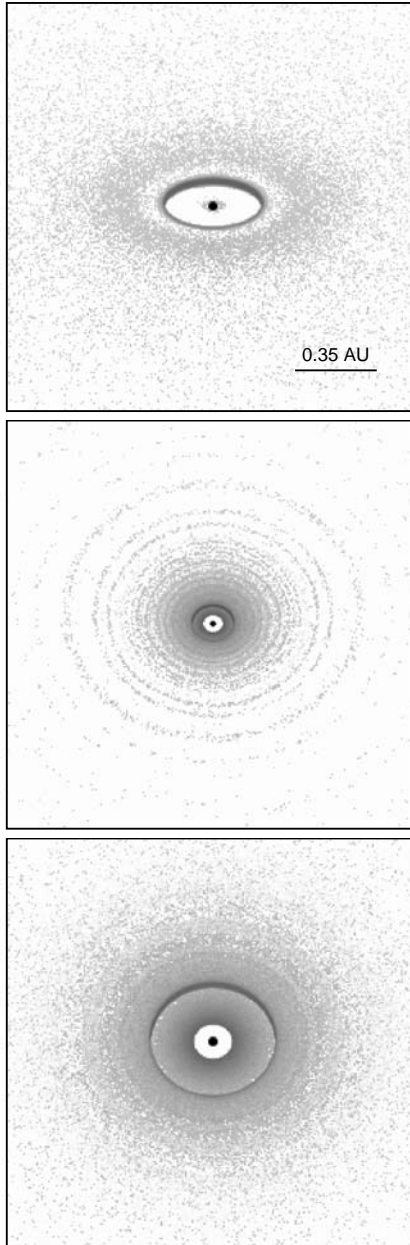
Figure 4.11: Model images for SU Aur (top), DR Tau (middle) and RY Tau (bottom). The flux has been scaled to the 0.15 power to provide better contrast in the image. Each image is 12.5 milliarcseconds or 1.75 AU across. For comparison, all models are shown with the same position angle.
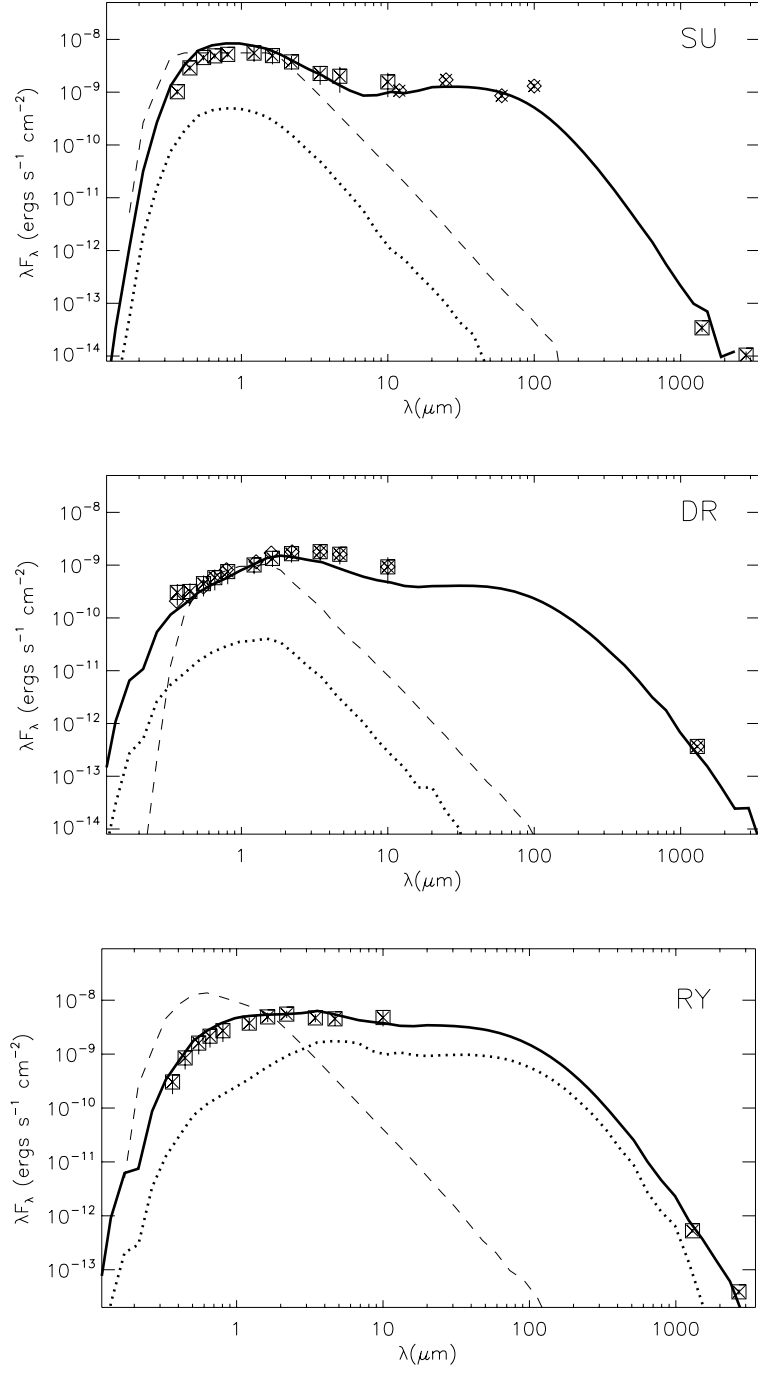
Figure 4.12: SED plots for best-fit models for SU Aur (top), DR Tau (middle) and RY Tau (bottom). The model total flux is given by the solid line, the input stellar spectrum by the dashed line and the scattering by the dotted line. Data from Kenyon & Hartmann (1995) are given by squares and from Eiroa et al. (2002) by circles.

RY Tau

Input stellar parameters for G2 type star RY Tau were $L_\star = 12.8\ L_\odot$, $R_\star = 3.6\ R_\odot$, $T_\star = 5782$ K and $M_\star = 2\ M_\odot$. For RY Tau, a kilogauss (kG) magnetic field is assumed and the gas disk is truncated at $5\ R_\star$ corresponding to $\alpha_t = 0.68$ in Eqn. 4.2 for the best fit SED model.

For RY Tau, the best-fit model is relatively close to the optimal parameters for both the PTI and SED data. The PTI data are best modelled by a higher total luminosity and accretion rate (model RY-B) than the SED data. The accretion models suggest the inner dust radius for this source is much greater than the other two sources meaning that the contribution to the K-band flux is largest for RY Tau. The significant gas disk emission explains why the simple ring model is an underestimate of R_{dust}. The relative flux of the gas and dust components for RY Tau can be seen in Fig. 4.13, which shows a cut through the model image with the inner dust wall facing the observer on the left in the plot.
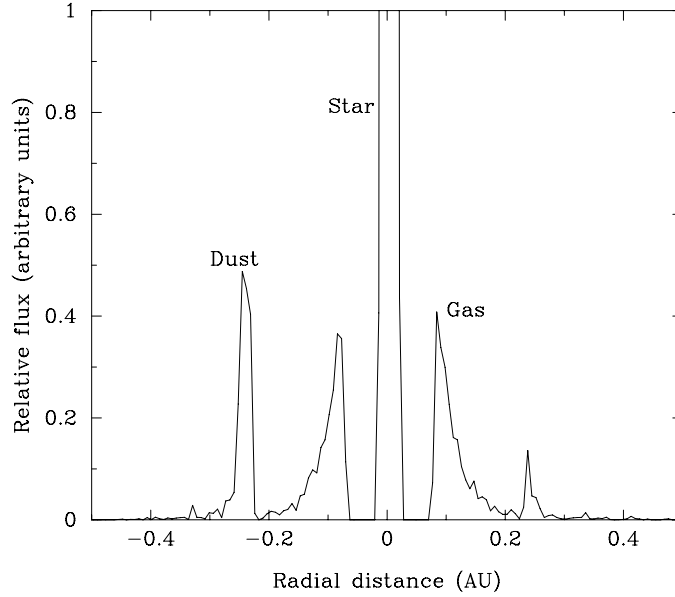
Figure 4.13: A cross section of the RY Tau model through the centre of the source showing the relative flux contributions of the gas and dust emission. The slice is oriented such that the inner dust wall facing the observer is on the left.

To confirm the effect of the gas emission, a model was constructed for RY Tau in which the gas was artificially removed from the region within R_{dust}, which was set to match the measured PTI visibilities. However, the SED fit for this model (Table 4.5, model RY-D) is not as good as for the model with gas emission.

A reflection nebulosity has been observed extending to 40 arcsec from RY Tau at visible wavelengths (Nakajima & Golimowski 1995). However, this is unlikely to contribute

substantially at K, as the reflection component is only 2% of the total flux at 0.9 μm, and scattering decreases with increasing wavelength. For RY Tau the effect of an envelope was also investigated. A model (RY-E) was calculated using the disk properties of model RY-A with an envelope using the same gas and dust radii and an envelope infall rate of 10^{-7} $M \odot$ yr^{-1}. This model does not fit either the SED or the visibilities as well. Other models with higher envelope masses were also calculated and had even worse fits to the SED. It may be possible to better match the SED with a different disk and envelope combination; however, no observational evidence for substantial near-IR emission from an envelope is known to exist.

Recently Calvet et al. (2004) classed RY Tau as a G1 star, substantially earlier than previous spectral type determinations. Their stellar properties however ($R_\star = 2.9$ $R_\odot$; $M_\star = 2.0$ $M_\odot$) agree reasonably well with the values used here (Table 4.4). A slightly lower effective temperature (5782 K compared to 5945 K) and a higher luminosity (12.8 $L_\odot$; compared to 9.6 $L_\odot$) were used here. A lower stellar luminosity would require a more massive disk and higher accretion to produce the same flux at longer wavelengths, but the general properties of a large R_{dust} would not change. The accretion rate of the model presented here, $2.5 \times 10^{-7} M_\odot$yr^{-1}, is actually slightly higher than the Calvet et al. (2004) estimate of $6.4 - 9.1 \times 10^{-8} M_\odot$yr^{-1}.

DR Tau

Input stellar parameters for K7 type DR Tau were $L_\star = 0.87$ $L_\odot$, $R_\star = 1.9$ $R_\odot$, $T_\star = 4064$ K and $M_\star = 1$ $M_\odot$. For DR Tau, kilogauss magnetic fields are again assumed and the gas disk is truncated at 5 $R_\star$ corresponding to $\alpha_t = 0.68$ for the best fit SED model. DR Tau is one of the most heavily veiled T-Tauri stars and is highly variable in the optical (Gullbring et al. 2000) and near-IR (Kenyon et al. 1994).

A single model that provided a good fit to both the SED and measured visibilities was not achieved for this source. A best fit model is listed in Table 4.5 however it has some shortcomings in that it underestimates the model visibilities and the SED in the near-mid IR. The geometric fits to the model PTI data suggest a very small inner disk radius, which contradicts the accretion diagnostics observed for this source (Kenyon et al. 1994; Muzerolle et al. 2003b). A model without accretion is presented (DR-E) and whilst this fits the visibilities best the SED fit is poor. The inclination of the detailed DR Tau model (30°) is also right at the lower limit of the estimate given by the geometric models of $60 \pm 30°$. One possible explanation for the inability to find models that are consistent may be the substantial variations in the optical that DR Tau is known to undergo. These

variations may mean there are issues with source variability which affect the compatibility of models presented here. The variability of DR Tau has been modelled as a hot spot on the stellar photosphere by Kenyon et al. (1994), but the models here do not attempt to model DR Tau with that level of detail.

4.3.5   Discussion

The geometric models and the radiation transfer models suggest similar inner dust radii. Most notably, the radiation transfer models support the simple geometric models in the large value of R_{dust} found for RY Tau and SU Aur. The radiation transfer models explored what effect an inner gas disk would have on the models. It is evident from the models of RY Tau, and to a lesser degree SU Aur, that emission from gas within R_{dust} is a significant component of the near-IR emission if R_{dust} is large. In comparison, for the DR Tau model a smaller R_{dust} is necessary to match the high visibilities measured at PTI and so R_{dust} and R_{gas} are similar. For DR Tau, a smaller value of R_{gas} than estimated from the stellar properties (2 $R_\star$ instead of 5 $R_\star$) was necessary to match the data. Note, R_{gas} should be considered approximate as this value has not been explored extensively in these models.

It has proven to be possible to reproduce the data for the objects SU Aur, RY Tau and DR Tau with extended emission beyond 10 milliarcseconds contributing less than 6% to the K-band emission, consistent with very tenuous or no remaining envelope supporting these objects as Class II sources. High resolution IR imaging observations would further constrain the extended emission component of these models.

CHAPTER 5

SELF-SHADOWING, DUST SETTLING AND GRAIN GROWTH
IN HERBIG Ae, T-TAURI AND BROWN DWARF DISK
SYSTEMS

Up until this point in the thesis, model disks have only been presented which are either in hydrostatic equilibrium such that their density structure can be calculated iteratively or they have a parameterized density with one dust species throughout. These models were deemed sufficient for the objects studied given the data available at the time of study. However, there is increasing evidence of dust settling and grain growth within disks. There has been some indication that grain growth is taking place with the need for the larger HH30 dust distribution in many models, however it is likely there will be a mix of small and large grains.

One set of objects that have been investigated in this way are Herbig Ae stars. These are discussed in Sect. 5.1 of this chapter. The models for Herbig Ae stars are not detailed, rather dust settling and grain growth is used as a possible explanation for the broad shape of the SED.

The study presented in Sect. 5.2 makes use of the recent public release of *Spitzer* data taken with the Infrared Spectrograph (IRS). The IRS collects data in the near-mid IR region of the spectrum which is sensitive to dust settling, and the size and composition of dust grains. Sect. 5.2 discusses the results of O'Sullivan et al. (2006) who have carried out an investigation into dust settling and grain growth in seven T-Tauri *Spitzer* sources using the IRS data.

Section 5.3 discusses the results of Scholz et al. (2006b). This study also makes use of *Spitzer* IRS data on Brown Dwarf sources in the Upper Scorpious star formation region. For sources where a significant IR excess was detected, indicative of a disk, the aim of this study was to establish trends regarding the structure of the Brown Dwarf disks

rather than produce detailed models of the individual sources. For five of the remaining sources models were generated with a view to establishing minimum inner hole sizes.

5.1 The Structure of Herbig Ae Disks

5.1.1 Introduction

In this section theoretical models are presented that study the structure of the Herbig Ae Disks. Herbig Ae stars were first identified by Herbig (1960) as intermediate mass counterparts of the T-Tauri stars, a typical Herbig Ae star having a stellar mass of $2 - 10 \, M_\odot$. They are thought to be the progenitors of Vega-type stars (see Waters & Waelkens 1998 for review). Fewer numbers and a faster evolution to the main sequence can largely explain why less observations exist for Herbig Ae stars than T-Tauri stars. However, since the early 1990s, it has become apparent Herbig Ae stars share many features suggestive of disks in T-Tauri systems. IR excess in the spectra of Herbig Ae stars has been modelled using both accretion disks and envelopes (Hillenbrand et al. 1992; Hartmann et al. 1993; Natta et al. 1993; Mannings et al. 1997; Simon et al. 2000, Chaing et al. 2001, Natta et al. 2001; Dullemond et al. 2001). Recently, it has become apparent they also show an excess at millimetre wavelengths. Flattened structures have been resolved around several sources on ≤ 1 AU scales in the near-IR (Eisner et al. 2003, 2004) and on ~ 100 AU scales at millimetre wavelengths (Mannings & Sargent 1997, 2000; Piétu et al. 2003). Further evidence of Herbig Ae disks comes from polarization measurements (e.g. Vink et al. 2002), signatures of disk accretion namely inverse P-Cygni profiles (Ghandour et al. 1994) and predominantly blue-shifted forbidden emission lines that may arise from disk driven winds and outflows (Corcoran & Ray 1997). They also exhibit rapid variability (e.g. Skrutskie et al. 1996). For a few stars there is also now imaging observations in scattered light (e.g. Grady et al. 1999b) and mid-IR thermal emission (Liu et al. 2003, 2005; Chen & Jura 2003; Pantin et al. 2005) which provide firm evidence for flattened or disk like large scale dusty structures. There is little doubt now that some Herbig Ae stars do have disks, however the morphology of the disk is still under debate.

Herbig Ae/Be stars with disks were divided into two groups by Meeus et al. (2001) based on ground-based photometry of 14 isolated objects. Herbig Be stars are the higher mass, B-type equivalent of Herbig Ae stars. Although there is now limited evidence to suggest these stars also have disks (e.g. Vink et al. 2002) they are not discussed here. The two groups are defined by the shape of the SED as illustrated below in Fig. 5.1. Group I have an almost flat distribution in the mid-IR, as seen in many CTTs, whilst Group II

show a steady decline toward the far-IR. As they are not associated with star formation regions it is likely these are evolved members of the Herbig Ae/Be group and as such their spectra show only emission from a disk, no envelope remains.
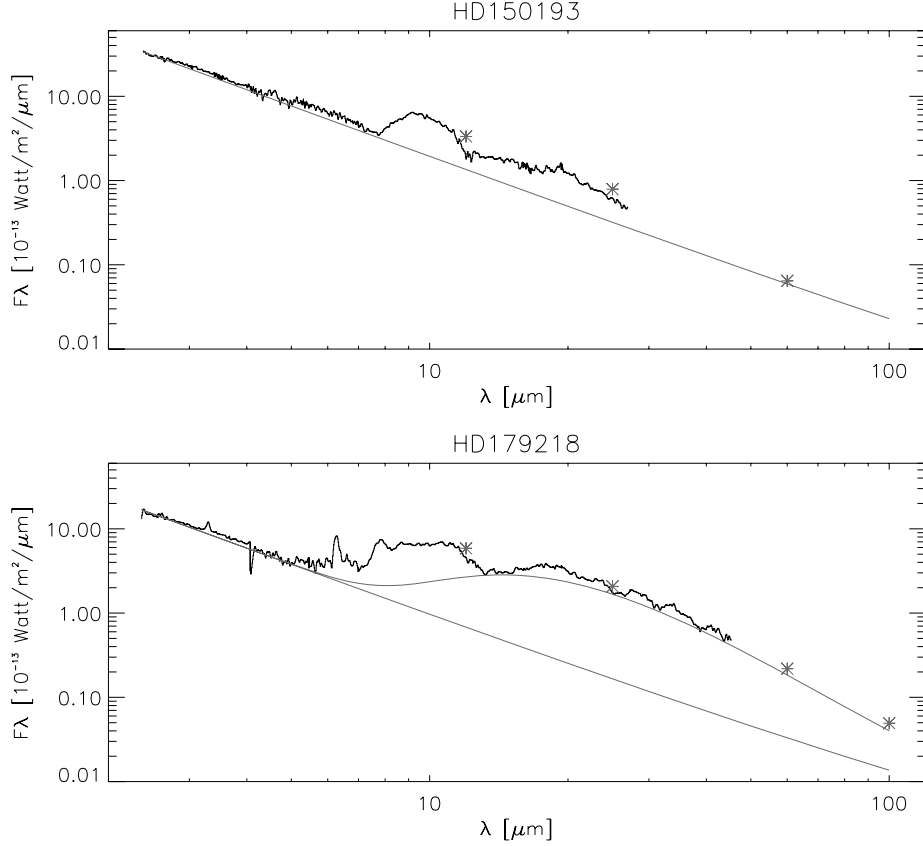
Figure 5.1: Two SED models from Meeus et al. (2001) which illustrate the main features of Group I and II sources (Group 1-lower; Group II-upper). The solid line is the observed spectra, the straight dotted line is a power law fit to the continuum and the curved dotted line in the lower plot is a blackbody continuum for $T \simeq 190\ K$. This blackbody continuum is required for the Group I sources but not for the Group II.

Kenyon & Hartmann (1987) showed that disk flaring would expose a greater disk area to direct stellar radiation and this could explain the degree of excess, the 'flatness of the SED', seen in CTTs. It therefore seems likely that Group I are again flared disks and the most likely explanation for group II is that the disk is less flared or disk material is more concentrated toward the mid-plane than one might expect. This is generally accepted, however, the EXACT cause of the decrease in the excess is still under debate with suggestions put forward that the disk may be heavily shadowed by a 'puffed-up' inner edge (Dullemond 2002; Dullemond & Dominik 2004b), that it may be a surface density effect in the disk or that grain growth and dust settling may be taking place (Dullemond & Dominik 2004a,b; Acke et al. 2004). For accurate disk modelling it is important to

understand the cause is of these differences, and for the study of stellar evolution and planet growth whether this is an age effect with the Group II objects more evolved than Group I.

5.1.2 Modelling of Steady Accretion Disks in Hydrostatic Equilibrium

Monte Carlo radiation transfer models are presented of Herbig Ae accretion disks that are assumed to be in vertical hydrostatic equilibrium. By exploring the equilibrium case it is possible to see what effects are the most likely cause of the group II models.

Common assumptions in models are that the disks are geometrically thin, $h(\varpi)/\varpi <$ 1, they are in vertical hydrostatic equilibrium, and dust and gas are coupled (Kenyon & Hartmann 1987; Chiang & Goldreich 1997, 1999; D'Alessio et al. 1998,1999a,2001; Dulemond 2002). Such models that solve for the disk structure have shown various effects including warm extended upper layers of the disk (D'Alessio et al. 1998) and possible shadowing of the outer disk by the disk's inner edge (Dullemond 2002; Dullemond & Dominik 2004b).

In Sect. 5.1.3 the Monte Carlo radiative equilibrium code is used to study models of 'typical' Herbig Ae disks and comparison CTTs disks that include accretion. All the common assumptions listed above apply. By enforcing vertical hydrostatic equilibrium, the disk density can be solved for iteratively (see Chapter 2 Sect. 2.1.4). It is also assumed, as in D'Alessio et al. (1998), that there is a steady accretion rate through the disk. The disk viscosity is described using the α prescription (see Eqn. 2.61) of Shakura & Sunyaev (1973) and a value of $\alpha = 0.01$ as suggested by Gullbring et al. (1998) and Hartmann et al. (1998) is assumed. For a given accretion rate an estimate of the disk mass can be derived. See Chapter 2 Sect. 2.2 for a description of the accretion emission algorithm. An aspect of the code considered important for this modelling is its inclusion of stellar radiation reprocessing at the inner edge of the disk (Natta et al. 2001; Dullemond et al. 2001) important for studying any self-shadowing effects.

5.1.3 Results

Figure 5.2 shows the SEDs for hydrostatic disks of different masses (accretion rates) surrounding CTTs and Herbig Ae stars heated by starlight and dissipation of viscous accretion. Figure 5.3 shows the temperature and density structure for the accretion disks of mass $M_{disk} = 10^{-4} \ M_{\odot}$. The models are for irradiated, steady accretion disks around a CTTs and Herbig Ae star with stellar parameters, disk masses, and accretion rates sum-

marized in Table 5.1. All model disks have an outer radius of 200 AU and an inner radius set by the dust destruction temperature, assumed to be 1600 K. The adopted dust grain model is HH30 previously used to fit the SEDs of several CTTs and Brown Dwarf disks (Wood et al. 2002a; Rice et al. 2003; Walker et al. 2004; O'Sullivan et al. 2005). The wavelength dependence of the absorption and scattering properties of this dust model are shown in Chapter 2 Sect. 2.1.2.

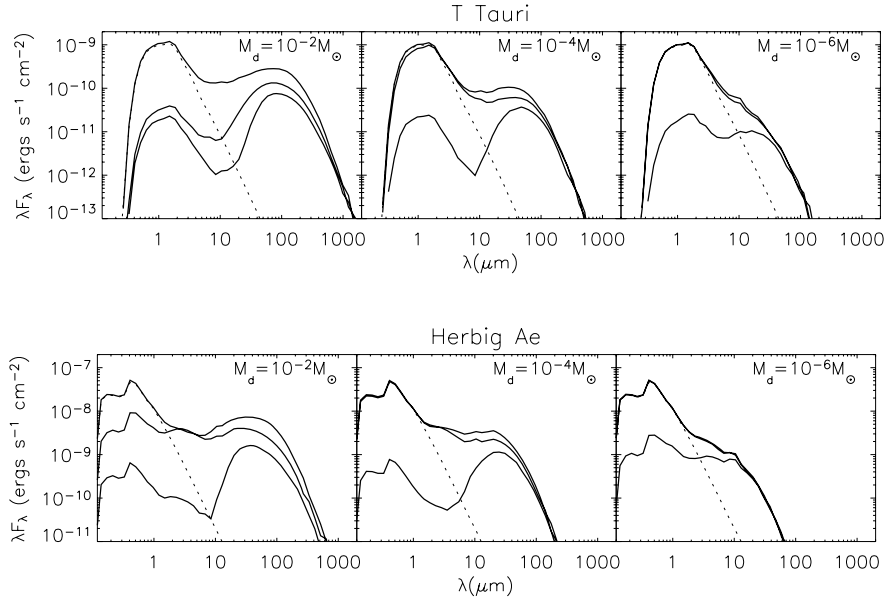| $T_\star$ (K)	$M_\star$ ($M_\odot$)	$R_\star$ ($R_\odot$)	M_{disk} ($M_\odot$)	$\dot{M}$ ($M_\odot yr^{-1}$)
4000	0.5	2	10^{-2}	5×10^{-9}
4000	0.5	2	10^{-4}	6×10^{-11}
4000	0.5	2	10^{-6}	6×10^{-13}
10000	2.5	2	10^{-2}	5×10^{-9}
10000	2.5	2	10^{-4}	6×10^{-11}
10000	2.5	2	10^{-6}	7×10^{-13}

Table 5.1: Accretion Disk Model Parameters

Figure 5.2: SEDs for hydrostatic disks around a T-Tauri (upper panels) and a Herbig Ae star (lower panels). Each panel shows SEDs for three viewing angles: 10° (upper line), 60° (middle), and 85° (lower). The input stellar spectrum is the dashed line in each panel. The disk mass is indicated in the plots and the accretion rates listed in Table 5.1.
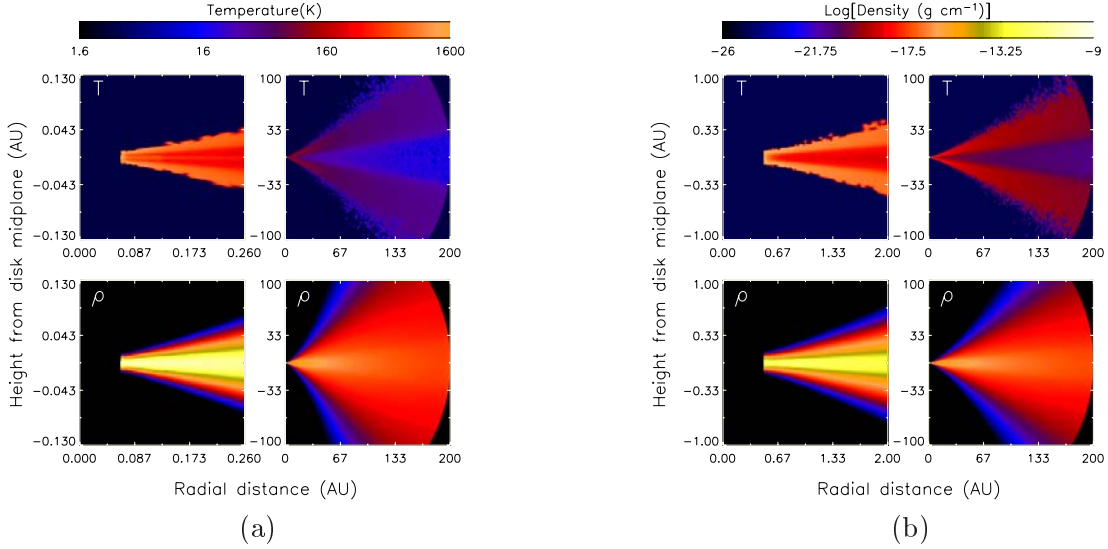
Figure 5.3: 2-D maps of the temperature and density structure on two size-scales for vertical hydrostatic disks of mass $M_{disk} = 10^{-4}$ $M_{\odot}$ around: (a) a T-Tauri star with $M_{\star} = 0.5$ $M_{\odot}$, $R_{\star} = 2$ $R_{\odot}$, $T_{\star} = 4000$ K; (b) a Herbig Ae star with $M_{\star} = 2.5$ $M_{\odot}$, $R_{\star} = 2$ $R_{\odot}$, $T_{\star} = 10000$ K. The Herbig Ae disk is less flared due to larger gravity of the central star. Note also that the inner edge of the disk is not significantly vertically extended (or puffed-up) compared to material just beyond it.

5.1.4   Discussion

The SEDs in Fig. 5.2 show the characteristic IR excess due to reprocessing of starlight and heating from viscous accretion. For edge-on viewing the SED is double peaked with scattered light at short wavelengths and thermal reprocessing at long wavelengths: see Fig. 9 in Wood et al. (2002a) for the component parts of the SED (direct starlight, scattered starlight, accretion energy, and reprocessed thermal radiation). As the disk accretion rate is decreased, the total disk mass is decreased as is the heating from viscous accretion, so the IR excess falls.

As found by D'Alessio et al. (1998), at large radii the disk scaleheight (taken from the mid-plane temperature) and the surface density scale roughly as $\varpi^{5/4}$ and ϖ^{-1} respectively. In Fig. 5.3 the density and temperature structure show that the inner edge of the disk shields material just beyond it. This results in a rapid drop in the temperature so that the inner edge appears slightly more vertically extended than radii just beyond it. The temperature structure shows the hot upper layers that intercept direct stellar radiation and lie at around three to five scaleheights above the mid-plane. The temperature plots, using the Bjorkman & Wood (2001) technique, show where stellar and thermal disk photons

are absorbed and reprocessed contributing to the infrared excess SED. Note, the model Herbig Ae disk is less flared than the CTTs disk due to the larger gravity of the higher mass star. For comparison, hydrostatic equilibrium disks around Brown Dwarfs are more flared due to the lower gravity of the central star (see Chapter 3). Low IR excess emission observed in the far-IR SEDs of some sources has been attributed to self-shadowing of the disk, however the disks in Fig. 5.3 are seen to flare over their entire extent and the inner edge does not cast a significant shadow so as to cause any extreme effects such as collapse of the outer disk (Bell et al. 1997; Dullemond 2002; Dullemond & Dominik 2004b).

5.1.5   Modelling of Hydrostatic Passive Disks using Power Laws

In the previous section it is shown that for disks with a steady accretion rate, irrespective of the total optical depth (mass) of the disk, no significant shadowing of the outer disk by the inner edge, which has been used to explain low far-IR excess emission in some sources, is observed here. As mentioned in Sect. 5.1.1 other suggestions are that low far-IR excess may be a surface density effect or that grain growth and dust settling may be taking place. The result from the previous section would suggest the assumed disk surface density and any dust settling have a greater impact on the SED shape. This section explores that hypothesis using passive disk models.

This section compares flared disk (power law) models to those that enforce hydrostatic equilibrium to determine the vertical structure. The aim is to isolate the effects of the vertical structure, and therefore a power-law surface density, $\Sigma(\varpi) \sim \varpi^{-p}$ is employed, for both cases. It is assumed that heating is dominated by starlight and the disk structure is solved by enforcing vertical hydrostatic equilibrium with the total mass in the disk held constant. Disk surface density gradients are usually in the range $1 \leq p \leq 2$, with $p = 3/2$ the value quoted for the minimum mass solar nebula (Hayashi 1981) and $p \approx 1$ found for irradiated steady accretion disks (D'Alessio et al. 1998).

The power law disks have the parameterized density structure,

$$\rho = \rho_0 \exp\left[\frac{-z^2}{2h(\varpi)^2}\right]\left(\frac{R_{dust}}{\varpi}\right)^{\alpha} \tag{5.1}$$

where the scaleheight $h(\varpi) = h_{dust}(\varpi/R_{dust})^{\beta}$. In this model the surface density is $\Sigma \sim \varpi^{-p}$ where $p = \alpha - \beta$. An attempt was made to recreate hydrostatic models with parameterized models for Herbig Ae sources illuminating passive disks of mass $10^{-2}, 10^{-4}, 10^{-6}, 10^8 M_{\odot}$, surface density power $p = 1, 2, 3, 4$ and disk radius 200 AU.

5.1.6 Results

It was found to be possible to reproduce the hydrostatic model SEDs of the disks with inclinations of less than 63°, $M_d = 10^{-2} - 10^{-4} M_{\odot}$ and surface density powers of $p = 1$ and $p = 2$ with a simple power law prescription where $\beta = 1.25$ is fixed, the radial density exponent is $\alpha = \beta + p$, and $h(\varpi)$ is scaled from the dust destruction radius, $h_{dust}/R_{dust} = 0.75 \times c_s/\Omega(R_{dust})$, where $c_s = \sqrt{kT/\mu m_{\mathrm{H}}}$ and $T = 1600$ K. For a hydrostatic disk at the inner edge one would expect $h_{dust}/R_{dust} = c_s/\ \Omega(R_{dust})$, however when trying to parameterize hydrostatic models a small reduction in h_{dust}/R_{dust} is to be expected given the model is trying to fit the global structure of the disk and not just the hot inner rim, which will be naturally more extended than the cooler material behind it. Figures 5.4 and 5.5 shows comparison SEDs for the $p = 1$ and $p = 2$ Herbig Ae models which illustrate the match achieved at four inclinations. The value $\beta = 1.25$ in this prescription is not unexpected as irradiated disks tend to have a temperature structure $T(\varpi) \propto \varpi^{-0.5}$, which gives a scaleheight $h(\varpi) \propto \varpi^{1.25}$. At lower disk mass the above prescription works for all surface density powers. The only models this prescription does not work for is those of high mass disks with a steep radial surface density gradient. This result is now discussed.

Figure 5.4: SEDs for passively heated disks of different mass and inclination as indicated with surface density $\Sigma \sim \varpi^{-1}$. Hydrostatic models are shown as solid lines and disks with power law densities given by Eqn. 5.1 are dashed lines. Power law disk models use the prescription of Sect. 5.1.6 for setting the scaleheight and flaring.
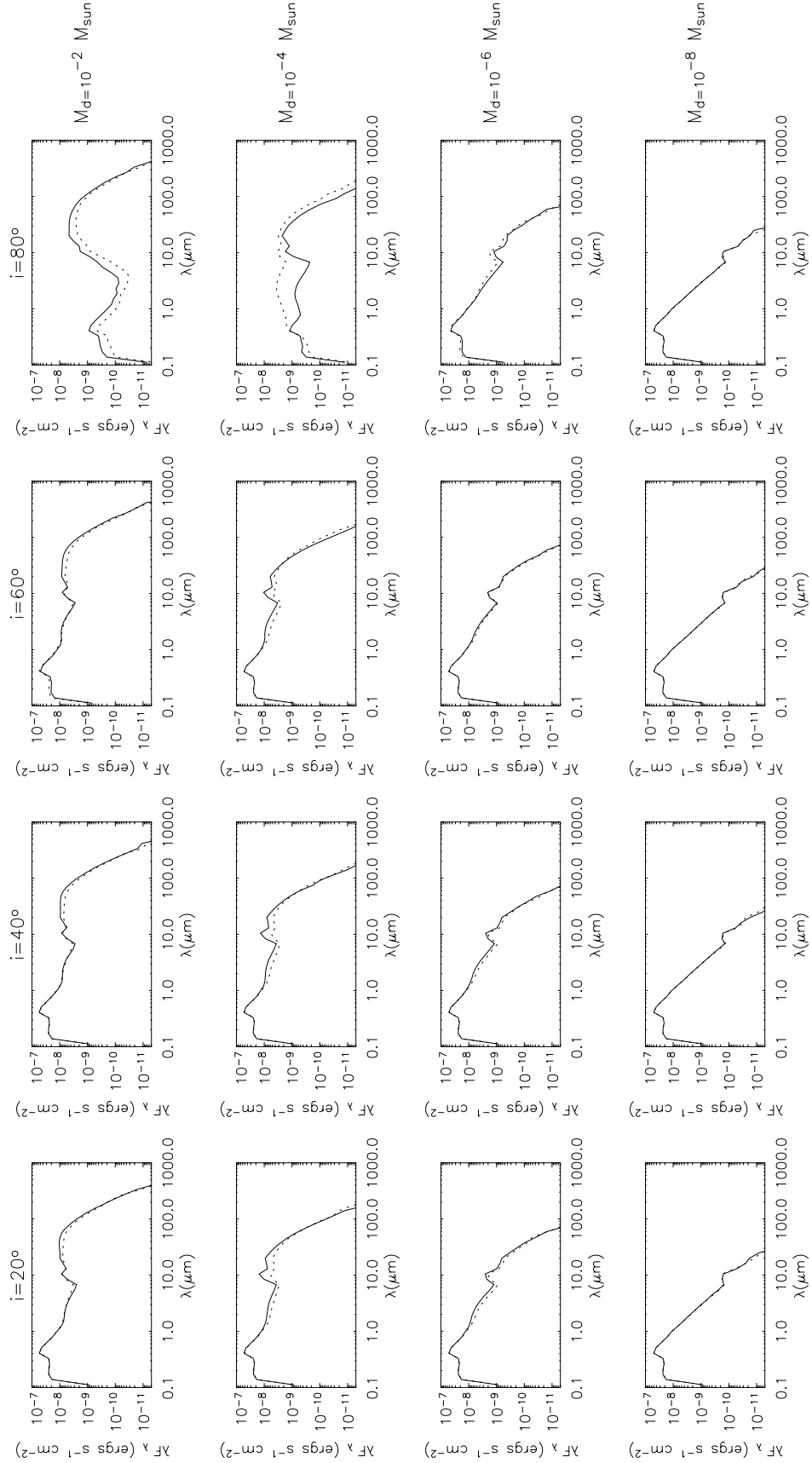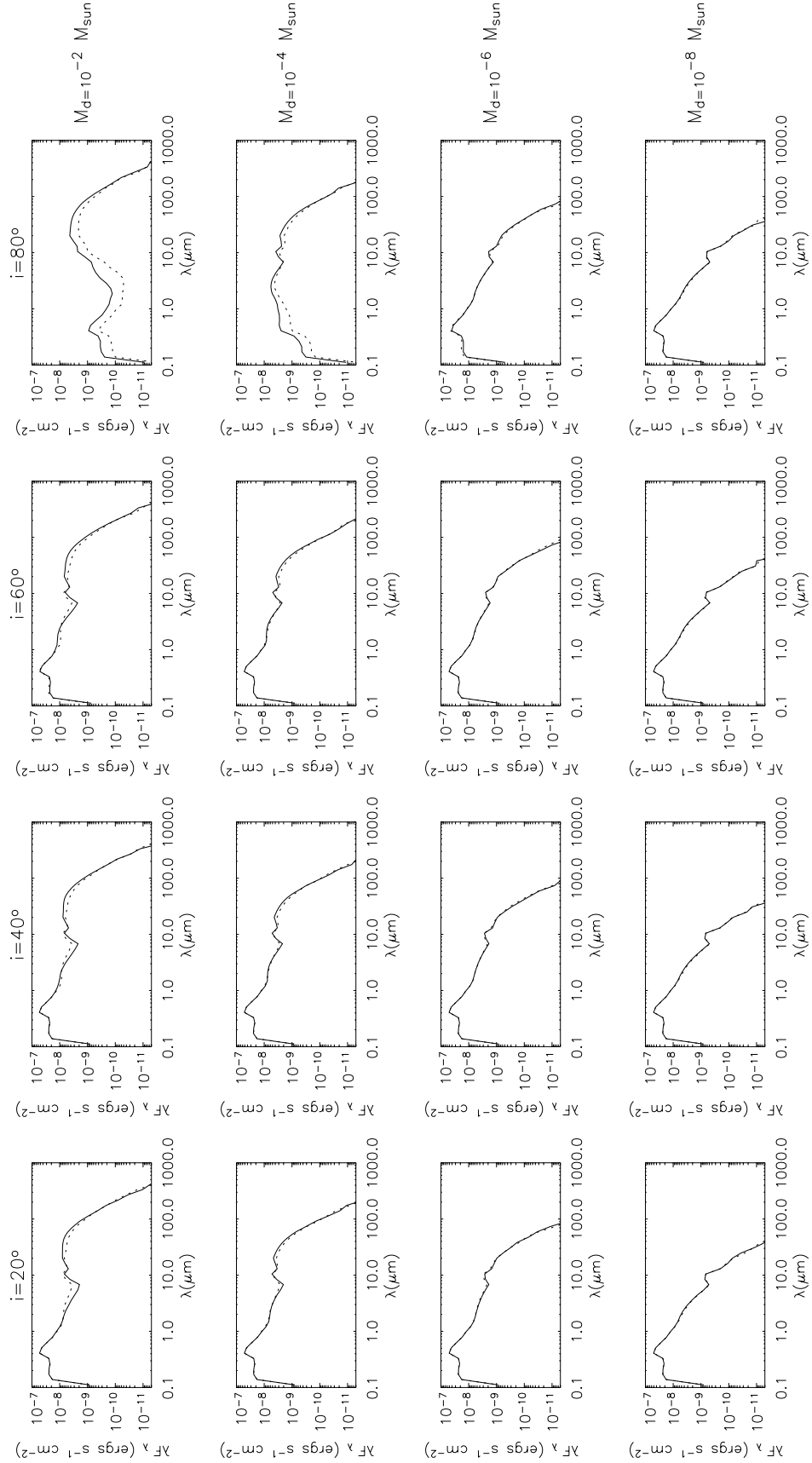
Figure 5.5: SEDs for passively heated disks of different mass and inclination as indicated with surface density $\Sigma \sim \varpi^{-2}$. Hydrostatic models are shown as solid lines and disks with power law densities given by Eqn. 5.1 are dashed lines. Power law disk models use the prescription of Sect. 5.1.6 for setting the scaleheight and flaring.

5.1.7 Discussion

Using the result of Sect. 5.1.6 this section discusses the role of disk mass, surface density, and the inner edge in determining the large scale disk structure. Recent models of disks in hydrostatic equilibrium with dust and gas well-coupled (Dullemond & Dominik 2004b) suggest that disks with steep surface densities or very low total mass result in a new class of 'self-shadowed' disks. For disks with steep surface density gradients (e.g. $p \geq 3$), the IR flux is lower than disks of the same total mass, but with shallower surface density exponents ($p = 1$). The shape of the SED and temperature structure of these steep surface density disks, led Dullemond & Dominik (2004b) to conclude that the inner edge of the disk casts a shadow on the outer disk, shielding it from direct stellar heating, and thus resulting in a disk structure that is flatter than $p = 1$ disks. Models with a very small total disk mass also exhibit small IR excesses and their temperature structure was also interpreted as being self-shadowed. Of course, optical depth effects will lead to *all* optically thick disks having regions that are shielded from direct stellar irradiation (i.e., self-shadowed). A result is that dust grains in the disk mid-plane have lower radiative equilibrium temperatures than grains at the same location that are directly exposed to stellar radiation. This has been explored as a means of moving the 'snow-line' (Hayashi 1981) to smaller radii in disks (Sasselov & Lecar 2000). The models of Dullemond & Dominik (2004b) take this shadowing effect further and suggest a new class of disks where shadowing by the inner edge dominates the structure in the outer regions of the disk. The drawings from Dullemond & Dominik (2004b) shown in Fig. 5.6 illustrate this interpretation, suggesting that the inner edge of the disk may be significantly puffed-up compared to material behind it, and the inner edge strongly influences the structure of the outer disk. Since all disks are self-shadowed (to at least some degree), the question addressed here is does the self-shadowing change the global structure of the disk, or does it simply affect a small region behind the inner wall?
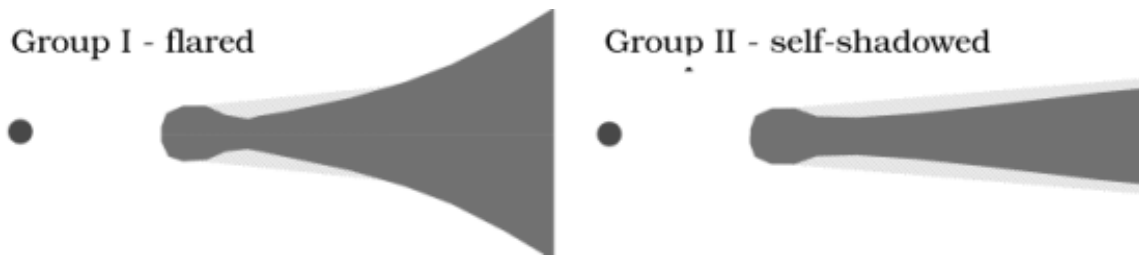

Figure 5.6: Illustration of the two Herbig disk geometries found by Dullemond & Dominik (2004b).

Low IR excess emission is a general feature of flat disks and also those with steep radial surface densities and/or low mass. Here it is suggested that this feature of low IR excess is present in the SEDs of both hydrostatic and flared power-law disks, so the low IR

emission is not a simple consequence of self-shadowing. The following section compares and discusses the effects of changing the total disk mass and radial surface density gradient on the global disk structure and SEDs of hydrostatic and power-law disks, so as to determine the relative importance of inner edge effects on the global disk structure. The models differ from Dullemond & Dominik (2004b) in that scattering is included. Note however, the inclusion of scattering is not expected to significantly influence the disk structure since scattering is not important in the IR where most of the heating occurs (at large radii in the disk). For this investigation ISM grains (Kim et al. 1994) are adopted, which have a wavelength-dependent opacity similar to those used by Dullemond & Dominik (2004b).

Passive Disks: Effects of Disk Mass

Section 5.1.6 discussed results showing that hydrostatic disks with radial surface density exponents in the range $1 \leq p \leq 2$ can be well approximated by the power-law disks described by Eqn. 5.1 and using the suggested recipe for the disk scaleheight. In this prescription, the disk scaleheight is a monotonically increasing function of radius. The recipe applies over a wide range of disk masses, so the interpretation of low mass hydrostatic disks is that it is the disk mass that determines the global SED shape and not any shadowing effects caused by the inner edge of the disk. Low mass disks also have very low surface brightnesses in scattered light and thermal images, which again can be interpreted as due to the small mass of disk material and not because of inner edge shadowing effects.

Passive Disks: Effects of Disk Surface Density

The fact that the SEDs of $1 \leq p \leq 2$ hydrostatic disks can be reproduced with power law disks whose scaleheights monotonically increase with distance from the star (so that the disk surface is always concave upward and capable of receiving radiation directly from the star) suggests that the small shadowing directly behind the inner edge of these disks has no significant impact on the far-IR SED or the structure of the outer disk in agreement with Dullemond & Dominik (2004b). However, for higher mass disks with steep power laws $(p \geq 3)$, the flared disk models do not match the mid-IR SEDs of the equivalent hydrostatic model (see Fig. 5.7). To match, h_{dust} must be further reduced by >20%, indicating that inner edge effects are more important for the global disk structure in disks with very steep surface densities. Note that using the prescription for h_{dust} and β, the IR excess is lower than that for a $p = 1$ disk of the same total mass. This indicates that the disk surface density has a big effect on determining how much radiation may be reprocessed in the disk. Steep surface densities move the disk mass to smaller radii, so that the cooler, outer

disk regions will contribute less to the IR excess. Therefore, the surface density gradient greatly influences the SED, but for very steep gradients shadowing by the inner edge also plays a role in determining the temperature structure of the disk.
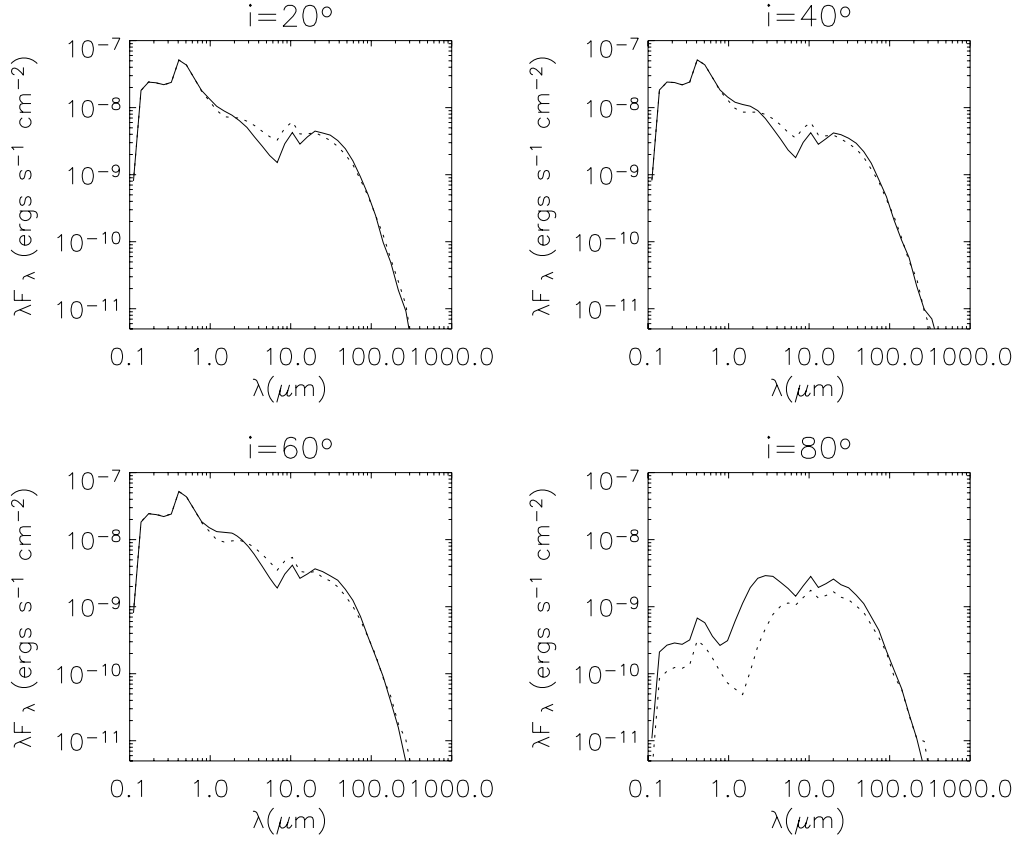

Figure 5.7: SEDs for passively heated disks with mass $M_{disk} = 10^{-2}$ $M_{\odot}$ and inclination as indicated with surface density $\Sigma \sim \varpi^{-3}$. Hydrostatic models are shown as solid lines and disks with power law densities given by Eqn. 5.1 are dashed lines. Power law disk models use the prescription of Sect. 5.1.6 for setting the scaleheight and flaring.

Another way to look for evidence of shadowing is to study temperature cross-sections of the disks. The upper panels in Fig. 5.8 show 2-D maps where the temperature is calculated at all points using the Lucy (1999) path-length technique, including where the medium is optically thin and does not contribute any emission. These figures clearly show that $p = 1$ disks exhibit flared surfaces, whereas the $p = 4$ disk does appear to be isothermal and in the shadow of the inner edge. A more instructive way to examine the temperature structure is, however, to plot the temperature only where Monte Carlo photons are absorbed and are reprocessed into the disk thermal spectrum (see Fig. 5.8, middle panels). The resulting temperature maps show that the $p = 4$ disk does in fact exhibit a flared surface. These 2-D temperature and density plots show that the inner edge is not significantly puffed-up and the disks are not self-shadowed at the levels suggested by the drawings presented in Dullemond (2002) and Dullemond & Dominik (2004b). Benchmark tests (see Chapter 2 Sect. 2.3) against the Dullemond & Dominik (2004b) code (Dullemond, private communication) would suggest our results are actually in agreement, they are simply interpreted differently. The drawings in Fig. 5.6 over-emphasize the effect and importance of inner edge on disk structure and long wavelength SED.
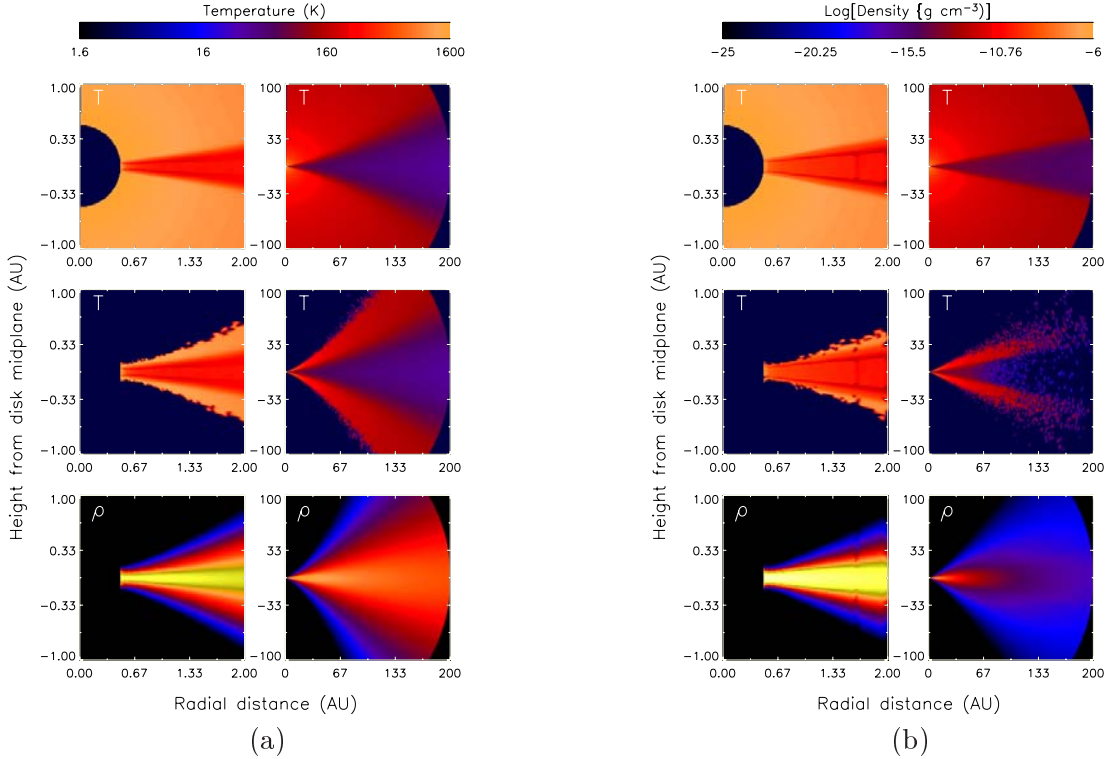
Figure 5.8: 2-D temperature and density slices on two size-scales for hydrostatic disks of mass 10^{-2} $M_\odot$ with varying surface density: (a) $\Sigma \sim \varpi^{-1}$, (b) $\Sigma \sim \varpi^{-4}$. Each set of plots show temperature (upper and middle) and density. The upper temperature plots show the temperature calculated everywhere in the grid. Lower temperature plots show the temperature only where photons have been absorbed in the disk.

5.1.8   Summary

The main conclusion of this study is that in some cases the inner edge of the disk casts a shadow on outer disk regions. The shadowed region is, however, very small. While the inner edge of the disk is important for determining the near-IR excess (Natta et al. 2001; Dullemond et al. 2001) and the photopolarimetric variability in magnetically accreting CTTs (Bouvier et al. 1999; Ménard et al. 2003; O'Sullivan et al. 2005), the models presented here (and similar models presented in other publications) suggest that it does not significantly affect the height of the irradiation surface. Although minimal shadowing of the outer disk by the inner edge may occur, disk radial surface density or dust settling are the dominant controls on the disk structure and shape of the far-IR SED. Unless disks have very steep surface density profiles (e.g. $\Sigma \sim \varpi^{-4}$) and high mass, shadowing by the inner edge is not responsible for producing the small IR excesses seen around some Herbig Ae stars.

Indeed, this effectively is the conclusion of Dullemond & Dominik (2004b) who investigated the difference between SEDs of Type I and II Herbig Ae/Be stars. Type I and II sources have similar (sub-)millimetre flux levels and therefore similar disk masses, but Type II sources have lower IR excesses than Type I. Models that reproduce the SED features of Type I have flaring surfaces, $\Sigma \sim \varpi^{-1}$, and $M_{disk} \geq 10^{-3}$ $M_{\odot}$. Dullemond & Dominik (2004b) note that because of their similar (sub-)millimetre flux levels, Type II sources are unlikely to have less massive disks than Type I and therefore require models with $\Sigma \sim \varpi^{-4}$ or very flat disks where large dust grains have settled to the mid-plane. Therefore, the low levels of IR excess emission observed in some sources are probably attributable to dust settling.

5.2   Dust Settling and Grain Growth in *Spitzer* T-Tauri Sources

5.2.1   Introduction

In this study hydrostatic equilibrium models were compared with multiple species dust models (O'Sullivan et al. 2006) of IRS data and data from the Kenyon & Hartmann (1995) compilation spanning a range from around 0.1 μm to a few 1000 μm for the seven objects detailed in Table 5.2. A departure from the hydrostatic equilibrium provides a strong indicator for the ongoing process of dust settling and the presence of grain growth.

The hydrostatic equilibrium models use the HH30 grain distribution (Wood et al.

Object	Spectral Type	T_{eff}(K)	M($M_\odot$)	R($R_\odot$)	References
AA Tau	K7	4000	0.8	1.85	Kenyon & Hartmann (1995), Bouvier et al. (1999)
CoKu Tau/4	M1.5	3720	0.5	1.9	D'Alessio et al. (2005b)
DM Tau	M1e	3720	0.65	1.2	Calvet et al. (2005)
GM Aur	K3/K5e/K7V	4730	1.2	1.5	Schneider et al. (2003)
GO Tau	M0	4000	0.8	1.3	Kenyon & Hartmann (1995), O'Sullivan et al. (2006)
LkCa 15	K5	4000	0.5	1.85	Kenyon & Hartmann (1995), O'Sullivan et al. (2006)
TW Hydra	K7	4000	0.6	1	O'Sullivan e al. (2006)

Table 5.2: The stellar parameters of the sources investigated.

2002a) whilst the multiple dust species models use a combination of ISM grain distributions, MRN (Mathis et al. 1977) or KMH (Kim et al. 1994), and the larger grained HH30 model. See Chapter 2 Sect. 2.1.2 for details of the KMH and HH30 dust models. The hydrostatic equilibrium models solve for the density structure whilst the mutliple dust species models, for each dust grain size distribution, use a parameterized flared disk density structure of Eqn. 5.1. The degree of flaring within the geometric disk models was varied by adjusting the value of β and h_0 in order to investigate to a first approximation the degree to which the disk is flattened compared to the vertical hydrostatic equilibrium case. The smaller ISM grains have a larger scaleheight than the larger HH30 grains providing a simple way to mimic dust grain growth and dust settling.

5.2.2 Results

It is found that some of the disks are not too far removed from hydrostatic equilibrium, however for all seven objects a multiple dust species model provides the best fit. The 'best fit' results are summarized in Table 5.3. For detailed discussion and analysis of these models see O'Sullivan, in preparation. Here a summary is presented that focusses on the hydrostatic equilibrium models.

	AA Tau	CoKu Tau/4	DM Tau	GM Aur	GO Tau	LkCa 15	TW Hydra
Inclination (deg)	71°	76°	40°	55°	75°	35°	0°
$M_{disk}(M_\odot)$	0.015	0.001	0.05	0.047	0.065	0.075	0.04
Inner Disk							
Radius (AU)	0-10	0-8.5	1-4.5	5-20.5	N/A	2-15	0-4
Small Grains							
Mass Fraction	0.1	5×10^{-6}	9×10^{-5}	0.007	N/A	2×10^{-4}	0.08
h0 ($R_\star$)	0.015	5×10^{-4}	0.007	0.0075	N/A	0.0125	0.01
h_{100AU} (AU)	0.026	0.032	0.029	0.049	N/A	0.042	0.052
Large Grains							
Mass Fraction	0	0	0	0	N/A	0	0
h0 ($R_\star$)	0	0	0	0	N/A	0	0
h_{100AU} (AU)	0	0	0	0	N/A	0	0
Outer Disk							
Radius (AU)	10-200	8.5-200	4.5-200	20.5-300	0-200	15-200	4-200
Small Grains							
Mass Fraction	0.3	0.01	0.05	0.009	0.015	5×10^{-4}	0.01
h0 ($R_\star$)	0.009	0.01	0.008	0.015	0.006	0.013	0.0135
$h_{100AU}(AU)$	9.34	10.31	9.25	15.75	6.8	13.49	16.35
Large Grains							
Mass Fraction	0.6	0.99	0.95	0.984	0.985	0.9993	0.91
h0 ($R_\star$)	0.005	0.01	0.0085	0.0075	0.0045	0.005	0.006
$h_{100AU}(AU)$	5.19	10.31	9.83	7.89	5.1	5.19	7.26

Table 5.3: SED fits using the multiple species dust model.

AA Tau

The earlier study (see Chapter 4 Sect. 4.2.1) of the variability of AA Tau suggested an inclination of 75°. At this inclination it was found that a hydrostatic model could not reproduce the stellar component of the SED due to the high degree of flaring in disk resulting in the outer regions of the disk obscuring the central star. Here the best multiple species dust model is for an inclination of 71°. This lower inclination still does not allow the hydrostatic equilibrium model to fit the stellar spectrum and now that more data is available it is evident that in comparison to the hydrostatic model there is a strong silicate feature and reduced mid-IR emission (Fig. 5.9) indicative of ongoing dust settling.

Figure 5.9: SED models for AA Tau. The broken line is the hydrostatic equilibrium model and the solid line is the multiple species model. The small filled dots are the *Spitzer* IRS data and the crosses are the IRAS data from the Kenyon & Hartmann (1995) compilation.

CoKu Tau/4

The best fit multiple species dust model for CoKu Tau/4 is for a disk inclined at 76° (see Fig. 5.10). The most obvious failing in the hydrostatic equilibrium model is that, as for AA Tau, at this high inclination the hydrostatic equilibrium model is unable to reproduce the stellar component of the SED due to obscuration from the flared disk. The inclination of this object is however debatable. D'Alessio et al. (2005b) suggest CoKu Tau/4 is more face on than suggested here which would improve the hydrostatic equilibrium model fit, however this requires extinctions of $A_v = 3$, which is high relative to values quoted for other objects in Taurus.

Figure 5.10: SED models for CoKu Tau/4. The broken line is the hydrostatic equilibrium model and the solid line is the multiple species model. The small filled dots are the *Spitzer* IRS data and the crosses are the IRAS data from the Kenyon & Hartmann (1995) compilation.

DM Tau

The best fit multiple species dust model for DM Tau is for a disk inclined at 40° with a large inner hole of 4.5 AU with a small amount of MRN gains within this. The hydrostatic equilibrium model, which does not include the small grains in the inner disk, does not fit the data exactly, however its closeness to the observations suggest that the disk of DM Tau is not too far removed from hydrostatic equilibrium (see Fig. 5.11). This is supported by the fact that for the best fit model most of the dust mass is in the outer disk and most of this is HH30 grains.
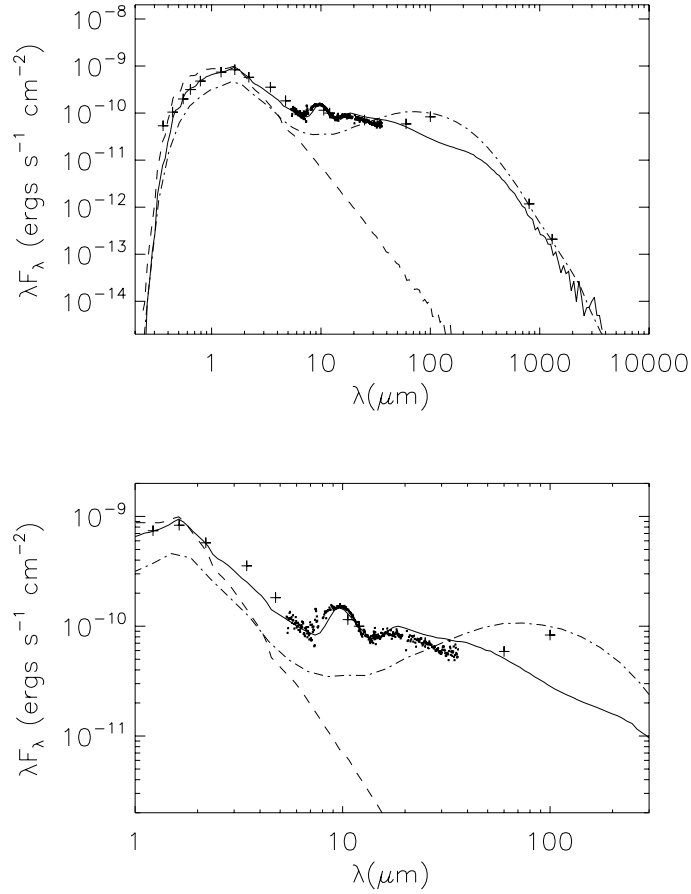

Figure 5.11: SED models for DM Tau. The broken line is the hydrostatic equilibrium model and the solid line is the multiple species model. The small filled dots are the *Spitzer* IRS data and the crosses are the IRAS data from the Kenyon & Hartmann (1995) compilation.

GM Aurigae

The best fit multiple species dust model for GM Aur is for a disk inclined at 55° with a large inner disk from 5 - 20.5 AU consisting of 0.7% of the disk mass in the form of MRN grains. As for DM Tau most of the mass in the outer disk is in HH30 grains and as for DM Tau the hydrostatic model therefore provides a close fit particularly to the outer part of the disk. The large inner hole, inner edge wall and large silicate feature is not well represented by the hydrostatic equilibrium model, hence the need for multi-species code (see Fig. 5.12).
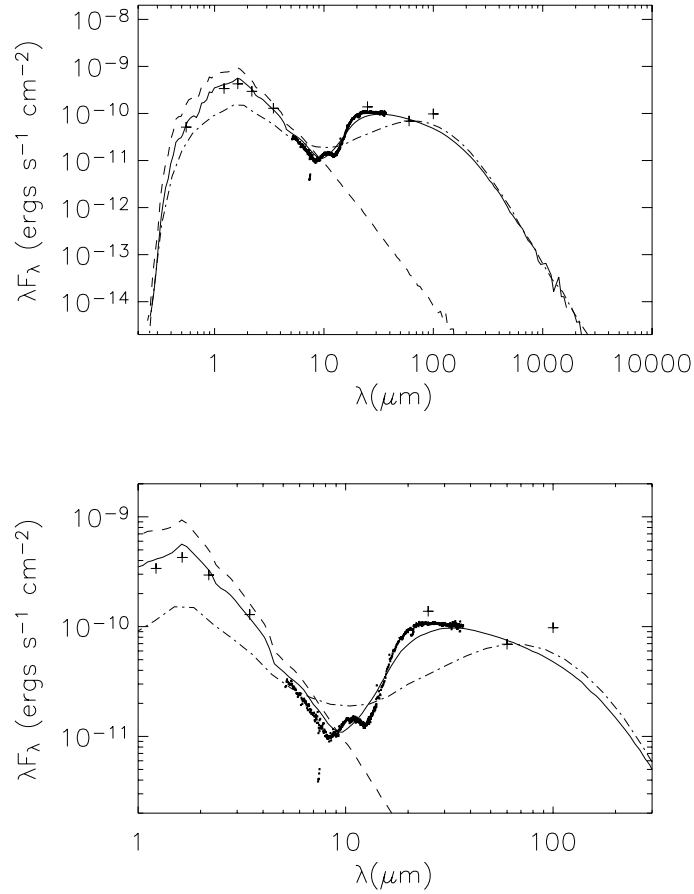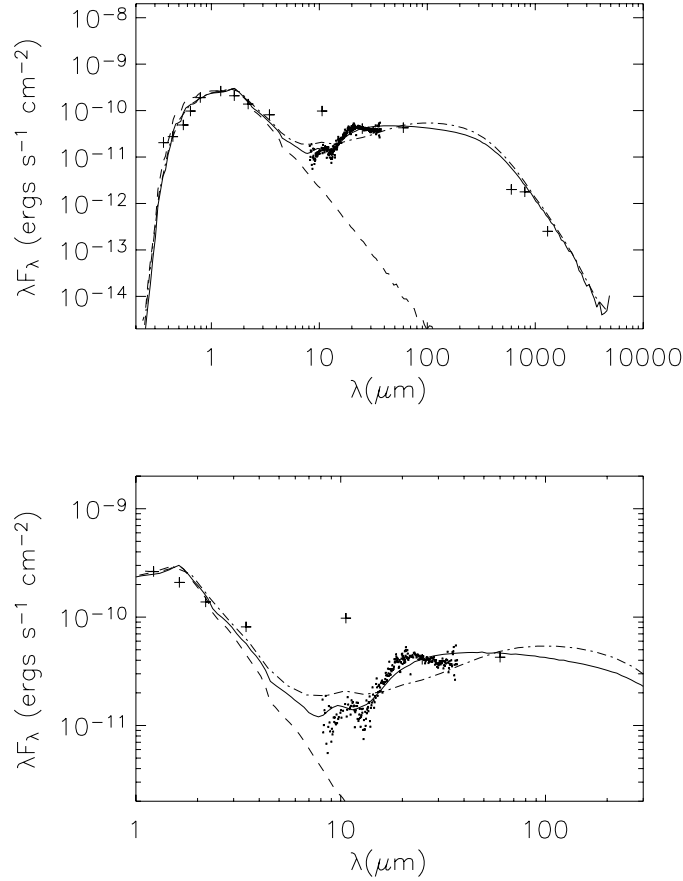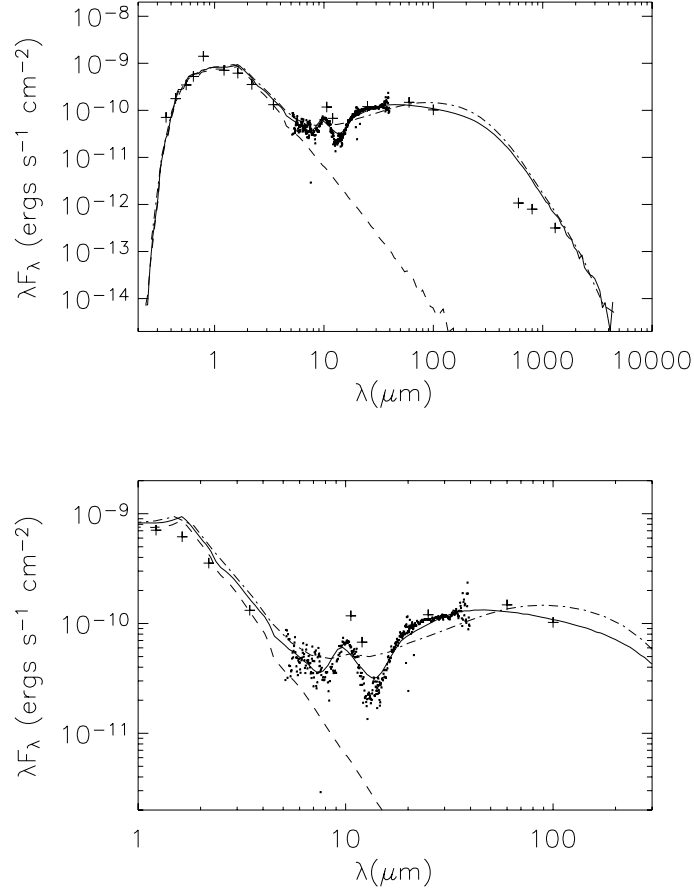

Figure 5.12: SED models for GM Aurigae. The broken line is the hydrostatic equilibrium model and the solid line is the multiple species model. The small filled dots are the *Spitzer* IRS data and the crosses are the IRAS data from the Kenyon & Hartmann (1995) compilation.

GO Tau

The best fit multiple species dust model for GO Tau is for a 0.065 $M_\odot$ disk inclined at 75°. Using these parameters the mid-IR emission is found to be much lower than expected for a disk in hydrostatic equilibrium and at this inclination a disk in hydrostatic equilibrium obscures the central star such that stellar emission is too obscured to fit the data (see Fig. 5.13). An inclination of 66° is required if the hydrostatic equilibrium model is to fit the stellar component, however this leads to too much emission at far-IR to millimetre wavelengths. This excess could be reduced by lowering the disk mass which would also increase the inclination up to which the stellar component of the SED would fit.

A high inclination is suggested by the HST NICMOS images which show a pronounced dark dust lane (see Fig. 5.14). While it is conceivable that a reasonable fit could be obtained using a hydrostatic equilibrium model with HH30 grains, the presence of a silicate feature does requires some small grains in the upper layers of the disk and its presence suggests some degree of dust settling is taking place.
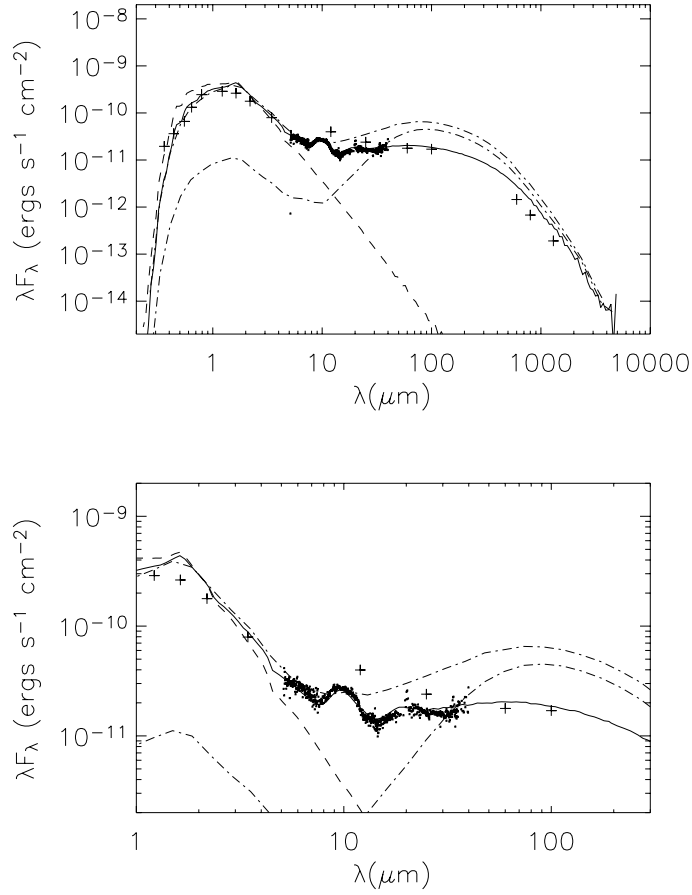
Figure 5.13: SED models for GO Tau. The broken lines are the hydrostatic equilibrium models (lower curve is for an inclination of 75° while the upper is for 66°) and the solid line is the multiple species model (at an inclination of 75°). The small filled dots are the *Spitzer* IRS data and the crosses are the IRAS data from the Kenyon & Hartmann (1995) compilation.
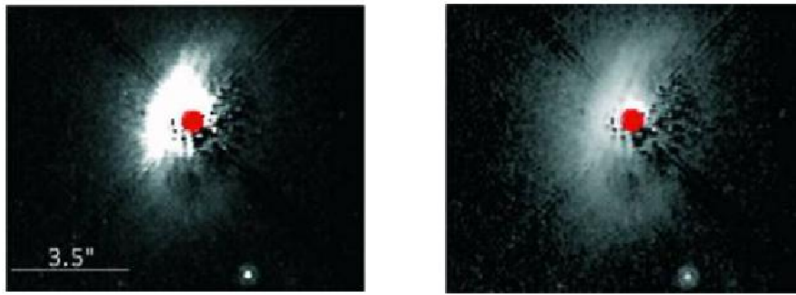
Figure 5.14: Images of GO Tau taken with NICMOS, the image on the right is a linear display of 0 - 0.134 mJy arcsec^{-2} and the image on the right is a logarithmic display from 0.02 - 3.2 mJy arcsec^{-2}. Both images are on the same scale shown on the right. Images taken from Schneider et al. (2005).

Lk Ca 15

The best fit multiple species dust model for Lk Ca 15 is for a disk inclined at 35° (see Fig. 5.15). The model fit requires an inner band of MRN grains separated from the main disk which is composed of 99.93% large HH30 grains. The best fit model requires a disk mass of 0.075 $M_\odot$ which is higher than the typical $-1 \leq \log(M_d/M_\star) \leq -3$ for T-Tauri stars (Natta et al. 2000; Klein et al. 2003). The hydrostatic equilibrium model using the same disk mass produces most noticeably too much emission at far-IR to millimetre wavelengths. Although a lower mass disk, which would be more in line with the 'typical' range stated above, might improve the fit at these longer wavelengths it is unlikely it would fit the very low mid-IR emission profile which suggests a flatter disk is present. Also, small grains are needed to explain the large silicate feature at 10 μm.
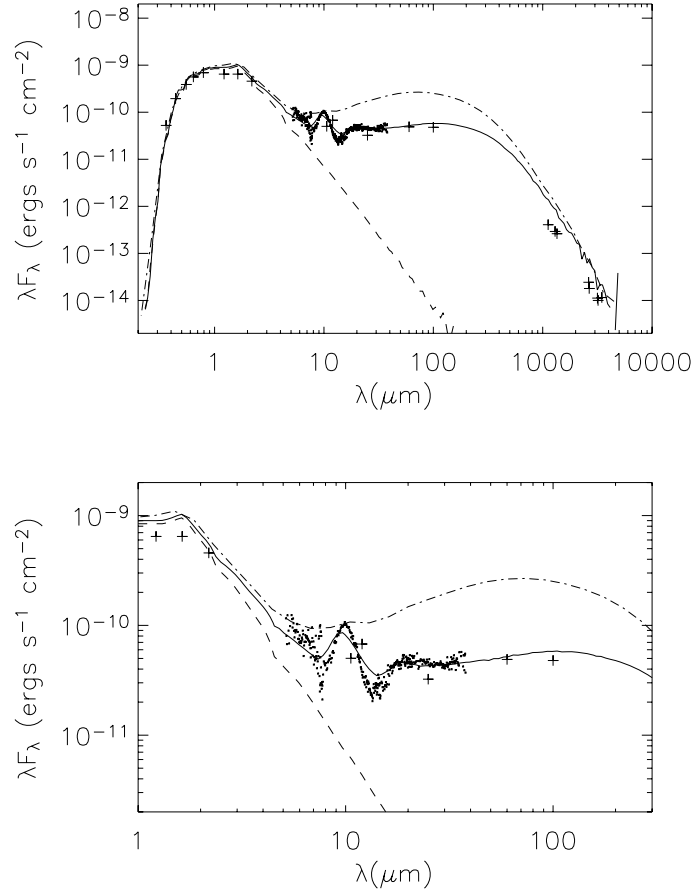
Figure 5.15: SED models for Lk Ca 15. The broken line is the hydrostatic equilibrium model and the solid line is the multiple species model. The small filled dots are the *Spitzer* IRS data and the crosses are the IRAS data from the Kenyon & Hartmann (1995) compilation.

TW Hydra

The best fit multiple species dust model for TW Hydra is for a face-on disk of mass of 0.04 $M_\odot$ (see Fig. 5.16), with an inner MRN disk out to 4 AU. Most of the mass in the outer disk is in HH30 gains indicating grain growth.
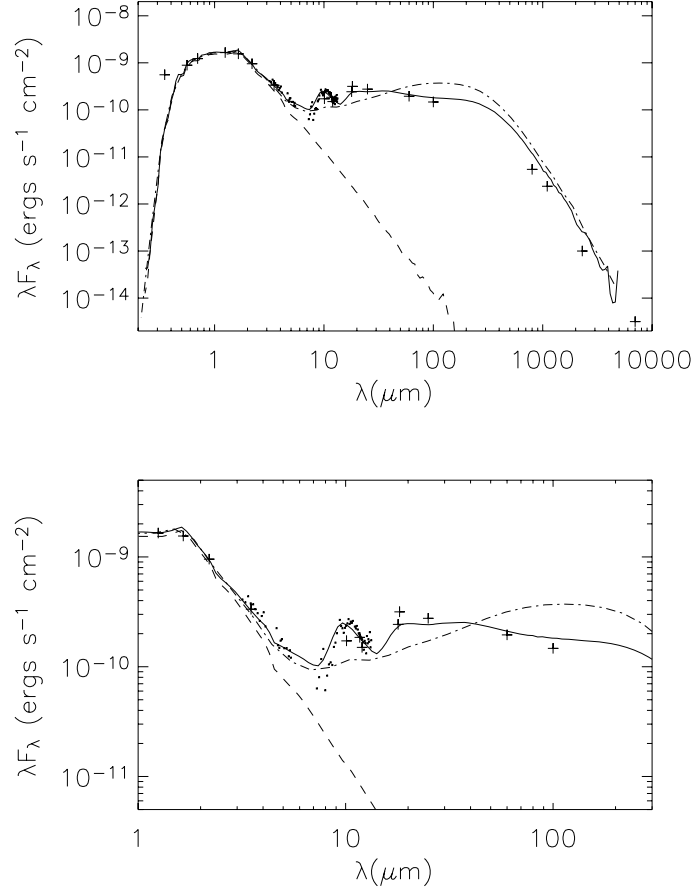
Figure 5.16: SED models for TW Hydra. The broken line is the hydrostatic equilibrium model and the solid line is the multiple species model. The small filled dots are the *Spitzer* IRS data and the crosses are the IRAS data from the Kenyon & Hartmann (1995) compilation.

The equivalent hydrostatic equilibrium model does not fit the data with too much emission at far-IR to millimetre wavelengths and too little emission at mid-IR wavelengths. Whilst a lower disk mass might improve the fit at longer wavelengths it would also reduce the emission at mid-IR making the fit to the IRS data worse. There is also a silicate feature that requires the presence of some small grains.

5.2.3   Discussion

O'Sullivan et al. (2006) have modelled the IRS data of seven objects of varying age using a multiple species dust model that has been used to simulate dust settling and grain growth. Comparison hydrostatic equilibrium models were also generated using the radiative equilibrium code with a deviation from these taken as an indicator of dust settling. For all seven objects the best fits to the SED were generated using a multiple species dust model, however in the case of DM Tau and GM Aur the departure from hydrostatic equilibrium appears to be small. In the case of GO Tau, the 'best fit' model uses a disk mass of 0.065 $M_\odot$. While it is conceivable that a reasonable fit could be obtained using a hydrostatic equilibrium model with HH30 grains if a lower disk mass was assumed, the presence of a strong silicate feature requires some small grains and therefore a multiple species model. In all cases the IRS data has revealed a silicate feature of varying strength requiring some degree of deviation from the hydrostatic equilibrium using large grains. Whilst the number of models presented is small, the models provide strong evidence of dust settling and grain growth in objects of varying age from < 1 Myr to 10's Myr. For many of the objects determination of the degree of deviation from hydrostatic equilibrium requires further observations to constrain the inclination and mass of the systems.

5.3   Dust Settling, Grain Growth and Inner Holes in *Spitzer* Brown Dwarf Sources

Recently mid-IR low resolution spectra and 24 μm photometry of 36 Brown Dwarfs in the ~5 Myr old Upper Scorpious star formation region were obtained with the IRS and MIPS instruments respectively on the *Spitzer* Space Telescope. Of these objects 12 show significant 24 μm excess emission indicating the likely presence of a disk (Scholz et al. 2006b). These objects were modelled using the radiative equilibrium code and the multiple dust species code (O'Sullivan et al. 2005) described in Sect. 5.2.1. The remaining objects show little or no excess which may indicate no disk is present or that a inner gap is present in the disk far in excess of the minimum inner hole size set by the dust destruction radius.

Models of disks in hydrostatic equilibrium were produced using the radiative equilibrium hydrostatic equilibrium code as described in Chapter 2. The multiple dust species code is an extension of the radiative equilibrium code that allows multiple populations of dust species within the disk. In this case models with two dust species, ISM grains (Kim et al. 1994) and larger HH30 grains (Wood et al. 2002a), were investigated.

5.4   Results

For all objects, if the disk is in hydrostatic equilibrium it would be necessary to have a disk mass of less than 10^{-5} $M_\odot$. This is broadly consistent with the findings in Chapter 3. As this is a very low disk mass further modelling assuming hydrostatic equilibrium has been left until millimetre data is available to suggest this might be the case. The parameterized models find that the sources with excess flux are all well modelled by flattened dusty disks suggesting grain growth and dust settling to the mid-plane. The 10 μm silicate feature is weak or absent in all of the sources supporting grain growth and dust settling. In 7 of the 12 sources, fits can be produced using only the larger HH30 grains. In the remaining 5 sources a small population of ISM grains provide a fit to the weak silicate feature, however most of the mass remains in the larger HH30 grains. A list of input parameters for all the models is given in Table 5.4 and the model SED fits are shown in Fig. 5.17.

Gaps in the data between 3 - 8 μm mean it is not possible to constrain the inner hole size of these sources and a dust destruction radius is assumed. Five of the remaining sources for which MIPs data is available, but no appreciable excess is observed, were modelled to determine minimum inner hole sizes. The model fits are shown in Fig. 5.18. All these models required an inner hole size of 5 AU or greater. Observations of a long wavelength excess is required to determine whether these are indeed disks.

$Object$	$T_\star$	$R_\star$	$M_\star$	$M_{disk}^a c$	R_{max}^b	h_0^{HH30}	h_0^{ISM}	f_{ISM}^c	β
	(K)	$(R_\odot)$	$(M_\odot)$	$(10^{-4} M_\odot)$	(AU)	$(R_\star)$	$(R_\star)$		
usco55	2800	0.65	4.5	100	0.26	0.015	-	0.0	1.15
usco112	2850	0.40	4.5	100	0.10	0.01	0.02	0.03	1.1
usco128	2600	0.30	4.5	100	0.01	0.0375	-	0.0	1.1
usd155556	2900	0.40	0.075	4.5	100	0.06	-	0.0	1.0
usd155601	2900	0.35	0.075	4.5	100	0.03	-	0.0	1.1
usd160603	2900	0.35	0.03	4.5	100	0.05	-	0.0	1.0
usd160958	2900	0.55	0.075	4.5	100	0.01	-	0.0	1.1
	2900	0.55	0.075	0.007	4.5	5	-	0.0	1.1
usd161006	2500	0.26	0.02	4.5	100	0.05	0.06	0.03	1.0
usd161103	2500	0.26	0.02	4.5	100	0.05	0.06	0.03	1.0
usd161833	3000	0.65	0.10	4.5	100	0.0055	-	0.0	1.2
usd161916	2600	0.25	0.03	4.5	100	0.015	0.025	0.03	1.1
usd161939	2750	0.50	0.04	4.5	100	0.03	0.04	0.03	1.15

Table 5.4: Model Parameters for Brown Dwarfs in Upper Sco

[a] It was assumed that all the 'disks' have a mass of 4.5×10^{-4} $M_\odot$ which was the typical Brown Dwarf disk mass found by Scholz et al. (2006a) for Brown Dwarfs in Taurus-Auriga.
[b] Without millimetre observations it is not possible to distinguish between disks of different outer radii and therefore an R_{max} of 100 AU was adopted which is within the typical range for T-Tauri disks. For one source, usco160958, a model with $R_{max} = 5$ AU was also presented due to a nearby companion.
[c] The total dust mass of the disk is given by the mass of the large HH30 grains (M_{disk}) and the mass for the KMH grains ($f_{ISM} M_{disk}$).
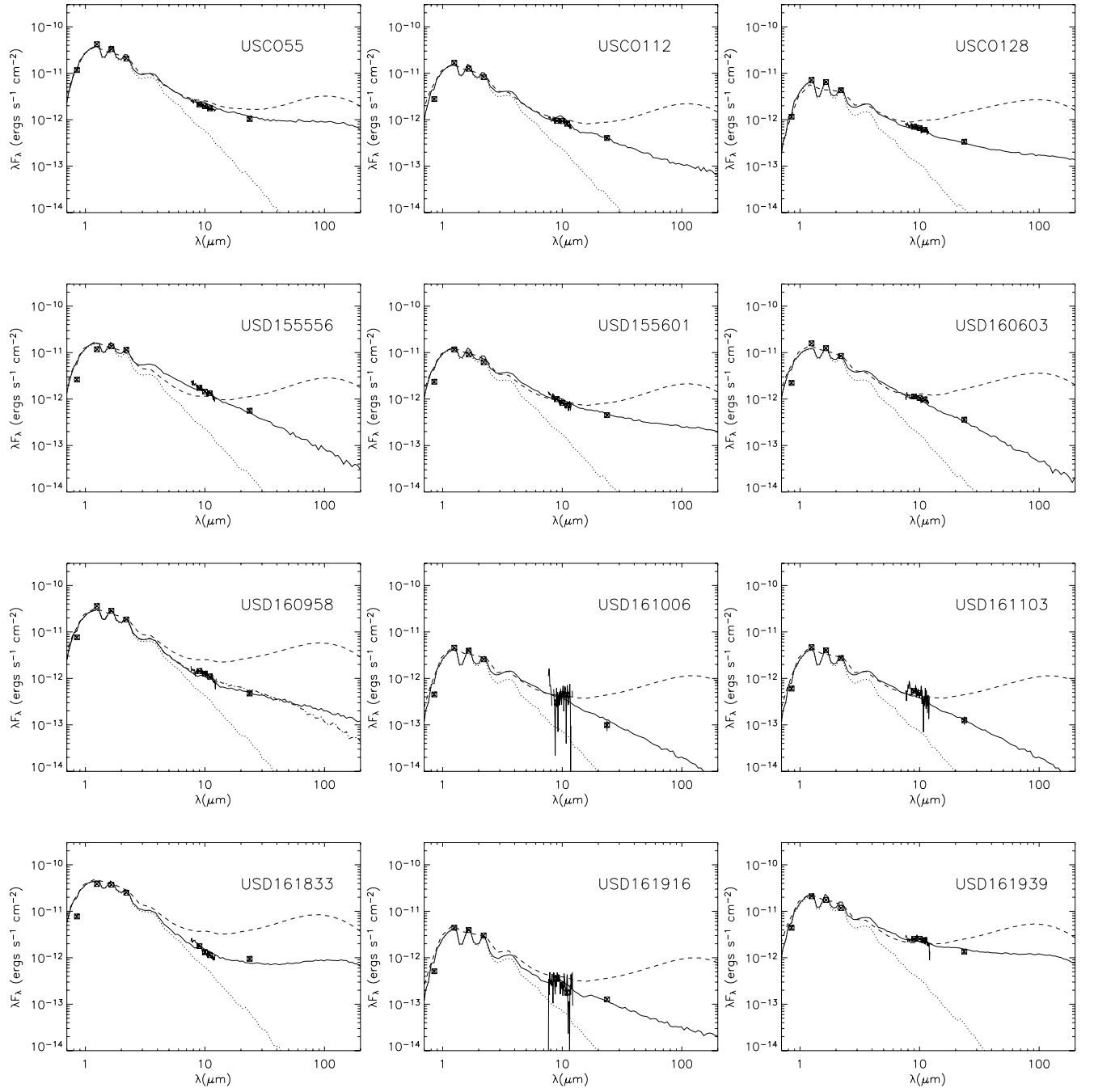
Figure 5.17: SED model fits (solid line) to MIPS and mid-IR low resolution IRS spectra data from *Spitzer* and comparative hydrostatic model (dashed line). USD160958 has a third model with $R_{max} = 5$ AU (dot dash line). In all cases the hydrostatic model does not fit for the assumed disk mass of 4.5×10^{-4} $M_{\odot}$; a lower mass disk may fit. Model parameters are given in Table 5.4. The input stellar spectra is also shown (dotted line). SEDs were produced by combining IRS and MIPS data with near-IR photometry from 2MASS and optical I-band photometry from Ardilla et al. (2000) and Martín et al. (2004). Models reddened according to Kim et al. (1994). NextGen model atmospheres used for the input spectra (Allard et al. 2001; Hauschildt et al. 1999).
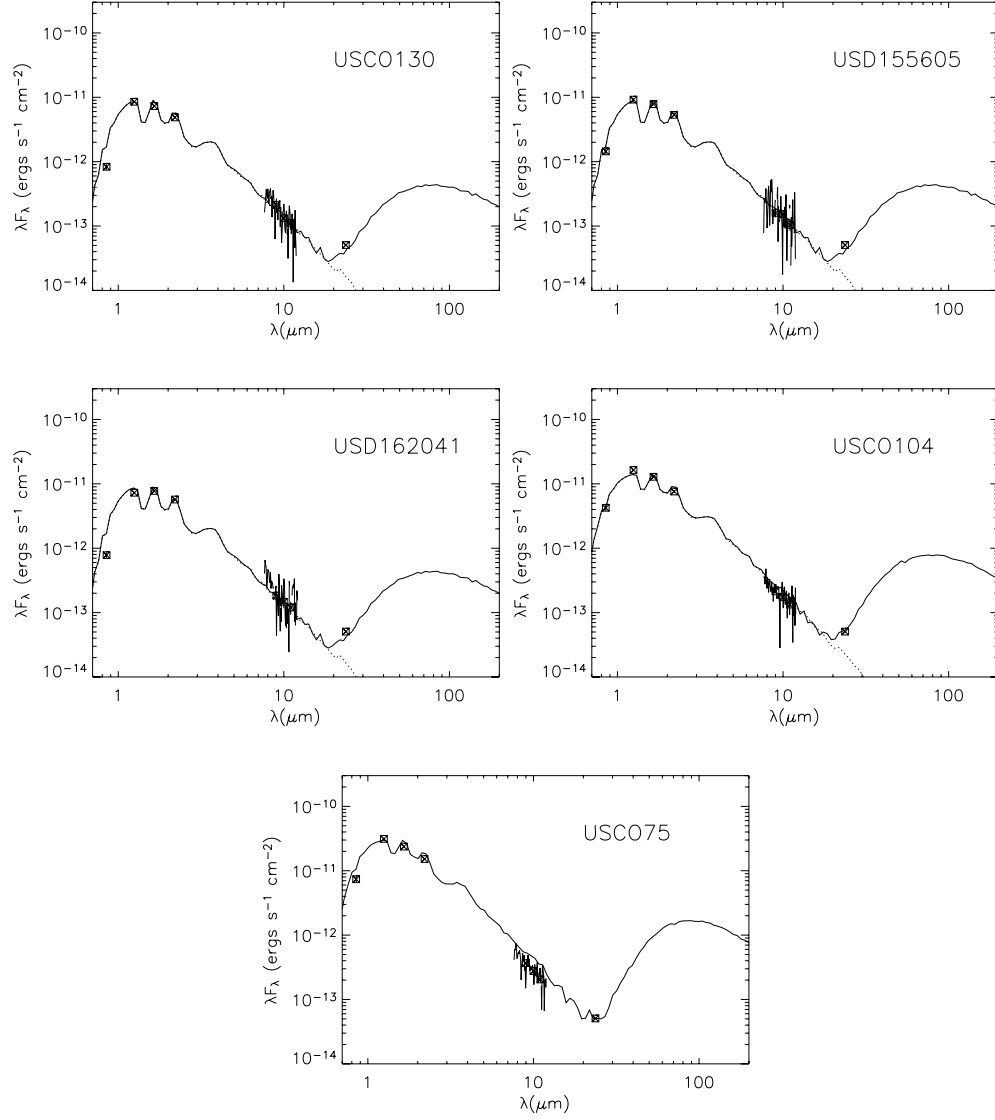
Figure 5.18: SED model fits (solid lines) to five sources that show low 24μm excess emission. SEDs are explained by way of a Brown Dwarf disk system with a large inner hole (5 AU for usco130, usd155605, usd162041; 7.5 AU for usco104, and 20 AU for usco75).

5.5   Discussion

As found in Chapter 3, if these Brown Dwarf disks are in hydrostatic equilibrium they must be of very low mass. The other explanation for their SEDs is that the disks are of higher mass but flatter. Observations at millimetre wavelengths of 5 Brown Dwarf disks in Taurus-Auriga suggest disk masses range from < 0.4 to several Jupiter masses however a larger sample is required to establish what is typical. The need for flatter disk models for all sources with appreciable excess at 24 μm would seem to suggest that Brown Dwarfs at $\sim$5 Myr are uniformly affected by grain coagulation and dust settling. A comparison with Brown Dwarfs in the younger Taurus-Auriga shows the Upper Scorpius disks are flatter suggesting this may be an evolutionary effect.

One explanation for the lack of 24 μm excess seen in the remaining sources is the presence of a disk with a large inner hole. Models of 5 such sources suggest inner gaps of 5 AU or greater which suggests that something is clearing away or disrupting the inner regions of the disk. This has been seen in T-Tauri disks with one hypothesis being that this gap is caused by an orbiting planetary body (e.g. Rice et al. 2003; Forrest et al. 2004) sweeping up more and more dust as it gets larger. A gap therefore pinpoints where possible planets may be forming. Observations at longer wavelengths are required to determine whether any excess is present which would indicate the presence of a disk. Future interferometry observations may be able to directly image gaps at millimetre wavelengths (Wolf et al. 2002). Future high-precision astrometric instruments may be able to detect the resultant motion of the central star due to an orbiting planet (Takeuchi et al. 2005).

CHAPTER 6

TWO CANDIDATES FOR MASSIVE CIRCUMSTELLAR DISKS AROUND HOT STARS

In this chapter *Spitzer* Space Telescope IRAC observations from the GLIMPSE survey are presented that show two objects with a bipolar morphology typical of close to edge-on disks. If located within the local spiral arm (≥ 1 kpc) models of the sources suggest these 'disks' must be massive. Conversely, the sources would need to be located within tens of parsecs for their 'disks' to be of typical T-Tauri size. The observations also show evidence for the presence of transiently heated polycyclic aromatic hydrocarbons (PAHs). PAHs can be excited by a stellar UV flux suggesting these may be massive UV luminous stellar sources. The influence of PAH emission is discussed.

6.1   Introduction

Although disks around higher mass stars have not been studied to as great an extent as the disks of the lower mass T-Tauri stars it seems likely, given that similar signatures indicate their presence, that there are similarities between the low and higher mass systems. However, there is also evidence to suggest that accretion disks around at least some higher mass stars can be larger than their lower mass T-Tauri counterparts and have masses of the order of the stellar mass (Cesaroni et al. 1997; Zhang et al. 1998). There is also evidence of PAH emission generally associated with hotter more massive systems that have high stellar UV flux (e.g. Habart et al. 2004).

The first PAH emission band, at 11.3 μm, was identified by Gillett et al. (1973). Subsequent observations have revealed further prominent PAH features at 3.3, 6.2, 7.7, 8.6 μm and in addition there are many weaker features and a broad plateau stretching from 3 to 20 μm (see Fig. 6.1). For many years these emission bands were referred to as the
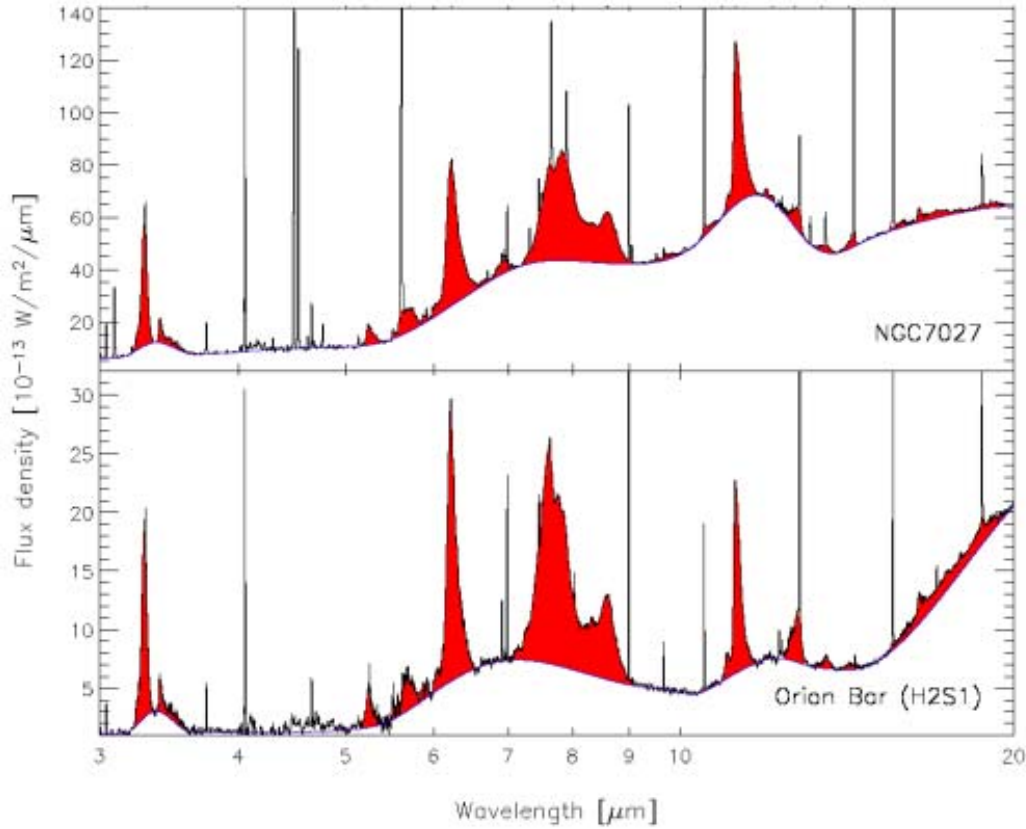
Figure 6.1: Spectra of the planetary nebula NGC 7027 and the Photo-Dissociation region at the Orion Bar illustrate the richness and variety of the 'Unidentified' IR spectrum. Taken from Peeters et al. (2004a).

Unidentified Infrared Bands (UIBs) (see Allamandola 1984 and Willner 1984 for a review). Andriesse (1978) and then Sellgren (1984) showed that thermal emission from small grains transiently heated following the absorption of a UV photon might provide an explanation. Léger and Puget (1984) identified PAHs as good candidates. They showed that the IR vibrational modes of these molecules could explain the UIBs. PAHs are molecules with 10's-100's of carbon atoms in the form of fused aromatic rings (Léger & Puget 1984; Allamandola et al. 1985; Allamandola et al. 1989; Cohen et al. 1986; Jourdain de Muizon et al. 1990; Léger & D'Hendecourt 1987). They are now thought to be the most abundant free organic molecules detected in the universe (Léger and Puget 1984). For further details of the chemistry and physical reasoning for the transient heating of PAHs see Draine et al. (2006), Léger et al. (1989), and references therein.

The two objects presented here were discovered in the *Spitzer* Space Telescope Galactic Legacy Infrared Midplane Survey Extraordinaire (GLIMPSE; Benjamin et al. 2003) in fields bright at Infrared Array Camera (IRAC) wavelengths. The candidate disks themselves are very bright at IRAC wavelengths (see Figs. 6.2 and 6.3). As fluorescent emission from PAHs dominates IRAC images in regions of massive star formation, this suggests there is a strong likelihood the objects are illuminated by massive, UV-luminous stars. Distances to the objects are unknown, but if they are associated with close by star formation within the IRAC field of view they may lie at distances greater than 1 kpc. As the candidate disks are around 18 arcsec and 36 arcsec in diameter this would imply disk radii of greater than $\sim 9\,000$ AU. While models presented here suggest this could be the case it is also possible these are nearby smaller disks or just random wisps of interstellar material. It will become clear throughout this chapter that further observations and improved modelling are required to determine if these are indeed disks.

6.2   Circumstellar Disks and Massive Stars

The star formation paradigm for low mass stars described in Chapter 1 is widely accepted. In comparison, high mass star formation is poorly understood. There is still debate as to whether massive stars form in a similar manner to low mass stars by accretion through a collapsing envelope and accretion disk (e.g. McKee & Tan 2002) or via mergers of lower mass stars in dense clusters (e.g. Bonnell et al. 1989). It was thought that radiation pressure would prevent a stable accretion flow (Kahn 1974; Yorke & Krügel 1977; Wolfire & Cassinelli 1987; Beech & Mitalas 1994), however this view is changing both in theoretical and observational fields. Recently radiation hydrodynamic models suggest that non-spherically symmetric systems may allow accretion to proceed through dense equatorial disks or tori which act as a shield to the intense stellar radiation field (Yorke & Sonnhalter 2002). Radiation transfer models also suggest accretion through a disk can be aided by the presence of protostellar outflows that reduce radiation pressure (Krumholz et al. 2005). McKee & Tan (2002) suggest that the pressure of the infalling gas in the densest regions of giant molecular clouds, where massive stars are observed to form, is more than sufficient to overcome the radiation pressure from the protostar. There are also now detections of infall and equatorially flattened density structures in massive star formation regions (e.g. Zhang et al. 2002; Wu & Evans 2003; Fuller et al. 2005) as well as observations indicating the presence of circumstellar disks around massive stars (e.g. Zhang et al. 1998; Zhang et al. 2002; Shepherd et al. 2001; Beltrán et al. 2004; Cesaroni et al. 2005; Beuther et al. 2005; Jiang et al. 2005; Patel et al. 2005).

Figure 6.2: Three colour mosaics of IRAC band 1, 3 and 4 images showing 0.3×0.3 degree field centred on object A at l = 314.2, b = 0.34. Image is aligned to galactic co-ordinates and is on a logarithmic scale.
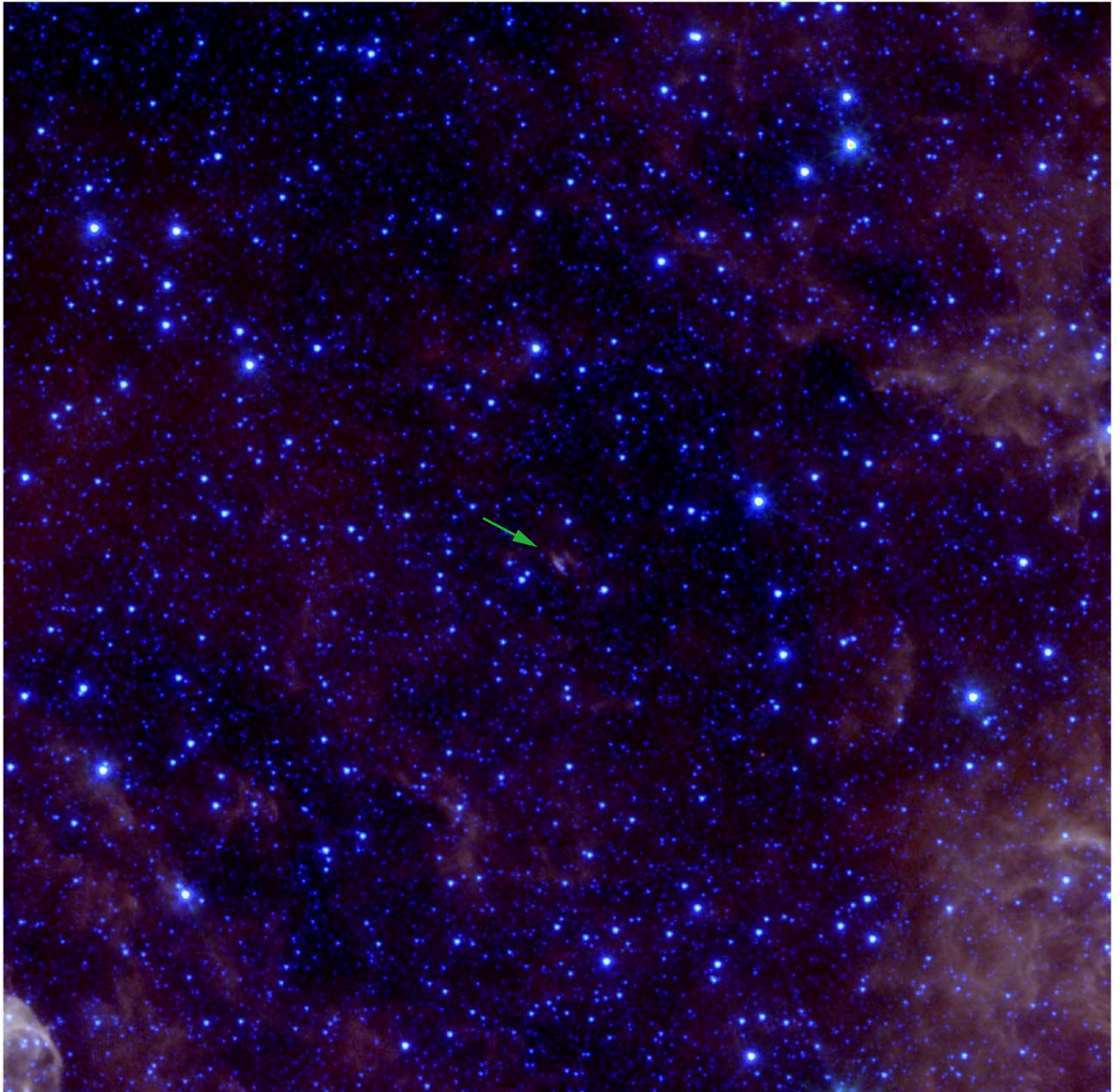
Figure 6.3: Three colour mosaics of IRAC bands 1, 3 and 4 images showing 0.3×0.3 degree field centred on object B at l = 305.96, b = 0.27. Image is aligned to galactic co-ordinates and is on a logarithmic scale.

As discussed in Chapters 4 and 5 there is indisputable evidence for circumstellar disks in both low mass T-Tauri and intermediate mass Herbig Ae objects. There is also indirect evidence to suggest the very low mass Brown Dwarfs may have disks (see Chapter 3). Furthermore, Brown Dwarf disks appear to exhibit similar structure to T-Tauri stars.

The accumulating evidence for circumstellar disks (or at least flattened structures) around Herbig Ae/Be stars (Eisner et al. 2003, 2004; Mannings & Sargent 1997, 2000; Piétu et al. 2003; Hillenbrand et al., 1992) and even more massive stars suggests that intermediate and even higher mass stars may also form by the accretion of material through a disk in a similar manner to lower mass stars. Massive stars are more luminous at UV wavelengths than low mass stars, and as discussed an additional spectral feature that is available for study is the fluorescent excitation of PAHs in their circumstellar disks, resulting in prominent mid-IR emission features (e.g. Peeters et al. 2004b). Indeed, mid-IR spectra of several Herbig Ae/Be stars are well explained with PAH fluorescence (Habart et al. 2004). In addition, recent high resolution mid-IR images have revealed PAH fluorescence in a 900 AU diameter disk surrounding WL16 (estimated spectral type B8 to A0) in the ρ Ophiuchi cloud (Ressler & Barsony 2003).

The advent of the *Spitzer* Space Telescope provides another opportunity for high resolution mid-IR imaging and spectroscopy to study PAHs in the circumstellar environment of massive stars. Preliminary results from the GLIMPSE survey shows that PAH emission in the IRAC images serves as a clear signpost for massive stars. Imaging at IRAC wavelengths will allow an investigation into whether disks glowing in PAHs are a common feature in massive star formation.

6.3   Observations

6.3.1   Disk Candidates

The two objects, hereafter referred to as A and B, which are identified as candidate circumstellar disks are shown in Fig. 6.4 and Fig. 6.5. The figures show near-IR images from the 2MASS survey along with the IRAC discovery images. The longest wavelength IRAC images at 8μm of both objects show a bipolar morphology. This morphology is reminiscent of observations and simulations of high inclination scattered light disks around T-Tauri stars where the dense mid-plane regions create a dark lane bisecting the scattered light nebula and blocking direct light from the central source (Whitney & Hartmann 1992; Burrows et al. 1996). Scattered light disks around T-Tauri stars are observed to have diameters in the range 100 AU to 600 AU and in the nearby Taurus-Auriga association

the angular diameters are a few arcseconds at most. In contrast, the IRAC images in Figs. 6.4 and 6.5 show nebulae that are $\sim$ 18 arcsec and $\sim$ 36 arcsec across, which if at the Taurus-Auriga distance of 140 pc (Elias 1978; Kenyon, Dobrzycka & Hartmann 1994) would imply disk diameters of thousands of AU. However, as discussed below, these two objects may well lie at even greater distances of around 1 kpc to 2 kpc, resulting in disk diameters greater than 9 000 AU. If these objects are disks around young stars they may be the largest yet discovered.

The co-ordinates, observation dates, and *Spitzer* observation identification number for objects A and B are given in Table 6.1.

Object	Galactic Co-ordinates	Date of Observations	ID
A	l=314.2, b=0.34	3/11/04	9225216
B	l=305.96, b=0.27	3/4/04, 7/21/04	9228288. 11768832

Table 6.1: Observation Details

The mid-IR observations were made as part of the GLIMPSE survey (Benjamin et al. 2003), using the Infrared Array Camera (IRAC) (Fazio et al. 2004) on the *Spitzer* Space Telescope (Werner et al. 2004). Data was obtained in all four IRAC bands (central wavelengths of 3.6 μm, 4.5 μm, 5.8μm, and 8.0μm). For object A these observations were taken on 3/11/04 (*Spitzer* Program ID 9225216), and were processed by the *Spitzer* Science Center (SSC) Pipeline (version S9.5.0). For object B these observations were taken on 3/4/04 and 7/21/04 (*Spitzer* Program ID 9225216 and 11768832) and were processed by the *Spitzer* Science Center (SSC) Pipeline (version S9.5.0 and S10.5.0). The data were further processed by the GLIMPSE pipeline to remove instrumental artifacts (Hora et al. 2004). Positional accuracies are better than 1 arcsec (Werner et al. 2004) and the pixel size in the IRAC images is 0.6 arcsec. Point source full-width-half-maximum resolutions range from $\simeq$ 1.6 arcsec at 3.6 μm to $\simeq$ 1.9 arcsec at 8 μm. Every part of the sky in the GLIMPSE survey was observed twice with an exposure time of 1.2 seconds. Mosaic images, which conserve surface brightness, were created using the Montage package[1].

Near-IR images of objects A and B at the J, H, and K bands were obtained from the 2MASS survey. Fluxes were extracted from the IRAC and 2MASS images using aperture photometry routines. The flux calibration of these images is estimated to be accurate to within 7%, based on comparisons of spectral synthesis models with observations of early A-type dwarf stars in the GLIMPSE survey (Cohen et al. 2003).

---

[1]available at http://montage.ipac.caltech.edu

Figure 6.4: 2MASS JHK and IRAC band 1, 2, 3, 4 images of object A stretched by a power of 0.3 and scaled to the object brightness. Images are 30 arcsec on a side. Bipolar structure becomes less evident as wavelength of observation decreases.
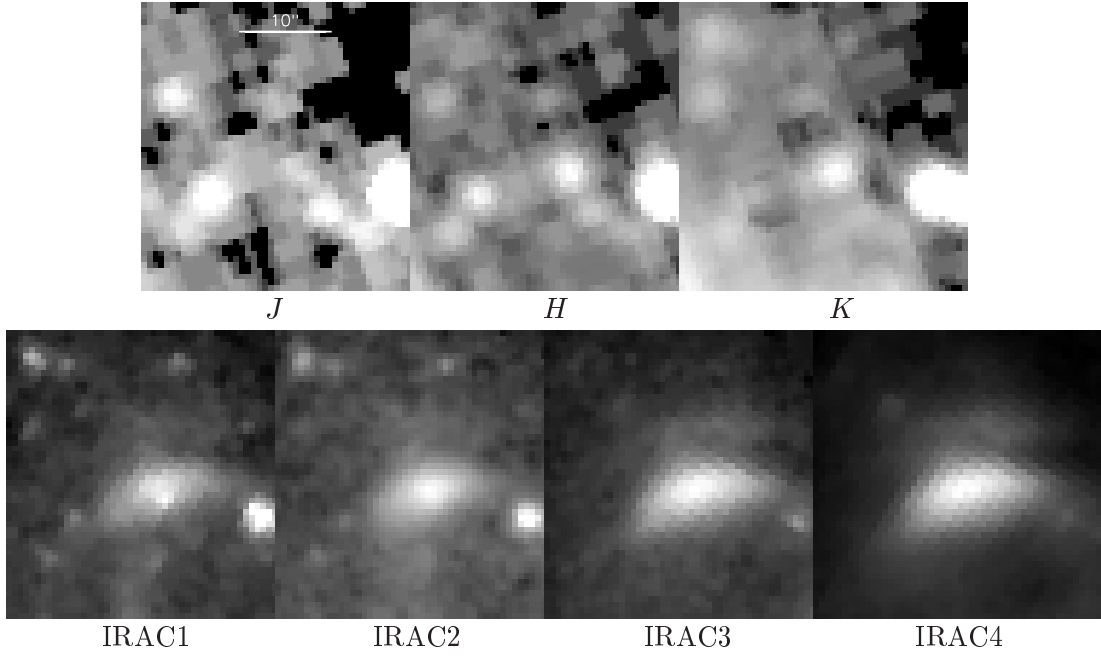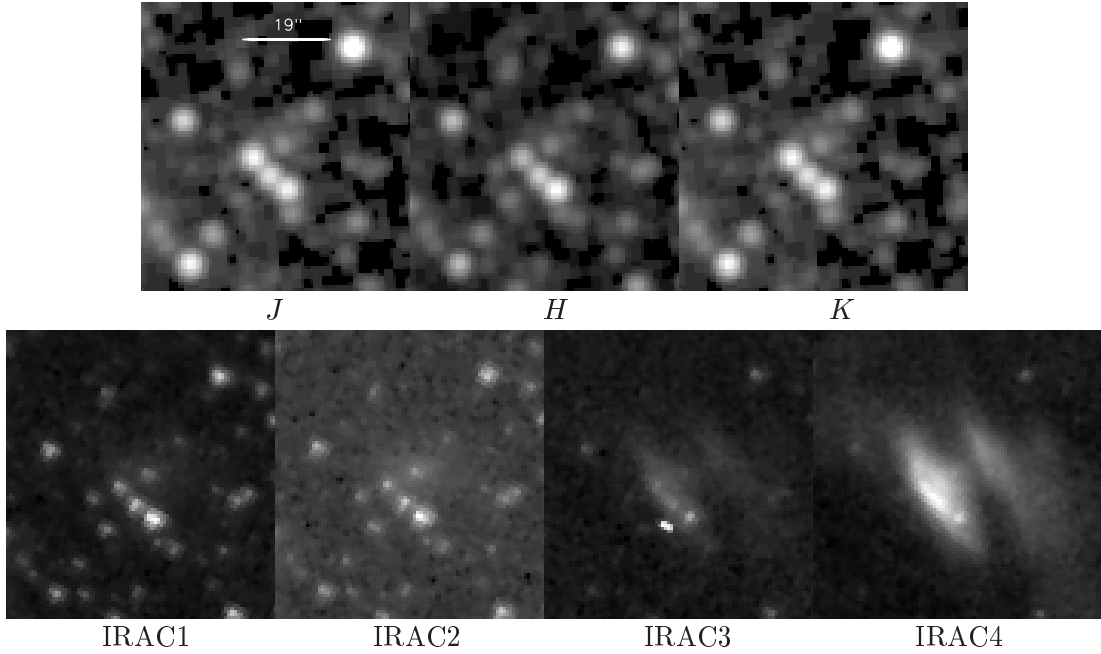

Figure 6.5: 2MASS JHK and IRAC band 1, 2, 3, 4 images of object B stretched by a power of 0.3 and scaled to the object brightness. Images are 57 arcsec on a side. Bipolar structure quickly disappears at wavelengths below IRAC band 4.

6.3.2   Local Environments and Distance Estimates

While the IRAC images in Figs. 6.4 and 6.5 resemble scattered light disks, it is instructive to consider the objects in a broader context with images that show the large scale environments in which they reside. Referring back to Figs. 6.2 and 6.3 which show mosaic three colour images formed from IRAC bands 1, 3, and 4 it is evident that both objects show similar brightness levels compared with the surrounding field. As stated in the introduction, bright emission in IRAC images is common in regions containing massive stars and is often attributed to the presence of PAHs that have been stochastically heated by UV photons (e.g. Uchida et al. 1998; Li & Draine 2002). One possible source for the UV flux being from massive star formation (e.g. Peeters et al. 2004b), which is often accompanied with clusters of low mass stars.

Both objects are in the sight-line of the inner Sagittarius spiral arm and if they are associated with star formation within it their distances could be in the range 1 kpc to 2 kpc (Becker & Fenkart 1970). The presence of ionized gas (Bronfman et al. 1996; Kuchar & Clark 1997; Paladini et al.(2003), radio emission [Cohen - private communication], and molecular gas (Avedisova 2002, and references therein) all lend support to active star formation in the field of object A. The field of object B appears sparser than that of object A and the nearest previously identified star formation region is located around 10 arcmin away (Avedisova 2002). If these objects are young with circumstellar disks they should be associated with nebulae or open clusters (regions where star formation is or has very recently taken place) and therefore object A presents itself as the more convincing pre-main sequence disk candidate. It is also possible these are more evolved objects as there is at least one notable observation (see Fig. 6.6) of an optically thick disk with radius $\sim 10\,000$ AU in the protoplanetary nebulae known as Gomez's Hamburger (Ruiz et al. 1987).

6.3.3   Image Brightness and Morphology

The small scale IRAC images of object A and B show that the bipolar disk-like morphology is brightest in the 8 μm images. The increasing surface brightness toward longer wavelengths is a tell-tale signature of PAH fluorescence and/or emission from very small grains. Note that the 4.5 μm IRAC band does not contain any strong PAH emission features (Peeters et al. 2004b), and consequently it exhibits a lower surface brightness than the other IRAC bands. At near-IR wavelengths the 2MASS images of object A show a hint of bipolar morphology at K, but just an unresolved source at J and H. For object B the bipolar disk-like morphology is not present at wavelengths shorter than 5.8 μm and

Figure 6.6: HST Wide Field Planetary Camera 2 image of Gomez's Hamburger, a star near the end of its life that is surrounded by a thick, dusty disk. Image Credit: NASA and The Hubble Heritage Team (STScI/AURA)

foreground sources contaminate the nebulosity at wavelengths shorter than 8 μm. The JHK bands do not contain prominent PAH emission, so if these objects are circumstellar disks the JHK images would be dominated by scattered starlight which is likely to be much fainter than the longer wavelength PAH emission. Deeper near-IR imaging is therefore required to determine if the objects exhibit the signatures of scattered light disks at JHK. This is discussed further in the modelling sections below.

6.4 Modelling

6.4.1 Radiation Transfer Simulations

The Monte Carlo radiation transfer code detailed in Chapter 2 is used to generate radiative equilibrium models. These models do not currently include non-equilibrium heating and emission from small dust grains or PAHs (see Misselt et al.(2001) for an example of a Monte Carlo code that does include these effects). A modified Monte Carlo scattered light code is then used to generate approximate PAH fluorescent models which allow examination of the qualitative morphology of PAH fluorescence in disks.

For the radiative equilibrium models the assumption is made that the image morphology seen in the IRAC 4.5 μm band is dominated by thermal reprocessed radiation and has negligible emission from small grains and PAHs. The larger grain HH30 dust model is adopted (see Chapter 2 Sect. 2.1.2). The PAH spectra presented in Peeters et al. (2004b) show that the 4.5 μm IRAC band does not contain strong PAH emission, but the emission contribution from the small grain continuum may be important (see models in Misselt et al. 2001). The radiative equilibrium models for object A are therefore tuned to fit the 4.5 μm IRAC flux and image morphology and as a result may not fit the other IRAC bands where PAH emission is important. For object B, an attempt is only made to fit the image morphology at 8 μm due to the severe contamination by foreground sources at shorter wavelengths. As the 8 μm images are bright in PAH emission the dust radiative equilibrium models for object B likely overestimate the source luminosity. All models presented below are for disks heated solely by radiation from the central star which, it is assumed, emits a blackbody spectrum.

As discussed above, the image morphologies of the IRAC images for objects A and B resemble scattered light disks. The PAH fluorescent process can be modelled qualitatively using modified Monte Carlo scattering codes where UV source photons are absorbed by PAHs and reprocessed to optically thinner mid-IR wavelengths. Therefore, qualitative PAH fluorescent models have been constructed using a modified scattered light code as follows. Source photons are emitted and the dust opacity and scattering properties (opacity (κ), albedo (a), and scattering phase function asymmetry parameter (g)) are set to be those appropriate for a dust mixture incorporating PAHs at UV wavelengths: $\kappa = 404.4$ cm^2 g^{-1}, $a = 0.5823$, $g = 0.5570$ (it is assumed the scattering may be represented by the Henyey & Greenstein (1941) phase function). These values are taken from Bruce Draine's webpage[2]. and are calculations from Draine (2003) for $\lambda = 3019\mathring{A}$, $R_v = 3.1$. a gas/dust ratio of

[2]http://www.astro.princeton.edu/~draine

123.6 and a C abundance in PAHs relative to H of 55.8 ppm. If a UV source photon (really a photon energy packet) is absorbed by PAHs, a fraction of its energy will be reprocessed into the PAH emission features present at IRAC wavelengths. The relative probabilities of re-emitting a Monte Carlo energy packet at IRAC wavelengths are 2%, 2%, 17%, 79% for IRAC bands 1, 2, 3, 4 respectively based on the direct integration of the Orion PAH spectrum from Peeters et al.(2004b). This is simulated by isotropically re-emitting the absorbed photons from their point of absorption and setting the dust properties for the subsequent radiation transfer of the simulated fluorescent PAH photons to be those at the appropriate IRAC wavelength as given by the assumed circumstellar dust model (see Table 6.2).

IRAC band	κ	a	g
	$(cm^2 g^{-1})$		
1	9.67	0.285	0.147
2	6.16	0.187	0.085
3	3.87	0.111	0.015
4	5.01	0.027	0.05

Table 6.2: Dust Properties at IRAC Wavelengths

With this algorithm it is possible to qualitatively examine the morphology of PAH fluorescence in disks and compare with simulated images from the radiative equilibrium dust codes that do not include PAH emission.

6.4.2 Circumstellar Density Structure

The following parameterization for the 2-D density structure of flared disks (e.g. Shakura & Sunyaev 1973) is adopted,

$$\rho = \rho_0 \left(\frac{R_\star}{\varpi} \right)^\alpha \exp -\frac{1}{2}[z/h(\varpi)]^2 , \tag{6.1}$$

where ω is the radial coordinate in the disk mid-plane and the scaleheight increases with radius, $h = h_0 (\varpi/R_\star)^\beta$. For this set of models it is also assumed that dust in regions close to the star is destroyed if temperatures rise above 1600 K (Duschl et al. 1996). Any remaining gas is assumed to be optically thin and therefore effectively there is an opacity gap in the disk (Lada & Adams 1992). The disk is sharply truncated at this inner edge. Simulated SEDs, thermal images (convolved with the appropriate IRAC spectral response curve), and simulated PAH fluorescent images are calculated as described above. Disk inclination, mass and scaleheight h_0 are varied in an attempt to model the observed

4.5 μm image morphology of object A and the 8 μm morphology of object B. To minimize the large parameter space, the parameters $\beta = 1.25$ and $\alpha = 2.25$ which are appropriate for irradiated disks around low mass stars (D'Alessio et al. 1999a) are fixed, giving a surface density $\Sigma \sim \varpi^{-1}$.

Accretion disks around classical T-Tauri stars are typically a few hundred AU in radius with masses in the range 10^{-4} to 10^{-1} $M_\odot$ (e.g. Calvet et al. 2000; Natta et al. 2000). Accretion disks around higher mass stars are not well understood, however there is evidence to suggest they can have masses of the order of the stellar mass (e.g. Cesaroni et al.1997; Zhang et al. 1998), but also be larger than their lower mass counterparts so that densities are not necessarily higher. The minimum diameter of object A and object B are estimated to be ~ 18 arcsec and ~ 36 arcsec respectively, which would give a considerable physical radius for both 'disks' if they are located beyond a few tens of parsecs. If the objects are in the Sagittarius spiral arm, they may be up to 2 kpc distant, implying radii of tens of thousands of AU. Therefore, in the models presented below two alternatives are considered: (1) the objects are associated with star formation in the Sagittarius spiral arm at a distance of 1.6 kpc and are very large disks; (2) the objects are located much closer and have smaller disk radii more comparable with a low mass star.

6.4.3   Results for Object A

For the radiative equilibrium models of object A disk radii of $1\,000$ AU and $20\,000$ AU are adopted, which correspond to distances of roughly 70 pc, and 1.6 kpc when compared to the observations. Stellar parameters, disk mass, scaleheight, and inclination are adjusted to provide a match to surface brightness and morphology. The best fit models are summarized in Table 6.3 and shown in Figs. 6.7 and 6.8. Many models were attempted in which the disk parameters were varied to fit by eye the overall image morphologies. In more quantitative modelling, comparisons were made between surface brightness levels and vertical cuts were made bisecting the bipolar nebulae in order to compare the shape and flux levels in the data and models. With the limited data presented in this section more detailed modelling analysis at this stage was not considered to be justified.

Model	$T_\star$	$M_\star$	$R_\star$	M_{disk}	R_{in}	R_{max}	h0	h(100AU)	h(500AU)	Incl.
	(K)	$(M_\odot)$	$(R_\odot)$	$(M_\odot)$	$(R_\star)$	$(x10^3\,AU)$	$(R_\star)$	(AU)	(AU)	(degr)
$A.1$	3500	0.4	2.2	0.08	5	1	0.015	15	112	76
$A.2$	14000	4	3	40	92	20	0.01	9	69	73
$A.3^a$	14000	4	3	40	92	20	0.01	9	69	73
$B.1$	16000	6	5.5	34	122	20	0.01	8	59	85

Table 6.3: Model parameters

^{a} PAH approximation model

(a)   (b)
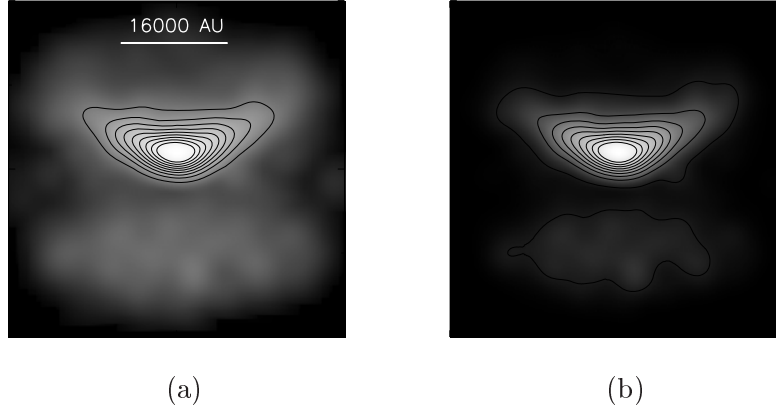
Figure 6.7: Models of object A at IRAC band 2. Model parameters are: $T_\star$ = 14000 K, R_{max} = 20000 AU, $\log(M_d/M_\star)$ = 1, i = 73°. Image (a) is convolved with a gaussian, and image (b) is as (a), but with a background of 7% added, which masks the lower level outer regions of the disks improving the model fit. Images have been scaled by a power of 0.3, however each contour represents a 10% drop in surface brightness with the highest contour being 90% of the peak value and the lowest being 10% of the peak value.

(a) (b) (c)

(d)
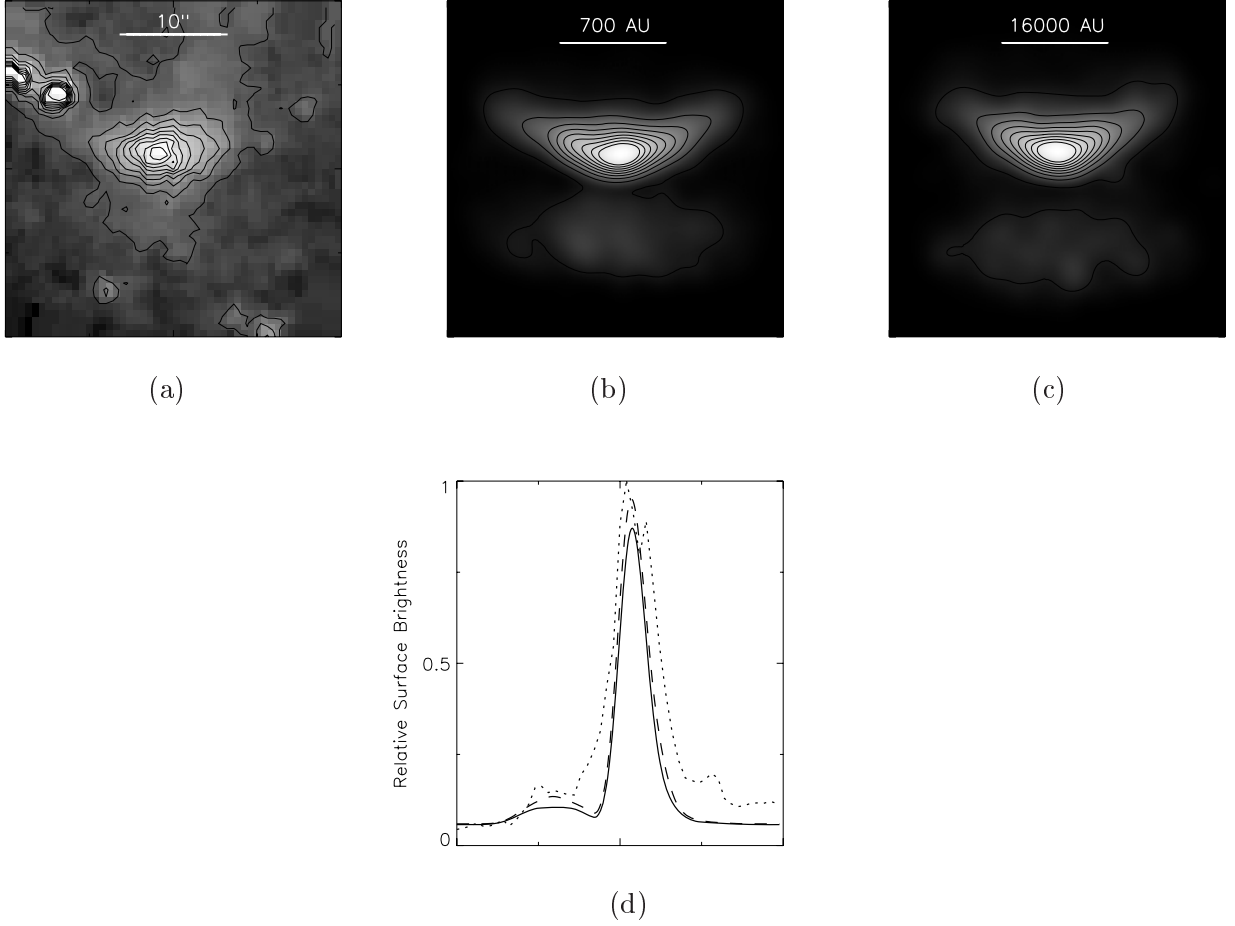
Figure 6.8: Comparison between IRAC band 2 data and models of object A. Image (a) shows a contour plot of the IRAC band 2 data. Contour plots of the 1000 AU and 20000 AU disks models are shown in (b) and (c) respectively. Image (d) compares a cross-section through the central region of the data and the two models shown in (b) and (c). Model parameters are detailed in Table 6.3. Images and contours scaled as in Fig. 6.7. Cross-sections are scaled to the maximum value of the observed data. All models have a background of ~7% added, which masks the lower level outer regions of the disks improving the model fit. The cross-sections perpendicular to the disk show that relative fall-off in flux is consistent between data (dotted) and models A.1 (dashed), A.2 (solid).

To make a comparison between the models and the IRAC images it was important to account for the foreground/background emission that is evident in the observations (see Figs. 6.2 and 6.3). For object A this emission is typically around 5% to 20% of the average surface brightness of the bipolar nebula. Adding a uniform background of this level to the simulations has a dramatic effect on the model images: masking the lower level outer regions of the model disks and making the upper bipolar lobe more prominent and rounder when compared to models without any simulated background emission. This is illustrated in Fig. 6.7a and Fig. 6.7b which respectively show one of the model images convolved with a Gaussian PSF to simulate the IRAC resolution, and the final product that has a uniform background added prior to the PSF convolution. All the model images in Fig. 6.8 have a background added and the addition of background emission improved fits to the observations. Figure 6.8 contains the IRAC 4.5 μm data in both image and cross-section format for comparison with the models. The cross-sections perpendicular to the disk show general agreement between models and data.

Once radiative equilibrium models that reproduced the image surface brightness and morphology at 4.5 μm were found, it was then investigated how these models compared to data at other wavelengths. No model was found that could reproduce the observed surface brightness at all IRAC wavelengths. This discrepancy in part could be due to the properties of the dust used, however as there is considerable background emission in all IRAC bands throughout the region in which this object is found it is suggested there may be a significant contribution from PAHs and small grains. As stated previously, PAHs and small grains will be particularly strong at IRAC bands 1, 3 and 4. In the case of the 20 000 AU model disk, which is found to require a stellar luminosity $L_\star \sim 300 L_\odot$ (corresponding to a main sequence spectral type of $\sim$ B7 [Cox 2000]), the star itself could easily provide the UV and optical photons required for non-equilibrium PAH heating. The inference of strong PAH/small grain emission makes the nearby small disk model unlikely, because the lower temperature central source will not provide enough UV luminosity to excite the PAHs. An intermediate model is more likely as 57% of Herbig Ae/Be stars observed with ISO show PAH emission features (Acke & van den Ancker 2004). This compares to PAH being detected in only 9% of T-Tauri stars and in most cases toward massive T-Tauri stars (Geers et al. 2005). External illumination is not an alternative for the small disk because the image morphology of an externally illuminated disk does not exhibit the dark dust lane of internally illuminated models.

Based on the simulated images and the likely presence of PAHs/small grain emission, it is believed that despite the unusually large disk the high luminosity model is the more likely. This is supported by the SED shown in Fig. 6.9 which shows the radiative equilibrium model SEDs and flux measurements for object A. Although the 1 000 AU disk
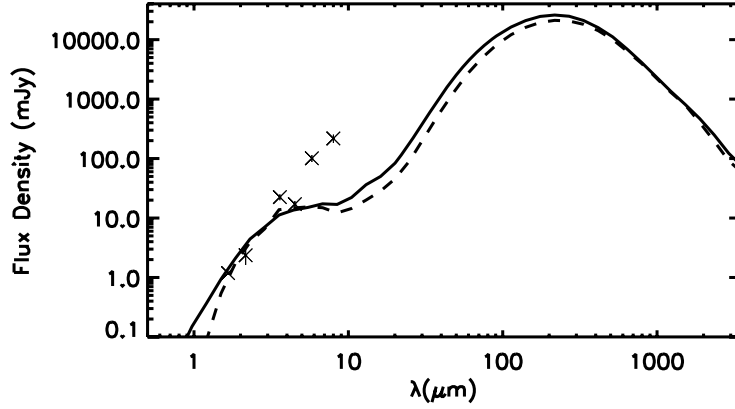
Figure 6.9: The SED of models A.1 (dashed), A.2 (solid) and the H,K, and IRAC band 1,2,3,4 observations of Object A. J band flux negligible and not plotted. Model SEDs have been reddened according to the empirical relationships from Cardelli et al.(1989) with R_v = 4.1 and using $A_\lambda \propto \lambda^{-1.9}$ from Kaas (1999) for $\lambda > 3.5$ μm. $A_v = 17$ and a distance of 70 pc applied to model A.1. $A_v = 6.2$ and a distance of 1600 pc applied to model A.2. These radiative equilibrium models do not fit at IRAC bands 1,3 and 4 possibly due to PAH heating, which is not accounted for here.

provides a reasonable match to the morphology of object A it requires a large extinction ($A_v = 17$) to match the H and K flux measurements, highly implausible at a distance of 70 pc. The 20 000 AU model on the other hand only requires an $A_v = 6.2$, which appears to be reasonable at a distance of 1.6 kpc for this sight-line (Neckel & Klare 1980).

It is also clear from Fig. 6.9 that a match is not achieved at IRAC bands 1, 3, and 4, possibly due to the absence of PAH/small grain emission in these models. To test that PAH fluorescence can produce images that qualitatively match the IRAC data, simulated PAH fluorescent images have been constructed using the modified Monte Carlo scattering code described above. Figure 6.10 shows the simulated PAH fluorescent images and cross-sections for the same disk density structure from the models in Fig. 6.8. The approximate PAH model images show disks that are slightly more flared than the earlier models. This is due to the UV optical depth $\tau = 1$ surface being at a larger height above the mid-plane so that UV photons are absorbed, and reprocessed, at larger heights than stellar photons in radiative equilibrium simulations. The image morphology is very similar to the data, showing that PAH fluorescence is indeed a plausible explanation for the IRAC data. Inclusion of PAH/small grain emission in the Monte Carlo codes is clearly required for more detailed models of these sources. However, the models presented here demonstrate that the data is consistent with the interpretation of large disks irradiated by a central source.

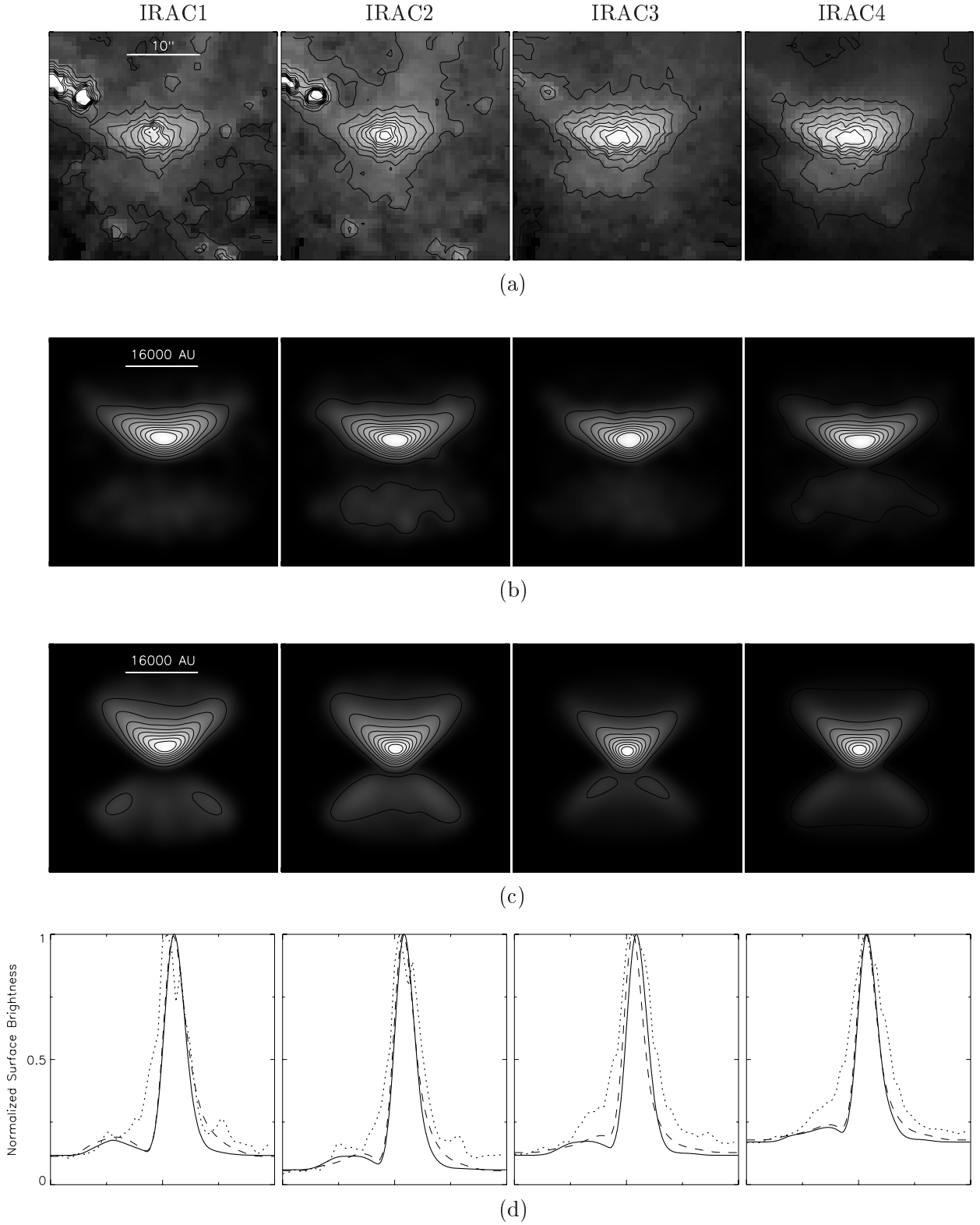Figure 6.10: Contoured IRAC band 1, 2, 3, 4 images (a), model A.2 (b), approximate pah model A.3 (c), and (d) cross-sections through the corresponding images (a-dotted),(b-solid) and (c-dashed). All are normalized to the maximum value of each data set and a background applied as in Fig. 6.7. A.3 images are more flared as the UV optical depth $\tau = 1$ surface is at a larger height above the mid-plane.

6.4.4 Results for Object B

For object B a single model for a disk of radius 20000 AU is presented, corresponding to a source distance of 0.85 kpc. The choice of disk radius for object B is somewhat arbitrary as an attempt is only made to fit the general morphology and not the fine details of this system. It does, however demonstrate once again that a large disk is required for source distances beyond tens of parsecs. Object B only has a clear bipolar structure in IRAC band 4. At wavelengths shorter than this foreground stars dominate the image. Object B was modelled at 8 μm to show that the general morphology of this object is characteristic of a highly inclined disk. Figure 6.11 shows an example model of a $20\,000$ AU disk inclined at $i = 85°$. This figure shows that a dark lane and two bright lobes, such as those evident in the observation of object B, are consistent with a very highly inclined model. Again adding a background, in this case 40%, improves the fit to the shape of the object. This is a huge disk, however given a comparison with the observations it would only be located at approximately 850 pc. There is no recorded active star formation in the direction of object B and it seems most likely that any young star+disk system would be located in the spiral arm. For this to be the case object B would have to have an enormous disk well in excess of any known to date and for this reason it seems more unlikely that this is a pre-main sequence circumstellar disk. One alternative explanation is that object B is not a disk, but is simply an optical illusion: it could just be wisps of interstellar material illuminated by the ambient interstellar radiation field. No attempt is made to characterize this object further.

(a)   (b)

(c)
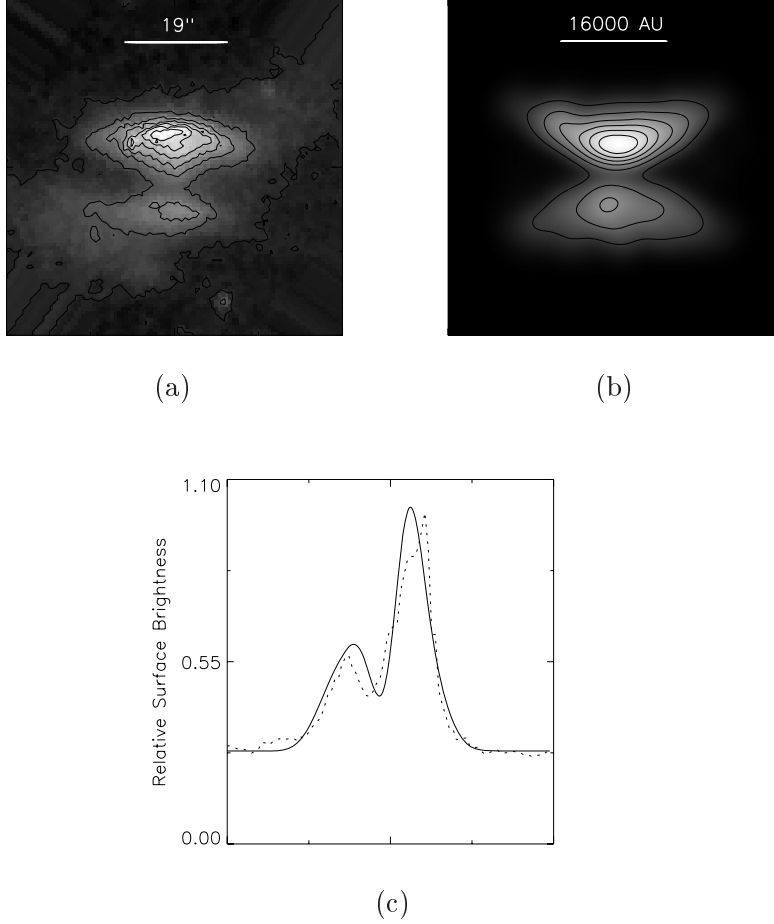
Figure 6.11: Comparison between IRAC band 4 data and model of object B. Image (a) shows a contour plot of the IRAC band 4 data. A contour plots of the 20000 AU disk model is shown in (b). Image (c) compares a cross-section through the central region of the data and the model shown in (b). Model parameters are detailed in Table 6.3. Images in the contour plots have been scaled by a power of 0.3, however each contour represents a 10% drop in surface brightness with the highest being 90% of maximum. The cross-sections are scaled to the maximum value of the observed data at IRAC band 4. The model has a background of ∼40% added, which masks the lower level outer regions of the disks improving the model fit. The cross-sections perpendicular to the disk show that relative fall-off in flux is consistent between data and models.

6.5 Discussion

New *Spitzer* observations from the GLIMPSE survey of two previously unidentified objects have been presented. Models suggest that the presence of highly inclined circumstellar disks could explain the bipolar morphology of these two objects. If these are disks associated with pre-main sequence objects they need to be either massive disks or very close by smaller disks. If object A lies at a distance of 70 pc, then it is possible to reproduce the general morphology of the IRAC images with $M_{disk} = 0.1\ M_\odot$, $R_{max} = 1\,000$ AU, $i = 76°$ and a central source with $L = 0.64\ L_\odot$, $T = 3\,500$ K. On the other hand, if it is associated with star formation in the Sagittarius arm and lies at a distance of 1.6 kpc, the image morphology is reproduced with $M_{disk} = 40\ M_\odot$, $R_{max} = 20\,000$ AU, $i = 73°$ and a central source with $L = 305\ L_\odot$, $T = 14\,000$ K. The relative brightnesses of the IRAC images suggests that PAH fluorescence is important for accurately modelling the data. Using a modified Monte Carlo scattering code, it is qualitatively demonstrated that PAH fluorescence can explain the IRAC image morphologies and relative brightnesses.

For object B foreground stars severely contaminate the images for wavelengths shorter than 8 μm and therefore an attempt was only made to model the morphology of this object at 8μm. Assuming object B is at 0.85 kpc, its 8 μm image morphology can be reproduced with $M_{disk} = 34\ M_\odot$, $R_{max} = 20\,000$ AU, $i = 85°$ and a central source with $L = 1754\ L_\odot$, $T = 16\,000$ K. Due to the contamination from foreground sources, the identification of object B as a circumstellar disk is much more circumspect than for object A and the limited data does not warrant more detailed modelling efforts.

The foreground/background nebulosity was found to be an important consideration in modelling these objects. Including a uniform foreground/background emission component in the radiation transfer simulations greatly improved the model fits. In the region of Object A the observed foreground/background emission is at the 5% to 20% level and for object B it is at the 40% level. The addition of foreground/background emission masks the outer, lower surface brightness regions of the disks, can change the relative prominence of the bipolar nebulosity, and makes the scattered light disk appear more rounded.

Although the modelling suggests that these objects may be massive circumstellar disks, the nebulae could simply be optical illusions that look like disks. With such large disk masses the question of gravitational stability arises. A reminder that the Toomre stability parameter Q_T is given by (Toomre 1964),

$$Q_T = \frac{c_s \Omega}{\pi G \Sigma} \tag{6.2}$$

where c_s is the local sound speed, Ω is the angular velocity, Σ the surface density and G the gravitational constant. The regions of the disk where $Q_T \geq 1$ are gravitationally

stable against axisymmetric perturbations. Analysis reveals that the massive disk models have Toomre parameter Q≪1 at all radii. If the objects are disks, this would suggest they are gravitationally unstable and may be short lived. However, recent work by Lodato & Rice (2005) suggests that the phases of massive disks are not necessarily short when a more realistic treatment of disk thermodynamics is included in numerical simulations specifically if the disks are not assumed to be isothermal.

Further observations are required to determine whether the objects are disks or just random wisps of interstellar dust. If images are formed by small disks casting a shadow on the cloud in which they are embedded, the cloud would need to be very flattened as models of this type produce much more extended morphologies (Hodapp et al. 2004). Near-IR polarimetry (Whitney & Hartmann 1992) and deeper near-IR imaging could reveal the scattered light disks, which would be expected to be much fainter than disks glowing in PAHs at the IRAC bands. Millimetre and radio interferometry could search for signatures of cold dust and whether the objects exhibit signatures of rotation. Further modelling including PAHs will also help to establish the true nature of these objects. This is currently under development. Object A has recently been detected at 24 μm (see Fig. 6.12) and 70 μm in the Multiband Imaging Photometer Inner Galactic Plane (MIPSGAL) *Spitzer* survey (Carey et al. 2005). These longer wavelength observations will help to constrain future models.
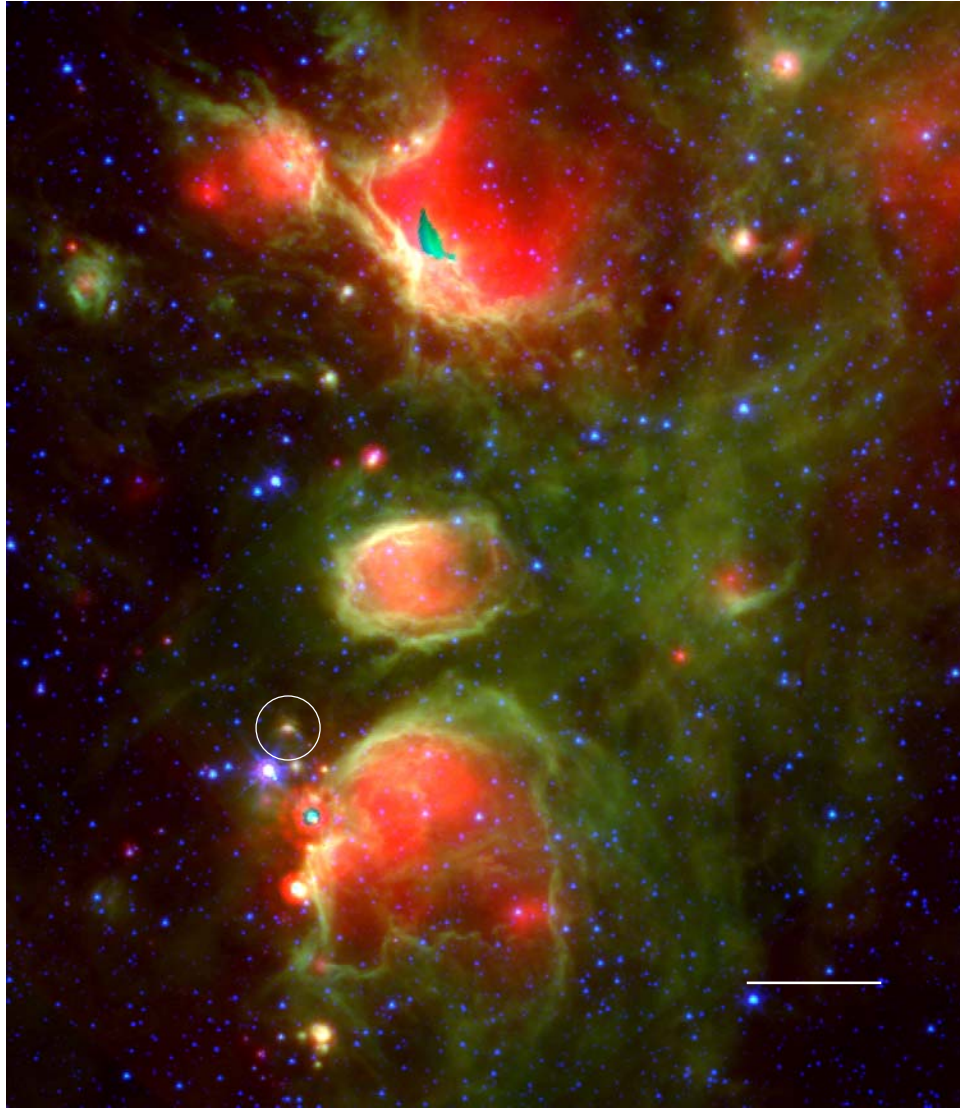
(a)
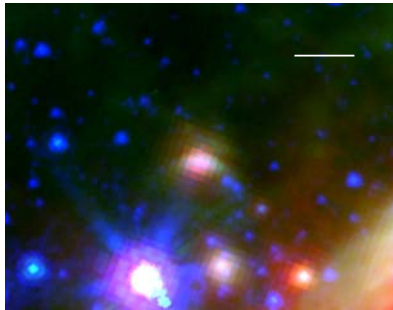
(b)

Figure 6.12: Three colour images of the disk candidate object A - IRAC band 2 (3.6 μm) in blue, IRAC band 4 (8 μm) in green and MIPS 24 μm in red. (a) shows the field surrounding object A while (b) is a close-up of object A. Scale bars are 2 arcmin in (a) and 20 arcsec in (b). Significant emission at 24 μm is evident from the object and throughout the larger field. Images are aligned in ra and dec.

CHAPTER 7

SUMMARY OF OBSERVATIONS & MODELLING

- Past, Present & Future

7.1 Observations

When disks were first hypothesised to exist in young star systems and for many years subsequently all the information on these systems was indirect i.e. from interpreting SEDs and accretion diagnostics such as inverse P-Cygni lines. Technology was not advanced enough to image these objects. In many cases the stars of many disk+star systems were imaged, but it was not possible to directly image the disk that compared to the illuminating star is very faint in the OIR, the wavelengths which most early surveys targeted. Although theoretical modelling made great leaps and bounds by suggesting the presence of a disk could tie together many indirect observations such as IR excesses, UV veiling and variability, images were needed to conclusively prove they existed.

For T-Tauri stars the major breakthrough came with the launch of the HST which produced the first images of disks in T-Tauri systems. Space based technology would appear to have a natural advantage over ground-based as it avoids the interference effects of the atmosphere, however adaptive optics are now being used to great affect to study disk systems. It is now thought disks are common place in a wide variety of pre-main sequence objects.

Disks around pre-main sequence objects are of interest primarily because they are one of the likely sites of planet formation and are key to the star formation process. To understand whether this is likely to be the case requires an understanding of disk evolution. Although many disk models already exist, statistically the sample for which there is enough information to create meaningful models is small. More data from observations are required.

The *Spitzer* Space Telescope, launched in August 2003 has already produced a wealth of data in the 3.5-180 microns range and will potentially do so for a further 1-2 years. On board it has 3 instruments the Infrared Array Camera (IRAC), Multiband Imaging Photometer (MIPS) and Infrared Spectrograph (IRS). Key goals of *Spitzer* include the study of protoplanetary disk structure from SEDs and composition from spectra, and the accumulation of a statistically significant number of disk observations for the study of disk evolution, observations of Brown Dwarfs, and observations of high mass star formation regions.

Within the next decade a number of further missions are planned that may produce IR observations useful for studying disks, most notably The James Webb Telescope (JWST) which will provide near-mid IR imaging and spectroscopy (see Gardner et al. (2006) for overview). Due for launch in 2013, a key goal of the JWST is to study the birth of stars and protoplanetary systems.

As discussed in Chapters 3, 5 and 6 millimetre measurements are also required in order to study disk properties such as disk mass, surface density, grain growth and velocity structure, and to discriminate between the flared disk models and alternative flat disk models. Millimetre imaging is also important for disk systems that are not favourably inclined or seen in silhouette. Some such images already exist however they are of low-resolution. Images would also confirm the disk structure and show how extensive the disks are, something that is difficult from the SED alone

A main scientific aim of the Atacama Large Millimetre Array (ALMA) will be the study of the formation of stars and planetary systems which naturally includes the protostellar disk phase. As well as millimetre measurements for a wide range of objects including low luminosity Brown Dwarfs, ALMA will be able to provide high precision images of disks with an angular resolution up to 5 milliarcseconds (Wilson et al. 2005) which is more than 10 times the resolution of HST and a dramatic improvement over what is currently available in the millimetre. Currently $\sim$0.1 arcsec resolution can be obtained with the best millimetre arrays e.g. CARMA, VLA. ALMA is due to be completed in 2012.

It is suggested in Chapter 4 Sect. 4.3.4 that a gas disk can make a significant contribution to the near-IR emission if the inner dust radius is large. There are a number of further reasons why the gas content of disks is of interest. The gas (and dust) in the inner disk <10 AU likely constitutes the materials from which planets form and the lifetime of gas in the inner disk places an upper limit on the timescale for giant planet formation (Zuckerman et al. 1995). There is also a suggestion that the evolution of gaseous inner disks may effect the efficiency of orbital migration and the eccentricity evolution of giant

and terrestrial planets (e.g. Ida & Lin 2004) and that the timing of the dissipation of the inner disk sets the final orbital radius of the planet (Trilling et al. 2002). Thus estimating how inner disks dissipate may impact on the understanding of the origin of planetary orbital radii. Residual gas in the terrestrial planet region may also play a role in defining final masses and eccentricities of terrestrial planets. Studies of inner gas disks also offer opportunities to probe the nature of the accretion process.

Despite gas making up the majority of mass in the disk it is effectively ignored in most models. That is the dust and gas in the disk are considered to be well mixed and the gas temperature in the disk is assumed to be equal to the local dust temperature. These assumptions follow from the generalisation that dust grains are the main opacity source in disks as they absorb radiation more efficiently than gas. This simplification, that the gas temperature will equal the dust temperature, is likely to be true in optically thick regions, but not in optically thin regions such as the surface layers of disks or inner holes where the gas will thermally decouple from the dust. Also in very hot regions dust will be destroyed, but gas may remain. The first models that attempt to characterize the gas temperature structure of the gas disk have only recently been published (Jonkheid et al. 2004; Kamp & Dullemond 2004; Nomura & Millar 2005).

The temperature of the gas disk depends on various heating and cooling processes which depend on the gas composition. To carry out accurate radiation transfer including the gas disk therefore requires knowledge of the density and chemical constituents of the gas disk as a function of radius. This requires high resolution spectroscopy that can spectrally resolve gas emission lines. Individual emission lines provide kinematic information by which emission regions can be spatially resolved.

A ground-based development due for completion in 2012 is the 30 m Giant Segmented Mirror Telescope (GSMT). A particular feature of the GSMT useful for the study of disks will be its high resolution spectroscopy capabilities in the near-mid IR. GSMT will be able to resolve gas emission lines and study the spatial structure of gas within the inner regions of disks. This will complement ALMA, which should be able to study the spatial structure of gas on scales greater than 10 AU. GMST and ALMA will extend current studies of gas emission that have at their disposal the near-IR Spectrograph NIRSPEC on the Keck II Telescope (e.g. Najita et al. 2003), GEMINI North Michelle mid-IR spectrometer (de Buizer & Fisher 2005), GEMINI South Pheonix near-IR spectrometer (Schommer et al. 2001) and the recently available GEMINI North TEXES mid-IR spectrograph, previously TEXES/IRTF (Richter et al. 2005). Work to date concentrates on the most abundant molecules e.g. H_2, CO, H_2O. Ideally want velocity resolved measurements of numerous molecular and atomic transitions. The hope is that this information can ultimately be

used to study the mass evolution of the gas disk.

7.2   Modelling

Building on from the first theoretical SED models of flared disks (Kenyon & Hartmann 1987), there have been increasingly sophisticated techniques to study the disk temperature structure and emergent spectra. Models by Calvet et al. (1991) showed the temperature inversion that occurs in the disk where the upper layers, that are heated by starlight, are warmer than the disk interior. Their radiation transfer in the disk is 1-D in the vertical direction and they treat the disk as a series of plane parallel annuli. This approach was extended to calculate the structure of steady accretion disks by D'Alessio et al. (1998; 1999a; 2001). The hot upper layers of the disk and cooler interior were incorporated into the two layer model of Chiang & Goldreich (1997; 1999). 2-D radiation transfer techniques for disk models include Monte Carlo (Wood et al. 2002a,b; Whitney et al. 2003a; Wolf 2001; Kurosawa et al. 2004; Dominik & Dullemond 2004b), and traditional radiation transfer techniques (Nomura 2004; Steinacker et al. 2004; Dullemond 2002).

The code presented here has been developed so that it can be applied to the increasing number of systems now thought to have disks. The foundation on which this code is built has evolved over the last fifteen years starting from the scattered light models of protostellar disks and envelopes of Whitney & Hartmann (1992). The main developments have been a radiative equilibrium techniques that solves for the dust temperature structure and emergent multi-wavelength images and spectra (Bjorkman & Wood 2001), calculations in a general three dimensional grid (Whitney et al. 2003a), the inclusion of a diffusion approximation for the most dense regions toward the disk mid-plane Bjorkman et al. (2003), and more recently the self-consistent determination of the structure of disks that are in vertical hydrostatic equilibrium (Walker et al. 2004). The code includes multiple anisotropic scattering and conserves flux exactly. The original Bjorkman & Wood (2001) technique calculated the temperature based on the number of photons absorbed in a given grid cell. The code has been updated as described in Walker et al. (2004) to also calculate temperatures using the path-length formula (Lucy 1999) for determining mean intensities and absorbed energy. The path-length technique provides higher signal-to-noise in the temperature determination and allows for temperature calculations in very optically thin cells. Emission from accretion can also be included in models (Wood et al. 2000; Akeson et al. 2005).

As increasing observations are made, this code could be used in its current form to model systems of different ages and masses helping to build up a picture of disk evolution.

There are, however, a number of improvements that could be made to the code. Following on from the study of Brown Dwarfs in Chapter 3 and of grain growth and dust settling in Chapter 5, an obvious addition would be a more complete treatment of multiple dust species within the models. Following on from Chapter 4 improvements that could be made to the code are shock emission from hot spots on star instead of uniform illumination and a more detailed treatment of the gas disk which should become possible as high resolution spectroscopy in the near-mid IR becomes increasingly available. Following on from the study in Chapter 6 PAH transient heating is currently being incorporated into the Monte Carlo radiation transfer code for use when studying higher luminosity systems.

GLOSSARY

ABSORPTION

The process by which the energy of a photon is taken up by another entity.

ACCRETION

An increase in the mass of a celestial object by the accumulation of surrounding interstellar gases, dust and larger objects by gravity.

ACTIVE DISK

A circumstellar disk where, in addition to heating due to illumination from the central star, significant heating is present due to viscous dissipation (accretion).

ADAPTIVE MESH REFINEMENT (amr)

A technique that allows higher spatial resolution in regions of interest and lower resolution on others. In TORUS this takes the form of cubes that may be split into 8 smaller cubes which in turn my be split into 8 further cubes and so on. The amr is detailed in (Symington 2004).

ADAPTIVE OPTICS

An optical system, usually modular based, which alters its shape and/or properties to compensate for optical effects introduced by the medium between the object and its image.

ALBEDO

The albedo of an object is a number between 0 and 1 that indicates the fraction of light that is reflected/scattered by the medium. Therefore, it represents probability of scattering.

ANGULAR MOMENTUM

A measure of the extent and direction of an object's rotation.

ANGULAR PHASE FUNCTION

This describes the probability of a 'particle' moving in a particular direction following a scattering event.

ANGULAR VELOCITY

A measure of the speed and direction of rotation.

AROMATIC RINGS

These are compounds that consist of carbon and hydrogen, which exist in a conjugated ring(s) that exhibit a high degree of stabilization. Polycyclic aromatic compounds are chemical compounds that contain at least three fused aromatic rings.

ASTEROIDS

Small rocky/metallic celestial bodies that drift in the solar system in orbit around the Sun.

ASTROMETRY

The measurement of the positions and motions of celestial bodies.

BLACKBODY

An object that absorbs all electromagnetic radiation that falls onto it. No radiation passes through it and none is reflected, yet it theoretically radiates every possible wavelength of energy.

BLACK DWARF

A white dwarf that has cooled down to a point where it emits negligible heat and light.

BROWN DWARF

A substellar ($\sim$0.013-0.09$M_\odot$) object that fails to sustain hydrogen burning, but may experience a short phase of deuterium and lithium burning. They are fully convective with no significant chemical differentiation with depth.

CENTRIFUGAL BARRIER

The point at which centrifugal and gravitational forces balance.

χ^2

Chi square is a non-parametric test of statistical significance that indicates the degree of confidence in accepting or rejecting an hypothesis. It is calculated by summing the square of the difference between observed and expected values divided by the expected value.

CIRCUMSTELLAR DISK

A general term that refers to disk of gas and dust around central condensations.

CLASS 0

The stage where a protostar is still deeply embedded in its parent cloud.

CLASS I

The stage where a protostar still has an envelope of material accreting onto it, but this envelope is gradually being cleared away due to winds and jets.

CLASS II

The stage where most parent material will have accreted onto the star or be in the process of accreting from a shrinking disk.

CLASS III

The stage where a star is highly visible in the optical region.

CLASSICAL T-TAURI STARS (CTTs)

T-Tauri stars characterized by both UV and IR excesses relative to a main sequence star of the same effective temperature. This excess is usually attributed to the presence of a protoplanetary disk.

COLOURS

This refers to flux ratios which are defined by subtracting the magnitudes in different filter bands.

CONTINUUM

This refers to the combination of all colours that an object such as the Sun emits, and also to the broad variation from colour to colour in how much light is emitted which is determined mostly by the temperature of the object.

CONVECTIVE

The transfer of potential energy by currents within liquids and gases.

CONVOLUTION

The integral of the product of the two functions after one is reversed and shifted.

CORONOGRAPHIC TECHNIQUES

Using an aperture to block out a bright region within a field of view in order to observe surrounding less bright regions.

CO-ROTATION RADIUS

Where the Keplerian angular velocity equals stellar angular velocity.

CUMULATIVE DISTRIBUTION FUNCTION (CDF)

The area under the PDF i.e. the value of the CDF at x is the area under the PDF up to x.

DEBRIS DISK

An optically thin gas-poor dust disk around main sequence stars which is thought to be debris from planet formation.

DECLINATION (dec)

The co-ordinate in the equatorial co-ordinate system in the sky that is similar to latitude on Earth. It ranges between -90 degrees at the southern celestial pole and +90 degrees at the northern celestial pole and is zero at the celestial equator.

DECONVOLUTION

A process used to reverse the effects of convolution on recorded data.

DEUTERIUM

A stable isotope of hydrogen, with a nucleus containing one proton and one neutron.

ELECTROMAGNETIC RADIATION

Self-propagating waves in space with electric and magnetic components. Electromagnetic radiation is classified into types according to the frequency of the wave: these types include, in order of increasing frequency, radio waves, microwaves, infrared radiation, visible light, ultraviolet radiation, X-rays and gamma rays.

EMISSIVITY

The ratio of energy radiated by an object to energy radiated by a black body at the same temperature. It is a measure of a material's ability to absorb and radiate energy.

EQUATORIAL CO-ORDINATES

Co-ordinates of objects in the sky relative to the celestial equator. The co-ordinates are: right ascension and declination.

EXTINCTION

A term used to describe the absorption and scattering of light emitted by astronomical objects by matter (principally dust and gas) between the emitting object and the observer.

FLUX

The rate of energy flow across unit surface area per unit time per unit frequency interval.

FORBIDDEN EMISSION LINES

Spectral lines emitted by atoms undergoing energy transitions not normally allowed by the selection rules of quantum mechanics.

FOURIER TRANSFORM

An image processing tool which is used to decompose an image into its sine and cosine components. The output of the transformation represents the image in the Fourier or frequency domain (u-v space), while the input image is the spatial domain equivalent. In the Fourier domain image, each point represents a particular frequency contained in the spatial domain image and changes in image position correspond to changes in the spatial frequency (or the rate at which image intensity values are changing in the spatial domain image).

FREE-FALL TIME

The characteristic time it would take a body to collapse under its own gravitational attraction, if no other forces existed to oppose the collapse.

FRINGE VISIBILITIES

An interferometer measures components of the visibility function by forming interference fringes between the apertures. The contrast and phase of these fringes give the amplitude and phase of the visibility function, respectively.

FROZEN ICES

The freeze out of gases forms ice coatings on dust grains.

FULL WIDTH HALF MAXIMUM

A term used to describe the extent of a function, given by the difference between the two extreme values of the independent variable at which the dependent variable is equal to half of its maximum value. Often used as a measurement of the width of an object in a picture, when that object does not have sharp edges.

FU ORI

A young pre-main sequence star which displays an extreme change in magnitude and spectral type due to high accretion flares.

GRAVITATIONAL POTENTIAL ENERGY

The energy per unit mass of an object due to its position in a gravitational field. This is usually defined as zero at infinity and is therefore more negative the closer the object is to the centre of the potential well.

GROUP 1 HERBIG

A Herbig Ae/Be star whose spectrum is almost flat in the mid-IR.

GROUP II HERBIG

A Herbig Ae/Be star whose spectrum steadily declines toward the far-IR.

HERBIG Ae/Be

An intermediate mass pre-main sequence object of spectral type A/B, characterized by emission lines in the Balmer series of Hydrogen.

HERBIG HARO (HH)

These are shocks which form as a jet propagates through its parent cloud, observable because as the post-shock gas cools it radiates.

HYDROSTATIC EQUILIBRIUM

When pressure and gravitational forces balance.

INFRARED (IR)

Wavelengths between approximately 0.7μm and 350μm subdivided into near-IR (0.7-1 to 5μm), mid-IR (5 to 25-40μm) and far-IR (25-40 to 200-350μm).

ISOTROPIC

A variable that is independent of direction.

JEANS MASS

The minimum mass for a cloud of given density and temperature to contract due to gravity.

JITTER

An abrupt and unwanted variation of one or more signal characteristics.

LUMINOSITY

The integral of the flux over area of emission.

MAGNETIC TRUNCATION RADIUS

For a significantly strong magnetic field (kG), there should be a radius in the disk at which the ram pressure of the accreting material is offset by the magnetic pressure. Where the two pressures are equal, if the accreting material is sufficiently ionized, its motion will start to be controlled by the stellar field. This is referred to as the magnetic truncation radius.

MAGNITUDE

A photometric measurement related to the flux by magnitude = -2.5 log (flux/0th magnitude flux for given filter). Bright objects have more negative magnitudes than faint objects.

MAIN SEQUENCE

The region on the Hertzsprung-Russell diagram occupied by stars burning hydrogen into helium in their cores.

MEAN FREE PATH

The average distance a particle travels between collisions with other particles.

MEAN INTENSITY

The specific intensity averaged over all angles.

MINIMUM MASS SOLAR NEBULA

A hypothetical minimum mass for the nebula from which our own star and solar system formed. This mass is arrived at by taking the known masses and compositions of the planets and adding whatever missing elements are needed to make them have the same relative abundances as the Sun.

MOLECULAR CLOUD

An interstellar cloud whose high density and low temperature permits the formation of molecules, H_2, He and many more. Molecular clouds typically have masses of $100 - 10^6 M_\odot$, cloud with masses greater than $10^3 M_\odot$ are often called giant molecular clouds.

MONOCHROMATIC

Consisting of a single wavelength or narrow band approximating a single wavelength.

MONTE CARLO

This refers to a simulation that utilizes sequences of random numbers.

NUCLEAR FUSION

The process by which multiple light nuclei overcome their mutual electrostatic repulsion and join together to form a heavier nucleus.

NUMBER DENSITY

The number of objects (e.g. particles) per unit volume.

OBSCURED SOURCE

This is defined here as a source whose near-IR flux is at least three magnitudes fainter than the corresponding face-on source.

OPACITY

The degree to which material is impenetrable to radiation.

OPTICAL

Electromagnetic radiation with wavelengths from ~ 0.380 to 0.7μm.

OPTICAL DEPTH

A measure of transparency or transmission, τ, of a material, defined as the negative natural logarithm of the transmission.

OPTICALLY THICK

This means that the optical depth is high i.e. most transiting light is attenuated.

OPTICALLY THIN

This means that the optical depth is small i.e. very little material is present and most transiting light can pass through unimpeded.

PASSIVE DISK

This refers to a circumstellar disk where all heating is assumed to be due to the central star.

P-CYGNI PROFILES

A spectroscopic feature characterized by strong emission lines with corresponding blue-shifted absorption lines. The latter are produced by material moving away from the star and toward us, whereas the emission comes from other parts of the expanding shell. Inverse P-Cygni profiles where the emission lines lie on the blue side of the absorption component are usually interpreted to mean an infall of matter.

PHOTO-DISSOCIATION REGION

Interstellar regions where UV radiation dominates the energetics and chemistry of the neutral gas.

PHOTO-EROSION

In the context used here this refers to the 'eating away' of a protostar due to ionization e.g. from a HII region.

PHOTOPOLARIMETRIC MODELLING

The modelling of photometry (the measurement of the flux or intensity of an object's electromagnetic radiation) and polarimetry (measurement of the polarisation of light) observations.

PHOTON PACKETS

Groups of photons that have the same energy but contain varying quantities of photons depending on frequency.

PLANETARY NEBULA

A glowing shell of gas and plasma formed by certain types of stars at the end of their lives when a star can no longer support itself by nuclear fusion.

PLANETESSIMALS

Small bodies that orbit in a protoplanetary disk that could potentially form planets.

POINT SPREAD FUNCTION (PSF)

The blurred light distribution of a point after passing through a lens.

POLARISATION

This is the property of electromagnetic waves that describes the direction of oscillation of their transverse electric field. More generally, the polarization of a transverse wave describes the direction of oscillation in the plane perpendicular to the direction of travel.

POPULATIONS I AND II

A division of the stars on basis of age. Population I stars are younger and generally hotter and bluer than population II stars.

POSITION ANGLE

The angle on the sky between two objects or two components of a single object. It is normally measured North - East and South - West, from 0 to 360°. With regard to disks, the position angle refers to the angle between the disk major axis and North.

PRE-STELLAR PHASE

This is used here to describe a T-Tauri-like phase and is the stage at which a protostar becomes optically visible and is accreting primarily from a disk.

PROBABILITY DISTRIBUTION FUNCTION (PDF)

A function that describes the likelihood a parameter will have a certain value.

PROTOPLANETARY DISK

A rotating disk of dense gas and dust surrounding a young, newly-forming star which may contain planetessimals, the building blocks of planets.

PROTOSTELLAR/PROTOSTAR

A condensation still in the process of accreting matter to form a star.

RADIATIVE EQUILIBRIUM

When radiative emission is balanced by radiative absorption.

RADIATION PRESSURE

The pressure exerted upon any surface exposed to incident electromagnetic radiation.

RADIATION TRANSFER

The study of the interaction between radiation and the matter it transits.

RADIATIVE TRANSFER

The propagation of radiation through an atmosphere which is itself emitting, absorbing and scattering radiation.

RAM PRESSURE

The pressure exerted on a body which is moving through a fluid medium due to the drag force.

REDDENING

A phenomenon associated with interstellar extinction where the spectrum of electromagnetic radiation from a radiating source changes characteristics from that which was emitted due to shorter wavelength photons being preferentially removed from the radiated spectrum.

REFLECTION NEBULA

Clouds of dust which reflect the light of a nearby star or stars, but are not ionized by the star(s), as is the case for an emission nebula.

RETROGRADE

Describes the motion of a body moving backward relative to other bodies within the system.

RIGHT ASCENSION (RA)

The co-ordinate in the equatorial coordinate system in the sky that is similar to longitude on Earth.

R_v

The slope of the extinction curve.

SCALEHEIGHT

The distance over which a quantity decreases by a factor of e.

SCATTERING

The physical process whereby some forms of radiation, such as light or moving particles, for example, are forced to deviate from a straight trajectory by one or more localized non-uniformities in the medium through which it passes.

SMOOTH PARTICLE HYDRODYNAMICS (SPH)

A computational method used for simulating fluid flows.

SNOW-LINE

The minimum radius at which ice exists.

SPECIFIC INTENSITY

The radiant energy passing through a unit surface area at an angle to the surface normal within a solid angle, in a frequency range and over a set time.

SPECKLE INTERFEROMETRY

An interferometric method for speckle imaging, which is the technique of taking very short exposure images of astronomical targets, and then processing the images so as to remove the effects of astronomical seeing.

SPECTROSCOPY

This is the study of spectra. Most large telescopes have spectrographs, which are used either to measure the chemical composition and physical properties of astronomical objects or to measure their velocities from the Doppler shift of spectral lines.

STARS

Objects that undergo sustained nuclear fusion after condensing from a molecular cloud to the point where gravitational forces are balanced by internal support e.g. radiation pressure, centrifugal forces, magnetic pressure.

STOCHASTICALLY

By way of a method involving chance or probability.

SUBLIMATION

The conversion of a substance between the solid and the gas phases.

SURFACE BRIGHTNESS

Flux density per unit solid angle.

SURFACE DENSITY

The integral of density over the path to the surface.

T-TAURI STARS

Young pre-main sequence objects thought to be progenitors of sun-like stars which are characterized by the presence of Balmer lines, Ca H and K lines in emission, a photospheric absorption spectra suggestive of late F type or later main sequence stars, and variability that occurs over a wide range of timescales from minutes to at least a century and can be quasi-periodic or highly irregular. T-Tauri stars are classified as either 'Weak Line T-Tauri stars' (WTTs) or 'Classical T-Tauri stars' (CTTs).

TURBULENT FRAGMENTATION

The process by which turbulent velocities compress gas in shocks, which generates structure over a wide range of sizes and densities.

ULTRAVIOLET (UV)

Electromagnetic radiation with wavelengths $\sim 0.001\text{-}0.38\mu$m.

U-V SPACE

see Fourier Transform

VAN CITTERT-ZERNIKE THEOREM

The normalized degree of spatial coherence is the Fourier transform of the intensity distribution for uncorrelated emitters.

VEILING

This term normally refers to optical/UV continuum excesses.

VISCOSITY

A measure of the resistance of a fluid to deform under shear stress.

WEAK LINE T-TAURI STARS (WTTs)

T-Tauri stars that display no UV excess, little or no IR excess and show very weak, if any, emission lines. They are thought to be more evolved than CTTs with little or no disk remaining.

WHITE DWARF

A dense, compact object that is produced when a low or medium mass suffers runaway gravitational collapse at the end of its lifetime.

ZERO AGE MAIN SEQUENCE

The position on the Hertzsprung-Russell diagram of a star that has just reached the main sequence, when it has reached hydrostatic equilibrium and thermonuclear reactions have begun in its core.

ABBREVIATIONS

ALMA	Atacama Large Millimetre Array
amr	adaptive mesh refinement
AU	Astronomical Unit 1 AU=1.496 $\times 10^{11}$ metres
CARMA	The Combined Array for Research in Millimetre-wave Astronomy
CDF	Cumulative Distribution Function
CLIRCAM	Claremont-Riverside-Infrared Camera
CO	Carbon Monoxide
CTTs	Classical T-Tauri stars
dec	declination
dof	degrees of freedom
GLIMPSE	*Spitzer* Space Telescope Galactic Legacy Infrared Midplane Survey Extraordinaire
GMST	Giant Segmented Mirror Telescope
H_2	Molecular Hydrogen
H_2O	Water
HH	Herbig-Haro
HH30	Grain distribution from Wood et al. (2002a)
HST	Hubble Space Telescope
IMF	Initial Mass Function
IR	Infrared
IRAC	Infrared Array Camera
IRAS	Infrared Astronomical Satellite
IRS	Infrared Spectrograph
ISM	Interstellar Medium
ISO	Infrared Space Observatory
JWST	The James Webb Telescope
KMH	ISM-like grains from Kim et al. (1994)
MIPS	Multiband Imaging Photometer
MIPSGAL	Multiband Imaging Photometer Inner Galactic Plane *Spitzer* survey
MRN	ISM-like grain distribution of Mathis et al. (1977)
NICMOS	Near-IR Camera and Multi-Object Spectrometer on HST
NIRSPEC	Near-IR Spectrograph on the Keck II Telescope
NRO/NMA	Nobeyama Millimeter Array
OIR	Optical and Infrared
PAH	Polycyclic Aromatic Hydrocarbons
PDF	Probability Distribution/Density Function
ppm	parts per million

PSF	Point Spread Function
PTI	Palomar Testbed interferometer
RA	Right Ascension
RADMC	2-D Monte-Carlo radiative transfer code for circumstellar disks and envelopes
SED	Spectral Energy Distribution
SPH	Smooth Particle Hydrodynamics
TORUS	A Monte-Carlo radiative-transfer code that is designed to compute polarization images and spectra from a three-dimensional opacity grid.
2MASS	Two Micron All-Sky Survey
UIBs	Unidentified Infrared Bands
UKIRT	United Kingdom Infrared Telescope
UV	Ultraviolet
VET	Variable Eddington Tensor
VLA	Very Large Array
WTTs	Weak Line T-Tauri stars
IRTF	NASA's Infrared Telescope Facility

Acke, B., & van den Ancker, M. E., 2004, *A&A*, 426, 151

Acke, B., van den Ancker, M. E., Dullemond, C. P., van Boekel, R., & Waters, L. B. F. M., 2004, *A&A*, 422, 621

Adams, F. C., Lada, C. J., & Shu, F. H., 1987, *ApJ*, 312, 788

Adams, F. C., & Shu, F. H., 1986, *ApJ*, 308, 836

Akeson, R. L., Ciardi, D. R.,van Belle, G. T., Creech-Eakman, M. J., & Lada, E. A., 2000, *ApJ*, 543, 313

Akeson, R. L., Ciardi, D. R., van Belle, G. T., & Creech-Eakman, M. J., 2002, *ApJ*, 566, 1124

Akeson, R. L., et al., 2005, *ApJ*, 622, 440

Allamandola, L. J., 1984, in *Galactic and Extragalactic IR Spectroscopy*, Ed. M. F. Kessler, J. P. Phillips, Reidel, Dordrecht

Allamandola, L. J., Teilens, A. G., Barker, J. R., 1985, *ApJL*, 290, L25

Allamandola, L. J., Tielens, A. G., & Barker, J. R., 1989, *ApJS*, 71, 733

Allard, F., Hauschildt, P.H., Alexander, D.R., Tamanai, A., & Schweitzer, A., 2001, *ApJ*, 556, 357

André Ward-Thompson, D., & Barsony, M., 1993, *ApJ*, 406, 122

Andriesse, C. D., 1978, *A&A*, 66, 169

Apai, D., Pascucci, I., Henning, Th., Sterzik, M.F., Klein, R., Semenov, D., Gunther, E., & Sterzik, B., 2002, *ApJ*, 573, L115

Appenzeller, I. & Mundt, R., 1989, *A&ARv*, 1, 291

Appenzeller, I., Oestreicher, R. & Jankovics, I., 1984, *A&A*, 141, 108

Ardilla, D., Martín, E., & Basri, G., 2000, *AJ*, 120, 479

Ardila D.R., et al., 2004, *ApJ*, 617, L147

Aspin, C., Sandell, G., & Russel, A. P. G., 1994, *A&AS*, 106, 165

Aumann, H. H., 1984, *BAAS*, 16, 483

Avedisova, V. S., 2002, *ARep*, 46, 193

Bachiller, R. 1996, *ARA&A*, 34, 111

Baes, M, et al., 2005, *New Astronomy*, 10, 523

Bally, J., O'Dell, C.R., & McCaughrean, M.J., 2000, *AJ*, 119, 2919

Baraffe, I., Chabrier, G., Allard, F., & Hauschildt, P.H., 2002, *A&A*, 382, 563

Barsony, M., Kenyon, S.J., Lada, E.A., & Teuban, P.J., 1997, *ApJS*, 112, 109

Basri, G.,& Bertout, C., 1989, *ApJ*, 341, 340

Bate, M.R., Bonnell, I.A., & Bromm, V., 2003, *MNRAS*, 339, 577

Becker, W., & Fenkart, R., 1970, in *The Spiral Structure of our galaxy*, IAU *symp.* No 38. Ed. W. Becker and G. Contopoulos, 205

Beech, M., Mitalas, R., 1994, textitApJS, 95, 517

Beckwith, S. V. W., Henning, T., & Nakagawa, Y. 2000, in *Protostars & Planets IV*, Ed. V. Mannings, A. P. Boss, & S. S. Russell (University of Arizona Press, Tucson), 533

Beckwith, S.V.W., & Sargent, A.I., 1991, *ApJ*, 381, 205

Beckwith, S. V. W., Sargent, A. I., Chini, R. S., & Guesten, R., 1990, *AJ*, 99, 924

Beichman, C. A., et al.,1986, *ApJ*, 307,337

Bell, K. R., Cassen, P. M., Klahr, H. H., & Henning, Th., 1997, *ApJ*, 486, 372

Bell, K. R., & Lin, D. N. C., 1994, *ApJ*, 427, 987

Bell K. R., Lin, D. N. C., Hartmann, L. W., & Kenyon, S. J., 1995, *ApJ*, 444, 376

Beltrán, M. T., Cesaroni, R., Neri, R., Codella, C., Furuya, R. S., Benjamin, R. A., et al., 2003, *PASP*, 115, 953

Bertout, C., 1989, *ARA&A*, 27, 351

Bertout, C., Basri, G., & Bouvier, J., 1988, *ApJ*, 330, 350

Bessell, M.S., & Brett, J.M., 1988, *PASP*, 100, 1134

Beuther, H., Zhang, Q., Sridharan, T. K., & Chen, Y., 2005, *ApJ*, 628, 800

Bjorkman, J. E., Whitney, B. A., & Wood, K., 2002, *BAAS*, 34, 1185

Bjorkman, J.E., & Wood, K., 2001, *ApJ*, 554, 615

Boden, A. F., Colavita, M. M., van Belle, G. T., & Shao, M., 1998, *SPIE Proc.*, 3350, 872

Bonnell, I. A., Bate, M. R., & Zinneker, H., 1998, *MNRAS*, 298, 93

Bontemps, S., André, P., & Kaas, A.A., et al., 2001, *A&A*, 372, 173

Born, M.,& Wolf, E., 1999, in *Principles of Optics* (7th ed.; Cambridge: Cambridge Univ. Press)

Bouvier, J., Cabrit, S., Fernández, M., Martin, E. L., & Matthews, J. M., 1993a, *A&A*, 272, 176

Bouvier, J., Cabrit, S., Fernández, M., Martin, E. L. & Matthews, J. M., 1993b, *A&A*, 61, 737

Bouvier, J., Stauffer, J. R., Martin, E. L., Barrado y Navascues, D., Wallace, B., & Bejar, V. J. S., 1998, *A&A*, 336, 490

Bouvier, J., et al., 1999, *A&A*, 349, 619

Bouvier, J., et al., 2003, *A&A*, 409, 169

Bouy, H., Brandner, W., Martín, E. L., Delfosse, X., Allard, F., & Basri, G., 2003, *Proc. of* IAU *symp.* No. 211, Ed. E. Martín. (San Francisco: Astronomical Society of the Pacific), 245

Bronfman, L., Nyman, L.-Å., & May, J. 1996, *A&AS*, 115, 81

Bryden, G., et al., 2004, *BAAS*, 36, 1554

Burrows, C. J., et al. 1996, *ApJ*, 473, 437

Cabrit, S., Edwards, S., Strom, S. E., & Strom, K. M., 1990, *ApJ*, 354, 687

Calvet, N., Hartmann, L., & Strom, S. E., 1997, *ApJ*, 481, 912

Calvet, N., Hartmann, L., & Strom, S.E., 2000, in *Protostars and Planets IV*, Ed. V. Mannings, A. P. Boss, & S. S. Russell (Tucson: Univ. Arizona Press), 377

Calvet, N. & Gullbring, E., 1998, *ApJ*, 509, 802

Calvet, N., Muzerolle, J., Briceño, C., Hernández, J., Hartmann, L., Saucedo, J. L., & Gordon, K. D., 2004, *AJ*, 128, 1294

Carey, S. J., et al., 2005, *BAAS*, 37, 1252

Cardelli, J.A., Clayton, G.C., & Mathis, J.S., 1989, *ApJ*, 345, 245

Carpenter, J. M., 2001, *AJ*, 121, 2851

Camenzind, M., 1990, *RvMA*, 3, 234

Cassen, P., & Moosman, A. 1981, *Icarus*, 48, 353

Cesaroni, R., Felli, M., Testi, L., Walmsley, C. M., & Olmi, L., 1997, *A&A*, 325, 725

Cesaroni, R., Neri, R., Olmi, L., Walmsley, C., & Hofner, P. 2005, *A&A*, 434, 1039

Chabrier, G., & Baraffe, I., 1997, *A&A*, 327, 1039

Chandrasekhar, S., & Fermi, E., 1953, *ApJ*, 118, 116

Chen, C. H., & Jura, M., 2003, *ApJ*, 591, 267

Chiang, E. I., & Goldreich, P. 1997, *ApJ*, 490, 368

—————1999, *ApJ*, 519, 279

Chiang E. I., Joung M. K., Creech-Eakman M. J., Qi C., Kessler J. E., Blake G. A., & van Dishoeck E. F., 2001, *ApJ*, 547, 1077

Choi, P.I. & Herbst, W., 1996, *AJ*, 111, 283

Clarke, C. J., Lin, D. N. C., & Pringle, J. E., 1990, *MNRAS*, 242, 439

Code, A. D., & Whitney, B. A., 1995, *ApJ*, 441, 400

Cohen, M. & Kuhi, L. V., 1979, *ApJ*S, 41, 743

Cohen, M., et al., 1986, *ApJ*, 302, 737

Colavita M. M. et al 1999, *ApJ*, 510, 505

Comerón, F., Rieke, G.H., Claes, P., Torra, J., & Laureijs, R.J., 1998, *A&A*, 335, 522

Comerón, F., Neuhäuser, R., & Kaas, A.A., 2000, *A&A*, 359, 269

Corcoran, M., & Ray, T. P. 1997, *A&A*, 321, 189

Cotera A. et al., 2001, *ApJ*, 556, 958

Cox, A. N. [Ed.], 2000, *Allen's Astrophysical Quantities* (4th ed.; New York: Springer-Verlag)

Dahn, C. C., et al., 2002, *AJ*, 124, 1170

D'Alessio, P., Cantó, J., Hartmann, L., Calvet, N., & Lizano, S., 1999b, *ApJ*, 511, 896

D'Alessio, P., Calvet, N., & Hartmann, L., 2001, *ApJ*, 553, 321

D'Alessio P., Calvet, N., Hartmann, L., Lizano, S., Cantó, J., 1999a, *ApJ*, 527, 893

D'Alessio, P., Cantó, J., Calvet, N., & Lizano, S., 1998, *ApJ*, 500, 411

D'Alessio, P., Calvet, N., Hartmann, L., Muzerolle, J., & Sitko, M., 2004, *Proc. of* IAU *symp.* No. 221, 403

D'Alessio, P., Merlín, B., Calvet, N., & Hartmann, L., 2005a, *RMxAA*, 41, 61

D'Alessio, P., et al., 2005, *ApJ*, 621, 461

need 2005b Dawkins, R, 2004, In *The Ancestors Tale*, Weidenfeld Nicholson Illustrated, ISBN: 0297825038

de Buizer, J. M., & Fischer, R. S., 2005, in *High Resolution Infrared Spectroscopy in Astronomy: Proc. of an* ESO *Workshop*, Ed. H. U. K:aufl, R. Siebenmorgen, and A. F. M. Moorwood. Springer-Verlag Berlin/Heidelberg, 84

Draine, B. T., 2003, *ARA&A*, 41, 241

Draine, B. T., & Aigen, Li., 2006, *astroph*/0608003

Duchêne, G., McCabe, C., Ghez, A. M., & Macintosh, B. A., 2004, *ApJ*, 606, 969

Dullemond, C. P. 2002, *A&A*, 395, 853

Dullemond, C. P., & Dominik, C., 2004a, *A&A*, 421, 1075

Dullemond, C. P., & Dominik, C., 2004b, *A&A*, 417, 159

—————2005, *A&A*, 434, 971

Dullemond, C. P., Dominik, C., & Natta, A., 2001, *ApJ*, 560, 957

Duschl, W. J., Gail, H. -P., & Tscharnuter, W. M., 1996, *A&A*, 312, 624

Eaton, N. L., Herbst, W. & Hillenbrand, L. A., 1995, *AJ*, 110, 1735

Edwards, S., Cabrit, S., Strom, S. E., Heyer, I., Strom, K. M., & Anderson, E.,1987, *ApJ*, 321, 473

Eiroa, C., et al., 2002, *A&A*, 384, 1038

Eisner, J. A., Lane, B. F., Akeson, R. L., Hillenbrand, L. A., & Sargent, A. I., 2003, *ApJ*, 588, 360

Eisner, J. A., Lane, B. F., Hillenbrand, L. A., Akeson, R. L., & Sargent, A. I., 2004, *ApJ*, 613, 1049

Elias, J. H., 1978, *ApJ*, 224, 857

Elsasser H., & Staude H. J., 1978, *A&A*, 73, L3

Elston, R. J., et al., 2003, *BAAS*, 202, 2809

Fazio, G., et al. 2004, *ApJS*, 154, 10

Folha, D. F. M. & Emerson, J. P., 1999, *A&A*, 352, 517

Forrest, W. J., et al., 2004, *ApJ*S, 154, 443

Fuller, G. A., Williams, S. J., Sridharan, T. K., 2005, *A&A*, 442, 949

Garaud, P., & Lin, D. N. C., *astroph*/0605110

Gardner., J. P., 2006, in *The Scientific Requirements for Extremely Large Telescopes*, IAU *symp.* No. 232, Ed. P. A. Whitelock; M. Dennefeld; B. Leibundgut (Cambridge: Cambridge University Press), 87

Geers, V. C., et al., 2005, *Protostars and Planets V*, LPI Contribution No. 1286, 8409

Ghandour, L., Strom, S. E., Edwards, S., & Hillenbrand, L. A. 1994, *ASPC*, 62, 223

Ghosh, P., & Lamb, F. K., 1979, *ApJ*, 232, 259

Gillett, F. C., Forrest, W. J., & Merrill, K. M., 1973, *ApJ*, 183, 87

Grady, C. A., 2004, *ASPC*, 321, 244

Grady, C. A., et al., 1999, *ApJ*, 523, L151

Grosso, N., Alves, J., Wood, K., Neuhäuser, R., Montmerle, T., Bjorkman, J. E., 2003, *ApJ*, 586, 296

Gullbring, E., Calvet, N., Muzerolle, J., & Hartmann, L., 2000, *ApJ*, 544, 927

Gullbring, E., Hartmann, L., Bricēno, C, & Calvet, N., 1998, *ApJ*, 492, 323

Habart, E., Natta, A., & Krügel, E., 2004, *A&A*, 427, 179

Haisch, K.E., Jr., Lada, E.A., & Lada, C.J. 2000, *AJ*, 120, 1396

Hartigan, P., Edwards, S., & Ghandour, L., 1995, *ApJ*, 452, 736

Hartmann, L., 2003, *ApJ*, 592, 266

Hartmann, L., Calvet, N., Gullbring, E., & D'Alessio, P., 1998, *ApJ*, 495, 385

Hartmann, L., Kenyon, S., & Calvet, N., 1993, *ApJ*, 407, 219

Hauschildt, P. H., Allard, F., & Baron, E., 1999, *ApJ*, 512, 377

Hayashi, C. 1981, *Prog. Theor. Phys. Suppl.*, 70, 35

Henyey, L. G., & Greenstein, J. L., 1941, *ApJ*, 93, 70

Herbig, G. H., 1960, *ApJ*S, 4, 337

Herbig G. H., 1961, *ApJ*, 133 337

Herbig, G. H., 1977, *ApJ*, 217, 693

Herbig, G. H., 1998, *ApJ*, 497, 736

Herbst, W., Herbst, D.K., Grossman, E.J. & Weinstein, D., 1994, *AJ*, 108, 1906

Hester, J. J., et al., 1996, *AJ*, 111, 2349

Hillenbrand, L. A., 1997, *AJ*, 113, 1733

Hillenbrand, L., Strom, S., Vrba, F., & Keene, J., 1992, *ApJ*, 397, 613 Hodapp, K.-W., Capps, R. W., Strom, S. E., Salas, L., & Grasdalen, G. L., 1988, *ApJ*, 335, 814

Hodapp, K.-W., Walker, C. H., Reipurth, B., Wood, K., Bally, J., Whitney, B. A., & Connelley, M., 2004, *ApJ*, 601, L79

Hogerheijde, M. 1998, *Ph.D. thesis*, Univ. Leiden

Hora, J. L., et al. 2004, *Proc. SPIE*, 5487, 77

Ida, S., & Lin, D. N. C., 2004, *ApJ*, 604, 388

Isella, A., & Natta, A., 2005, *A&A*, 438, 899

Jayawardhana, R., Ardila, D. R., Stelzer, B., & Haisch, K. E. 2003b, *AJ*, 126, 1515

Jayawardhana, R., Luhman, K. L., D'Alessio, P., Stauffer, J. R. 2002, *ApJ*, 571, L51

Jayawardhana, R., Mohanty, S., & Basri, G., 2003a, *ApJ*, 592, 282

Jeans, J. H., 1902, *Phil. Trans. R. Soc. Lond. A*, 199, 1

Jiang, Z., Tamura, M., Fukagawa, M., Hough, J., Lucas, P., Suto, H., Ishii, M., & Yang, J., 2005, *Nature*, 437, 7055, 112

Jonkheid, B., Faas, F. G. A., van Zadelhoff, G.-J., & van Dishoeck, E. F., 2004, *A&A*,

428, 511

Jones, B. F., & Herbig, G. H., 1979, *AJ*, 84, 1872

Jourdain de Muizon, M., d'Hendecourt, L. B., & Geballe, T. R., 1990, *A&A*, 227, 526

Joy, A., 1945, *ApJ*, 102, 168

Kahn, F. D., 1974, *A&A*, 37, 149

Kamp, I., & Dullemond, C. P., 2004, *ApJ*, 615, 991

Kawazoe, E., & Minesshige S., 1993, *PASJ*, 45, 715

Kenyon, S. J., Dobrzycka, D., & Hartmann, L., 1994, *AJ*, 108, 1872

Kenyon, S. J., & Hartmann, L., 1987, *ApJ*, 323, 714

Kenyon, S.J. & Hartmann, L., 1995, *ApJS*, 101 117

Kenyon, S.J., Whitney, B.A., Gómez, M., & Hartmann, L., 1993, *ApJ*, 414, 773

Kenyon, S.J., et al., 1994, *AJ*, 107, 2153

Kim, S.-H., Martin, P. G., & Hendry, P. D. 1994, *ApJ*, 422, 164

Kirkpatrick, J.D., et al., 2000, *AJ*, 120, 447

Kitamura, Y., Momose, M., Yokogawa, S., Kawabe, R., Tamura, M., & Ida, S., 2002, *ApJ*, 581, 357

Klein, R., Apai, D., Pascucci, I., Henning, Th., & Waters, L.B.F.M., 2003, *ApJ*, 593, L57

Klessen, R., 2001, *ASPC*, 243, 139

Kley, W., 1989, *A&A*, 208, 98

Koerner, D.W., 2001, *ASPC*, 231, 563

Koerner, D. W. & Sargent, A. I., 1995, *AJ*, 109, 2138

Koerner, D. W., et al., 1998, *BAAS*, 30, 1363

Königl, A., 1991, *ApJL*, 370, L39

Königl, A., & Ruden, S. P. 1993, in *Protostars and Planets III*, Ed. E. H. Levy & J. I. Lunine (Tucson: Univ. Arizona), 641

Krist J. E., et al., 2005, *AJ*, 129, 1008

Kroupa, P, & Bouvier, J., 2003, *MNRAS*, 346, 369

Krumholz, M. R., McKee, C. F., & Klein, R. I., 2005, *ApJL*, 618, L33

Kuchar, T. A., & Clark, F. O., 1997, *ApJ*, 488, 224

Kumar S. S., 1963, *ApJ*, 137, 1121

Kurucz, R.L., CD-ROM 19, *Solar Abundance Model Atmospheres for 0,1,2,4,8 km/s* (Cambridge:SAO)

Lada C. J., & Adams F. C., 1992, *ApJ*, 393, 278

Lada, C., & Wilking, B., 1984, *ApJ*, 287, 610

Landolt, A. U., 1992, *AJ*, 104, 340

Larson, R. B., 1981, *MNRAS*, 194, 809

Léger, A., & Puget, J. L., 1984, *A&A*, 137, L5

Léger, A., & D'Hendecourt, L., 1987, *Proc. of* IAU *symp.* No 120, Ed. M. S. Vardya and

S. P. Tarafdar (Dordrecht: Reidel), 557

Léger, A., D'Hendecourt, L., & Defourneau, D, 1989, *A&A*, 216, 148

Li, A., & Draine, B. T. 2002, *ApJ*, 572, 232

Li, Z.-Y., & Shu, F. H. 1996, *ApJ*, 472, 211

Lin, D. N. C., Faulkner, J., & Papaloizou, J., 1985, *MNRAS*, 212, 105

Liu, M.C., Najita, J., & Tokunaga, A.T., 2003, *ApJ*, 585, 372

Liu, W. M., Hinz, P. M., Meyer, M. R., Mamajek, E. E., Hoffmann, W. F., & Hora, J. L., 2003, *ApJ*, 598, L111

Liu, W. M., Hinz, P. M., Hoffmann, W. F., Brusa, G., Miller, D., & Kenworthy, M. A., 2005, *ApJ*, 618, L133

Lodato, G., & Rice, W. K. M., 2005, *MNRAS*, 358, 1489

Low F. J., & Smith B. J., 1966, *Nature*, 212, 675

Lucas, P. W. & Roche, P. E. 1998, *MNRAS*, 299, 723L

Lucy, L. B., 1999, *A&A*, 344, 282

Luhman, K.L., 1999, *ApJ*, 544, 1044

Luhman, K.L., 2000, *ApJ*, 544, 1044

Luhman, K.L.,Briceño, C., Rieke, G.H., & Hartmann, L., 1998, *ApJ*, 493, 909

Luhman, K. L., et al., 2005, *ApJ*, 631, 69

Lynden-Bell, D. & Pringle, J. E., 1974, *MNRAS*, 168, 603

MacCabe, C., Duchêne, G., & Ghez, A. M., 2003, *ApJ*, 588, 113

McCaughrean, M. J., & O'Dell, C. R., 1996, *AJ*, 111, 1977

Mahdavi, A., & Kenyon, S. J., 1998, *ApJ*, 497, 342

McKee, C. F., & Tan, J. C., 2002, *Nature*, 416, 59

Mannings, V., & Sargent, A. I., 1997, *ApJ*, 490, 792

————2000, *ApJ*, 529, 391

Martín, E. L., Delfosse, X., & Guieu, S, 2004, *AJ*, 127, 449

Martín, E.L., Dougados, C., Magnier, E, Ménard, F., Magazzú, A., Cuillandre, J.-C., & Delfosse, X. 2001, *ApJ*, 561, L195

Mathis, J.S., Rumpl, W., & Nordsieck, K.H., 1977, *ApJ*, 217, 425

Mayama S et al., 2006, *PASJ*, 58, 375

Meeuss, G., Waters, L. B. F. M., Bouwman, J., van den Ancker, M. E., Waelkens, C., & Malfait, K.,et al., 2001, *A&A*, 365, 476

Ménard, F., Bouvier J., Dougados C., Melnikov S. Y., & Grankin K. N., 2003, *A&A*, 409, 163

Mendoza V., & Eugenio E., 1966, *ApJ*, 143, 1010

Mendoza V., & Eugenio E., 1968, *ApJ*, 151, 977

Mestel, L., 1965, in *Protostars and Planets II*, Ed. D.C.Black, M. S. Matthews, 320

Metropolis, N. C., & Ulam, S. M., 1949, *The Monte-Carlo method J. Amer. Stat. Assoc.*,

44, 335

Meyer, M. R., Calvet, N., & Hillenbrand, L. A., 1997, *AJ*, 114, 288

Misselt, K. A., Gordon, K. D., Clayton, G. C., & Wolff, M. J. 2001, *ApJ*, 551, 277

Monnier, J. D. & Millan-Gabet, R. 2002, *ApJ*, 579, 694

Monin, L.-L. & Bouvier, J. 2000, *A&A*, 356, L75

Montmerle, T., Feigelson, E. D., Bouvier, J., & André, P. 1993, in *Protostars and Planets III*, Ed. E. H. Levy & J. I. Lunine (Tucson: Univ. Arizona Press), 689 Mouschovias, T. Ch., 1976, *ApJ*, 207, 141

Muench, A.A., Alves, J., Lada, C.J., & Lada, E.A., 2001, *ApJ*, 558, 51

Muench, A.A., Lada, E.A., Lada, C.J., & Alves, J., 2002, *ApJ*, 573, 366

Mundt, R., & Fried, J. W., 1983, *ApJ*, 274, 83

Mundy, L. G., et al., 1996, *ApJL*, 454, L169

Muzerolle, J., Bricẽno, C., Calvet, N., Hartmann, L., Hillenbrand, L., & Gullbring, E., 2000, *ApJ*, 545, L141

Muzerolle, J., Calvet, N., Hartmann, L., & D'Alessio, P., 2003b, *ApJL*, 597, L149

Muzerolle, J., D'Alessio, P., Calvet, N., & Hartmann, L., 2004, *ApJ*, 617, 406

Muzzerolle, J., Hillenbrand, L., Calvet, N., Briceño, C., & Hartmann, L., 2003a, *ApJ*, 592, 266

Muzerolle, J., Luhman, K. L., Briceño, C., Hartmann, L., & Calvet, N., 2005, *ApJ*, 625, 906

Myers, P. C., Fuller, G. A., Mathieu, R. D., Beichman C. A., Benson, P. J., Norman, C., & Silk, J., 1980, *ApJ*, 238, 158

Najita, J., Carr, J. S., & Mathieu, R. D., 2003, *ApJ*, 589, 931

Najita, J.R., Tiede, G.P., & Carr, J.S., 2000, *ApJ*, 541, 977

Nakajima, T. & Golimowski, D. A., 1995, *AJ*, 109, 1181

Nakajima, T., Oppenheimer, B. R., Kulkarni, S. R., Golimowski, D. A., Matthews, K., & Durrance, S. T. 1995, *Nature*, 378, 463

Natta, A., Grinin, V.P., & Mannings, V., 2000, in *Protostars and Planets IV*, Ed. V. Mannings, A. P. Boss, & S.S. Russell (Tucson: Univ. Arizona Press), 559

Natta A., Palla, F., Butner, H., Evans, N., & Harvey, P., 1993, *ApJ*, 406, 674

Natta, A., & Testi, L., 2001, *A&A*, 376, L22

Natta, A., Testi, L., Comerón, F., Oliva, E., D'Antona, F., Baffa, C., Comoretto, G., & Gennari, S., 2002, *A&A*, 393, 597

Natta, A., Prusti, T., Neri, R., Wooden, D., Grinin, V. P., & Mannings, V., 2001, *A&A*, 371, 186

Neckel T., & Klare G.,1980, *A&AS*, 42, 251

Nomura, H., & Millar, T. J., 2005, *A&A*, 438, 923

Norman, C., & Silk, J., 1980, *ApJ*, 238, 158

Oasa, Y., Tamura, M., & Sugitani, K., 1999, *ApJ*, 526, 336

O'Dell, C. R., & Wong, K., 1996, *AJ*, 111, 846

Oliveira, J. M., Jeffries, R. D., Kenyon, M. J., Thompson, S. A., & Naylor, T., 2002, *A&A*, 382, 22

O'Sullivan, M., PhD Thesis, University of St Andrews, in preparation O'Sullivan, M., Truss, M., Walker, C., Wood, K., Matthews, O., Whitney, B., Bjorkman, J. E., 2005, *MNRAS*, 358, 632

Paladini R., Burigana C., Davies R., Maino D., Bersanelli M., Cappellini B., Platania P., Smoot G., 2003, *A&A*, 397, 213

Padgett, D. L., Brandner, W., Stapelfeldt, K. R., Strom, S. E., Tereby, S., & Koerner, D. 1999, *AJ*, 117, 1490

Padman, R., Bence, S. J., & Richer, J. S. 1997, in *Herbig-Haro Flows and the Birth of Low-Mass Stars*, IAU *symp.* No. 182, Ed. B. Reipurth & C. Bertout (Dordrecht: Kluwer), 123

Padoan, P., & Nordlund, A., 2002, *ApJ*, 576, 870

Pantin, E., Bouwman, J., & Lagage, P. O., 2005, *A&A*, 437, 525

Patel, N. A., et al., 2005, Nature, 437, 7055, 109

Pavlenko, Y., Zapatero Osorio, M.R., & Rebolo, R., 2000, *A&A*, 355, 245

Peeters, E., Allamandola, L. J., Hudgins, D. M., Hony, S., & Tielens, A.G.G.M., 2004a, *ASPC*, 309, 141 Peeters, E., Spoon, H. W. W., & Tielens, A. G. G. M., 2004b, *ApJ*, 613, 986

Piétu, V., Dutrey, A., & Kahane, C., 2003, *A&A*, 398, 565

Press, W. H., Teukolsky, S. A., Vetterling, W. T., & Flannery, B. P. 1992, *Numerical Recipes in FORTRAN* (2d ed.; Cambridge Univ. Press)

Pringle, J. E. 1981, *ARA&A*, 19, 137

Pudritz, R. E., Ouyed, R., Fendt, C., & Brandenburg, A., 2005, in *Protostars and Planets V*, Sect. 3-5

Raga, A., & Cabrit, S. 1993, *A&A*, 278, 267

Ray, T. P., & Bacciotti, F., 2003, *RMxAC*, 15, 106

Rebolo, R., Zapatero Osorio, M. R., & Martín, E. L., 1995, *Nature*, 377, 129

Rebull, L.M., et al., 2002, *AJ*, 123, 1528

Reipurth, B., Chini, R., Krugel, E., Kreysa, E., Sievers, A., 1993, *A&A*, 273, 221

Reipurth, B., & Clarke, C., 2001, *AJ*, 122, 432

Ressler, M. E., & Barsony, M., 2003, *ApJ*, 584, 832

Rice W. K. M., Wood, K., Armitage P. J., Whitney B. A., Bjorkman J. E., 2003, *MNRAS*, 339, 1025

Richter, M. J., Lacy, J. H., Greathouse, T. K., Jaffe, D. T., & Blake, G. A., 2005, in *High Resolution Infrared Spectroscopy in Astronomy: Proceedings of an ESO Workshop*, Ed. H.

U. K:aufl, R. Siebenmorgen, and A. F. M. Moorwood (Springer-Verlag Berlin/Heidelberg), 197

Ruiz, M. T., et al., 1987, *ApJ*, 316, L21

Rydgren A. E., Schmelz J. T., & Vrba F. J., 1982, *ApJ*, 256, 168

Sasselov, D. D., & Lecar, M. 2000, *ApJ*, 528, 995

Schild R. E., & Emerson, J. P., 1987, *ApJ*, 319, 340

Schneider, G., Wood, K., Silverstone, M., Hines, D. C., Koerner, D. W., Whitney, B., Bjorkman, J. E., Lowrance P. J., 2003, *AJ*, 125, 1467

Schneider, G., et al., 2005, in *Protostars and Planets V*, LPI Contribution No. 1286, 8540

Scholz, A., Jayawardhana, R., & Wood, K., 2006a, *ApJ*, 645, 1498

Scholz, A., Jayawardhana, R., Wood, K., Meeus, G., Walker, C., & O'Sullivan, M., 2006b, in preparation

Scire, E., Penprase, B., & Akeson, R., 2004, *BAAS*, 36. 774

Sellgren, K., 1984, *ApJ*, 277, 623

Shakura, N. I., & Sunyaev, R. A., 1973, *A&A*, 24, 337

Shepherd, D. S., Claussen, M. J., & Kurtz, S. E., 2001, *Science*, 292, 1513

Schommer, R. A., et al., 2001, *BAAS*, 33, 1466

Shu, F.H., Adams, F.C., & Lizano, S., 1987, *ARA&A*, 25, 23

Shu, F., Najita, J., Ostriker, E., Wilkin, F., Ruden, S., & Lizano, S., 1994, *ApJ*, 429, 781

Skrutskie, M. F., Meyer, M. R., Whalen, D., & Hamilton, C. 1996, *AJ*, 112, 2168 Smith, B. A., & Terrile, R. J., 1984, *Science*, 226, 1421

Spitzer, L., 1978, in *Physical Processes in the Interstellar Medium* (New York: Wiley), 333

Spitzer, L., 1968, in *Nebulae and Interstellar Matter, Stars and Stellar Systems*, Ed. B. Middlehurst, L. H., Aller, 7:1. (Chicago: Univ. Press)

Stahler, S. W., 1983, *ApJ*, 274, 822

Stapelfeldt, K. R., Krist, J. E., Menard, F., Bouvier, J., Padgett, D. L., & Burrows, Ch. J., 1998a, *ApJ*, 502, L65

Stapelfeldt, K., & Moneti, A., 1999, in *The Universe as Seen by ISO* Ed. P. Cox & M. F. Kessler. ESA-SP 427., 521

Stapelfeldt, K.R., Padgett, D.L., Menard, F., Wolf, S. & Stecklum, B., 2005, in *Protostars and Planets V*, LPI Contribution No. 1286, 8540 Stapelfeldt, K. R., et al., 1998a, *ApJ*, 508, 736

Stapelfeldt, K. R., et al., 1999, *ApJ*, 516, L95

Stassun, K., & Wood, K., 1999, *ApJ*, 510, 892

Strom, S. E., Edwards, S., & Skrutskie, M. F., 1993, in *Protostars and Planets III*, Ed. Levy, E. H. & Lunine, J. I. (Tuscon: Univ. of Arizona Press), 837

Symington, N.H., 2004, *PhD Thesis*, Univ. of Exeter

Takeuchi, T., Velusamy, T., & Lin, D. N. C., 2005, *ApJ.* 618, 987

Tarter, J. C., 1975, *Ph.D Thesis*, Univ. California-Berkeley

Terebey, S., Shu, F. H., & Cassen, P., 1984, *ApJ*, 286, 529

Testi, L., Natta, A., Oliva, E., D'Antona, F., Comeron, F., Baffa, C., Comoretto, G., Gennari, S., 2002, *ApJ*, 571, L155

Toomre, A., 1964, *ApJ*, 139, 1217

Trilling, D. E., Koerner, D. W., Barnes, J. W., Ftaclas, C., & Brown, R. H., 2001, *ApJ*, 552, L151

Trilling, D. D., Lunine, J. I., & Benz, W., 2002, *A&A*, 394, 241

Uchida, K. I., Sellgren, K., & Werner, M. 1998, *ApJ*, 493, L109

Ulrich, R. K. 1976, *ApJ*, 210, 377

Unruh, Y. C., et al., 2004, *MNRAS*, 348, 1301

Vink, J. S., Drew, J. E., Harries, T. J., & Oudmaijer, R. D., 2002, *MNRAS*, 337, 356

Vrba, F. J., Rydgren, A. E., & Zak, D. S., 1985, *AJ*, 90, 2074

Walker, C., Wood, K., Lada, C. J., Robitaille, T., Bjorkman, J. E., & Whitney B. A., 2004, *MNRAS*, 351, 607

Waters, L. B. F. M., & Waelkens, C., 1998, *ARA&A*, 36, 233

Watson, A. M., & Stapelfeldt, K. R., 2004, *ApJ*, 602, 860

Watson, A. M., Stapelfeldt, K. R., Krist, J. E., & Burrows, C. J., 2000, *BAAS*, 32, 1481

Weidenschilling, S. J., 1980, *Icarus*, 44, 172

Weidenschilling, S. J., 1984, *Icarus*, 60, 553

Werner, M. W., et al. 2004, *ApJ*S, 154, 1

Wetherill, G. W., 1980, *ARA&A*, 18, 77

Whelan, E. T., Ray, T. P., Bacciotti, F., Natta, A., Testi, L., & Randich, S., 2005, in *Protostars and Planets V*, LPI Contribution No. 1286., 8073

White, R. L., 1979, *ApJ*, 229. 954

White, R. J., & Basri, G., 2003, *ApJ*, 582, 1109

White, R. J. & Ghez, A. M., 2001, *ApJ*, 556, 265

Whitney, B. A., & Hartmann, L. 1992, *ApJ*, 395, 529

—————1993, *ApJ*, 402, 605

Whitney, B.A., Kenyon, S.J., & Gomez, M., 1997, *ApJ*, 485, 703

Whitney, B. A., & Wolff, M. J., 2002, *ApJ*, 574, 205

Whitney, B. A., Wood, K., Bjorkman, J. E., & Cohen, M., 2003b *ApJ*, 598, 1079

Whitney, B. A., Wood, K., Bjorkman, J. E., & Wolff, M. J. 2003a, *ApJ*, 591, 1049

Whitworth, A. P., & Goodwin, S. P., 2005, *Astronomische Nachrichten*, 326, 89

Willner, S. P., 1984, in *Galactic and Extragalatic IR Spectroscopy*, Ed. M. F. Kessler, J. P. Phillips, Reidel, Dordrecht

Wilson, T. L., Beasley, A. J., & Wootten, H. A., 2005, *ASPC*, 344, 232

Witt, A. N., 1977, ApJS, 35, 1

Wolf, S., Gueth, F, Henning, T., & Kley, 2002, *ApJ*, 566, L97

Wolfire, M. G., & Cassinelli, J. P., 1986, *ApJ*, 310, 207

—————1987, *ApJ*, 319, 850 Wood, K., Bjorkman, J. E., Whitney, B. A., & Code, A. D., 1996a, *ApJ*, 461, 828

Wood, K., Kenyon, S. J., Whitney, B. A., & Bjorkmann, J. E., 1996b, *ApJ*, 458, L79

Wood, K., Kenyon, S. J., Whitney, B. A., & Turnbull, M., 1998, *ApJ*, 497, 404

Wood, K., Smith, D., Whitney, B., Stassun, K., Kenyon, S. J., Wolff, M. J., & Bjorkman, K. S. 2001, *ApJ*, 561, 299

Wood, K., Lada, C. J., Bjorkman, J. E., Kenyon, S. J., Whitney, B. A., & Wolff, M. J., 2002b, *ApJ*, 567, 1183

Wood, K., & Whitney, B. A., 1998, *ApJ*, 506, L43

Wood, K., Wolk, S. J., Stanek, K. Z., Leussis, G., Stassun, K., Wolff, M., & Whitney, B., 2000, *ApJ*, 542, L21

Wood, K., Wolff, M. J., Bjorkman, J. E., & Whitney, B. A., 2002a, *ApJ*, 564, 887

Wu, J., & Evans, N. J., 2003, *ApJ*, 592, L79

Yorke H. W., & Krügel, E., 1977, *A&A*, 54, 183

Yorke, H. W., & Sonnhalter, C. 2002, *ApJ*, 569, 846

Yusef-Zadeh, F., Morris, M., & White, R. L., 1984, *ApJ*, 278, 186

Zhang, Q., Hunter, T. R., & Sridharan, T. K., 1998, *ApJ*, 505, L151

Zhang, Q., Hunter, T. R., & Sridharan, T. K., & Ho, P. T. P., 2002, *ApJ*, 566, 982

Zucherman, B., Forvelle, T., & Kastner, J. H., 1995, *Nature*, 373, 494

Zuckerman, B., & Palmer, P. 1974, *ARA&A*, 12, 279